UNIVERSITÉ DE STRASBOURG

ECOLE DOCTORALE PHYSIQUE ET CHIMIE-PHYSIQUE (ED182)
INSTITUT PLURIDISCIPLINAIRE HUBERT CURIEN, CNRS, UMR 7178

THÈSE présentée par

Cécile BOPP

soutenue le : **13 Octobre 2014**

pour obtenir le grade de : **Docteur de l'Université de Strasbourg**
Discipline/Spécialité : **Physique subatomique pour la santé**

Le proton : sonde dosimétrique et diagnostique

The proton as a dosimetric and diagnostic probe

THÈSE dirigée par :

David BRASSE	Directeur de recherche, PHC Strasbourg
Marc ROUSSEAU	Maître de conférences, IPHC Strasbourg

RAPPORTEURS :

Katia PARODI	Professor, LMU München
Joël HERAULT	Physicien Médical, CAL Nice

EXAMINATEURS :

Benoît GALL	Professeur, IPHC Strasbourg
Jean COLIN	Professeur, LPC Caen

A ma maman,
qui m'a donné envie d'étudier la physique!

"I always heard there is no end to 'em. It's all down to dimensions, I heard, like what we see is only the tip of the whatever, you know, the thing that is mostly underwater –"
"Hippopotamus?"
"Alligator?"
"Ocean?"

– Terry Pratchett

REMERCIEMENTS

Ce manuscrit conclut trois années de travail au sein du groupe ImaBio de l'Institut Puridisciplinaire Hubert Curien. Ce furent trois années hautes en couleur et très enrichissantes.

Je remercie vivement Katia Parodi, Joël Hérault et Benoît Gall pour avoir participé à mon jury de thèse. Je tiens à remercier tout particulièrement Jean Colin, pour avoir été à l'origine de l'idée de ce travail de thèse. Merci, j'ai trouvé cela passionnant! Merci également pour l'intérêt porté à mon travail, et les discussions intéressantes qui s'en sont suivies.
Durant ces trois années, j'ai travaillé sous la direction de David Brasse et Marc Rousseau, envers lesquels je suis reconnaissante de la chance qu'ils m'ont donnée. Merci particulièment à David pour avoir été un "mentor" depuis bien plus longtemps que ça, et avoir grandement contibué à mon choix de carrière. Merci de m'avoir aiguillé dans ce travail, pour les discussions conceptuelles, et pour les quelques tirades dont je garde des citations... intéressantes. Merci chef!

Je tiens également à remercier les nombreuses personnes qui ont relu mon manuscrit. Chaque point de vue a été constructif. Merci donc à David et Marc, mais aussi à Patrice Marchand, Harold Barquero, Marie Vanstalle, Christian Finck, Valérie Brasse, Alex (non, tu n'auras pas le droit à ton nom entier), à mon père et surtout à Regina Rescigno, qui a lu ce document maintes et maintes fois!

Surtout, je tiens à remercier l'ensemble du groupe ImaBio. Quelqu'un m'a dit un jour que je m'amusais tellement à travailler que je ne remarquais même plus que je travaillais. Cela n'était pas faux. C'est grâce à tout le groupe.

J'ai eu la chance d'être accompagnée au quotidien par mes co-locataires successifs du bureau 138. Je remercie Khodor Koubar, pour avoir supporté mes grimaces pendant plus de deux ans. Je remercie Emmanuel Brard, pour l'ambiance qu'il a mis dans ce bureau (la différence a été notable après ton départ!), ainsi que pour toute l'aide qu'il m'a apporté et tout ce que j'ai pu apprendre en le regardant travailler. Je suis encore loin de coder aussi proprement, mais tu as été une bonne source d'inspiration! Je remercie également Harold Barquero, pour avoir fait ces trois ans de chemin avec moi. Ce fut un plaisir de partager les bons moments et les périodes de stress épiques avec toi! Je remercie aussi Benjamin Auer, mon jumeau caché / retrouvé, pour m'avoir rendu mes grimaces coup pour coup. Bon courage pour la suite! Enfin, je tiens à remercier tout particulièrement Regina Rescigno, pour la vie dans le bureau, ainsi que pour les heures et jours de discussions sur l'imagerie proton. Je suis ravie que nous ayons pu partager ce thème de travail. Ce fut un plaisir de travailler avec toi dans la bonne humeur et avec une motivation infaillible.

Et au reste du groupe, qui a rendu chaque jour très agréable, merci également. Merci au chef, pour l'animation du groupe. Je remercie aussi tout particulièrement Virgile Bekaert, pour la place réservée dans son bureau et pour m'avoir bien aidé à conserver ce qu'il me reste de santé mentale pendant la rédaction. Merci aussi à Bernard Humbert, pour le petit moment de discussion qui met de bonne humeur tous les matins... j'attends encore la neige! Je remercie également Ali Ouadi et Patrice Marchand, pour leur humour toujours très délicat. Patrice, merci non seulement pour ta companie "agréable" en pause café, mais aussi pour toutes les discussions qui m'ont permis d'avoir une meilleure vue d'ensemble sur beaucoup de choses. Je tiens à remercier Jacques Wurtz, qui sait toujours tout! Merci également à Lionel Thomas, pour avoir motivé l'équipe piscine. Je ne pense pas que j'aurais tenu si longtemps sans ta motivation sans faille. A Patrice Laquerrière, je tiens à dire merci du fond du coeur pour la glace! Je remercie également Bruno Jessel, pour les karaokés dont je garde des souvenirs... terrifiants! Merci aussi à Marie Vanstalle, pour les *"clap clap clap clap clap"* et à Christian Finck, pour avoir été une bonne victime de nos sourires. Et merci Marc, pour avoir ajouté un côté salé aux pauses café. Et je n'oublie évidemment pas les autres, qui ont participé à la bonne humeur et à l'ambiance du groupe durant ces trois ans : Nicholas Chevillon, Arnaud Bertrand, Ziad El Bitar, Jean-Michel Galonne, Jackie Sahr, Rachid Sefri, Xiaochao Fang et Christian Fuchs.
Merci à tous, et tout spécialement merci pour les pingouins lors de ma soutenance! Vous étiez beaux avec vos t-shirts!

Merci également à Nicholas Rudolf et Christophe Helfer, qui ne font pas partie d'ImaBio, mais c'est comme si...

Je tiens ensuite à remercier tous mes amis, les facultatifs évidemment, qui m'ont accompagnée depuis bien longtemps et en particulier pendant ces années de thèse. Merci Julien, Nono, Camille, Papillon, Tutur, Aurore, Max, Christophe, Manu, Marsou, Anne-Cha, Cécile, Marc et Marie-Laure.

J'exprime également toute ma gratitude envers ma famille, qui m'a toujours soutenue et encouragée dans mes choix. Merci à mes parents. Un clin d'oeil spécial à ma maman, sans qui j'aurais dû manger au RU... je suis convaincue que ta cuisine à été déterminante dans ma réussite de cette thèse! A Muriel, Emilie, Jean-Christophe et Nathan, pour avoir été là pour moi.
Merci également à Marie-Odile, qui a grandement participé au succès qu'a été mon pot de thèse ainsi qu'à Noélie et Nina: le jour de ma soutenance a été l'accomplissement de ma thèse, mais aussi de ce que j'attendais depuis de nombreuses années (LE coussin!!). Merci à tous ceux qui sont venus pour ma soutenance, et à ceux qui n'ont pas pu venir

mais qui ont pensé à moi.
Merci aussi à François, pour s'être toujours enquis de l'avancement de mes travaux, en me demandant semaine après semaine : *"Alors, tu les as trouvés tes protons?"*.

Enfin, merci Alex, pour avoir été à mes côtés pendant cette aventure qu'a été la thèse. Merci de m'avoir soutenue et supportée, merci pour tout!

Contents

SUMMARY IN FRENCH
RÉSUMÉ DE LA THÈSE EN FRANÇAIS

Le cancer est la première cause de mortalité au monde [International Agency for Research on Cancer, 2008]. Avec une élévation continue des risques, le nombre de morts dues au cancer est en constante augmentation. Trois grandes catégories de traitements sont accessibles de nos jours : la chirurgie, la radiothérapie et les traitements médicamenteux (chimiothérapie et immunithérapie). Au total, près de la moitié des patients atteints de cancer sont traités par radiothérapie, seule ou combinée à un autre traitement. La radiothérapie dite “conventionnelle” est basée sur l'utilisation de rayons X afin d'irradier un tissu cancéreux. Cependant, il est également possible d'utiliser des particules chargées pour déposer de l'énergie dans l'organisme. L'idée date de 1946, lorsque Robert R. Wilson suggère que la forme du dépôt de dose de protons, caractérisé par un pic en fin de parcours, pourrait être avantageuse lors d'un traitement [Wilson, 1946]. Depuis une décénie, les méthodes thérapeutiques utilisant des faisceaux de protons ou d'ions carbones (nommées de façon générale hadronthérapie) sont en plein essor. Il y a, à l'heure actuelle, deux centres de traitement par protonthérapie en France : le Centre Antoine Lacassagne à Nice et le Centre de Protonthérapie d'Orsay. Dans le cadre du projet d'infrastructure “France HADRON”, deux projets de centres de traitement par ions carbones sont également évoqués: le projet ETOILE à Lyon et le projet ARCHADE à Caen.

Deux arguments existent pour l'utilisation de particules chargées en radiothérapie. Le premier est qu'elles présentent un atout de nature physique : la courbe de dépôt de dose en profondeur des particules chargées est intrinsèquement plus avantageuse que celle des photons (comme illustré sur la Figure 1.1 page 7). Le pic de Bragg en fin de parcours des particules permet de cibler précisément une zone à irradier, tout en épargnant de façon efficace les tissus sains adjacents. Il n'y a, dans le cas d'une irradiation avec des protons, aucune dose déposée en aval du pic de Bragg. Pour les particules plus lourdes, telles les ions carbone, la courbe de dépôt de dose présente une extension, c'est à dire un dépôt de dose en aval du pic de Bragg, dûe aux particules secondaires génerées par les interactions nucléaires. Le deuxième argument, qui concerne principalement les ions carbones, est qu'il existe un avantage biologique à l'utilisation de ces particules. En effet, le transfert d'énergie linéique (TEL) des ions carbone est bien plus élevé que celui des photons. De ce fait, les ionisations au passage des particules sont plus concentrées autour de la trace de l'ion et la probabilité de générer des lésions complexes à l'ADN, c'est-à-dire de détruire efficacement des cellules, est plus grande. De plus, les particules à TEL élevé présentent également une efficacité accrue sur les tumeurs hypoxiques. L'avantage du carbone n'est pas tant le TEL élevé (c'est également le cas des neutrons) mais le fait qu'il augmente au fur et à mesure de la propagation dans le matériau, venant renforcer l'avantage conféré par le pic de Bragg.

La planification de traitement en hadronthérapie est calculée à partir d'images acquises avec un tomodensitomètre X. Elle peut être basée soit sur des modèles de propagation analytiques des faisceaux, soit sur des simulations Monte Carlo. Dans le premier cas, il faut connaître le pouvoir d'arrêt des matériaux afin de prédire la position du pic de Bragg; dans le second, il faut connaître la densité et la composition chimique des matériaux. Dans les deux cas, une conversion de l'image de tomodensitométrie X, représentant les coefficients d'atténuations moyens de rayons X, est nécessaire. Ces conversions ne sont ni linéaires, ni bijectives, et introduisent une incertitude sur le parcours des particules [Jiang et al., 2007; Yang et al., 2012; Paganetti, 2012]. A cela s'ajoute une incertitude sur les valeurs reconstruites dans l'image de tomodensitométrie X, dûe à des phénomènes physiques tel que le durcissement de faisceau, à des effets de reconstruction tels la taille des voxels, le bruit, les effets de volume partiel ou les artéfacts métalliques [Schaffner and Pedroni, 1998; Chvetsov and Paige, 2010; España and Paganetti, 2011; Wei et al., 2006; Jäkel et al., 2007]. Au final, l'incertitude sur le parcours des particules a comme conséquence l'élargissement des marges nécessaires autour de la zone à irradier. Des exemples de marges sont donnés par Paganetti [2012]: 3.5% du parcours + 1 mm pour le Massachussets General Hospital; 3.5% du parcours + 3 mm pour le MD Anderson Proton Therapy Center, Loma Linda University Medical Center, Roberts Proton Therapy Cernter; et 2.5% + 1.5 mm pour le University of Florida Proton Therapy Institute.
A cette incertitude s'ajoute également une incertitude sur la dose déposée. Celle-ci provient d'une incertitude sur l'efficacité biologique relative (la pondération à apporter à la dose physique déposée pour obtenir la dose biologique), ainsi que d'une incertitude sur la dose physique déposée. En effet, pour prédire avec précision la dose déposée, il faut connaître non seulement les pouvoirs d'arrêt des matériaux, mais également la diffusion des particules ainsi que les interactions nucléaires. Pour la planification de traitement analytique, une conversion à partir des images de tomodensitométrie X est possible. Comme pour les pouvoirs d'arrêt, des courbes de calibration ont été établies [Szymanowski and Oelfke, 2003; Palmans and Verhaegen, 2005; Batin, 2008]. Cela permet de réduire les erreurs à quelques pourcents. Cependant, dans la mesure où les processus physiques impliqués sont très différents, ces conversions restent approximatives.

Lors d'une planification de traitement par rayons X, l'image de tomodensitométrie qui est utilisée est acquise en utilisant la même sonde que pour le traitement. Dans la mesure où ça n'est pas le cas en hadronthérapie, des conversions sont nécessaires. Les incertitudes induites par la conversion d'informations représentatives des interactions de photons dans la matière en interactions de particules chargées font que les traitements en hadronthérapie ne sont probablement pas aussi précis qu'ils pourraient l'être. L'imagerie proton a été proposée comme solution afin de cartographier directement les pouvoirs d'arrêts des tissus et de s'affranchir ainsi de la conversion des images X. Cela permettrait de réduire l'incertitude sur le parcours des particules, de diminuer les marges autour de la zone à irradier et ainsi d'accroître l'intérêt et l'efficacité de la hadronthérapie.

La recherche en imagerie proton est passée par deux phases distinctes. Entre les années 1960 et 1980, l'utilisation des protons en imagerie médicale a été étudiée sans *a priori*. Pendant cette période, différentes possibilités pour l'utilisation des protons ont été examinées:

- L'imagerie proton utilisant la perte d'énergie des particules [Cormack, 1963, 1964; Cormack and Koehler, 1976; Hanson et al., 1978]. Le principe est détaillé plus loin dans le texte. Les bases de l'imagerie proton telle qu'elle est étudiée actuellement, utilisant la perte d'énergie des protons pour produire des images du pouvoir d'arrêt des particules dans les tissus, ont été établies. Des expériences ont été menées, et il en est ressorti que la qualité des images produites était similaire à celle obtenue en tomodensitométrie X, pour une dose inférieure. L'impact des multiples diffusions de Coulomb sur la résolution spatiale des radiographies était important, mais pas rhédibitoire dans la mesure où l'imagerie X était également de moindre qualité que de nos jours. Cependant, comme aucun avantage significatif en matière de diagnostic n'a été montré et qu'une installation avec un accélerateur est nettement plus coûteuse qu'un tube à rayons X, l'idée a été délaissée.

- L'imagerie proton utilisant la fin de parcours [Koehler, 1968; Steward and Koehler, 1973*b*,*a*, 1974; Steward, 1976]. Il s'agit d'une imagerie de transmission, où le nombre de protons transmis est compté. L'objet à imager est placé dans un bain d'eau, afin que la même longueur soit parcourue par le faisceau pour toutes les positions d'une radiographie. L'énergie du faisceau est choisie de sorte que la position du film radiographique, en sortie de la cuve d'eau, corresponde à la pente descendante du pic de Bragg. Ainsi, une faible variation dans la densité de matériau traversé résulte en un décalage de la position du pic, qui se traduit par une importante différence dans le nombre de particules détectées. Outre les diffusions de Coulomb, l'inconvénient principal de cette méthode est la nécessité de plonger l'objet dans un bain d'eau et d'ajuster l'énergie du faisceau et le contraste pour chaque objet imagé.

- L'imagerie utilisant les diffusions nucléaires [Saudinos et al., 1975; Charpak et al., 1976; Berger and Duchazeaubeneix, 1978; Charpak et al., 1979]. Des protons de haute énergie (entre 500 MeV et 1 GeV) sont envoyés sur un objet et les protons largement déviés par les interactions quasi-élastiques avec les noyaux sont détectés. Les vertex d'interactions peuvent ensuite être reconstruits et sont indicatifs de la composition de matériaux. Les images reconstruites étaient, à l'époque, de qualité similaire à l'imagerie X. En outre, il a été montré que l'utilisation des informations sur les noyaux de reculs détectés permet de produire des images correspondant à la concentration en hydrogène des matériaux. Comme pour les autres méthodes d'imagerie utilisant les protons, les travaux se sont arrêtés au début des années 1980. Il est raisonnable de penser que cela est dû aux progrès en imagerie X et à l'émergence de l'imagerie par résonance magnétique permettant de visualiser l'hydrogène dans les tissus.

– L'imagerie utilisant les diffusions multiples [West and Sherwood, 1972; West, 1975]. L'idée est de détecter les interfaces entre différents matériaux en exploitant les irrégularitées génerées sur le flux de photons. Des objets relativement fins sont imagés avec des faisceaux d'assez haute énergie (150-200 MeV pour des souris) afin que l'amplitude des diffusions soit relativement faible et que le flux soit peu atténué. Cette méthode étant difficilement applicable à des objets épais, aucune utilisation clinique n'a pu être envisagée.

A la fin de cette période d'exploration, les travaux sur l'imagerie proton ont été délaissés au profit d'autres modalités d'imagerie médicale. Au début des années 1990, la hadronthérapie a géneré un regain d'intérêt pour l'imagerie proton utilisant la perte d'énergie des particules, afin de l'utiliser à la place de l'imagerie X pour la planification de traitement.

Le principe est le suivant : des protons, d'énergie suffisamment élevée pour que le pic de Bragg se situe en aval de l'objet, sont envoyés (typiquemment, 200 MeV pour l'image d'une tête, 250 MeV pour un torse). En mesurant l'énergie ou le parcours résiduel des particules en sortie, et en se basant sur l'équation de Bethe-Bloch décrivant la perte d'énergie de particules chargées dans un milieu, il est possible de reconstruire une image des pouvoirs d'arrêt relatifs des matériaux (relatifs à celui de l'eau). Ce processus est détaillé dans l'équation 2.14 page 45. Il est à noter que l'équation de Bethe-Bloch décrit la perte d'énergie moyenne des particules sur leur chemin. Du fait des diffusions multiples de Coulomb, considérer que les protons traversent l'objet en ligne droite résulte en une résolution spatiale dans l'image reconstruite très dégradée.

Afin de pouvoir tenir compte au mieux de la trajectoire de chaque proton, un tomographe à protons est constitué, en plus du calorimètre ou détecteur de parcours ("range-meter"), de deux ensembles d'au moins deux trajectographes, en amont et en aval du patient [Schulte et al., 2004]. Un tel système est illustré sur la Figure 2.6 page 46. Plusieurs groupes ont développé des prototypes de scanners à protons, basés sur différentes technologies : détecteurs gazeux, détecteurs à scintillation ou détecteurs silicium pour la trajectographie [Pemler et al., 1999; Gearhart et al., 2012; Saraya et al., 2013; Sadrozinski et al., 2013; Civinini et al., 2013; Amaldi et al., 2011]; calorimètres en cristal inorganiques, ou détecteurs de parcours en scintillateurs plastiques pour la mesure de l'énergie ou du parcours résiduel [Pemler et al., 1999; Gearhart et al., 2012; Saraya et al., 2013; Sadrozinski et al., 2013; Civinini et al., 2013; Amaldi et al., 2011; Hurley et al., 2012].

Les études publiées jusqu'à présent indiquent qu'une résolution sur les pouvoirs d'arrêts reconstruits de l'ordre de 1% (ce qui serait satisfaisant pour la planification de traitement) est atteignable en imagerie proton, pour une dose inférieure à celle délivrée lors d'une acquisition tomographique en rayons X [Schulte et al., 2005; Erdelyi, 2010]. En ce qui concerne la résolution spatiale, les études ont montré qu'une résolution spatiale de l'ordre de 1 mm pourrait être atteinte, ce qui serait satisfaisant pour la planification de traitement [Penfold et al., 2010; Rit et al., 2013]. Cependant, la résolution spatiale dans une image est très dépendante de l'algorithme de reconstruction choisi.

Il y a actuellement deux catégories d'algorithmes de reconstruction considérés pour l'imagerie proton. D'une part, la reconstruction analytique, basée sur des données

arrangées en projections; d'autre part les reconstructions basées sur des méthodes algébriques, qui peuvent être effectuées en mode liste, c'est à dire proton à proton. Cette deuxième catégorie est particulièrement adaptée à la prise en compte de la trajectoire individuelle de chaque particule.
L'approximation la plus précise dont on dispose actuellement pour l'estimation de la trajectoire d'une particule dans un milieu est la trajectoire la plus probable dans un milieu homogène [Williams, 2004; Schulte et al., 2008]. Celle-ci est calculée à partir des informations sur les positions et directions de chaque proton, en entrée et sortie de l'objet considéré. Pour l'imagerie proton, nous supposons que l'objet est constitué d'eau. En utilisant une approximation gaussienne aux diffusions multiples de Coulomb, il est possible d'exprimer la probabilité de passage d'une particule à une position et avec un angle donné, connaissant ses positions et directions en entrée et en sortie.

L'idée principale de ces travaux de thèse est d'étudier le potentiel de l'imagerie proton, sur la base d'un système idéal. Un système tel qu'étudié actuellement permet d'avoir accès, en plus de l'information sur l'énergie ou le parcours restant, à des informations sur le taux de transmission des particules ainsi que sur la diffusion de chaque proton. Actuellement, ces données ne sont pas exploitées en tant que sources potentielles d'informations sur les matériaux. Cependant, elles sont représentatives des interactions des particules dans la matière. En partant de cette constatation, le but a été de déterminer si, et dans quelle mesure, ces données peuvent être exploitées. Quelles informations sur les matériaux peut-on en extraire? Y a-t-il un intérêt, pour le diagnostic ou pour améliorer la planification de traitement, à utiliser ces informations?

Afin d'étudier un tomographe à protons, des simulations Monte Carlo utilisant Geant4 [Agostinelli et al., 2003] on été effectuées. Un scanner à protons a été simulé en utilisant la plateforme Gate [Jan et al., 2011], qui est basée sur le code Geant4. L'avantage de Gate est que la plateforme a été développée spécifiquement pour les activités en imagerie médicale, simplifiant la gestion du temps et des mouvements de détecteurs. Les outils nécessaires à la reconstruction d'images ont été implémentés lors de cette thèse.

Une étude préliminaire (section 5.1 page 106), considérant un faisceau de protons mono-énergétique et unidirectionnel envoyé dans des cubes de matériaux homogènes, a été effectuée. Différentes observables ont été définies : la moyenne de la distribution en énergie, la déviation standard de la distribution en énergie, l'angle moyen de sortie ainsi que le taux de transmission des particules. Les résultats ont indiqué que l'information sur la déviation standard de la distribution en énergie ne sera pas exploitable : les valeurs observées varient très peu selon les matériaux, et une résolution en énergie du calorimètre de l'ordre de 0.1% serait nécessaire. Les informations sur la diffusion et le taux de transmission de particules, pourraient cependant être utilisables afin d'aider à distinguer des matériaux présentant des pouvoirs d'arrêt proches. Néanmoins, l'incertitude statistique sur ces observables est beaucoup plus élevée que sur l'énergie mesurée, ce qui sera un désavantage majeur pour l'exploitation de ces données. Afin de pouvoir considérer un nombre élevé de protons sans déposer une forte dose dans une région localisée, des acquisitons tomographiques ont été considérées.

Une étude de reconstruction qualitative des informations sur la transmission et la diffusion des particules a été menée (section 5.2 page 112). Une acquisition tomographique d'un fantôme de tête, dans laquelle deux tumeurs de compositions chimiques différentes mais de pouvoir d'arrêt similaire ont été insérées. Différentes images ont été reconstruites, en utilisant un algorithme de reconstruction analytique :

- des images du pouvoir d'arrêt relatif, pour réference.
- des images utilisant directement l'information sur l'angle moyen des particules en sortie.
- des images utilisant une information sur la diffusion cumulée. En effet, il est possible que deux particules entrent et sortent d'un objet avec le même angle, mais en ayant diffusé de manière différente. Afin d'avoir une information plus représentative du parcours des particules, la trajectoire de chaque proton a été estimée utilisant la trajectoire la plus probable. La diffusion cumulative a ensuite été définie comme la distance de déviation spatiale entre l'entrée et la sortie de l'objet, calculée en additionnant le module de l'angle de diffusion à chaque profondeur estimée. Ceci est représenté sur la figure 5.5 page 114.
- des images utilisant le taux de transmission des protons, reconstruites de façon similaire à l'imagerie X, en considérant la loi d'atténuation de Beer-Lambert.
- des images utilisant un taux de transmission linéaire, pour laquelle seuls les protons détectés avec une déviation spatiale inférieure à un seuil (ici, 10 mm) sont considérés comme transmis.

Le rapport signal à bruit, le contraste et le rapport contraste à bruit dans des régions d'intétêt des images ont été étudiés. Les résultats montrent que l'utilisation des différentes informations permet d'améliorer le contraste entre des régions de pouvoirs d'arrêt similaires et d'accentuer des différences de composition entre les tissus. L'image de diffusion cumulée, en particulier, présente des caractéristiques visuelles très intéressantes : un contour d'intensité plus élevée à l'interface de certains tissus permet de distinguer facilement les tumeurs. Cela pourrait être un atout en matière de diagnostic. Bien que les études actuelles sur l'imagerie proton ne soient pas axées sur l'utilisation potentielle en diagnostic, ces résultats pourraient inciter à reconsidérer la question.

Cependant, les images présentant les propriétés visuelles les plus intéressantes en terme de contraste et de détectabilité des tumeurs sont également les plus difficiles à interpréter de manière quantitative. En effet, les valeurs reconstruites dans les voxels des images de diffusion, diffusion cumulative et transmission linéaire en particulier sont représentatives de plusieurs processus physiques. Afin de pouvoir extraire des informations quantitatives des images reconstruites en utilisant la diffusion et la transmission des protons, les processus physiques impliqués ont été examinés plus en détails (section 5.3 page 127) :

- le taux de transmission des particules dans un milieu est représentatif des interaction nucléaires inélastiques. Dans la gamme d'énergie utilisée en imagerie proton (80 à 250 MeV), les sections efficaces d'interactions nucléaires de la plupart des élements constituant les tissus sont dans une région de plateau, et donc constantes. De ce fait, une reconstruction de coefficient d'atténuation, sur le même principe que l'imagerie X, permet de reconstruire une carte de ces sections efficaces d'interactions nucléaires.

- la diffusion de particules chargées dans un milieu dépend des propriétés en termes de diffusion du dit milieu, ainsi que de l'énergie des particules (et donc les propriétes des matériaux en termes de perte d'énergie). De ce fait, l'information sur la diffusion des protons qui est enregistrée à la sortie de l'objet est le résultat de ces deux propriétés. Afin d'isoler la partie dépendant uniquement des propriétés de diffusion, il est nécessaire d'estimer l'énergie des particules. Cela peut être fait en utilisant l'image de pouvoir d'arrêt relatif. En conséquence, les deux composantes peuvent être déconvoluées, et il est possible de cartographier les propriétés de diffusion des tissus, représentés dans ce travail par la longueur de diffusion ("scattering length" en anglais).

Les résultats ainsi obtenus constituent la preuve de concept qu'il est possible de reconstruire des images quantifiables en utilisant les informations sur la diffusion et le taux de transmission des protons. Dans le contexte de la planification de traitement en hadronthérapie, deux applications peuvent être entrevues : la première est l'utilisation directe de ces informations pour la planification de traitement analytique; la seconde est l'extraction des informations sur la composition stoechiométrique des matériaux afin d'améliorer la planification de traitement basée sur la simulation Monte Carlo. Les résultats obtenus ont permis de mettre en évidence que l'on dispose, au final, de trois équations pour caractériser chaque matériau (une venant du pouvoir d'arrêt relatif, une de la diffusion, une de la transmission). Le détail est présenté section 5.3.3 page 134. Cependant, il faut connaître la densité ainsi que les proportions massiques de tous les élements pour caractériser un matériau. De ce fait, déterminer directement la composition chimique à partir des informations obtenues est impossible, car le système est sous-déterminé. Néanmoins, l'information additionnelle obtenue par la diffusion et le taux de transmission pourrait être utilisée comme contrainte supplémentaire lors d'une conversion de l'image des pouvoirs d'arrêt en composition chimique.

Les limites de ces deux approches pour améliorer la planification de traitement en hadronthérapie dépendront toutefois de la précision et de l'exactitude des images de sections efficaces d'interactions nucléaires et des longueurs de diffusion reconstruites. Les images reconstruites dans ce travail souffrent d'un bruit important, dû à l'incertitude statistique sur les mesures, et d'une résolution spatiale limitée. Il est possible de diminuer l'impact de l'incertitude statistique en augmentant le nombre de particules utilisées pour une acquisition (en multipliant par 10, c'est-à-dire en utilisant 1000 protons par millimètre carré de projection et 256 projections, la dose à l'objet est du même ordre que lors d'une acquisition avec un tomodensitomètre X). Plusieurs pistes pour améliorer la qualité de ces images ont été dégagées à l'issue de ce travail et sont brièvement résumées dans les deux paragraphes suivants.

- Imagerie de transmission :

  Bien qu'augmenter d'un facteur supérieur à dix le nombre de particules étudiées ne puisse pas être envisagé en raison de la dose, il serait possible de réarranger le nombre de protons par projection et le nombre de projections. Cela permettrait d'atteindre un équilibre différent, potentiellement plus favorable, entre l'incertitude statistique et les effets en termes de reconstruction d'images dûs à la réduction du nombre de projections.

  La trajectoire rectiligne utilisée pour la reconstruction analytique du taux de transmission pourrait être complexifiée. Il serait possible d'améliorer les images reconstruites en considérant un chemin de projection et rétro-projection plus réaliste, tenant compte de la diffusion des particules au fur et à mesure de leur propagation. Une possiblilité pour cela serait dans un premier temps de considérer que l'objet est constitué d'eau. Il serait également possible d'utiliser l'image de diffusion afin d'adapter l'élargissement du faisceau constitué par les protons considérés en fonction des matériaux traversés.

  La supposition que les sections efficaces d'interactions nucléaires sont constantes dans la gamme d'énergie utilisée est moins appropriée pour les élements les plus lourds tel que le calcium présent dans les os par exemple. Pour améliorer cette approximation, il serait possible de procéder de manière itérative, en utilisant une première image pour segmenter l'os, estimer la proportion d'élements lourds, et corriger la reconstruction des sections efficaces d'interaction en fonction de l'énergie des particules (qui peut être estimée, ici aussi, à partir de l'image de pouvoir d'arrêt).

- Imagerie de diffusion :

  Une reconstruction proton à proton, en mode liste et tenant compte de la trajectoire de chaque particule, pourrait permettre d'améliorer la résolution spatiale des images de la longueur de diffusion. Dans un cadre différent, l'imagerie utilisant les muons cosmiques pour détecter les matériaux à numéro atomiques élevés pour des applications de sécurité, utilise également la diffusion des particules [Perry, 2013]. Un algorithme statistique, muon à muon, a été proposé [Schultz et al., 2007]. La grande différence par rapport à l'imagerie proton est que dans notre cas, il faudra tenir compte de la perte d'énergie dans l'objet. Or, la méthodologie présentée précédemment, utilisant l'image de pouvoir d'arrêt, permet de faire cela. Un algorithme statistique, type ML-EM, pour une reconstruction proton à proton, pourrait donc être considéré.

Pour ce travail, les reconstructions des différents processus physiques ont été effectuées de manière séparée. Cependant, un parangon d'algorithme de reconstruction pour l'imagerie proton serait multi-paramétrique afin de prendre en compte toutes les informations simultanément. Un algorithme statistique serait un bon candidat, avec pour but de maximiser la probabilité de détecter un ensemble de {longueur équivalent eau (énergie), taux de transmission, diffusion} pour chaque particule ou groupe de particules considéré.

De telles perspectives ne sont pas uniques à l'imagerie proton et des études similaires pourraient être menées en imagerie carbone par exemple.

Le travail présenté dans cette thèse et la preuve de concept de la possibilité d'une imagerie quantitative utilisant la diffusion et le taux de transmission de protons, sont basés sur des simulations Monte Carlo. De ce fait, en plus de l'optimisation des algorithmes de reconstruction, une validation sur des données expérimentales sera nécessaire avant de conclure réellement sur le potentiel de l'approche proposée.

Dans des conditions cliniques, deux facteurs additionnels devront être considérés : les caractéristiques du faisceau et les caractéristiques des détecteurs.
Les caractéristiques du faisceau en termes de dispersion en énergie et de dispersion spatiale auront un impact sur les résultats. La dispersion en énergie impactera principalement l'image de pouvoir d'arrêt, mais également toute autre image basée sur la perte d'énergie. La dispersion spatiale et angulaire du faisceau aura des conséquences négatives sur les images reconstruites à partir des données organisées en projections. Une reconstruction particule à particule, pour le pouvoir d'arrêt et la diffusion, pourra atténuer cet effet.
Les caractéristiques du système de trajectographie joueront un rôle essentiel dans l'imagerie de la diffusion et du taux de transmission des protons. Pour la transmission, une efficacité de détection inférieure à 100% ajoutera à l'incertitude statistique déjà importante. En ce qui concerne l'imagerie utilisant la diffusion des protons, il est probable que, si un intérêt clinique y est trouvé, des trajectographes avec une résolution spatiale meilleure que celle des prototypes actuels seront préférés.
L'effet des propriétés du système de trajectographie, plus précisément de la résolution spatiale, du budget de matière ("material budget", rapport entre l'épaisseur et la longueur de radiation du matériau) et du positionnement des trajectographes sur l'estimation de la trajectoire la plus probable a également été étudié (section 4.3 page 92). Pour ce faire, une formulation analytique de la propagation d'incertitude a été développée. La méthode proposée permet de mettre en avant les points clés dans le développement d'un système de trajectographie pour un tomographe à protons. La résolution spatiale et le budget de matière sont de la plus haute importance. Cependant, pour un système donné, la position des plans de trajectographe peut être optimisée afin de limiter l'erreur sur la trajectoire. Cette méthode pourra être utilisée dans les phases de recherche et de développement afin de comparer des choix instrumentaux.

De manière plus génerale, le cahier des charges d'un tomographe à protons en termes de flux de particules à soutenir est représentatif des défis qu'il reste à relever avant que ce type de système puisse être utilisé en routine clinique pour la planification de traitement. Il est estimé que la durée d'une acquisition devrait être de l'ordre de 5 minutes [Schulte et al., 2004]. Pour obtenir une résolution suffisante sur les pouvoirs d'arrêts reconstruits, il faut utiliser environ 100 fois plus de protons qu'il n'y a de voxels dans l'image [Sadrozinski et al., 2011]. Pour une image de tête, de 300×300×200 mm^3 avec des voxels de 1 mm^3, et en comptant qu'environ 20% des protons sont arrêtés en raison des interactions nucléaires, cela revient à un flux de particules de 7.5 MHz (sur tout le détecteur). Cependant, la structure temporelle du faisceau de l'accélerateur doit également être considérée. L'accélérateur du centre de protonthérapie d'Orsay est un cyclotron IBA Proteus 235 qui délivre des paquets de protons de 3.2 ns toutes les 9.37 ns [Richard, 2012] : cela ne pose pas de défi particulier au niveau des détecteurs. Le nouvel accélerateur du centre de protonthérapie de Nice est un IBA S2C2, un synchrocyclotron qui délivre des paquets de 50 µs toutes les 1 ms [Conjat et al., 2013]. Pour obtenir un taux moyen de particules de 7.5 MHz, le taux de particules au sein d'un paquet doit être d'environ 150 MHz. Il faut également noter que les accélérateurs de traitement ne sont pas conçus pour délivrer des intensités aussi basses (7.5 MHz de particules représente une intensité de 1.2 pA) et qu'il faudra donc adapter la ligne de faisceau pour l'imagerie.

Au début de ce travail de thèse, le système d'acquisition du prototype le plus rapide pouvait soutenir un flux limité à 1 MHz par le calorimètre [Johnson et al., 2013]. Au vu des flux de protons à soutenir pour passer en routine clinique, tout laisse à penser que pour les prochaines génerations de prototypes, des scintillateurs plastiques rapides seront préférés pour la mesure d'énergie ou de parcours restant. Un résultat encourageant en ce sens est l'annonce très récente d'un nouveau système, basé sur des fibres scintillantes pour la trajectographie et le détecteur de parcours [Lo Presti et al., 2014]. Ce prototype en cours de développement devrait pouvoir soutenir des flux de 10 MHz.

L'imagerie proton est une modalité exceptionnelle, dans la mesure où chaque particule subit une longue série d'interactions et que chaque interaction est une source d'information sur le matériau traversé. Cela génère des défis, notamment en terme de traitement de données, reconstruction d'images et d'analyse. Cependant, il s'agit également d'une formidable source d'informations. Au vu des résultats présentés dans cette thèse, l'utilisation des informations sur la diffusion et le taux de transmission des particules pour obtenir des informations qualitatives pourrait avoir un intérêt diagnostique. Les images reconstruites en utilisant la diffusion cumulée, en particulier, permettent de distinguer clairement les tumeurs dans le cerveau.
Dans le contexte de la hadronthérapie, il y a actuelement deux applications à l'imagerie proton. La première est l'imagerie portale, afin de vérifier le positionnement du patient ou d'utiliser le faisceau de protons comme sonde pour vérifier que leur parcours est en adéquation avec ce qui est prédit dans la planification de traitement. La deuxième est l'utilisation de la tomographie proton afin d'être utilisée comme base pour la planification de traitement. Pour la planification de traitement analytique, l'imagerie proton permet de reconstruire les pouvoirs d'arrêt relatifs des matériaux, ce qui aiderait à réduire l'incertitude sur le parcours des particules. De plus, les informations quantitatives obtenues à partir des images reconstruites utilisant la diffusion et le taux de transmission pourraient aider à améliorer la prédiction de la dose déposée. Cependant, les méthodes Monte Carlo deviennent de plus en plus importantes, et avec le portage des codes sur processeurs graphiques et le subséquent gain en temps de calcul, cette tendance va probablement s'accentuer. Pour la planification de traitement Monte Carlo, les images de pouvoir d'arrêt relatif n'apportent d'information que sur une seule propriété des matériaux, exactement comme l'imagerie X. La conversion en composition chimique sera toujours requise. L'imagerie proton présente l'avantage par rapport à l'imagerie X que les pouvoirs d'arrêt relatifs ne sont pas la seule information qui peut être exploitée. La dernière section de ce travail a montré un premier pas vers l'exploitation quantitative

de ces informations afin de caractériser la composition chimique des tissus. Même si les résultats ont montré que la caractérisation complète et directe n'est pas possible, il a été mis en avant que ces informations pourraient apporter des contraintes à la conversion de pouvoir d'arrêt en composition chimique, et donc améliorer la planification de traitement en terme de prédiction de parcours et de dépôt de dose.

Les travaux qui feront suite à cette thèse devront explorer les limites de l'approche multi-paramétrique de l'imagerie proton présentée ici. Le plus grand défi restera d'obtenir une précision suffisante sur les informations extraites de la diffusion et du taux de transmission, malgré l'incertitude statistique sur les mesures. Pour cela, multiplier le nombre de particules étudié par un facteur dix sera bienvenu, mais les conséquences sur le flux de particules qu'un tomographe devra soutenir sont importantes. Une étude complète de l'amélioration que cela pourra apporter à la précision de la planification de traitement sera donc nécessaire, afin de déterminer si des développement instrumentaux seront justifiés.

LIST OF FIGURES

List of Tables

Glossary

Acronyms used in the document

ART	Algebraic Reconstruction Technique
ASD-POCS	Adaptive Steepest Descent - Projection Onto Convex Sets
CNR	Contrast to Noise Ratio
CPU	Central Processing Unit
CT	Computed Tomography
CTV	Clinical Target Volume
DECT	Dual-Energy (X-ray) Computed Tomography
FBP	Filtered Back-Projection
GEM	Gas Electron Multiplier
GPU	Graphical Processing Unit
GTV	Gross Target Volume
IMRT	Intensity-Modulated RadioTherapy
IMPT	Intensity-Modulated ProtonTherapy
IVI	Interaction Vertex Imaging
kV-CT	kilo-Voltage (X-ray) Computed Tomography
LET	Linear Energy Transfer
MCS	Multiple Coulomb Scattering
MLP	Most Likely Path
MRI	Magnetic Resonance Imaging
MV-CT	Mega-Voltage (X-ray) Computed Tomography
OER	Oxygen Enhancement Ratio
pCT	proton Computed Tomography
PET	Positron Emission Tomography
PMMA	Poly(methyl methacrylate)
PMT	Photomultiplier tube
PTV	Planning Target Volume
RBE	Relative Biological Effectiveness
RE	Relative Error
RSP	Relative Stopping Power
RMS	Root Mean Square
ROI	Region of Interest
SiPM	Silicon photomultiplier

SNR	Signal to Noise Ratio
SOBP	Spread-Out Bragg Peak
SPECT	Single Photon Emission Tomography
TV	Total Variation
WEPL	Water-Equivalent Path Length

Symbols used in the document

A	Mass number
c	speed of light
E	Energy
I	Ionization potential
m_e	electron mass
$\mathcal{M}_u$	molar mass constant
n	electron density
N	atomic density
$\mathcal{N}_A$	Avogadro number
p	momentum (of a particle), product of m and v
r_e	classical electron radius
S	stopping power
T	scattering power
v	velocity (of a particle)
w	mass proportion
X_0	radiation length
X_S	scattering length
Z	Charge number

α	fine-structure constant
β	ratio between v and c
ϵ_0	vacuum permittivity
κ	total macroscopic nuclear cross-section
μ	mass attenuation coefficient sometimes used to denote a mean value
ρ	density (of a material)
ϱ	relative stopping power (RSP)
σ	microscopic nuclear cross-section sometimes used to denote the root mean square of a distribution
Φ	particle fluence

INTRODUCTION

Cancer is a disease characterized by an unregulated cell growth leading to the formation of malignant tumours. The earliest known descriptions of cancer appear in papyri that were discovered and translated in the 19th century. The *Edwin Smith* and *George Ebers* papyri contain descriptions of cancer written around 1600 BC. It is believed that they date from sources nearly one millennium older. The word cancer itself originates from Antiquity. Hippocrates, by comparing tumours to a crab, with a central body and extensions appearing as "legs", gave for the first time the Greek names of "karkinos" and "karkinoma".

Cancer is the leading cause of death in the world, causing about 7.6 million deaths in 2008 [International Agency for Research on Cancer, 2008], which corresponds to about 13 % of the deaths. In France, it is the first cause of death for men, and the second for women (the first being circulatory diseases, but cancer is a close second), with a total of 148,000 deaths in 2012. The same year, 355,000 new cases have been diagnosed. Between 1980 and 2012, the number of cancers increased by 110 %, with 40 % to 55 % due to the elevation of the risks (the rest being due to the increase and ageing of the population) [Grosclaude et al., 2013]. The worldwide expected number of deaths due to cancer in 2030 is 13.1 million.

There are three major approaches available for the treatment of cancer.

- Surgery remains the foundation of cancer treatments. It aims at curing the cancer by removing the cancerous lesion. It is a local treatment, and while undoubtedly effective if the whole tumour is removed and there are no metastases, it is limited by the accessibility of the lesion.

- Drug-based treatments, such as chemotherapy and immunotherapy are non-localized treatments. This in an advantage because these treatments can aim at treating metastasis or cancer cells that have not been detected during the diagnosis. Chemotherapy aims at curing the cancer using drugs that will affect the cancerous cells. Limitations of current chemotherapy mainly involve the delivery of the drug to the tumour through blood vessels: this may be a problem for brain tumours or for hypoxic tumours that do not have the appropriate blood supply. Immunotherapy is less common in clinical routine, but uses drugs to influence the patient's immune response. Limitations involve the targeting of the lesion, that may differ between patients for example.

– Radiotherapy is a local or regional treatment of cancer using ionizing radiations in order to damage the DNA of cancerous tissues and lead to cell death. Two kinds of radiotherapy can be distinguished: (i) internal radiotherapy, also called brachytherapy or curietherapy. A radioactive element is inserted inside the lesion. This technique will be limited by the possibility to insert the radioactive element in the target; (ii) external radiotherapy, which will be simply referred to as radiotherapy throughout this document. The lesion is irradiated by a beam, from one direction or from multiple ones. Limitations will depend on the ability to target precisely the tumour while sparing the healthy tissues and organs at risk.

All three approaches can be used either alone or combined together, whether for curative or palliative purposes. Between 45 % and 55 % of all cancer patients receive radiotherapy during the course of their treatment, more than half of them with a curative intent (the intent being palliative for the other cases).

The emergence of medical physics began at the end of the 19th century. The “kickstart” was given by the discovery of X-rays by Röntgen in 1895. X-rays were soon used for imaging purposes. From the first experiments, it was noticed that these radiations could generate acute skin reactions. The idea to use these radiations for treatment soon followed. The first therapeutic use of X-rays dates back to January 1896. Around the same time, Becquerel discovered radioactivity, and the Curies, radium. The beginning of the 20th century saw the first texts about radiotherapy, as well as those about the use of radium for treatment (curietherapie).

The idea to use heavier and charged particles came later. The first to propose protons for a medical use was Wilson [1946]. He suggested that the way protons deposit their energy along their path could be of benefit for treatment. The first clinical use occurred in 1954 in Berkley [Skarsgard, 1998]. In the following years, other particles were tested: pi-mesons, helium, heavier ions (such as carbon, neon, ...).

In France, about 200,000 patients are treated every year with external radiotherapy. There are 174 treatment facilities with 444 (more or less sophisticated) machines in the country [IAEA, 2013], amongst which two centres for proton therapy: the Centre de Protonthérapie d’Orsay (CPO), and the Centre Antoine Lacassagne (CAL) in Nice; others are in project. In the context of the national infrastructure “France HADRON” project, there are two potential centres for carbon therapy [ARCHADE; ETOILE].

According to the data centralized by the Particle Therapy Cooperative Group [2014], there are nowadays in the world:

- 6 centres for carbon ion therapy, and more than 5 in project
- 37 centres for proton therapy, and more than 34 in project

Since the beginning, more than 100,000 patients have been treated with ion beam therapy (all ions considered). Current studies estimate the need for such treatments to 1 proton therapy facility (with 3 to 4 treatment rooms) per 5 million inhabitants, and one carbon ion therapy centre per 35 million inhabitants [Amaldi and Kraft, 2006].

Throughout this work, the terms “particle therapy”, “particle beam therapy” or “hadron therapy” will be used in order to designate proton or ion beam therapy. The other particles, that have also been used for medical purposes like neutrons or mesons for example will not be included in these terms. Moreover, the generic term of “ion beam therapy” will refer to beams of particles from helium to carbon. This term was preferred to “heavy ion” therapy or “light ion” therapy, as both terms are currently in use, and can cause ambiguities. As an example, the Japanese facility HIMAC (Heavy Ion Medical Accelerator in Chiba) refers to heavy ions, whereas the european project ENLIGHT (European Network for LIGht ion Hadron Therapy) refers to light ions [Wambersie et al., 2004].

The terms “standard radiotherapy” and “conventional radiotherapy” will encompass all techniques of X-ray therapy.

In the context of particle beam therapy, proton imaging is being investigated as a mean to improve treatment planning. Indeed, treatment planning nowadays makes use of X-ray CT images, and requires a conversion from the information it brings on interactions of photons in matter, in order to predict the interaction of charged particles in the tissues. Proton imaging has been put forward as a mean to directly map the relative stopping power of the particles in the tissues. In order to do so, the energy loss of the particles is recorded.

The main objective of this thesis was to investigate the potential use of all information recorded during a pCT scan. The data on the scattering of the particles is currently used to take multiple scattering into account; however, it is also representative of the interactions of the particles in the tissues, and could bring information. Moreover, since the positions and directions of each particle are recorded both upstream and downstream from the object, information on the transmission rate of the particles is also available. To this day, these data are not used as a source of information on the nature of the tissues. Could they be? How much information on the materials can we extract from these data? Will there be an interest, for either treatment planning or diagnostics, to the use of these information?

The first chapter presents an overview of particle beam therapy, pointing out the many advantages as well as the challenges that remain to this day. Indeed, the ballistic of charged particles is undoubtedly an asset of both proton therapy and carbon therapy. An additional advantage in terms of biological effects (tumour cell death for a given dose deposit) needs to be considered for carbon therapy. However, uncertainties on the range of the particles and on the delivered dose prevent these techniques from being as efficient as they could be. In this context, proton imaging has been put forward to improve the estimation of the range of the particles.

The second chapter presents the state of the art of proton tomography. Many paths were explored before proton imaging was put forward and studied in the context of particle beam therapy treatment planning. The aim is now to map the relative stopping power of the materials. One key point to image reconstruction in proton tomography is the estimation of the proton paths. Therefore, a proton tomograph records not only the energy loss of the particles, but also their positions and directions. Two research axes are developed in this work. The first concerns the path estimation, the second concerns the potential use of all information gathered during a proton scan.

Chapter three describes the Monte Carlo simulation of a proton scanner set up using the Gate platform. The algorithms and tools implemented for image reconstruction are also detailed.

The fourth chapter describes the studies carried out on the path approximation. The most accurate path estimation available nowadays is the “most likely path”, computed using the positions and directions of each particle, assuming the object has the energy loss and scattering properties of water. Therefore, the definition of the most likely path of a particle in a non-uniform medium, made of slabs, was put forward. Then, a method for fast analytical uncertainty propagation in the most likely path computation is detailed. It was used to evaluate the impact of the tracking system properties in terms of spatial resolution, material budget and positioning, on the path estimation.

The fifth and last chapter describes the investigation on the use of the diverse information recorded during a proton scan, and more particularly the scattering and the transmission rate of these particles. A preliminary study highlights the potential interest as well as the limitations of the use of these pieces of information. Then, a qualitative reconstruction study draws attention to the possible use of the combination of the physical processes for diagnostic purposes. Finally, a quantitative study of images reconstructed using all the information available is proposed, and shows a path to get closer to the chemical composition of the tissues, indicating that these data could be of use for treatment planning.

Finally, the main conclusions on proton imaging and on the use of the transmission rate and scattering of the particles are presented. Perspectives in terms of image reconstruction are highlighted, and directions for future work in terms of proton imaging for hadrontherapy treatment planning are given.

CHAPTER 1

PARTICLE THERAPY AND THE NEED FOR PARTICLE IMAGING

Contents

1.1 Particle beam therapy

Radiation therapy aims at breaking the DNA of cancerous cells, leading to their death. In order to do so, a dose is deposited, as locally as possible to avoid damaging healthy tissues. The damage to the lesion will then depend on two main factors: the physical dose deposit (quantifying the amount of radiation sent to the region) and the effectiveness of this radiation on the cancerous cells. The damages can be either direct (by breaking the sugar backbone of the DNA) or indirect (through the generation of free radicals that, in turn, will damage the DNA).

Today, the rationale and means of proton and heavier ion therapy are well documented in the literature [Schardt et al., 2010; Linz, 2012; Goitein, 2010]. This section will go over the basic principles, both interesting and pertinent to give an overview and basic knowledge on the context of this work on proton imaging.

1.1.1 The ballistic advantage

The main argument put forward when particle therapy is discussed is the particularly advantageous depth-dose distribution of these particles. The dose delivered in a volume is defined as the total absorbed energy per mass unit of the irradiated material:

$$D = \frac{d\bar{\epsilon}}{dm} \tag{1.1}$$

with $d\bar{\epsilon}$ the mean energy transferred by the ionizing radiation to the mass of matter dm. The dose is expressed in Gray (Gy), with 1 Gy = 1 J/kg.

The aim of radiotherapy has always been to deliver a dose to a defined target while sparing the healthy tissues around it. The ideal case would be to have the possibility to localize the whole dose deposition into the target, while delivering no dose at all to the surrounding tissues. This, however, is impossible with external beam therapy. Nevertheless, particle beams allow for a dose distribution that is much more favourable, in light of this consideration, than photon beams. The next two sections will present the depth-dose distributions of photons and of charged particles, illustrating this point.

1.1.1.1 Photon depth-dose distribution

In the range of energy used in conventional radiotherapy (X-rays of voltage typically between 4 and 25 MV), photons generate secondary electrons when going through materials. These electrons, in turn, produce multiple ionization events, and damage the cells, which is of interest in radiotherapy. As most of the damages are caused

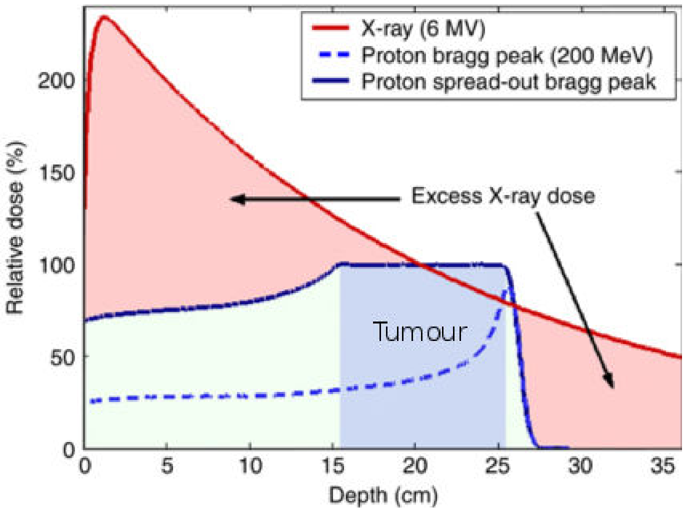

Figure 1.1: Depth-dose distributions for a X-ray photon beam (red), the Bragg peak (Section 1.1.1.2) of an individual proton beam (dashed blue), and a spread-out Bragg peak combining multiple proton beams to cover the target (solid blue). The excess X-ray dose at entrance and at exit is highlighted. Figure from [Efstathiou et al., 2013].

---

by the secondary electrons, photons are indirectly ionizing radiations. More and more electrons are produced until an equilibrium is reached, generating an increase in the dose deposit over the first few centimetres of material. However, the photons are attenuated following an exponential law described by Beer and Lambert [Beer, 1852; Lambert, 1760]. The attenuation coefficient depends on the Compton scattering, photo-electric and pair production cross-sections of the photons at the given energy in the material. Thus, after the first few centimetres, the dose deposit decreases exponentially with the photon fluence decrease, as illustrated on Figure 1.1 in red.

Because of this, the highest dose is not delivered at the tumour site, but a few centimetres after the entrance in the object. Moreover, tissues located in the beam path after the target also receive a dose that can not be neglected. Several methods can be applied to optimize treatment, such as the use of multiple beams from different directions and with different outer shapes. This allows for a good conformation to the target and less dose to the healthy tissues and organs at risk. This is the principle of intensity-modulated radiation therapy (IMRT).

1.1.1.2 Protons and heavier ions depth-dose distribution

Protons and heavier ions are directly ionizing particles and exhibit a radically different depth-dose distribution, as can be seen in Figure 1.1 in blue. The specifics of interactions between charged particles and matter will be detailed in Section 2.1. The depth-dose curve of charged particles is characterized by a “plateau” region at the entrance and a maximum at the end of their range, called the Bragg peak, with a steep falloff. The obvious advantage is that a major part of the delivered dose can be concentrated in the target. Moreover, their finite range allows for very little dose delivery (in the case of ions) to no dose delivery (in the case of protons) after the Bragg peak. As the depth of the Bragg peak in a given material is dependent on the initial energy of the particles, it is possible to adjust the depth of maximum dose deposit to match with the depth of the target. By superimposing beams of slightly different energies, a Spread-Out Bragg Peak (SOBP) can be created. This enables a rather uniform coverage of the target in depth, while delivering a rather low dose upstream and downstream. Spatial conformation of the dose distribution to the tumour was first obtained only on the distal plane of irradiation with passively scattered beams [Koehler et al., 1977; Grusell et al., 1994]. The most recent gantries allow for pencil-beam scanning: the volume to irradiate is swept by the beam and painted. Pencil-beam scanning techniques can take the form of discrete spot scanning [Kanai et al., 1980; Pedroni et al., 1995], raster scanning [Kraft, 2000] or continuous line scanning [Zenklusen et al., 2010]. These techniques make it possible to perform intensity-modulated proton – or ion – therapy [Lomax et al., 1999]. This enables a great dose conformation to the tumour in three dimensions (not just on the distal plane), and good possibilities to spare organs at risk.

It has been shown that the overall dose delivered during a proton therapy treatment is less than that delivered during a photon treatment [Lomax et al., 1999]. This better sparing of normal tissue can significantly reduce the risk of secondary cancers (by a factor of two at least, and up to ten in some cases, for organs inside the primary radiation field) [Paganetti et al., 2012].

The major difference between protons and heavier ions, such as carbon, is that the latter can undergo fragmentation processes leading to the generation of more secondary charged particles and resulting in a tail to the dose distribution after the distal edge of the Bragg peak. While this results in a less favourable dose distribution, the heavier particles present biological advantages over protons that make them quite interesting.

1.1.2 Biological advantage

The advantage of particle beam therapy in terms of biological effect on the cancerous cells depends highly on the particle used. As particle beam therapy treatments are currently performed with either protons or carbon ions, the case of these two particles will be discussed here.

Linear Energy Transfer (LET)

The LET characterizes the rate at which the energy is transferred from the radiation to the medium, locally [ICRU report 60, 1998] :

$$LET_{\Delta} = \frac{dE_{\Delta}}{dl} \tag{1.2}$$

It is usually expressed in keV/µm. Only the collisions with energy transfers less than some specified value Δ are considered. Collisions with greater energy transfer generate electrons with an energy sufficient to travel and ionize materials further from the initial track. The LET is different from the dose, but both are linked through the following relation:

$$D = \frac{\Phi \cdot \mathrm{LET}}{\rho} \tag{1.3}$$

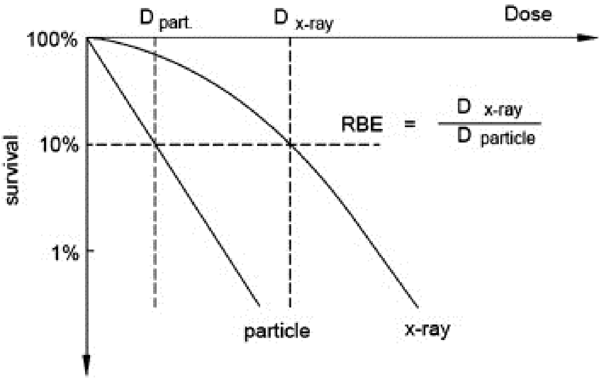

Figure 1.2: Definition of relative biological effectiveness RBE, illustrated for cell survival curves. Figure from [Fokas et al., 2009].

with D the dose, ρ the volumetric mass of the material, and Φ the particle fluence.

Energy losses that are less than 30-50 keV/µm are considered as low LET, while those greater than 50 keV/µm are considered as high LET. Gamma rays and proton are low LET radiations. Heavier particles, from alpha particles on and including carbon ions, are high LET radiations. So are neutrons.

1.1.2.1 Relative biological effectiveness

When considering particle beams, the biological effect of a radiation does not only depend on the dose. In order to characterize the response of a tissue to a radiation, the relative biological effectiveness (RBE) is used:

$$\mathrm{RBE} = \left.\frac{\text{Dose in Gy from reference radiation}}{\text{Dose in Gy from the other radiation}}\right|_{\text{same biological effect}} \tag{1.4}$$

This is illustrated on Figure 1.2: in order to reach the same biological effect, a lesser dose of “particle” radiation is required. The reference radiation is usually chosen as 250 kV X-rays, or ^{60}Co γ-rays [IAEA and ICRU, 2008].

Typically, the RBE is about 1.1 for protons [Paganetti et al., 2002], and of the order of 3 to 5 for carbon ions [Weyrather and Kraft, 2004]. This difference is explained by the high LET of the carbon beam: the high local ionization densities can generate a lot of very localized, “clustered” damage to the DNA, as can be seen from Figure 1.3.

However, the notion of RBE is not as straightforward as it appears. A given value of RBE depends on many factors, such as the particle type, the LET spectrum, the cell type (more precisely the DNA repair capacity), the dose level, and the biological endpoint (i.e. the surviving fraction chosen) that are considered [Fokas et al., 2009].

As an example, Figure 1.4 shows the RBE as a function of the LET. The “thickness” of the curve is explained by the different tissues and biological endpoints considered. The general bell-shape of the curve can be explained by the so-called “overkill” effect [Butts and Katz, 1967], illustrated in Figure 1.5. As a certain amount of damage is needed in order to kill a cell; low LET radiations, for which the number of hits per

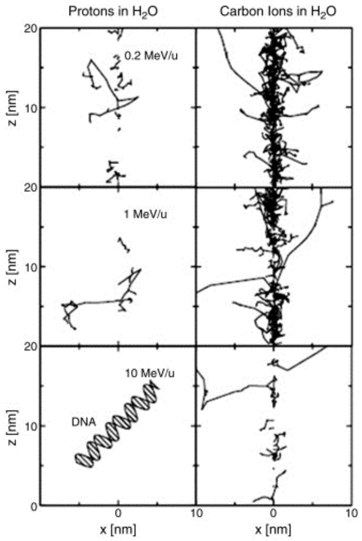

Figure 1.3: Proton and carbon ion tracks are for the same energy per nucleon. It can be seen that the ionizations generated on the carbon ion track (right side), at energies corresponding to the Bragg peak (top and middle row), are much more important than for protons. For comparison of the probability of generating clustered damage to DNA, a DNA molecule is drawn on the bottom left area. Figure from [Fokas et al., 2009].

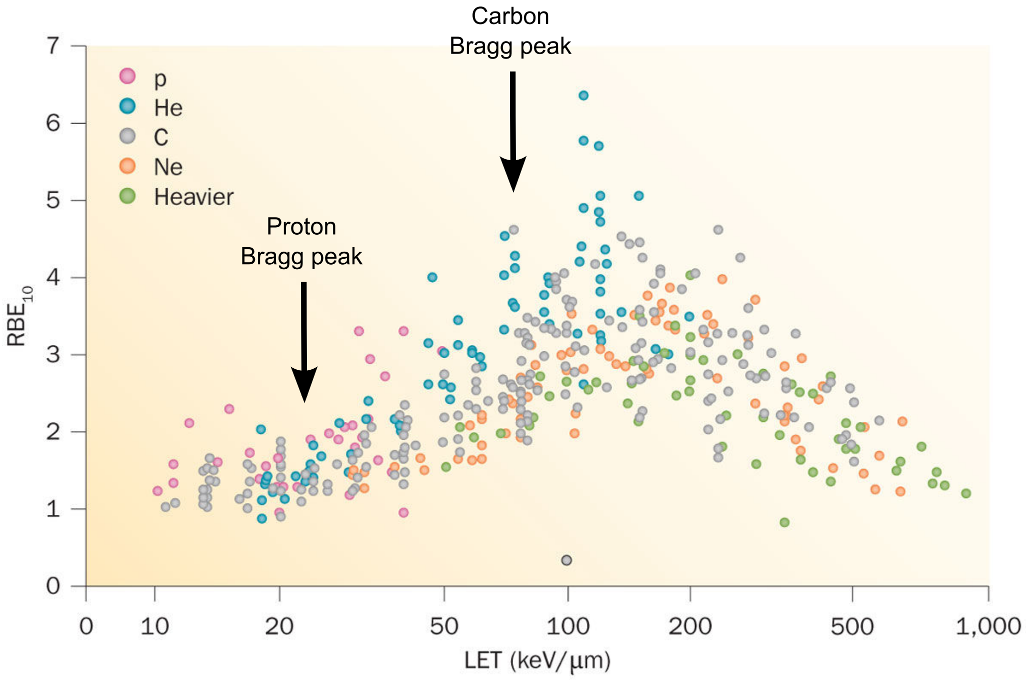

Figure 1.4: RBE versus LET from published experiments on in vitro cell lines. Figure modified from [Loeffler and Durante, 2013]

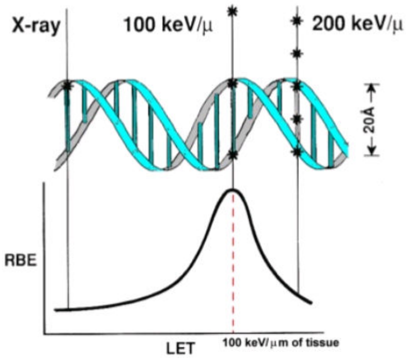

Figure 1.5: Diagram illustrating why radiation with a LET of 100 keV/μm has the greatest RBE for cell killing, mutagenesis, or oncogenic transformation. For this LET, the average separation between ionizing events coincides with the diameter of the DNA double helix (typically about 2 nm). Radiation of this quality is most likely to produce a double-strand break from one track for a given absorbed dose. Figure from [Hall and Hei, 2003].

particle in the beam is rather low, require a high dose to kill the cell. With increasing LET, the effectiveness of the particle increases to a maximum: this is when the number of hits per particle is sufficient to kill the cells with no wasted dose. Should the LET be further increased, the radiations damage the cells more than what is needed to kill them. Each impinging particle considered individually will thus be less effective, as part of the delivered dose is wasted.

It can be noted that RBE increases with depth in a spread-out Bragg peak (as illustrated in Figure 1.6 for carbon), diminishes with increasing dose per fraction, and is usually higher for *in vitro* experiments that what is found for *in vivo* experiments [Paganetti et al., 2002]. This last difference may be due to the difference in the endpoints considered – usually cell death for *in vitro* experiments, and tissue response for *in vivo* ones – or to collective or higher-order effects such as inter-cell communication in the cellular matrix. It has been put forward that the bystander effect [Little, 2003; Mothersill and Seymour, 2006], accounting for the cells that can suffer genetic damage or biological response to radiation without undergoing direct exposure to an irradiation beam, should not be in effect for the high doses involved in therapy [Fokas et al., 2009].

From physical dose to biological and clinical dose

The RBE leads to the need for differentiating the physical dose from the biological one, sometimes called effective dose. The biological dose is the product between the physical dose and the relative biological effectiveness. When a biological dose is prescribed for treatment, the physical dose needs to be adapted accordingly, with the knowledge of the RBE and of the properties of the particles sent.

However, in a clinical context, there is a need for a "one number" biological dose measure, characterizing the effectiveness of a treatment at one point and taking into

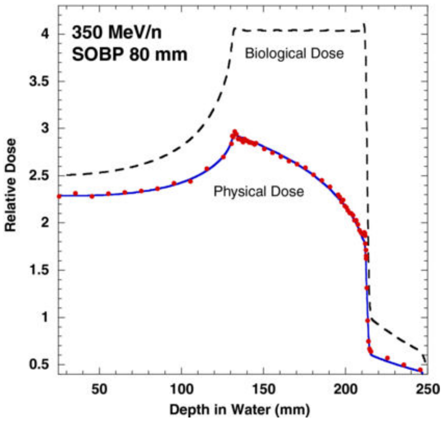

Figure 1.6: Physical and biological dose of a carbon ion spread out Bragg peak. Figure adapted from [Sakama et al., 2012]

account the complexity of the RBE [Dale et al., 2009]. This has lead Wambersie [1999] to propose a differentiation between the "clinical RBE" and the "reference RBE". In this context, the clinical RBE is the clinical decision of affecting a weighting factor to the physical dose, taking into account the heterogeneity of the dose distribution for example, and relying upon clinical experience. The reference RBE, however, is a very specific measurement in reference conditions of dose, endpoint and so on. The reference RBE can then be used in order to communicate, exchange and compare data.

The question of the RBE value to use in clinic is complex: the RBE can vary within a treatment site, and the RBE variations with fractionation and LET in different tissue types is not fully known yet [Jones et al., 2011].

As far as proton beam therapy is considered, a RBE of 1.1 is usually used. Paganetti et al. [2002] argument that this generic value is reasonable, as there is still too much uncertainty on the RBE values to propose a specific value depending on the tissue, dose per fraction, proton energy, ... Moreover, the use of a constant RBE of 1.1 has not generated any noticeable increase in complication (negative secondary effects) frequency to this day.

As far as carbon therapy is concerned, the complex dependencies of the RBE and the lack of precise quantitative data have lead to the development of different approaches. One solution put forward is the adaptation of RBE values of neutron beams, known from clinical experience [Kanai et al., 1999]. Another solution is the development of biophysical models, such as the Katz model [Katz et al., 1971; Katz and Cucinotta, 1999], or the Local Effect Model (LEM) [Scholz and Elsässer, 2007; Grün et al., 2012].

1.1.2.2 The oxygen effect

A tumour is said to be hypoxic when it is less oxygenated than the normal tissues from which it arose. Hypoxic cells are found in solid malignant tumours. Oxygen pressure can be measured *in vivo* by different means [Scifoni et al., 2013]. The reference is the use of an Eppendorf probe [Lynga et al., 1997], but this technique is highly invasive. As a consequence, efforts have been directed to tracers for Positron Emission Tomography (PET), although challenges, such as the difficulty to correlate the uptake to the effective oxygen content, remain. The potential use of functional Magnetic Resonance Imaging (MRI) has also been put forward [Krishna et al., 2001].

It was shown quite early in the history of radiotherapy that hypoxic tumours are resistant to X-rays, which can lead to a failure of the therapy [Moulder and Rockwell, 1987]. This is characterized by the Oxygen Enhancement Ratio (OER), which is defined as the ratio between the dose required to cause an effect in a hypoxic cell to the dose required to cause the same effect to a normal cell:

$$\mathrm{OER} = \left.\frac{\text{Dose required in hypoxic conditions}}{\text{Dose required with standard oxygenation}}\right|_{\text{same biological effect}} \tag{1.5}$$

Indeed, for low-LET particles, hypoxic cells are 2.5 to 3 times more radio-resistant than well oxygenated cells. This effect diminishes with increasing LET of the impinging particles, with the OER tending towards one for high-LET particles [Barendsen et al., 1963; Wambersie et al., 2004].

A generally accepted explanation for this is the “oxygen fixation hypothesis” [Hall and Giaccia, 2012]: in the presence of oxygen, the free radicals produced by the radiation in the cell can form an organic peroxide, which is a non-restorable form of the target. As this can not happen without the presence of molecular oxygen, it is said that oxygen fixes (sets) the damage. Thus, the quantity of damage inflicted to a cell is higher when the oxygen pressure is higher.

Most of the damages produced by high-LET particles are so-called direct damages, breaking the DNA. Low-LET radiations, however, rely more heavily on indirect damages induced by free radicals, and their effect is therefore more dependent on the oxygen status.

1.1.2.3 Dependence of the phase in the cell cycle

The radio-sensitivity of cells also depends on their replication phase [Fidorra and Linden, 1977]. This can be explained by the change in DNA compactness, or by the presence of a replication check-point. For example, the cells regularly “check” if the replication process was performed correctly (in phase G2), leading to a decrease in the radio-sensitivity just before the beginning of this phase [Hansen Ree et al., 2006]. Tissue cells are usually asynchronous, but an extreme stress such as a first irradiation modifies that. Because of this, it is important during fractionated treatment of radiotherapy to randomize the time of irradiation in order to reduce the risks of recurrently hitting in a radio-resistant phase.

It was shown that high-LET particles are more potent inducers of cell cycle delays, and are less sensitive to the cell phase [Fournier and Taucher-Scholz, 2004]. The benefit of the reduction in the variation of the cell radio-sensitivity along its mitotic cycle in the case of high-LET particles remains unclear [Wambersie et al., 2004].

1.1.2.4 In brief...

Particle beam therapy, in this context carbon therapy even more so than proton therapy, shows a great radio-biological advantage over standard radiotherapy, with a high RBE and a low OER. The benefit for treatment however, is not strictly due to these characteristics; neutron beams also show high RBE and low OER [Weyrather and Kraft, 2004]. The superiority of ion beam therapy comes from the fact that the beam quality changes along the depth, and that the RBE increases, reinforcing the advantages of the depth-dose distribution. This leads to a good tumour response without the severe side effects in the normal tissues of neutron therapy [Skarsgard, 1998]. However, much research on the RBE values, mechanisms of cell death and repair pathways, is still ongoing [Dale et al., 2009].

1.1.3 Clinical trials, cost and cost-effectiveness

Hadron therapy is currently quite a trendy topic. From the previous sections, one can see all the advantages that these treatments can bring. However, even more questions come with it. Because of the difference in the LET and biological effects, the cases of protons and carbon ions are not the same.

1.1.3.1 Protons

Proton beams can present a much higher dose conformity to the lesion than X-ray beams. Four arguments are put forward by Goitein [2010]:

> - *For the same dose to the target volume, protons deliver a lower physical dose to the uninvolved normal tissues than do high energy X-rays*
> - *There is very little difference in tissue response per unit dose between protons of therapeutic energies as compared with high-energy X-rays, so that the only relevant differences are physical*
> - *There is no medical reason to irradiate any tissue judged not to contain malignant cells*
> - *Radiation damages normal tissues, as it does tumors, and the severity of that damage increases with increasing dose*

The conclusion is that protons are intrinsically better than photons for therapy. However, it has not been demonstrated yet that, in a clinical setting, protons are better for all tumour localisations. The use of proton beams to treat prostate cancer, for example, is subject to controversies [Efstathiou et al., 2013]. Two distinct points are discussed. The first is whether or not particle beam therapy is better than X-ray beam therapy. The second is whether particle beam therapy is worth the additional expenses, compared to conventional radiotherapy.

While physicists in general have no trouble stating that protons are intrinsically more favourable than photons for treating tumours, the conclusion that it should be widespread and put into routine clinical practice is not so obvious for all the scientific community. As an example, W. Robert Lee advocates that *"the burden of proof lies upon a person making claims rather than shifting the burden of proof to the others"* [Sakurai et al., 2012]. Thus, people claiming that particle beam therapy is better have to support this claim with clinical results, ensuing from randomized clinical trials. As pointed out by Olsen et al. [2007], this position is also supported by the Helsinki declaration (a text adopted by the world medical association on the ethical principles for medical research involving human subjects). Article 6 therein states:

> *Even the best proven prophylactic, diagnostic, and therapeutic methods must continuously be challenged through research for their effectiveness.*

These arguments for randomized clinical trials comparing proton treatments to photon treatments are the source of a problem of ethics for some. The main cause is the need for the two arms of a trial (here, the two treatments compared) to be in equipoise: one needs not to know whether one is better or not – otherwise it would mean sending patients to receive a treatment that you believe is not the best. Goitein [2010] highlights this notion of equipoise:

> *There is a school of thought which distinguishes between 'clinical equipoise' (the lack of definitive clinical results which show the arms to be different) and what is somewhat pejoratively described as 'theoretical equipoise' which is based on other than clinical data.*

It can also be stated that no such phase III clinical trials were requested before the use in routine of intensity-modulated radiotherapy, or stereotaxic radio-surgery for example [Suit et al., 2008]. In turn, randomized clinical trials are better suited and can bring very useful to compare one thing at a time, so that it can be scientifically interpreted [Goitein, 2010]. Randomized trials are undeniably useful to help determine an optimized fractionation schedule for example, or to answer the 'bath or shower dilemma': whether a low dose to a large area of healthy tissues is preferable or not to a more localized higher dose. Another imperative of randomized clinical trials is the time frame in which they take place [Glimelius and Montelius, 2007]. The gain needs to be clinically relevant and detectable within three to five years. However, treatment technology is evolving today at a rate so fast that it means to acquire "*today's evidence on yesterday's technology*" [Olsen et al., 2007]. Clinical trials therefore need to be a worldwide effort not to take too much time to collect the necessary data. Current clinical trials can be found onlune at [Particle Therapy Cooperative Group] and [US National Institute of Health]. Some phase III randomized trials involve the evaluation of side-effects for prostate cancer for example. Indeed, as a polemic surrounds the pertinence of directing prostate cancer patients towards proton therapy, the clinical trials could help bring an answer.

Nevertheless, even though the ethics of randomized clinical trials can be discussed in the scientific community, a last argument gives incentive to perform them. One reason why there is such debate about proton treatments, when there was not for other treatment modalities, is the cost of particle beam therapy [Goitein and Cox, 2008]:

> *Can anyone seriously believe that, if protons were cheaper than X-rays, there would be similar objections raised as to their widespread use?*

Current societies rely on health insurance systems to pay for treatments. And as in any such system, the question of cost-effectiveness of the treatments appears. It can not be neglected because a high cost associated to a treatment with no clear advantage over a cheaper one limits the availability of resources for other patients [Efstathiou et al., 2013].

The main problem encountered is that studies reporting on the cost-effectiveness of particle beam therapy often have to rely on assumptions, and authors suffer from the lack of data, both on the cost and on the effectiveness [Lundkvist et al., 2005]. Different studies have evaluated the cost of a proton treatment to be between two and four times that of X-ray therapy [Goitein and Jermann, 2003; Peeters et al., 2010]. However, a reduction in the number of fractions of a proton treatment may reduce this ratio. Similarly, the widespread use of proton therapy may reduce the costs.

It has been put forward that the key to cost-effectiveness for proton therapy may reside in the selection of patient [Ramaekers, 2013]. Not all patients would benefit from a proton treatment rather than IMRT. For some cases, such as paediatric cancer or specific treatment sites close to organs at risk (eye, head and neck), there is very little doubt that proton therapy is advantageous. For tumour sites that are not recognized as systematically better treated by protons, the scientific community in Netherlands for example has proposed a system of patient selection based on normal tissue complication probability and *in silico* treatment plans [Eekers, 2014]. Results collected after treatment of these patients may then help improve models and evaluate the efficiency for a well-selected patient population, that surely will be more advantageous than to consider all potential patients.

1.1.3.2 Carbon ions

The case of randomized clinical trials for carbon beam therapy is not as controversial as for proton beam therapy. The main reason is the difference in the biological impact of the high-LET particles: the effectiveness is quite different than that of photons. Randomized clinical trials would be of great interest to test the impact of LET by comparing protons to carbon ions for example. Such current trials involve, amongst others, the comparison of proton therapy to carbon therapy for skull-base chondrosarcoma [US National Institute of Health, 2014].

However, the same question in the matter of cost-effectiveness stands. It is an important question, not so much from the scientific point of view of a physicist, but from the point of view of the clinical world, and investment politics. This is because "*We do not yet know whether, overall, any improvements in clinical results achieved with hadron therapy are sufficient to warrant such an extensive investment of time and money*" [Lodge et al., 2007].

There are indications that particle beam therapy could be cost-effective, for locally recurrent rectal cancer [Mobaraki et al., 2010] or some tumours which are typically treated by a combination of surgery and radiotherapy and for which the tumour control rate can clearly be increased using ions [Jäkel et al., 2007].

The lack of data however, both on the cost and on the effectiveness, is greater than for protons, due to the limited number of centres and patients treated [Mobaraki et al., 2010]. Few facilities have been operating for long enough to have "good" data, leading to large uncertainties on the cost estimates [Jäkel et al., 2007]. The cost of carbon therapy amounts up to nearly five times that of X-ray therapy [Peeters et al., 2010]. However, the potential reduction of the number of fractions and the increased tumour control probability could lead to a reduction of long term cost and relative cost compared to standard radiotherapy [Goitein and Jermann, 2003; Pijls-Johannesma et al., 2008;

Peeters et al., 2010]. As far as the effectiveness is concerned, randomized clinical trials would be a good way to quantify this.

1.2 Treatment planning and uncertainties in particle beam therapy

1.2.1 Treatment planning for particle beam therapy

Like for conventional radiotherapy, the treatment planning for particle beam therapy is based on the information about the tissues obtained from an X-ray computed tomography (CT) image. On this image, the contours of the tumour region and the organs at risk are drawn by the physician. Other imaging modalities can be used for complementary information, such as positron emission tomography (PET) or magnetic resonance imaging (MRI) images. A treatment plan based on MRI images was also proposed by Rank et al. [2013], but the values were converted to pseudo CT numbers. Therefore, even in that case, the following explications stand from section 1.2.1.2 on. The CT image is then used in the treatment planning system, in order to calculate and optimize the dose delivery. Two types of treatment plan calculation exist nowadays: the first is analytical, the second is based on Monte Carlo simulations. For analytical dose calculations, the X-ray CT image is converted into a relative stopping power (RSP) image, with water as a reference. Beam spread and nuclear interactions are also scaled using the CT image. For Monte Carlo dose calculations, the CT numbers are converted into material compositions.

The following sections briefly describe the principle of X-ray imaging, and the conversion from CT numbers used for treatment planning.

1.2.1.1 X-ray CT imaging

The basic principle of X-ray CT is the following: after sending an X-ray flux I_0, the flux I upon exit from the object can be measured. Usually, a photon beam of voltage between 30 and 150 kV is sent through matter. The photon flux is attenuated following an exponential law, according to the linear attenuation coefficient of the materials. This linear attenuation coefficient $\mu(x, y, z, E)$, in a point of coordinates (x, y, z), depends on the energy of the photons E. For a given ray reaching the detector at the position (u, v) after the path L_i, the projection measurement is:

$$I(u,v) = \int I_i(E) \exp\left(-\int_{L_i} \mu\left(x,y,z,E\right) dl\right) dE \tag{1.6}$$

where $I_i(E)$ takes into account the energy dependence of the incident ray source spectrum, and the detector sensitivity.

The images acquired with a CT scanner are usually scaled to represent a map of the CT numbers of the tissues. The CT numbers are expressed in Hounsfield Units (HU), defined as:

$$CT = \left(\frac{\mu_{mat} - \mu_{water}}{\mu_{water}}\right) \times 1000 \tag{1.7}$$

with μ_{water} the linear attenuation coefficient of water.

Because the source emission presents an energy spectrum, the values of mass attenuation coefficients, and therefore CT numbers, represent average values for the given spectrum.

The linear mass attenuation coefficient μ can be semi-empirically expressed as follows [Jackson and Hawkes, 1981]:

$$\mu = \rho n_e \left(K^{ph} \tilde{Z}^{3.62} + K^{coh} \hat{Z}^{1.86} + K^{KN} \right) \tag{1.8}$$

with ρ the density of material. For a material composed of different elements:

$$\tilde{Z} = \left[\sum \lambda_i Z_i^{3.62} \right]^{1/3.62} \tag{1.9}$$

$$\hat{Z} = \left[\sum \lambda_i Z_i^{1.86} \right]^{1/1.86} \tag{1.10}$$

$$\lambda_i = \frac{(n_e)_i}{n_e} \tag{1.11}$$

where Z_i is the atomic number of each element, $(n_e)_i$ the electron density of each element, n_e the total electron density and K^{ph}, K^{coh} and K^{KN} are coefficients for the photoelectric effect, coherent (Rayleigh) scattering and Compton scattering respectively.

1.2.1.2 Conversion of X-ray CT numbers

To proceed to analytical dose calculation for ion beam therapy, it is necessary to convert the CT numbers into the RSP of the materials (described in section 2.1), in order to predict the energy loss of the particles. It can be seen from Figure 1.7 that CT numbers and RSP are strongly correlated. This is because the electron density of the materials greatly contributes to both. The use of such a conversion in order to use X-ray CT scans for radiotherapy treatment planning was introduced by Mustafa and Jackson [1983]. Different methods can be used to obtain a conversion curve, the most frequently used being the stoichiometric approach [Schneider et al., 1996], based on the elemental decomposition of tissue substitutes. Because of the X-ray CT acquisition, the calibration is scanner-dependent. It also depends on the position of the object in the field of view. The data obtained from the calibration can then be fitted, by a broken line for example. The method has been improved with patient-specific optimization of the Hounsfield look-up table [Schneider et al., 2005]. Other approaches have also been put forward, such as the polybinary tissue model-based calibration [Kanematsu and Matsufuji, 2003].

Monte Carlo simulations, on the other hand, require the description of materials with their elemental composition and mass density. It means that a conversion from CT numbers to materials is required. In order to do so, conversions based on a stoichiometric calibration, similar to the one that can be used for the conversion to relative stopping power, have been put forward [Jiang et al., 2007]. The principle is the following [Schneider, 2000]: the CT image is segmented and thresholds are applied to differentiate groups of materials with similar CT numbers. A constant elemental composition is attributed to each group, and the materials are adjusted inside each group by varying the mass density.

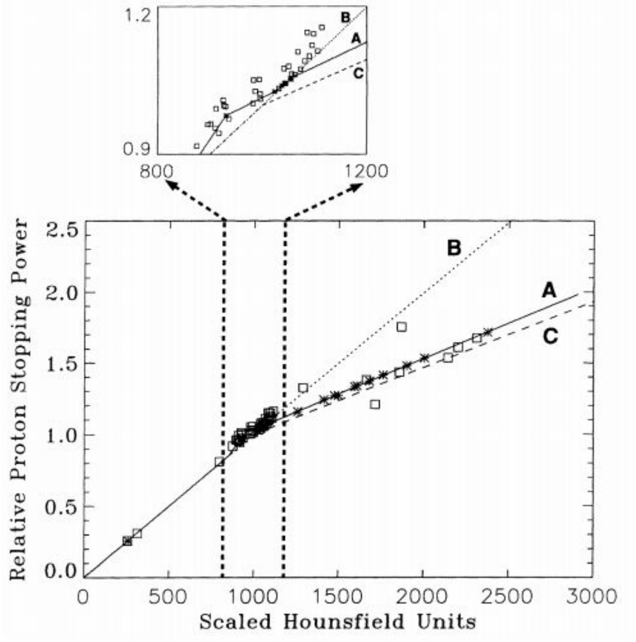

Figure 1.7: Calibration curves for the transformation of Hounsfield values into relative stopping power. The small plot shows in detail the Hounsfield number range corresponding to soft tissue. Figure from [Schneider et al., 1996].

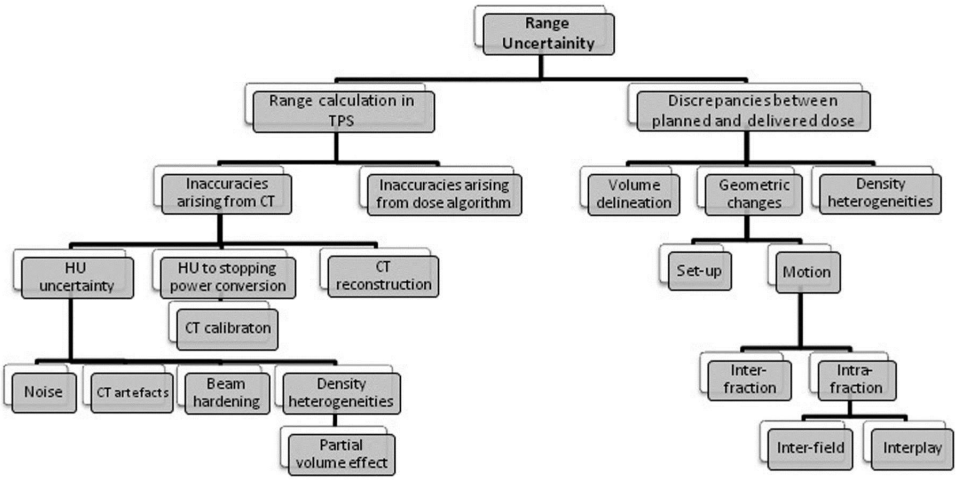

Figure 1.8: Schematic of sources of range uncertainties in proton radiotherapy. Figure from [McGowan et al., 2013].

1.2.2 Range uncertainty

In photon beam therapy, a slight change in the composition or amount of material that is in the path of the beam does not have a very important impact. For particle beam therapy, it is crucial to know and control the range of the beam because of the sharp falloff in the dose distribution after the Bragg peak. One can not afford to deliver a high dose to an organ at risk located close to the distal part of the spread out Bragg peak. In a similar fashion, one can not afford to overestimate the range of the particles: the distal end of the tumour would receive less dose than intended, resulting in a reduced tumour control probability.

Various factors can impact the range prediction accuracy, as shown in Figure 1.8. Some of these causes will be detailed here, leaving out the delineation, patient positioning and motion.

1.2.2.1 Origins of the range uncertainty

Patient-related origin

The most direct consequence of treatment fractionation is the fact that the irradiations take place during a time lapse of weeks. Treatment plans are established on the base of a CT scan before the beginning of the treatment. However, during the course of treatment, changes in the patient anatomy can occur, due to weight loss or gain, or tumour mass reduction. There can also be daily changes in the filling of internal cavities such as nasal cavities, bowel, rectum or bladder. These changes may affect the range of the particles and have an impact on treatment.

Biological range uncertainty

As far as protons are concerned, the average value of the RBE at the centre of a SOBP (spread-out Bragg peak) was shown to be 1.1 [Schulz-Ertner et al., 2006]. This approximation of a single, generic RBE is frequently used in clinical therapy centres and does not take the LET-dependence into account. Therefore, the use of such a single value has been reassessed and it was shown that while the approximation is reasonable, a local "hot region" at the end of the SOBP generates an extension of the biological range [Paganetti et al., 2002]. This extension can be of the order of the millimetre. This difference builds up with the increasing range of the incoming particles, but decreases with the dose, and thus is dependent on the fractionation scheme [Carabe et al., 2012]. These uncertainties will affect the precision of the dose calculation algorithm.

Physical origin of range uncertainty

As the range is computed based on the converted CT images, range uncertainty has two sources: the CT numbers themselves (accuracy, noise, artefacts in the image), and the conversion [Yang et al., 2012].

- Voxel size, noise, and partial volume effect:
  These factors have been shown to have an impact on the predicted range of the particles. For a given system, the noise in the image is inversely proportional to the size of the image voxels. It was shown that an increase in the noise of the CT image, and thus a fluctuation of the CT numbers that are converted to stopping power, leads to a linear increase in the range uncertainty [Chvetsov and Paige, 2010]. As an illustration, they reported an uncertainty (standard deviation) of the range between 0.3% and 0.7% for voxels in the CT image of 3×3×3 mm^3 and a 2.5% noise level. However, large voxel size also has a negative effect on the range calculation [Chvetsov and Paige, 2010; España and Paganetti, 2011], especially because small inhomogeneities have an impact on the calculated range. This effect is important in regions such as the lung. España and Paganetti [2011] show, for example, a difference between planned and expected range up to 4 mm for a heterogeneous random lung, assuming treatment plan with a 2×2×2.5 mm^3 grid.

- Beam hardening:
  X-ray sources used for CT images are polychromatic, meaning that a spectrum of energy is generated, generally between 30 and 140 kV for clinical CT scanners. However, the linear mass attenuation coefficients that rule the fluence loss of the photons are energy-dependent, as can be seen in Equation 1.6. Thereby the spectrum is modified and its mean shifted towards higher energies throughout the penetration in the object to image. This generates artefacts in the reconstructed CT image typically characterized by a cupping effect (the profile of an homogeneous medium appears brighter on the extremities and darker at the centre where CT numbers are under-estimated) and by dark streaks in the image. It has been shown that beam hardening effects can cause considerable errors in the range prediction, especially for high-density materials [Schaffner and Pedroni, 1998]. They estimate that the determination of the stopping power value from calibrated CT images in

clinical situations and in high-density material is therefore only accurate to about ±1.5% due to beam hardening.

- Metal artefacts:
  The presence of metal, for hip prosthesis or dental filling for example, greatly degrades the accuracy of the reconstructed image. The density of metal is beyond the normal range that can be handled by the acquisition system of a CT scanner. The resulting extreme attenuation of photons generates incomplete attenuation profiles which, in turn, translates into very bright spots in the image at the location of the metal and in bright and dark streaks coming from that point. As a consequence, the reconstructed CT numbers are erroneous. This can have a great impact on the treatment plan accuracy for proton and heavier ion beam therapy, with a range variation up to 18% for steel hip prosthesis should the beam go through the implant [Jäkel and Reiss, 2007]. Because of this, treatment planners do their best to avoid beam paths through the metal. However, the artefacts cause variations of the CT numbers of the tissues in the whole image, affecting the other tissues as well. The impact is less important in these other tissues, but can not be neglected. While metal artefacts also have an impact on treatment plans of other radiations, whether photons or electrons, it was shown that its impact is most important for particle therapy due to the potential error on the range prediction [Wei et al., 2006].

- Conversion from CT numbers:
  The accuracy on the obtained RSP values also depends on the parametrisation of the fit for the calibration curve, the goodness of the approximation between the tissue substitutes and the composition of real body tissues, the mean excitation potential chosen for the calculation and the energy-dependence of the RSP [Yang et al., 2012]. It is estimated that the use of a stoichiometric calibration generates an uncertainty of about 0.5% [Paganetti, 2012]. It can be noted that, even with a very accurate calibration procedure, an uncertainty will always remain: because of the difference in the interaction mechanisms between charged particles and photons in matter, the transformation from CT numbers to RSP is not bijective.

Monte Carlo dose calculations allow for accurate considerations of the physical processes. However, information on the elemental composition and mass density of each tissue is needed and extracted from the planning CT image. This process also relies on the calibration of material composition and density with the CT numbers. In a similar fashion to the RSP conversion, the transformation from one to the other is not linear, and assumptions on the materials and density are made. Jiang et al. [2007] conclude their study by stating that "*Radiation therapy with heavy charged particle beams requires more accurate knowledge on the relative stopping power in order to convert Hounsfield numbers* [to materials] ". Nevertheless, Paganetti [2012] estimates that the uncertainties on the range using this method should be smaller than the ones for analytical dose calibration.

1.2.2.2 Consequences for treatment planning and treatment

Range uncertainty and margins for treatment planning

One consequence is that the beam direction is never chosen so that a critical structure is placed just distal to the Bragg peak, for fear of over-shooting and damaging the critical structure. Beam directions are chosen so that the lateral penumbra, which is rather well-known, is used to spare critical organs. This means that the sharpness of the peak and the advantage of the no-dose behind it are not fully exploited.

Another consequence is the increase of the 'safety margins' and thus the irradiated volume, also called planning target volume (PTV). Typically, the PTV is defined in the following way: the Gross Tumour Volume (GTV) seen on X-ray CT, MRI, PET or SPECT (Single-Photon Emission Computed Tomography) images is delineated. This GTV is contained in a larger volume, the Clinical Target Volume (CTV), that aims at taking into account the potential microscopic spread of the disease that could not be seen on the images. The PTV encapsulates the last volumes adding margins accounting for uncertainties in planning or treatment delivery.

In order to take the range uncertainty into account, the margins added when establishing the PTV in particle therapy are rather large. Here are examples of margins used for proton therapy [Paganetti, 2012]:

- Massachusetts General Hospital (Boston): 3.5% of range + 1 mm
- MD Anderson Proton Therapy Center (Huston), Loma Linda University Medical Center, Roberts Proton Therapy Center at the University of Pennsylvania: 3.5% + 3 mm
- University of Florida Proton Therapy Institute: 2.5% + 1.5 mm

The need for these margins somehow reduces the attractiveness of ion beam therapy. While a precision weapon is available, allowing for better a sparing of the normal tissues, we are limited by the range uncertainty, causing the voluntary irradiation of a portion of normal tissue.

Quality control for ion beam therapy

The question of the precision in the irradiation has produced the need to worry more about quality control in ion beam therapy than previously for conventional radiotherapy. Means to verify the conformity of the irradiation to the treatment plan were investigated, and different methods have been proposed [Knopf and Lomax, 2013]. Amongst these methods, some are real-time measurements during the irradiations, others are pre- or post- irradiation controls; some methods are invasive, others not. Here is a brief summary of the potential solutions that have been investigated:

- Range probes and particle radiography (pre-irradiation control):

  The idea of a range probe is the following: before treatment, a particle pencil beam of energy sufficient to pass completely through the patient is sent and the residual range is measured upon exit. This makes it possible to check the expected range [Romero et al., 1995; Watts et al., 2009; Mumot et al., 2010]. This approach has been implemented in many proton therapy centres. It was shown on Monte Carlo simulations performed using real X-ray CT data that *in vivo* range estimates at the level of 0.5% could be achieved [Mumot et al., 2010]. The dose delivered is low – in the plateau region – and the method is fast. Based on the same principle of measuring the residual range of the particles, the proton radiography concept makes use of a two-dimensional fluence of protons. In order to increase spatial resolution, a proton radiography system measuring the entrance and exit coordinates with the range measurements has been proposed [Schneider and Pedroni, 1995].

These concepts, first developed with protons, work the same way for ions, like carbon [Ohno et al., 2004; Shinoda et al., 2006; Parodi, 2014].

- Point dose measurements (real-time control, direct, invasive):

  It has been proposed to control the dose deposit *in vivo* using implantable dosimeters and using the time-dependence of the distribution delivered by range modulated passive scattering fields, using ionization chambers [Lu, 2008*b*] or semiconductor diodes [Gottschalk et al., 2011]. This proposition was later generalized to measuring SOBPs generated by complementary field pairs [Lu, 2008*a*] and for intensity modulated proton therapy (IMPT) plans [Lu, 2009]. The advantage of this method is that it provides a real-time and precise measurement of the dose deposit. The potential sub-millimetric precision has yet to be confirmed in clinical studies on patients. Nevertheless, this technique presents the major drawback of being invasive and provides information on a limited number of points that have to be carefully chosen.

- Positron emission tomography (real-time or post-irradiation, indirect):

  Nuclear interactions of protons or ions in the matter can generate the activation of the materials [Graffman and Jung, 1975; Bennett et al., 1978]. The production of β^+ emitters, of half life between 2 and 20 minutes in particular, is appropriate for PET. Proton beams generate mostly ^{11}C, ^{13}N, ^{15}O [Litzenberg and Bajema, 1992], while carbon beams produce ^{10}C, ^{11}C, ^{15}O [Enghardt, 2004*a*]. The detection in coincidence of the photon pairs resulting from the annihilation of the emitted positrons with electrons in the medium then allows for *in vivo* range verification. The activity profile obtained depends on the nature of the beam but is, both for proton and carbon therapy, strongly correlated to the dose distribution [Enghardt, 2004*b*].

  It has been shown that this technique makes it possible to detect deviations in the patient positioning or local changes in the patient anatomy in the course of a fractionated treatment [Enghardt, 2004*b*; Schardt et al., 2010].

  PET monitoring can be performed either in-beam (during the irradiation) or off-line (just after the irradiation). Off-line PET imaging has the obvious advantage that commercially available scanners can be used. In contrast, in-beam PET requires the inclusion of the PET system around the treatment bed, generating higher costs and challenges in image reconstruction due to the limited angle. Nevertheless, downsides of off-line PET are the diminished activity due to the waiting time between the irradiation and the imaging, and a degraded spatial correlation between the activity map and the dose distribution due to the biological washout processes [Parodi, 2012].

- Prompt gamma imaging (real-time control, indirect):

  The de-excitation process of nuclear interactions occurring as the protons or ions pass into the matter generates the prompt emission of photons. The presence of these gammas was first considered in the context of PET imaging for dose monitoring of therapy, as background noise [Parodi et al., 2005]. The idea to use them as actual information was proposed soon thereafter for proton beams [Min et al., 2006; Polf et al., 2009] and for carbon beams [Testa et al., 2008]. The prompt gamma emission profile is correlated to the Bragg peak position and could thus be used in order to verify its position. However, the falloff of the gamma profile does not correspond to the dose falloff. As a consequence, only a consistent and predictable falloff difference enables range verification [Moteabbed et al., 2011]. Prompt gamma imaging can be performed in a similar fashion to SPECT imaging, using a collimated gamma-camera [Bom et al., 2012; Smeets et al., 2012], or using a Compton camera [Kormoll et al., 2011; Roellinghoff et al., 2011].

- Interaction vertex imaging (real-time control for ion beam therapy, indirect):

  Interaction vertex imaging (IVI) is based on the detection of secondary charged particles exiting from the patient during the irradiation with ions (not with protons) [Amaldi et al., 2010; Henriquet et al., 2012]. The advantage of IVI over prompt gamma and PET monitoring is the potentially greater number of particles to detect. However, the difficulty resides in the fact that the charged particles detected undergo multiple Coulomb scattering before their exit from the patient, challenging the spatial resolution achievable with such a technique [Rescigno et al., 2014].

- Magnetic resonance imaging (post-irradiation verification):

  MRI can not be used to verify the treatment delivered during or just after the delivery, but makes it possible to see changes in the tissues as a consequence of the irradiation, one or two weeks after. MRI-visible changes in the tissues enable the observation of the delivered dose *in vivo*. However, it was shown that visual analysis of MRI images only was not sufficient to detect the distal dose edge after proton therapy treatment of the spine [Gensheimer et al., 2010]. Different methods are still being investigated.

The use of range probes or particle radiography makes it possible to check before irradiation if the energy loss of the particles used as probes corresponds to that predicted by the image of the treatment plan. Range prediction inaccuracies and potential patient mis-alignment or anatomical changes could be detected, thus reducing the range uncertainty. This technique does not, however, enable verification of the delivered treatment.

To be able to check in real time if the dose delivered during irradiation corresponds to that planned would be ideal. However, the point dose measurement is the only method currently available that can give this information before the treatment is complete. The major drawback is that it is invasive, and limited in the number of measurement points. As far as the non-invasive methods are concerned, prompt gamma imaging has the advantage that the time-scale of the emission is small enough not to be affected by biological washout processes. The production rate is higher than for PET. However, the potentially lower detection efficiency or resolution of a SPECT imager or Compton camera compared to a PET imager may result in an unfavourable trade-off. Moreover, prompt gamma monitoring is, like interaction vertex imaging, still in an rather early stage of research and development, whereas off-line PET has already been used extensively in routine [Parodi, 2012].

1.2.3 Delivered dose uncertainty

The uncertainty on the delivered dose during particle beam therapy has two sources: one is the uncertainty on the biological dose, knowing the physical dose exactly; the second is the uncertainty on the physical dose delivered.

1.2.3.1 Biological dose uncertainty

The uncertainty on the biological dose delivered is a direct consequence of the uncertainty on the RBE values (see Section 1.1.2.1). It was shown that the higher the degree of normal tissue sparing, the less important the radiobiological factors become. This is favourable to particle beam therapy except, maybe, in very hypo-fractionated treatments [Jones et al., 2011]. Nevertheless, Dale et al. [2009] conclude their study on the impact of RBE uncertainty that "*an overall dosimetric uncertainty of around ±3%, as sought with conventional X-ray therapy, will be impossible to attain without comprehensive appreciation of, and allowance for, RBE effects*".

1.2.3.2 Physical dose uncertainty

In order to obtain an accurate treatment plan, knowledge of the stopping power of the materials is essential, but not sufficient. Information about the spread of the beam as well as the fluence of the particles is needed in order to predict the dose deposition. Because the range uncertainty can result in direct failure of the treatment or unforeseen damage to critical organs, it is considered of utmost importance. While the uncertainty on the delivered dose probably has less consequences, it is also worth mentioning.

As a first approach, both the scattering of the particles and the fluence attenuation of the beam were assumed to be that of water for all the materials considered, adjusting only the density to ensure the range accuracy with conventional heterogeneity-correction algorithms. It was shown to be a practical and sufficient approximation [Matsufuji and Tomura, 1998]. However, different works have shown a strong correlation between CT numbers and not only relative stopping powers but also scatter angle

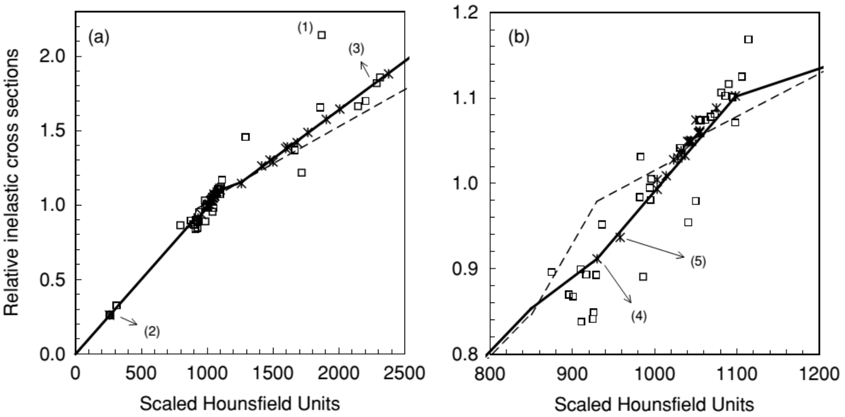

Figure 1.9: Relative nonelastic cross section per unit of volume for 219 MeV protons as a function of scaled Hounsfield unit, with water as reference using ICRU 63 data. On the left, for the whole HU range and on the right, detail for the HU range between 800 and 1200. The solid line is a calibration curve based on the tissues only. For comparison, the calibration curve for the relative stopping powers from Schneider et al (1996) is represented as a dashed curve. Figure from [Palmans and Verhaegen, 2005].

and nuclear reactions [Matsufuji and Tomura, 1998; Szymanowski and Oelfke, 2003; Kanematsu et al., 2012]. Thus, it was proposed to use a separate calibration, based on a stoichiometric method similar to the one developed for the conversion of CT numbers to relative stopping power [Schneider et al., 1996]. This information on materials may then be used for analytical calculations of the dose distributions in treatment planning systems [Szymanowski and Oelfke, 2003; Palmans and Verhaegen, 2005].

The importance of taking into account the nuclear interactions in the different materials was put forward [Palmans and Verhaegen, 2005]: establishing a scaling curve for nuclear interactions as a function of the CT numbers allowed for a reduction of the error on the dose estimation from 2-3% to less than 0.5%.

Nevertheless, a phenomenon similar to the case of the relative stopping power conversion can be seen: while a strong correlation allows for the establishment of conversion tables and the reduction of errors, the variables considered are not representative of the same physics processes and the conversion remains approximative, as can be seen from Figure 1.9 and Figure 1.10.

1.2.4 Improving treatment planning

Different aspects of treatment planning are under study, the aim being to improve its accuracy [McGowan et al., 2013]. The LET, for example, needs to be considered in order to take full advantage of the properties of protons and heavier ions. The definition of the PTV by simply adding margins to the CTV is being questioned by the optimization robustness to the range uncertainty of treatment plans. In order to address the problem of range uncertainty, different possibilities of imaging, image treatment and conversion to RSP are being studied: improving the accuracy of CT images, improving the conversion,

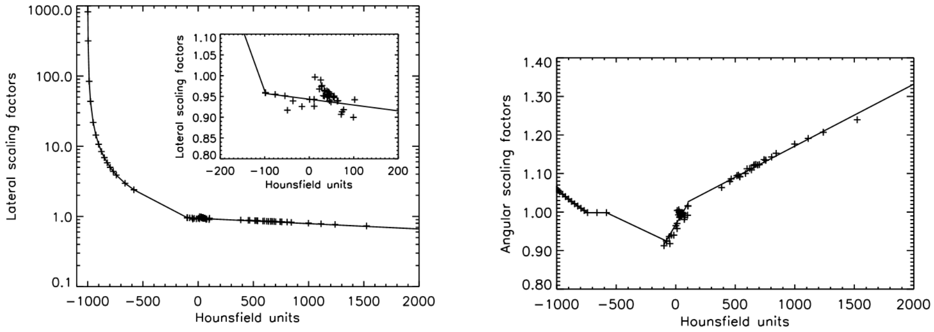

(a) (b)

Figure 1.10: (a) Lateral scaling factors and (b) angular scaling factors as a function of the CT Hounsfield units, for the tissues tabulated by White et al (1987), Woodard and White (1986) and the mixtures lung-air and lung-blood. Figure from [Szymanowski and Oelfke, 2003].

---

developing models for biological treatment planning or using charged particles to obtain the RSP image directly.

1.2.4.1 Taking full advantage of the LET

As the LET of the particles impacts greatly the biological effects of the treatment, it was proposed to use high-LET radiation as a boost in a precise region of the irradiation, and to optimize not only the dose distribution but the LET distribution in the volume to irradiate, in order to take full advantage of the properties of the particles used [Bassler et al., 2010]. The local increase in the LET at the end of the range of the protons, for example, can be considered during treatment planning. The fact that plans with identical dose conformation can lead to different repartitions of the LET is particularly important with active scanning [Grassberger and Paganetti, 2011]. Thus, there is a need to consider a LET-dependent RBE [Tilly et al., 2005]. Recently, a LET-guided plan optimization (with both dose and LET objectives) was proposed, in order to maximize the dose average LET in the tumour and minimize it in normal tissues [Giantsoudi et al., 2013].

1.2.4.2 PTV definition and treatment plan optimization

As mentioned previously, the planning target volume is usually defined - for photon therapy as well as particle beam therapy - as the clinical target volume to which margins are added to take into account the uncertainties of treatment delivery. However, this definition used for conventional radiotherapy is not quite appropriate for particle beam therapy. It has been shown that, should the range uncertainty not be taken into account, the margins between PTV and CTV can be reduced from photon to proton therapy [Thomas, 2006]. However, when considering the range uncertainty, margins is not the answer to improve treatment plan robustness for highly modulated IMPT (though it was found satisfying for other deliveries of protons such as single-field uniform dose and low modulation of IMPT) [Albertini et al., 2011]. This is because the degradation of dose uniformity inside the target has some importance in IMPT. Heuristic approaches such as choosing beam angles with the less inhomogeneities in the beam path, or placing no organ at risk just behind the distal edge of the peak have been applied. It was also proposed to define a beam-specific PTV [Park et al., 2012], taking into account the range uncertainty and setup errors independently for each beam angle.

Rather than the re-definition of a more appropriate planning target volume, some efforts are also put towards the inclusion of the uncertainties directly into the planning system in order to determine the most robust solution [McGowan et al., 2013]. Different methods have been proposed, such as a probabilistic approach [Unkelbach et al., 2007], a robust formulation [Unkelbach et al., 2007] or a worst-case optimization [Pflugfelder et al., 2008]. More recently, the inclusion of robustness to range uncertainty in a multi-criteria objective framework was implemented [Chen et al., 2012]. These approaches have been tested, and showed less sensitivity to range and setup errors that traditional margins, assuring a better coverage of the clinical target volume.

1.2.4.3 Improving CT images

The improvement of the CT image quality, mainly the reduction of beam hardening and metal artefacts, leads to a more accurate range prediction. Different methods for image artefact correction have been proposed.

Beam hardening correction

Three kinds of methods for beam-hardening correction exist. The first is filtering: the beam is hardened so that the measured spectrum tends towards a monochromatic one [Paiva et al., 1998; Krimmel et al., 2005]. The second way to proceed is linearisation [Herman, 1979; Hammersberg and Mångård, 1998; Kachelrieß et al., 2006]: the acquired projections are corrected to mimic monochromatic data. The third kind of method is post-reconstruction [Nalcioglu and Lou, 1979; Olson et al., 1981], for which a first reconstructed image of the object is used in order to estimate the distribution of the different materials, and their effect on the energy spectrum.

Metal artefacts correction

Metal artefact reduction techniques are either based on the completion of missing data using synthetic data, or on the modification of the reconstruction algorithm to ignore the missing data [Man et al., 2000; Abdoli et al., 2012]. Another possibility is the registration of kilo-voltage (kV) and mega-voltage (MV) CT images [Newhauser et al., 2008]. It has been shown that correcting for metal artefacts improves significantly the quality of the treatment plan [Wei et al., 2006] and diminishes the risk of potentially dramatic errors.

1.2.4.4 Improving the conversion to RSP with DECT

Dual-energy X-ray CT (DECT) acquisition has been put forward as a possible tool to improve treatment planning and reduce the range uncertainty. MV-CT has been put forward as a mean to overcome the problem of metal artefacts in kV-CT [Newhauser et al., 2008]. In the aforementioned paper, the use of an hybrid approach using registered kV- and MV-CT images has been proposed. This makes it possible to keep the better sensitivity and contrast of kV-CT. DECT can be even more interesting, in that it makes it possible to access more information on the materials.

Principle of DECT

DECT is a technique that has been first proposed in the late seventies [Alvarez and Macovski, 1976]. The attenuation coefficient of a material (Equation 1.8) can be rewritten to take into account a continuous spectrum of energy j:

$$\mu_j = n_e \sum_i w_{ij} \left[Z^4 F\left(E_{ij}, Z\right) + G\left(E_{ij}, Z\right) \right] \tag{1.12}$$

with n_e the electron density of the material, w_i the fraction by weight of element i serving as the weighting factor for the energy E_{ij}, and Z the effective atomic number [Johns, 1983] defined as:

$$Z = \left(\sum_i w_i Z_i^{3.5} \right)^{1/3.5} \tag{1.13}$$

with Z_i the atomic number of the element i.

A CT acquisition with two different energy spectra gives access to two linear attenuation coefficients. Thereby, two different evaluations of Equation 1.12 are available that can be solved iteratively for Z which makes it possible, in turn, to calculate n_e.

Application to treatment planning

DECT gives access to the electron density of the materials, which is a great part of the relative stopping power. An electron density image obtained from kV-kV DECT used for the conversion to Water-Equivalent Path Length (WEPL, projection of the RSP, detailed in Section 2.3.1) makes it possible to reduce the range uncertainty, and the image shows less noise than single energy CT [Hünemohr et al., 2013]. The other component of the stopping power depends on the ionization potential of the material. An empirical relationship between the logarithm of this ionization potential and the effective atomic number has been put forward [Yang et al., 2010]. It was shown that kV-MV DECT gives better results than kV-kV or MV-MV DECT [Yang et al., 2011].

Nevertheless, performing DECT is not so trivial, as it either requires the registration of two CT images, or a simultaneous acquisition with two sources. Moreover, while DECT involving MV-CT shows great results, the image is still affected by beam hardening and the trade-off between the image quality and the dose needs to be carefully considered.

1.2.4.5 Upcoming possibilities for X-ray CT imaging?

Other modalities of X-ray CT imaging exist, that have not been investigated in the context of treatment planning for particle beam therapy, but could be of interest.

Spectral CT

Spectral CT consists in detecting and exploiting the energy distribution of the transmitted photons [Giersch et al., 2005]. The principle is similar to that of DECT, except that spectral CT only uses one source but employs energy thresholds in the detector.
The advantage over DECT is that it does not require image registration, nor multiple sources. It could moreover bring more information in the sense that it is not limited to two energies. However, challenges in the covering of large areas, high resolution, uniform performance and long duration operation remain [Shikhaliev and Fritz, 2011; Xu et al., 2012].

Phase contrast CT

Phase contrast CT [Momose et al., 1996] is a technique that makes it possible to access the two informations of DECT, namely the electron density and effective atomic number, with only one CT acquisition, thus only one dataset [Qi et al., 2010]. The electron density can be determined from refractive index decrement through a linear relationship. The effective atomic number can be explicitly derived from the ratio of the linear attenuation to refractive index decrement using a power function plus a constant. If proven efficient, this method could have the advantage over DECT due to the lower dose (only one CT acquisition) and because there is no need for registration nor for two sources and detectors.

Neither spectral CT nor phase contrast CT have been considered yet for improving treatment planning – as both are in rather early developmental stages and challenges remain to their spread in clinical setting [Xu et al., 2012; Bravin et al., 2013]. Nevertheless, they may one day become potential solutions.

1.2.5 Proton imaging as a potential answer?

As we have seen in section 1.2.2.2, proton imaging can help reduce range uncertainty by checking the expected range with the treatment planning stopping power. However, proton imaging may well help reducing range uncertainty by being an alternative to the conversion of CT numbers, and directly mapping the relative stopping power of the materials. This is why proton computed tomography is currently being investigated by different groups and collaborations worldwide. Moreover, a proton beam carries more information on the materials encountered than just its energy loss. Whether this information could also be useful to reduce the delivered dose uncertainty is a path that has not been explored yet. Chapter 2 describes the principles of proton imaging, and Chapter 5 describes the investigations on the potential use of all the information recorded during a proton scan to help reduce range and dose uncertainties.

Summary

- Particle beam therapy presents many advantages in terms of dose deposit and sparing of healthy tissues.
- Treatment planning for particle beam therapy requires the conversion from CT numbers either to stopping powers of charged particles in the tissues, or to stoichiometric composition of the tissues.
- The uncertainty on the range of particles results in an increase of the margins around the volume to irradiate.
- The uncertainty on the dose deposit is higher than for X-ray therapy.
- Proton computed tomography has been put forward as a mean to reduce the range uncertainty.

CHAPTER 2

PROTON IMAGING STATE OF THE ART

Contents

This chapter goes over the interactions between protons and matter in a first part. A second part is dedicated to the history of proton imaging, leading to the state of the art. Finally, this thesis is introduced in its context.

2.1 Review of the physics principles: interactions of protons with matter

This section consists in an overview of the principles of interactions of proton with matter. Protons going through a medium lose their energy through inelastic collisions with atomic electrons. This energy loss is described by the Bethe-Bloch formula, detailed in Section 2.1.1. Protons also undergo elastic collisions with electrons and nuclei, that deflect them from their trajectory. However, as the electrons weigh much less than the protons, this contribution to the energy loss is not significant. The scattering of protons in matter is detailed in Section 2.1.2. The inelastic collisions with nuclei that particles also undergo are presented in Section 2.1.3.

2.1.1 Proton energy loss

Inelastic collisions of protons with atomic electrons lead to excitations (where electrons are still bound to the nucleus) and ionizations (where electrons are stripped off the nucleus). In the energy range considered for proton imaging (typically between 20 and 300 MeV), the mean energy loss per unit path length, also called stopping power S, is well-described by the Bethe-Bloch theory [Bethe, 1930; Bloch, 1933]:

$$S\left(I,E\right) = -\frac{dE}{dx} = \frac{4\pi n_e}{m_e c^2 \beta^2}\left(\frac{e^2}{4\pi\epsilon_0}\right)^2 \left[\ln\left(\frac{2m_e c^2\beta^2}{I\left(1-\beta^2\right)}\right) - \beta^2\right] \tag{2.1}$$

where e is the proton charge, ϵ_0 the vacuum permittivity, $\beta = v/c$ with v the particle velocity and c the speed of light, m_e is the rest mass of the electron and I is the mean excitation potential (also called mean ionization potential). Here, n_e represents the density of electrons in the material, that can be expressed as:

$$n_e = \frac{\mathcal{N}_A \cdot Z \cdot \rho}{A \cdot \mathcal{M}_u} \tag{2.2}$$

where ρ is the density of material, Z and A are its atomic and mass numbers, $\mathcal{N}_A$ is the Avogadro number and $\mathcal{M}_u$ the molar mass constant.

Shell and density corrections can be added to the formula, but are unnecessary in the context of proton imaging - they affect the end of the range of the particle that is not considered in proton imaging. The electronic stopping power of protons in water is represented in Figure 2.1.

Through Equation 2.1, one can see what leads to the peculiar shape of the Bragg curve, that characterizes the stopping power of the material as a function of the depth, and particularly the peak (Bragg peak) for low values of β at the end of the range, as can be seen of Figure 2.2.

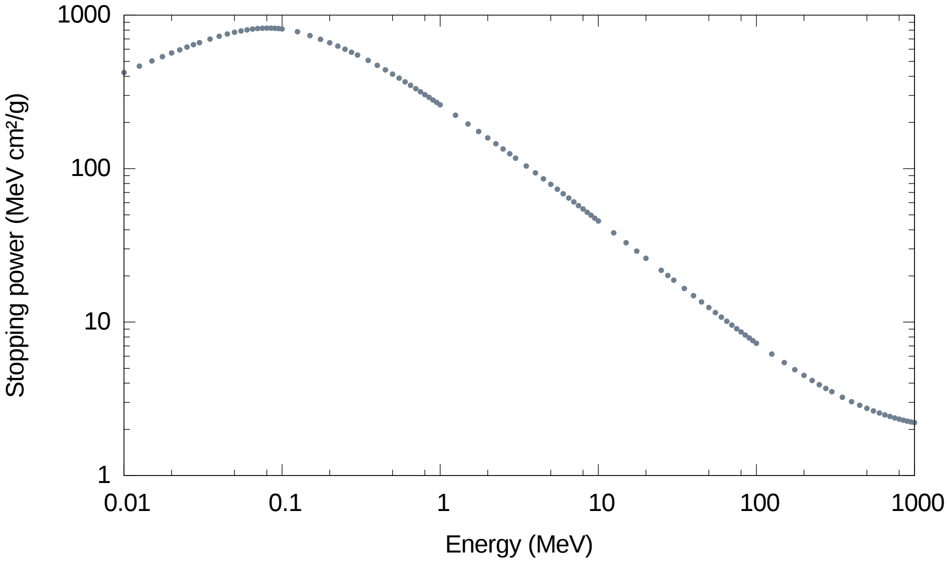

Figure 2.1: Electronic stopping power of protons in water. Data from the PSTAR database [NIST, 2014].

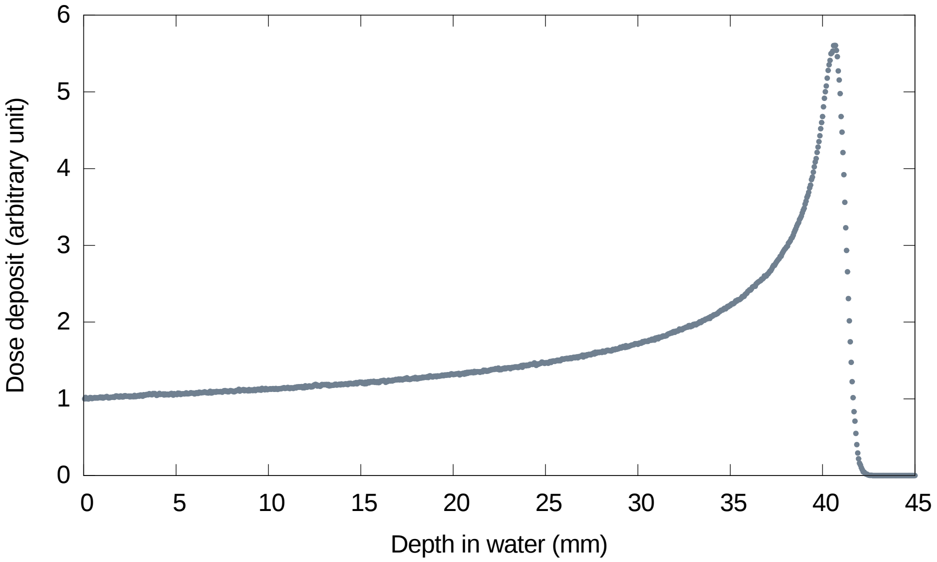

Figure 2.2: Dose deposit of 70 MeV protons in water, normalized to the entrance dose. Data obtained by running a Geant4 simulation of protons sent into a segmented water cube.

As a first approximation, the ionization potential of atoms can be determined as:

$$I = (10\ \text{eV}) \cdot Z$$

where Z is the atomic number of the atoms of the material. Nevertheless, the approximation does not fit the data very well for elements of atomic number less than 15, and more precise tabulated data are now available [ICRU report 48, 1994]. The ionization potential of atoms and molecules depends on their atomic structure, and also on the state of the material (gas or condensed material). The determination of the I-values is particularly complex in the case of compounds. As an example, a wide range of values has been put forward for the ionization potential of liquid water, ranging from 67.2 eV to 81.8 eV [Besemer et al., 2013].

An approximation for the calculation of the I-value of compound materials, recommended by the ICRU [ICRU report 37, 1984] is:

$$\ln I = \frac{\sum_{i=1}^{n} \left(\frac{w_i Z_i}{A_i} \ln I_i \right)}{\sum_{i=1}^{n} \left(\frac{w_i Z_i}{A_i} \right)} \tag{2.3}$$

with w_i, Z_i, A_i and I_i the mass proportion, the atomic and mass numbers, and the I-value of the element i respectively.

Straggling of the energy loss

Both the number of collisions and the energy transferred for each collision are ruled by statistical processes. A mono-energetic beam of protons sent through a material will exit with an energy distribution, representing these statistical fluctuations. This straggling of the energy loss can be characterized by the variance of the outgoing energy distribution. It was shown [Schulte et al., 2005] that for thinner objects ($\leq$ 15 cm), this variance is best described by Bohr's theory [Bohr, 1948]. Let us define:

$$\kappa_2(x) = \eta_e \frac{4\pi n}{m_e c^2} \left(\frac{e^2}{4\pi\epsilon_0} \right)^2 \frac{1 - \frac{1}{2}\beta^2 \left(E\left(E_{in}, x\right)\right)}{1 - \beta^2 \left(E\left(E_{in}, x\right)\right)} \tag{2.4}$$

where η_e is the relative electron density with respect to water.
Let d be the thickness of material. Bohr's theory then predicts:

$$\sigma_B^2(d) = \int_0^d \kappa_2(x)\, dx \tag{2.5}$$

For thicker objects, Tschalar's theory [Tschalär, 1968*b*,*a*] is more appropriate:

$$\frac{d}{dx}\sigma_T^2(x) = \kappa_2(x) - 2\left(\frac{d}{dE} S\left(E(x)\right)\right) \sigma_T^2(x) + \text{higher order terms} \tag{2.6}$$

Therefore, the straggling depends on the energy of the protons, and on the electron density of the materials.

2.1.2 Multiple Coulomb scattering

Protons in the energy range considered undergo multiple small-angle deflections due to the Coulomb field of the nuclei, and deviate from their original path. The Coulomb scattering distribution can be represented by the theory of Molière [Molière, 1947, 1948; Bethe, 1953]. The distribution of exit angles and positions of a mono-energetic, unidirectional beam of particles is roughly gaussian for small angles but shows a tail at larger angles. In the framework of proton computed tomography (pCT), the gaussian approximation of multiple Coulomb scattering (MCS) will be used to estimate the trajectory of the particles during image reconstruction (Section 3.3.2). The exit angular distribution of a mono-energetic parallel beam of protons for "thin" objects ($l \ll X_0$) in this approximation is a normal distribution of which the mean is zero and the standard deviation can be described by the following empirical formula [Lynch and Dahl, 1991]:

$$\sigma(l, E) = \frac{13.6}{\beta(E)p(E)}\sqrt{\frac{l}{X_0}}\left[1 + 0.038 \cdot \ln\left(\frac{l}{X_0}\right)\right] \tag{2.7}$$

where β and p are the scaled velocity and momentum of the proton at energy E, X_0 is the radiation length of the material and l the proton path length in the material. For thicker objects, an integration of this equation on the energy range in the material needs to be considered.

Other approximations exist, both for the central gaussian part of the distribution, as well as for the whole distribution with corrections for single scattering [Kanematsu, 2008; Gottschalk, 2009]. Some will be of interest for the study presented in Section 5.3 and are detailed in Appendix B.

The radiation length of a material is defined as the mean length required to reduce the energy of an electron by the factor $1/e$ by bremsstrahlung. It is usually measured in g.cm^{-2}. For a single element of charge and mass numbers Z and A respectively, it can be approximated by the following empirical formula:

$$X_0 = \frac{716.4 \cdot A}{Z(Z+1)\ln\frac{287}{\sqrt{Z}}} \quad g.cm^{-2} \tag{2.8}$$

For compound materials, the combined radiation length X_0 of a sample of mass W_0 can be expressed as:

$$\frac{W_0}{X_0} = \sum_i \frac{W_i}{X_i} \tag{2.9}$$

with W_i and X_i the mass and radiation length of the i-th component.

This, however, remains an approximation. The calculation of the radiation length of water using this formula gives 35.2 g.cm^{-2}, whereas the value of 36.1 g.cm^{-2} is well established [Hagiwara, 2002]

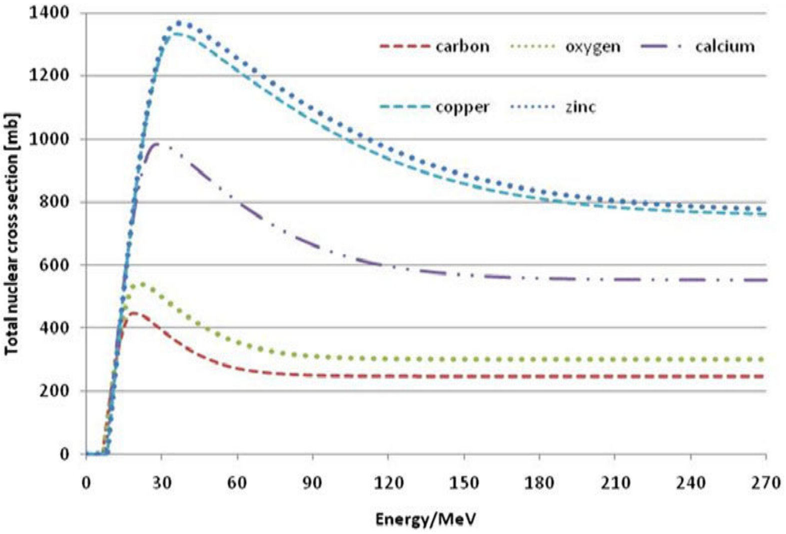

Figure 2.3: Total nuclear cross-section for protons on C, O, Ca, Cu and Zn, image taken from [Ulmer and Matsinos, 2010].

2.1.3 Nuclear interactions

Inelastic nuclear interactions lead to a reduction of proton fluence with increasing thickness of the object. This decrease in the proton fluence (Φ) of a beam going through a depth l of material, can be evaluated by the knowledge of $\kappa\left(x, y, z, E\right)$ the macroscopic inelastic nuclear cross section for protons in the material at the point of coordinates (x, y, z) [Segrè, 1964]:

$$\Phi(l) = \Phi_0 \exp\left(-\int_l \kappa\left(x, y, z, E\right) \mathrm{d}l\right) \tag{2.10}$$

The energy dependence of the cross-section for some elements is represented on Figure 2.3.

Nuclear interactions of protons in matter also generate secondary particles: neutrons, protons or heavier recoil fragments. Recoil fragments will deposit their energy locally. Neutrons can either exit the patient or produce another nuclear interaction. Secondary protons, in the case of pCT, may be further transported.

The total nuclear cross section of charged particles in materials made of different elements can be recomposed by knowing the cross sections of its elements.

As an example, it has been shown that the double differential cross section of fragmentation of ^{12}C on PMMA ($C_5H_8O_2$) can be reproduced using the following [Dudouet et al., 2013]:

$$\frac{d\sigma}{d\Omega}(\mathrm{PMMA}) = 5 \times \frac{d\sigma}{d\Omega}(\mathrm{C}) + 8 \times \frac{d\sigma}{d\Omega}(\mathrm{H}) + 2 \times \frac{d\sigma}{d\Omega}(\mathrm{O}) \tag{2.11}$$

2.2 The first era of proton imaging - discovery

The work on proton imaging went through two distinct eras. Between the 1960's and the 1980's the potential of proton medical imaging was explored for the first time. Different means to use protons for medical imaging were proposed: the concept of proton computed tomography nowadays known uses the energy loss of the particles (Section 2.2.1), but it evolved from marginal range radiography (Section 2.2.2). During the same time, nuclear scattering imaging (Section 2.2.3) and multiple scattering imaging (Section 2.2.4) were also investigated. After the beginning of the 1980's, with the development and improvement of X-ray imaging, and considering the "intrinsic" limitations of the proton imaging concepts proposed (the deterioration of the spatial resolution due to multiple scattering), the research in this field was put on hold. The interest in proton imaging was only renewed in the 1990's, with the explicit intent to help with range control and treatment planning for particle beam therapy.

2.2.1 Proton computed tomography using energy loss

The first suggestion of proton imaging was made by Cormack [1963, 1964]. He suggested *"the determination of a variable density of matter with constant chemical composition, using the energy loss of charged particles in the matter"*. This idea was exposed as an application amongst others in the formulation of the image reconstruction problem. He put forward, in his paper, that this problem can be posed in the same manner than the attenuation of X-rays for imaging, if one can assume that the tissues vary only in density and not in chemical composition. This assumption, in the case of an object consisting of bone and soft tissue, is a rough approximation that will impact the results. In this line of thought, Cookson et al. [1972] measured the "density profile" of an object by looking at the energy loss of a 12 MeV proton beam.

The same year saw the first tomographic reconstruction of an object imaged with 840 MeV alpha particles. The stopping power along the beam line was computed from the average energy degradation: the basic principle was the same as what is done nowadays [Goitein, 1972]. Still with alpha particles, of 900 MeV this time, a clinical brain imaging system was proposed, with three multi-wire proportional counters upstream from the patient to measure the beam position and a range counter telescope consisting in 13 scintillation counters for measuring the residual range of the particles upon exit. In this configuration, the patient sat upright on a rotating chair, with the top of the head in a water bath [Crowe et al., 1975], in order to even the depth of materials the particles go through. The brain images reconstructed from the alpha particle scan showed good density resolution with a dose advantage of an order of magnitude compared to X-ray images.

Experiments on computed tomography using the energy loss of protons were performed at the Harvard cyclotron laboratory shortly after that [Cormack and Koehler, 1976]. The proposed system used a hyperpure germanium calorimeter to measure the exit energy of the particles. At the time, advantages and disadvantages of protons over X-rays were described [Hanson et al., 1978]:

> *The advantages of proton over X-ray CT are as follows:*
>
> a. *lower dose for a given density resolution*
> b. *lack of beam hardening artefacts*
> c. *fast scans may be possible since the number of protons required (about* 10^8*) can easily be supplied in a very short time interval*
>
> *The disadvantages of protons are:*
>
> a. *accelerators which supply protons of sufficient energy are considerably more complicated, bulky and costly than X ray sources*
> b. *delivery of a proton beam to a supine patient is more difficult than for X rays, but not impossible*
> c. *spatial resolution of proton scans is limited by multiple Coulomb scattering. Use of heavy ions instead of protons may alleviate this problem.*
> d. *since there are no huge Z effects in proton stopping power as there are in X-ray attenuation, the important diagnostic use of contrast agents is precluded.*

The work on proton tomography did not end here. The spatial resolution was improved by measuring the exit position of each particle [Hanson, 1979; Hanson et al., 1981]: by binning the exit positions for each entrance position of the beam, the data was re-projected using a straight line approximation. It can be noted that it was suggested at that time that an even bigger gain in spatial resolution could be achieved if the reconstruction algorithm could incorporate curved projection paths. Acquisitions of data and image reconstruction with human specimens (heart and brain) were compared to X-ray CT images [Hanson et al., 1982]. They conclude that the image quality obtained is quite similar to that of X-ray images for the *in vitro* study.

This paper marked the end of a period of investigation for the proton tomography using the energy loss of the particles. The technique did have some qualities over X-rays, the most important being dose between four and twenty times lower depending on the CT scanner used as a reference [Hanson et al., 1982]. Nevertheless, as the image quality for diagnosis was not significantly better than that of X-rays, this did not warrant the spread of the technique for routine diagnostics. Most efforts in research were put towards improvement of X-ray imaging.

While it is the most remembered, proton imaging using the energy loss of the particles was not the only path explored. In the same years, the potential of imaging using other properties of the protons were investigated.

2.2.2 Marginal range radiography

The first experimental studies on proton imaging concerned marginal range radiography. The principle of marginal range radiography is illustrated in Figure 2.4. The object is placed in a water bath in order to minimize the effect of shape variation of the object imaged on the radiography. A radiographic film is positioned on the exit face of the

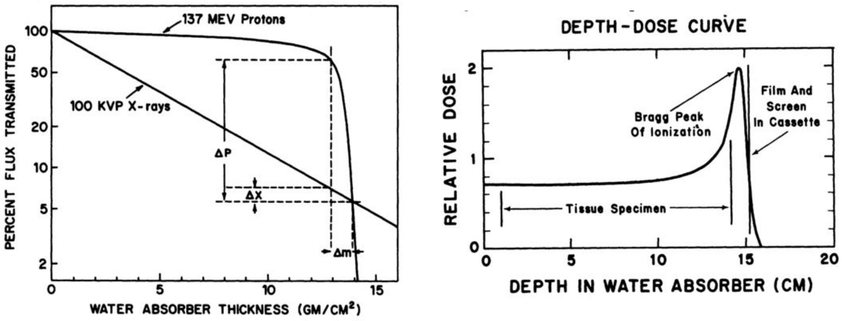

(a)

(b)

Figure 2.4: Illustration of the marginal range radiography concept. (a) illustrates the flux-depth curves for protons and X-rays passing through a homogeneous medium, and highlights the higher sensitivity of protons. (b) shows the depth-dose curve of protons as well as the setup of the specimen and photographic film. The figures are from [Steward, 1979].

water tank. The beam energy is set so that the film is situated at the middle of the sharp fluence descent following the Bragg peak. The information exploited is the number of particles impinging on the emulsion.

The first experiment was performed by Koehler [1968]. It was followed by others, and this technique demonstrated great promises for diagnostics of tumours, strokes, or breast carcinoma [Steward and Koehler, 1973*b*,*a*, 1974]. The technique showed good detectability of the malignancies compared to the X-ray radiographs available at the time, despite the limitation in the spatial resolution caused by the scattering of protons. This method made it possible to have a much higher contrast than with X-rays for a given, or even less, dose [Steward, 1976].

This technique, however, requires careful consideration to properly match the beam energy to the object and to the placement of the detector. Indeed, the contrast is set by the falloff region of the Bragg peak: the sharper the falloff, the higher the contrast; but the shorter the range of structural variations that can be seen. Thus, this can be also performed with ions, but a compromise between the range of variations and the contrast needs to be established for each application [Steward, 1979]. The second drawback of this technique is that multiple scattering degrades the spatial resolution.

2.2.3 Nuclear scattering imaging

The application of nuclear scattering to radiography (NSR) was proposed in 1975 [Saudinos et al., 1975]. The principle is to use higher energy protons, between 500 MeV and 1 GeV. The idea is to detect protons scattered at wide angles by nuclear interactions. The positions and directions of the particles are recorded upstream from the object to image with two position-sensitive detectors. Downstream from the object, other position-sensitive detectors are used to record the passage of largely scattered protons and recoil protons. The intersection of the lines describing the trajectory of the incoming and scattered particle give the position of the interactions. This makes it possible to obtain three-dimensional images using a single beam direction. This technique is, however, intrinsically limited in its spatial resolution due to the multiple scattering of the secondary protons in the object.

Further work demonstrated the possibility to separate the contributions of scattering on hydrogen from that on heavier elements, such as carbon or oxygen [Charpak et al., 1976]. Experiments on biological materials confirmed this possibility to treat the data in order to obtain "hydrogen" radiographs in addition to the "standard" nuclear scattering radiographs [Berger and Duchazeaubeneix, 1978]. Later experiments made it possible to reconstruct images from a preserved human head [Charpak et al., 1979; Duchazeaubeneix et al., 1980]. The images were compared to those obtained with an X-ray tomograph. Charpak et al. [1979] conclude that:

> *As compared to X-ray CAT* [computer-assisted tomography]*, NSR offers the following advantages:*
>
> - *the same image quality can be obtained with radiation doses several times smaller, mainly because of the large effective use of the incoming radiation (about 6% of beam particles produce useful nuclear scattering events, in a 20 cm thick object with unit density);*
> - *the image obtained is fully three-dimensional allowing the display of the density distributions in arbitrary planes of reference by simple data manipulation;*
> - *the unique feature of hydrogen selection allows one level of chemical analysis that may prove useful to detect structure having very close density but different hydrogen content.*

As for the other techniques for imaging with protons, no further work was published after the beginning of the 1980's. One possible explanation for that is the following: as X-ray imaging technology progressed greatly, the "same image quality" soon became unreachable. Furthermore, with the development of magnetic resonance imaging, a different possibility to visualize the hydrogen became available, without the need for high-energy proton accelerators.

2.2.4 Multiple scattering radiography

Another, less explored, way of producing images with protons was shown to be multiple scattering radiography. The concept was first explained in the beginning of the 1970's by West and Sherwood [1972]. The idea is the following: when a parallel beam of protons goes through a uniform depth of material, the intensity of particles exiting is uniform, as every point receives an equal number of Coulomb scattered particles. The same goes for outside of the object. At the boundary, however, less particles reach the detector: particles impinging just on the edge of the object are scattered in the non-object part of the edge. This discontinuity makes it possible to generate bright and dark outlines of the object on radiographic film, as illustrated on Figure 2.5.

Again, this technique provides information of a different nature compared to the other methods of imaging with protons. As it is particularly well-adapted to thin objects, it

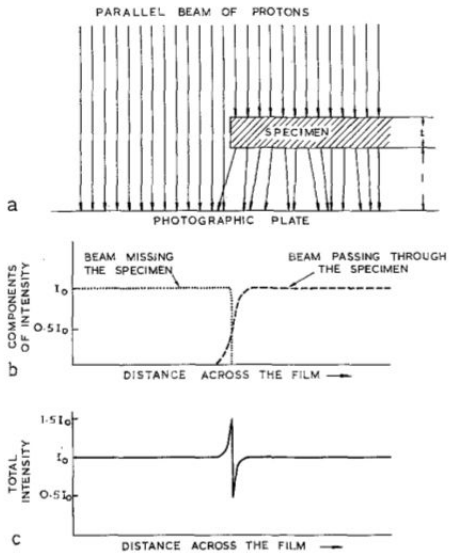

Figure 2.5: Illustration of how multiple scattering produces its characteristic edge pattern. Image taken from [Cookson, 1974].

was applied to obtain radiographs of a mouse, for example, with 160 MeV protons [West, 1975]. Nevertheless, the edge-delineation using scattering becomes quite difficult when considering thick objects, as the intensity measured will be representative of scattering along a long path, where multiple edges of heterogeneity can be encountered, rendering its application to clinical imaging impossible.

2.2.5 In brief

Several projects put forward different means and potential for proton imaging throughout this “exploration” period. Multiple scattering was not applicable to clinical imaging, and no real interest for its edge-delineation properties was really found for medical imaging. Nuclear scattering radiography proved interesting, but the main advantage was the quantification of the hydrogen content. This interest was greatly diminished by the development of MRI. Marginal range radiography was very interesting because of the contrast in the produced images. However, the poor spatial resolution due to scattering, and the constraints inherent to this technique – i.e. careful match between the object and the beam energy – presented serious disadvantages. In the same line of thought, proton imaging using the energy loss of the particles was a good match at the beginning, compared to X-ray tomography. However, multiple scattering was here again a drawback, and while the dose reduction to the patient compared to X-ray CT was interesting, it did not justify the cost of a proton or heavier charged particle accelerator.

2.3 The second era of proton imaging - treatment planning and quality assurance

The expansion of charged particle therapy at the beginning of the 1990's changed this situation. Proton imaging nowadays is considered for two applications, albeit very close. The first application is the potential for portal imaging on treatment accelerators, in order to produce radiographs to verify patient positioning and the calibration of the treatment plan with respect to the stopping powers of the materials (Section 1.2.2.2). The second application is the use of proton tomography to directly map the relative stopping power of the tissues, in order to be used in treatment planning instead of converted CT numbers.

It is precisely the use of proton imaging for these purposes that generated the renewal of the interest in this modality. Hanson et al. [1982] concluded that :

> *"If the only advantage of the proton technique is better dose utilization, the anticipated extra expense of implementing charged particle CT may not be justified for widespread routine diagnostic studies. [...] Charged particle CT may also be valuable for special purposes such as treatment planning for charged particle therapy."*

The need for more precision in treatment planning has generated a new paradigm: we seek precisely the information on the stopping powers of the materials. Accelerators are available – for treatment – and gantries make it possible to deliver the beam to a supine (as opposed to vertical) patient with no difficulty. This answers most disadvantages put forward by Hanson et al. [1978] and cited previously (Section 2.2.1). The remaining inconvenience stays multiple Coulomb scattering. We shall see in the following section that the use of curved path estimation for each particle has been put forward as a solution. The use of an energy modulation of the beam [Zygmanski and Gall, 2000], or the use of different calorimeters or range meters with a bigger energy range in order to measure the energy of the protons downstream from the object [Schneider, 1994], makes it now possible to scan the objects without need for a water bath.

2.3.1 Proton computed tomography for imaging the relative stopping power

The idea behind proton computed tomography (pCT) is the following: a beam of protons, of energy sufficient to go through the patient or object to image is sent. The beam characteristics, more precisely the energy characteristics of the beam, are known. Upon exit from the patient, the residual energy or the residual range of the particles is recorded. The information on this residual energy (or range) is used to compute the water-equivalent path length (WEPL) of the protons and the relative stopping power (RSP) of the materials.

The RSP, here noted ϱ, of a material is defined as the ratio between the stopping power (defined in Equation 2.1) of the material to that of water:

$$\varrho = \frac{S_{material}}{S_{water}} \tag{2.12}$$

The WEPL, here noted L, of a particle at the exit of the patient is the distance this particle would have had to go through in water to exit with the same energy, and is calculated by:

$$L = \int_l \varrho\left(\vec{r}\right) dl \tag{2.13}$$

with l the path of the proton in the material.

From the integration of the Bethe-Bloch formula, the WEPL is equal to the integration of the reciprocal stopping power of water, thus:

$$\int_{E_{in}}^{E_{out}} \frac{dE}{S_{water}\left(E\right)} = \int_l \varrho\left(\vec{r}\right) dl \tag{2.14}$$

By measuring the energy E_{out} upon exit from the patient, and knowing the energy E_{in} at the entry, the left side of Equation 2.14 can be computed. As an alternative, a calibration of the system makes it possible to access directly pre-computed WEPL [Hurley et al., 2012]. In consequence, it is possible to reconstruct the RSP on the right side of the same equation. It can be noted that, in order to do so, the path l of a proton needs to be estimated.

It can be put forward that, since the stopping powers depend on the energy (Section 2.1.1), so do the RSP, and the reconstructed values are an average over the energy of the particles throughout their propagation. However, in the energy range considered for proton imaging, this variation can be neglected. Indeed, consider an image of a head with a 200 MeV beam; the energy of the exiting protons will be approximately of 80 MeV. The variation in the RSP values will be less than 0.1% for materials such as muscle or adipose tissue, and less than 0.3% for skull for example (using the materials defined in Appendix A), which is less than the expected resolution of 1% on the RSP values (Section 2.3.3.2).

Terminology: On relative stopping power and relative electron density in pCT

Early papers on proton imaging state that the aim of a pCT image reconstruction is to map the relative electron density of the materials. More recent papers state that the aim is to map the relative stopping power of the materials. The difference is lexical. In the first approach, one wants to reconstruct the values of the relative electron density but, as no information on the ionization potential of the material is known, it is assumed to be that of water. The reconstruction of the RSP is strictly equivalent, except that the unknown ionization potential of the material remains implicit in the formulation, avoiding the approximation. The result is the same, the terminology was modified in order to not have to make an assumption on the ionization potential.

Nevertheless, for quantification of the images, the “precision” of estimation of the relative stopping power values is characterized by the “density resolution”, even when it is said that the RSP is reconstructed.

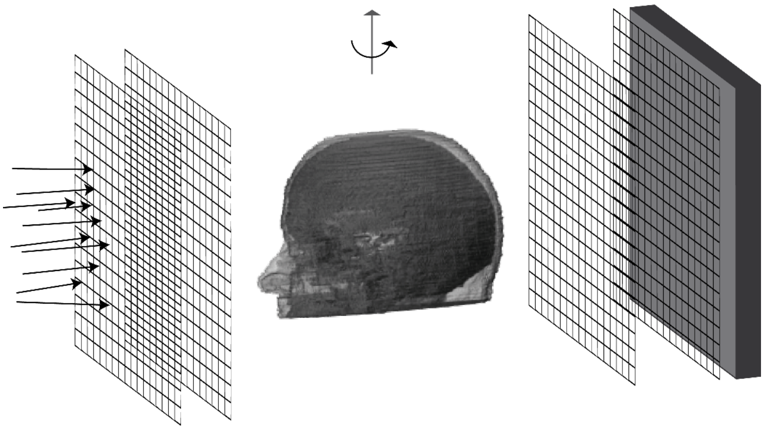

Figure 2.6: Proton tomograph as studied nowadays. It consists in four trackers, two upstream and two downstream of the object and of a calorimeter or range meter. The particles are tracked one by one.

2.3.2 Proton tomographs

The multiple scattering and explicit apparition of the proton path l in Equation 2.14 lead to a proposition design for a pCT scanner that to records the positions and directions of the particles, upstream and downstream from the object, as well as the energy of the particles. An attempt was made to record both the positions and energy of the protons using silicon strip detectors (SSD) [Johnson et al., 2003]. However, the limited energy resolution (around 20%) lead to the separation of the tracking and the energy measurement systems. The typical design of proton CT apparatus studied nowadays consists of:

- two sets of (at least) two tracker planes, upstream and downstream from the object, giving access to the information on the positions and directions of each particle,
- a calorimeter or range meter in order to measure the residual energy or range of each proton.

Such a system is illustrated on Figure 2.6.

The specifications of a proton CT apparatus have been described by Schulte et al. [2004], and are detailed in Table 2.1.

Different groups are currently working on proton radiography and tomography, amongst which some are more advanced:

- in the U.S.A., the pCT collaboration, with the University of California Santa Cruz, Loma Linda University and California State University San Bernardino. Other works have been published by the Northern Illinois University and Fermilab.
- in Italy, the PRIMA collaboration involving researchers from Insituto Nazionale di Fisica Nucleare (INFN) and the University of Firenze.
- in Switzerland, the Paul Scherrer Institute and TERA foundation.

Table 2.1: Design specifications for a pCT scanner for therapeutic applications, taken from [Schulte et al., 2004].

Category	Parameter	Value
Proton source	Energy	$\simeq$ 200 MeV (head) $\simeq$ 250 MeV (trunk)
	Energy spread	$\simeq 0.1\%$
	Beam intensity	$10^3 - 10^7$ protons/sec
Accuracy	Spatial resolution	< 1 mm
	Electron density resolution	$< 1\%$
Time efficiency	Installation time	< 10 min
	Data acquisition time	< 5 min
	Reconstruction time	< 15 min (treatment planning) < 5 min (dose verification)
Reliability	Detector radiation hardness	> 1000 Gy
	Measurement stability	$< 1\%$
Safety	Maximum dose per scan	< 5 cGy
	Minimum distance to patient surface	10 cm

Different instrumental approaches have been chosen for both the tracking and the energy/range measurement, that will briefly be reviewed.

2.3.2.1 Tracking

Tracking system requirements are based on three criteria: (i) the spatial resolution, which determines the accuracy of the measured positions and directions, and thus impacts the spatial resolution in a reconstructed image; (ii) the material budget of the tracker planes (ratio between the thickness and radiation length), that determines the amount of scattering the protons undergo, and therefore the additional uncertainty on the directions measured; (iii) time resolution and readout performances, that are essential to event-by-event proton tracking. An exact requirements sheet in terms of these criteria is not known, as the overall result in an image will be impacted by the different parameters. Nevertheless, the best spatial resolution, lowest material budget and fastest acquisition rate will obviously be looked for. Prototypes have been developed following different approaches:

- The first group to work on proton scanners presenting a design similar to that studied nowadays used scintillating fibres [Pemler et al., 1999]. These fibres had a square section of 2 mm, were assembled in two layers for better light collection and position resolution. They were read by photomultiplier tubes (PMT). More recently, it was proposed to use circular fibres of 0.5 mm diameter, also in two layers, but read by silicon photomultipliers (SiPM) [Gearhart et al., 2012]. It was also suggested to use such a tracker to obtain the information on the energy of the particles [Koybasi et al., 2012], however, no quantification of the potential resolution achieved with this method was given.

- Other groups have chosen to use silicon detectors, more precisely Silicon Strip Detectors (SSD) [Saraya et al., 2013; Sadrozinski et al., 2013; Civinini et al., 2013]. The pitch of such detectors in the different groups was around 200 µm, and the thickness varying between 200 and 400 µm. Moreover, as such detectors cover a rather small surface compared to the size needed for a head detector, work was done in order to reduce edge size in order to diminish material overlap. The use of CMOS pixel detector was also investigated [Seco and Depauw, 2011; Poludniowski et al., 2014].

- The TERA foundation project proposes the use of gaseous detector, and more precisely triple-GEM detectors, for the tracking of protons. The Gaseous Electron Multiplier (GEM) modules provide two-dimensional coordinates readout on orthogonal strips at 400 µm pitch and can achieve a position accuracy up to 100 µm [Amaldi et al., 2011].

In terms of material budget, a prototype with 2 mm diameter scintillating fibres arranged in four tracking planes on each side of the patient will result in a very important scattering of the protons compared to the triple-GEM and silicon detectors. However, the reduction of this diameter from 2 mm to 0.5 mm makes it so that the triple-GEM approach then presents the most important material budget. In terms of spatial resolution, 0.5 mm scintillating fibres present a more important pitch than the solid state detectors that are considered and the triple-GEM. However, there may be some disadvantages to gaseous detectors in a clinical context. As mentioned before, the spatial resolution of the reconstructed image will depend on these parameters, as they will impact the path estimation. The evaluation of their importance will be presented in Section 4.3.

Last but not least is the need to consider timing performances and data acquisition rate of a prototype. The event-by-event tracking of the particles generates a particular challenge. Different projects for proton scanners are well on their way towards clinical applications. However, increasing the data rate to support clinically useful proton fluxes is an essential step [Sadrozinski et al., 2013]. In terms of single-proton tracking, the simultaneous recording of two events on the tracking planes makes it impossible to match trajectories before and after the patient; the information can therefore not be treated. As a consequence, for a given number of proton histories to get a certain image quality, the acquisition time as well as the dose to the patient will depend on the particle rate that can be handled. Developments on the acquisition system are made, in order to sustain data rates exceeding 1 or 2 MHz with the silicon trackers [Sadrozinski et al., 2011, 2013; Steinberg et al., 2012; Johnson et al., 2012, 2013]. This requirement has been estimated for the synchrotron beam of the Loma Linda Univesity Medical Center: proton bunches are spaced by 110 ns intervals, and only single-proton bunches can be used because of the particle rate supported by the calorimeter [Johnson et al., 2013]. The group working with GEM detectors reported the development of a fast acquisition system in order to sustain a particle rate of 1 MHz [Bucciantonio et al., 2013].

2.3.2.2 Energy/range measurement

As far as the energy/range measurement is concerned, the most important criterion is the resolution on the measured WEPL. The two approaches, i.e. calorimeter and range-meter, have been explored:

- The first approach consists in recording the energy of the outgoing protons and calculate or calibrate their WEPL accordingly. For this, different crystal calorimeters were investigated: NaI(Tl) crystal read by a PMT [Saraya et al., 2013], CsI(Tl) crystal read by photodiodes [Hurley et al., 2012] or YAG:Ce crystal read by silicon photodiodes [Civinini et al., 2013]. Hurley et al. [2012] show that direct calibration of detector response to WEPL is possible. However, the use of segmented block calorimeters results in a non-uniformity of the detector response.

- The second option is to record the residual range of the particles that gives access, in the same fashion, to the WEPL. Range counters using stacks of plastic scintillator plates, of thickness between 3 and 4 mm were proposed. The light emission can then be either directly collected [Sadrozinski et al., 2013] using SiPM readout, or indirectly collected, through the use of wavelength shifting fibres and readout by PMTs [Pemler et al., 1999] or by SiPMs [Amaldi et al., 2011].

Resolution on the measured WEPL using a block calorimeter depends on the WEPL. For large WEPL, an increase in the sensitivity to the deposited energy in the calorimeter results in a decrease of uncertainty [Hurley et al., 2012]. The range-meter approach, however, shows a constant resolution on the measured WEPL, depending only on the thickness of the slabs constituting the range meter [Sadrozinski et al., 2011]. Therefore, the calorimeter approach shows an advantage for larger WEPL while the range-meter approach is more interesting for shorter WEPL.

In order to take advantage of both approaches, a hybrid multi-stage solution was proposed by Sadrozinski et al. [2013]. It consists of two polystyrene blocks read by PMTs, which would perform better than the CsI calorimeter over the entire range of interest, and only slightly worse than the 4-mm slabs range-meter for short WEPL. Nevertheless, the increase in the acquisition rate of the tracking system may generate an additional constraint on the calorimeter in terms of particle rate to handle.

Comment on other charged particle imaging

It can be put forward that other charged particles can be used for imaging of the relative stopping power. Carbon imaging, in particular, is also investigated since there are clinical facilities that have carbon ion accelerators. Carbon imaging is very similar to proton imaging in its concept [Parodi, 2014]. The idea is to use the energy loss of carbon ions to produce images of the electron density (or RSP) of the materials. The main difference is that carbon ions undergo less scattering in the materials. Therefore, there is no need to measure the directions of the particles. For the energy/range measurements, different experimental approaches were taken, such as the use of plastic scintillators [Ohno et al., 2004; Shinoda et al., 2006], flat-pannel detector [Telsemeyer et al., 2012] or the use of an ionization chamber (IC) stack [Rinaldi et al., 2013]. The same technologies could be used for proton imaging.

2.3.3 Expected performances of pCT

2.3.3.1 Path estimation and spatial resolution

As proton radiographic images are greatly affected by multiple scattering, leading to a spatial resolution much less satisfying than X-ray CT, the estimation of individual proton trajectories for image reconstruction has taken a lot of importance. Different algorithmic approaches have been investigated for reconstruction, either using analytical or iterative reconstruction algorithms. In the case of analytical reconstruction, the data is binned into projection for reconstruction, while iterative reconstructions make it possible to consider individual trajectories for each proton. This will be discussed more in detail in the next chapter.

Nevertheless, the path of the protons, denoted l in Equation 2.14, is of key importance to reach the millimetric spatial resolution (Table 2.1). The first approach that was taken, in a similar fashion to X-ray CT, consisted in only taking into account the position of the particles on the calorimeter [Hanson et al., 1981], as illustrated on Figure 2.7(a). With the addition of a position-sensitive tracker before the object [Pemler et al., 1999], one may define the trajectory of a proton as a straight line between an upstream and a downstream tracker, as illustrated on Figure 2.7(b). With further addition of trackers in order to record the angle of the particles before and after the object, one may define the trajectory of protons as broken straight lines [Li et al., 2004; Vanzi et al., 2013] (Figure 2.7(c)). However, an additional advantage can be found in the knowledge of the direction of each particle, in that it allows the definition of curved trajectories, as

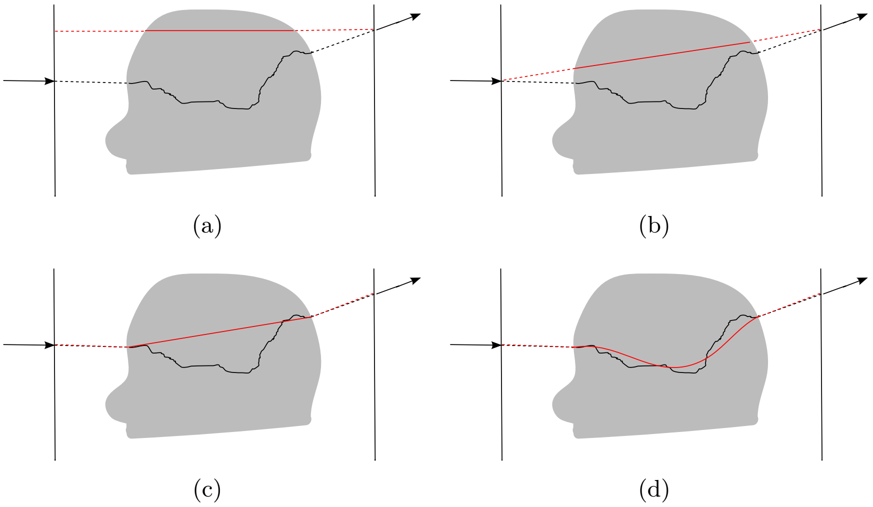
(a) (b) (c) (d)

Figure 2.7: Illustration of different path estimations for image reconstruction. In black, the proton trajectory, in red estimations made: (a) knowing only the position on a downstream detector; (b) knowing the positions upstream and downstream from the object; (c) knowing the positions and directions upstream and downstream from the object; (d) estimating the most likely path using the positions and directions upstream and downstream from the object.

suggested by Hanson et al. [1981]. Two different approximations of the trajectory of the protons by a curved path have been proposed: the first is a cubic spline approximation, called cubic spline path (CSP); the second is the most likely path (MLP) considering the object has scattering and energy loss properties of water [Williams, 2004]. The latter is illustrated on Figure 2.7(d), and is discussed in more detail in section 3.3.2. Iterative image reconstruction using algebraic methods has shown to be advantageous compared to analytical image reconstruction in that it allows more flexibility in the chosen path. It has been highlighted that the most likely path estimation gives better results in terms of spatial resolution of the reconstructed image than the use of CSP or of a straight line (SL) approximation [Li et al., 2006] (though not by much compared to the CSP). Such reconstruction can also be performed starting from an analytically reconstructed image [Penfold, 2009]. Nevertheless, analytical image reconstruction can be improved from the simple horizontal straight line approximation by either removing the data of protons that strayed too far from the straight line during their way in the object, estimated using the MLP [Cirrone et al., 2011]; by binning the data at the middle of the path between two detectors [Vanzi et al., 2013]; or by using a distance-driven binning taking the MLP into account [Rit et al., 2013].

Published studies show that sub-millimetric spatial resolution can be reached when considering objects of a few centimetres thickness and proton beams of energies greater than 100 MeV [Song et al., 2008; Amaldi et al., 2011; Saraya et al., 2013]. Whether or not a head-sized object can be imaged with a sub-millimetric spatial resolution with protons of 200 MeV has not yet been demonstrated with experimental data.

2.3.3.2 On dose and density resolution

For improvement of treatment planning, it is necessary to reach a resolution on the reconstructed relative stopping powers of less than the 3% achievable with X-ray CT, with 1% being ideal. The density resolution that can be achieved with a pCT depends on the energy of the protons and on the number of protons available per voxel of the reconstructed image. This leads to a trade-off between the delivered dose and the density resolution [Satogata et al., 2003; Denyak et al., 2011].

Impinging particles with lower energy will lose more energy, leading to an increase in the dose deposit for a given number of protons. However, since the particles deposited more energy, a greater contrast is expected. On the contrary, the use of higher energy protons makes it possible, for a given dose to the patient, to have more protons to calculate the average energy loss on, and the effects of multiple scattering will be less important. In addition, the range straggling will be smaller. Therefore, a compromise between the energy and the number of particles is needed, but higher energy protons may be of interest because of the reduction in scattering. Nevertheless, the increase in the energy of the beam is constrained by the technical specificities of the clinical accelerators for proton therapy, most of which can reach energy of 230 MeV [Particle Therapy Cooperative Group, 2014]. Most studies performed nowadays, in the context of proton imaging for a head scanner, consider protons of energy close to 200 MeV [Coutrakon et al., 2013; Sadrozinski et al., 2013; Amaldi et al., 2011].

For a given beam energy and object size, the density resolution depends on the number of impinging particles and voxel size. Current studies are based on a ratio of 100 between the number of protons detected and the image volume (in mm^3) [Sadrozinski et al., 2011] or, in the context of radiography, 100 protons per mm^2-projection pixel [Amaldi et al., 2011]. Different estimations of the achievable density resolution were made [Schulte et al., 2005; Erdelyi, 2010], and results are in agreement (with a $\sqrt{2}$ factor difference unaccounted for). Nevertheless, these studies indicate that a 1% density resolution should be achievable for a dose to the object of a few mGy.

2.3.4 Different approaches to pCT

It can be noted that, since the beginning of this work, other groups have shown interest in investigating proton imaging under different angles. The use of multiple scattering information in order to detect tissue inhomogeneities was investigated by Raytchev and Seco [2013]. They demonstrated the possibility to use this information in order to measure the depth and thickness of an inhomogeneity using a graphical fingerprint method, for simple geometries. Multiple scattering images were also investigated by Aso et al. [2012] and Plautz et al. [2012].

2.4 Positioning of this work

The work presented in this thesis aims at exploring the potential of proton computed tomography. The design of a proton scanner, as studied nowadays, has been presented in the last section. Two points can be considered:

- The aim of proton imaging today is the mapping of the relative stopping power of the materials, in order to be used in treatment planning for particle therapy. It has been shown that this technique makes it possible to access this information with a 1% uncertainty, which would reduce the range uncertainty and considerably increase the benefit of ion beam therapy. However, reaching a satisfactory millimetric spatial resolution in a reconstructed image remains a challenge.

- With a system that records not only the residual range or energy of each particle, but also their positions and directions upstream and downstream from the object, information on the scattering and transmission rate is available. This information is little used to this day: the scattering is used to estimate a trajectory but not as an information in itself; the transmission rate is not exploited at all. It was presented in the first chapter that, in addition to an uncertainty on the range of particles, charged particle therapy also suffers from uncertainty on the dose deposit. Part of this uncertainty is on the physical dose deposit in the tissues, due to the incomplete knowledge of tissue composition and properties for treatment planning.

These assertions are at the origin of the work presented in the next chapters. After setting up the tools for simulation and reconstruction of pCT images, detailed in Chapter 3, investigations on most likely path estimation are presented in Chapter 4. In particular, the definition of the MLP as well as the impact of the tracking system properties (spatial resolution, material budget and location) on the path estimation were studied. Chapter 5 focuses on the potential use of all the outputs of a proton scanner in order to gain more information on the tissues and their composition. This information might, in turn, help reduce the uncertainty on the dose deposit.

Summary

- Through the years, different means to use protons for medical imaging have been put forward.
- Today, proton computed tomography using the energy loss of the particles in order to map the relative stopping powers of the particles in the tissues is studied.
- In addition to the calorimeter or range-metre, a proton tomograph makes use of a tracking system to record the position and direction of each particle upstream and downstream from the object. This makes it possible to take the scattering of the particles into account during the image reconstruction process.
- Previous studies have shown that a resolution on the relative stopping power values of the order of 1% is achievable for a dose to the patient of a few mGy. A sub-millimetric spatial resolution stays a challenge, but may be reached by using a curved path estimation for each proton.

CHAPTER 3

SIMULATION AND RECONSTRUCTION PLATFORM FOR PROTON CT

Contents

In order to investigate the potential of proton imaging, a dedicated simulation and reconstruction platform was set up.

3.1 Simulation of a proton tomograph

The simulation of the proton tomograph was set up using the GATE platform. This section details the simulation.

3.1.1 Monte Carlo simulation using GATE

Monte Carlo methods are a broad class of computational algorithms that rely on random (or pseudo-random) number generation to calculate numerical results. The application of Monte Carlo methods to particle transport dates from the 1940's, first by E. Fermi for modelling properties of the neutron, soon followed by J. von Neumann, S. Ulam and N. Metropolis in the context of the Manhattan project [Metropolis and Ulam, 1949]. The latter developed a program in order to simulate the stochastic process of neutron transportation. The code-name "Monte Carlo" was chosen at the time as a reference to the city, known for the gambling games.

The particle is generated at a given position, with a given direction and energy. The principle of particle transport in a Monte Carlo simulation code can be schematically explained in three steps:

(i) First, the mean free path λ of the particle in the considered medium is computed. The interaction length of the particle (the distance that will be travelled before the next interaction), noted x is then randomly selected. It follows a probability density defined as:

$$p(x) = \frac{1}{\lambda} \exp\left(-x/\lambda\right) \tag{3.1}$$

For this distance, the particle will go in a straight line, in the direction defined at the end of the previous step, and with the energy defined previously.

(ii) The physical process happening during the interaction is randomly selected in the list of possibilities, according to the cross-section of each process.

(iii) Once the interaction process is selected, the final state of the particle after the interaction can be computed: the new energy and direction of the particle is thus known for the next step.

The trajectory of each particle is modelled step by step until exit of the medium or complete absorption.

The use of Monte Carlo techniques and simulations for applications in medical physics, imaging or treatment, saw a rapid growth since the beginning of the 1970's [Raeside, 1976].

3.1.1.1 GEANT4

The Geant4 (GEometry ANd Tracking 4) simulation code [Geant4 website] is an open access toolbox [Agostinelli et al., 2003] developed by the CERN and written in C++. It was initially conceived for high-energy physics in order to track particles in an experimental setup. The detector response can be simulated and particles can be tracked inside volumes. It makes use of both models and experimental cross-sections.

One precision concerning the workflow of Monte Carlo simulations, detailed in the previous section, can be made concerning multiple Coulomb scattering (MCS, section 2.1.2). The "detailed" simulation of MCS, with all the collisions and interactions, is computationally very expensive. This has lead to the development of "condensed" simulations: the global effect of the collisions is simulated after each track segment. Most Geant4 multiple scattering models belong to this second class [Urban, 2006], though hybrid approaches using both condensed and detailed simulation processes also exist [Ivanchenko et al., 2010].

For condensed MCS models, multiple scattering is not selected amongst the processes in step (ii), but is applied at each step. The basis function for each Monte Carlo step of charged particles in a media becomes [Ivanchenko et al., 2010]:

- propose step limit,
- convert this step length into "true" step length taking into account scattering along the step,
- sample scattering angle and turn particle direction at the end of the step,
- sample displacement of end point.

Geant4 is nowadays used in many scientific fields, such as biological and medical sciences, radioprotection, aeronautics, or for spatial applications. In the context of pCT, it was validated in the pertinent energy range [Milhoretto et al., 2012] and extensively used for detector development [Cirrone et al., 2007; Steinberg et al., 2012; Zatserklyaniy et al., 2012]. It was also very often used as a basis of work for image reconstruction developments [Williams, 2004; Li et al., 2004; Penfold, 2010; Aso et al., 2012].

3.1.1.2 GATE

While Geant4 is a complete toolbox, allowing for a total control on the simulation, the management of time is quite complex. This has lead to the specific development of simulation codes dedicated to medical imaging, that are based on Geant4, such as GATE (Geant4 Application for Emission Tomogaphy). GATE [Jan et al., 2011] is nowadays developed by a dedicated international collaboration, OpenGate [Opengate collaboration]. It has the advantage of allowing an easy management of time, including movement of the source(s) and detector(s) as well as a simplified management of geometry for detectors and phantoms.

Easy setup of a simulation is made possible by a user interface. All aspects of the simulation are described in a macro file:

- geometry and movements of the detectors,
- geometry and movements of the source,
- geometry and movements of the phantom,
- physical interactions of each particle type,
- response function of the detector.

As indicated by the name, GATE was developed for emission tomography purposes. It has however expanded over the years, supporting imaging systems such as a generic scanner type and adapting for radiotherapy applications.

3.1.2 Scanner description

A proton tomograph was simulated with GATE version 6.2 using a “CTscanner” geometry. The scanner, illustrated on Figure 3.1, contains two “modules”, one upstream and one downstream of the phantom. Throughout this work, a 30×30 cm^2 proton source generating the mono-energetic 200 MeV protons all in the same direction was used. The upstream module contains one tracking plane: this parallel beam geometry, and the subsequent knowledge of the direction of the particles makes the second one unnecessary. The downstream module contains two tracking planes and a calorimeter.

As this work aims at exploring the potential of proton imaging, a “perfect” scanner was simulated. The silicon tracker planes were 10 µm thick, and recorded the exact position of interaction of the particles without pixelization. Cuts on the particles energy were applied in the calorimeter region so that any proton reaching this volume would deposit all its energy immediately. The inner trackers were separated by 50 cm. The distance between the two downstream trackers was set to 20 cm. These geometrical parameters were set arbitrarily because, as the exact positions are recorded, they have no effect on the computation of the direction of the particles. However, it was chosen to implement a scanner, and not just an upstream and downstream plane with actors, to make it easily possible to include detector effects in further works.

3.1.3 Data output

During the simulation, GATE generates a “Hits”, a “Singles” and a “Run” file.
The “Run” file contains the number of particles generated per run, i.e. per projection angle. The “Hits” file contains the information on all interactions in the sensitive materials (where interactions are recorded), here the trackers and the calorimeter. It contains, amongst others: the run ID, the ID of the event and of the primary parent particle, the ID of the volume of interaction, the interaction position and energy deposit. The “Singles” file is slightly different as it contains information averaged over the detection element. It is associated to the notion of “digitizers”. The digitizer module aims at simulating the behaviour of the scanner detectors and signal processing chain.

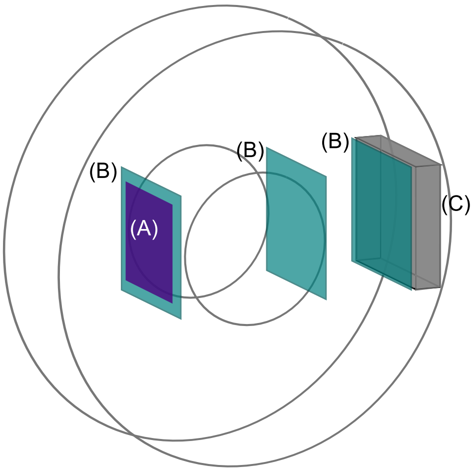

Figure 3.1: The scanner in GATE with (A) the source, (B) the three tracker planes and (C) the calorimeter.

However, as no detector response was included in the simulation, digitizers were not used, and the Hits and Singles files are very similar.

In order to be used in listmode (proton-by-proton) reconstruction, the output files from the simulation were pre-processed and only the necessary information was kept. The data was split according to the run ID and for each event, the information kept consists in:

- the run ID
- the interaction position on the upstream tracker plane
- the interaction position on the inner downstream tracker plane
- the downstream direction
- the energy of the proton
- the computed water-equivalent path length (WEPL, defined in Section 2.3.1)

For each particle, the WEPL was computed using Equation 2.13. This process could be accelerated by computing it only once for each energy and storing the result in a lookup table. Secondary protons were not included in the listmode. This does not impact the results, as it was shown that a filter on the energy could separate the secondary protons in a realistic case [Schulte et al., 2005]. Protons that did not reach the downstream detectors because of nuclear interactions were kept in the listmode file with the information upstream from the object only. This information will be of use for the study on the transmission rate presented in Chapter 5.

3.1.4 Execution of the simulations

Consider a tomographic acquisition consisting in 256 projections over 360°, with 1000 protons generated per square millimeter of source. For the 30×30 cm^2 source, this represents about $2.3 \cdot 10^{10}$ protons to simulate.

In order to reduce the time required, the simulations were performed in parallel on a computational grid [IPHC computational grid], following a workflow implemented in the group in the framework of simulations for pre-clinical PET imaging [Brard, 2013]. The "Multiple Replication In Parallel" method [Glynn and Heidelberger, 1991] was used. It is a direct "embarrassingly parallel" method, particularly appropriate for tasks independent from each other. It is perfectly appropriate for this application, as neither pixelization, pileup nor any other detector or electronics effects were considered. The independence of the parallel simulations depends necessarily on the pseudo-random number generator. In this workflow, a parametrization method associated to the Mersenne Twister [Matsumoto and Nishimura, 1998] generator is used.

Thus, the GATE simulation is parallelized as follows: the simulation is fractionated so that each sub-simulation represents a fraction of the number of protons to generate. These sub-simulations are executed on the computational grid, each independently on a Worker Node. The output files are pre-processed to generate the listmode files, that are concatenated and stored on a server that acts both as user interface for the submission of the jobs and as storage element. This server can be accessed by the local servers for further processing.

3.1.5 Description of the phantoms used

3.1.5.1 The Forbild phantom

The semi-anthropomorphic Forbild head phantom [Lauritsch and Bruder] was used in order to get quantitative data on image reconstruction quality. The original phantom, of which an axial slice is shown on Figure 3.2, is an X-ray CT dedicated phantom. It contains very small inserts to test spatial resolution (up to 20 line pairs per centimetre in the left ear) as well as low contrast inserts. In the description provided, a material density is attributed to each region. The phantom was implemented in GATE using analytical shapes. As the phantom is based on ellipsoids that were not available in version 6.2 of GATE, this work generated the occasion to implement them in the source code. They have been transmitted to the GATE collaboration and are now available in version 7.0 [Opengate collaboration wiki].

The original Forbild phantom is described in terms of material density. To be included in the simulation, a chemical composition and mass density were attributed to each region (described in Appendix A). Some materials were kept with their original compositions. In order to reproduce the contrast of the original phantom, the density of the brain was modified in some regions.

The high spatial resolution pattern of the left ear was modified. In the idea of a millimetric spatial resolution (at best) and the reconstruction of an image with 1×1×1 mm^3 voxels, the 1.4 to 2 line pairs per mm pattern were ill-proportioned. Therefore, this pattern was replaced by rows of spherical inserts of water of 4 mm, 3 mm and 2 mm diameter, with RSP values 50%, 5%, 1% and 0.5% higher than that of the brain.

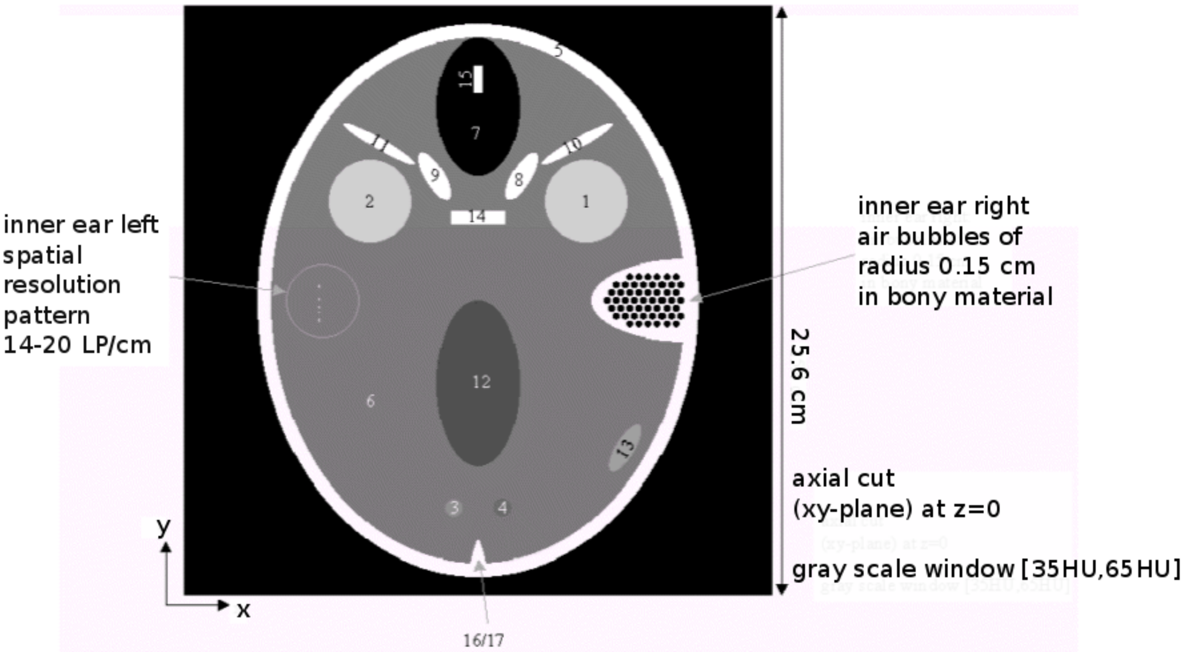

Figure 3.2: Original Forbild phantom. Image from [Lauritsch and Bruder].

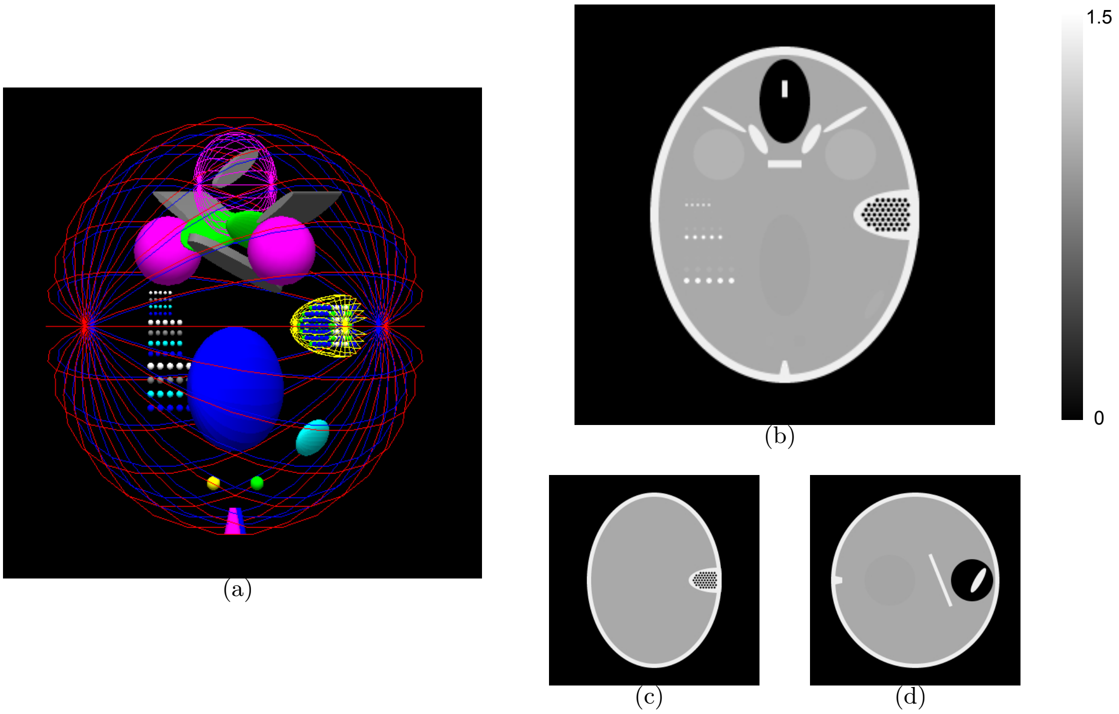

(a)

(b)

(c)

(d)

Figure 3.3: (a) Forbild phantom in GATE; Forbild RSP with (b), (c) and (d) transverse, coronal and sagittal views of the Forbild phantom in RSP.

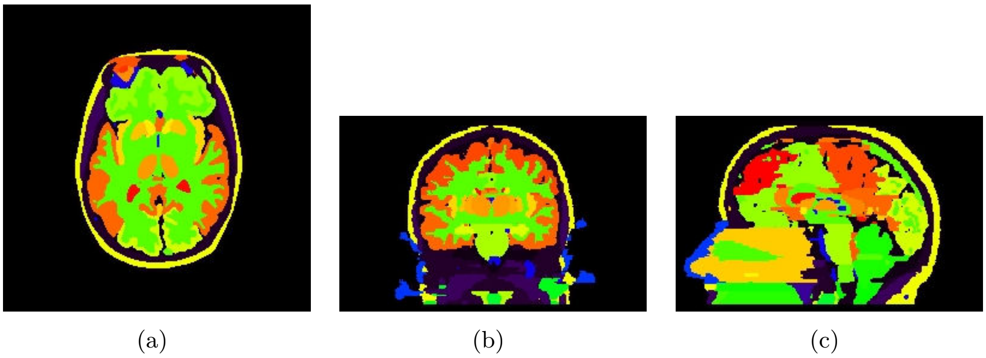
(a) (b) (c)

Figure 3.4: Original Zubal phantom. The colours represent the reference numbers used to distinguish the different parts of the phantom.

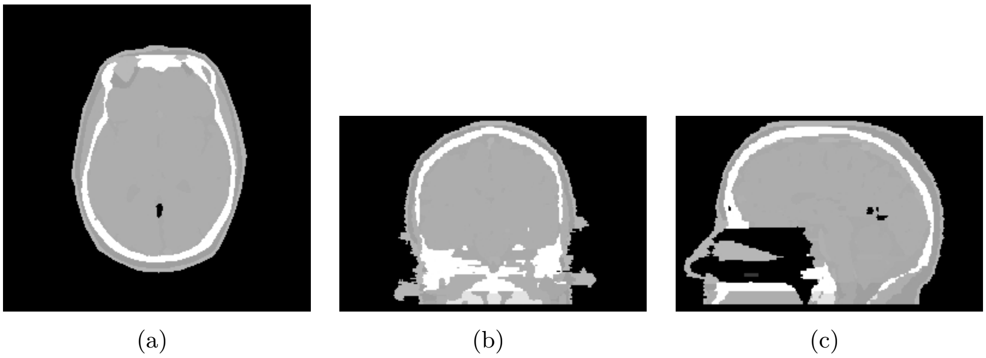
(a) (b) (c)

Figure 3.5: Zubal phantom converted to a grayscale representing the RSP of the materials attributed to each region.

Figure 3.3(a) shows a view of the Forbild phantom in the GATE simulation. Figures 3.3(b), (c) and (d) show views of the modified Forbild.

3.1.5.2 The Zubal head phantom

The anthropomorphic Zubal head phantom [Zubal et al., 1994] was also used in order to evaluate the potential of proton CT for imaging complex objects. This three-dimensional voxelized head phantom was generated using transverse T2 slices of an MRI image set. The 256×256×128 image is available online [Zubal], with voxel size of 1.1×1.1×1.4 mm^3 voxels. The head is labelled in 63 different regions.

In order to be used in the simulation, the 63 regions were attributed 18 different material compositions. The detail of the materials used as well as their properties can be found in Appendix A. Figure 3.4 shows the transverse, coronal and sagittal slices of the phantom with the different colours representing the labelled regions. Figure 3.5 illustrates the phantom in grey levels corresponding to the RSP of the materials attributed to each region.

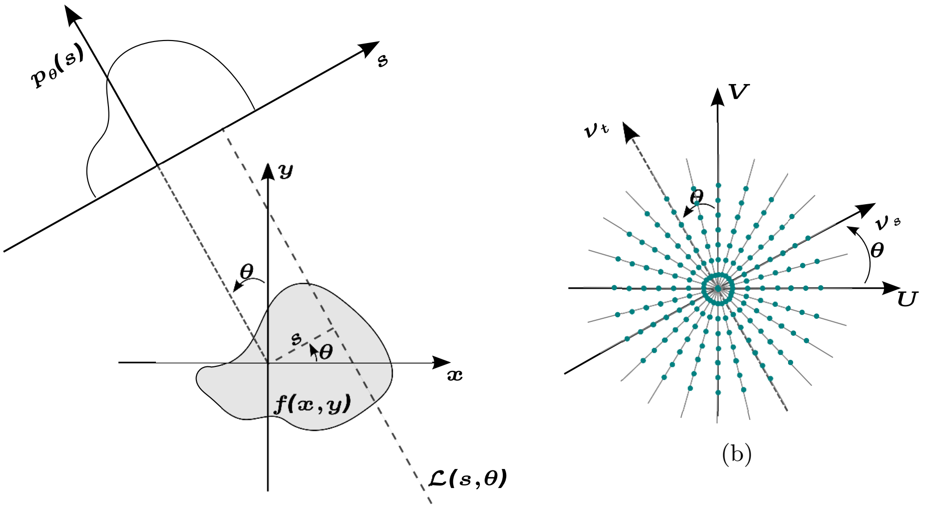

(a) (b)

Figure 3.6: (a) Illustration of the geometry of line integral associated to the Radon transform; (b) the Fourier transform of the projection in the frequency space, illustrating the central-slice theorem.

3.2 Analytical image reconstruction

The simulated data were used to reconstruct images, using an analytical and an iterative reconstruction algorithm. This section describes the principle and the specificities of the analytical reconstruction algorithm used.

3.2.1 2D Radon transform

Radon [1986] described the principle of tomography in order to reconstruct the image of an object using a set of projections. The concept of the two-dimensional Radon transform will be reviewed in this section, as it is the foundation of analytical image reconstruction.

The Radon transform relates a 2D function $f(x,y)$ to the collection of line integrals of this function. Let $\mathcal{L}(s,\theta)$ be the line at angle θ and at the distance s from the origin. Then, $p_\theta(s)$ denotes the line integral through $f(x,y)$ along the line $\mathcal{L}(s,\theta)$, as illustrated on Figure 3.6(a). This line integral can be expressed as:

$$p_\theta(s) = \int_{\mathcal{L}(s,\theta)} f\left(x,y\right) dl \tag{3.2}$$

$$= \int_{-\infty}^{+\infty} f\left(x,y\right) \delta\left(x\cos\theta + y\sin\theta - s\right) dydx \tag{3.3}$$

The projection of f at angle θ, denoted p_θ, is the one-dimensional function regrouping the $p_\theta(s)$ for all s.

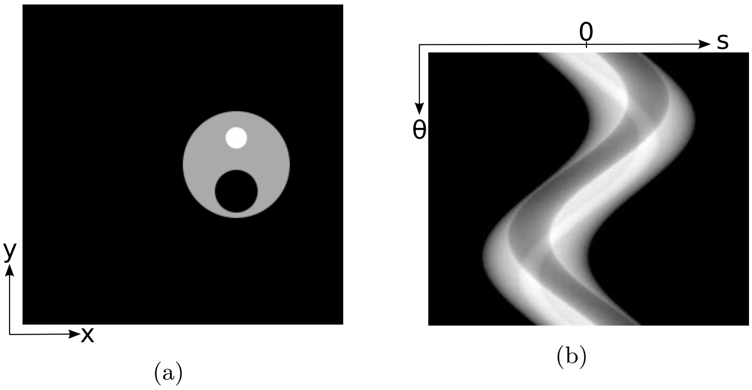

(a) (b)

Figure 3.7: (a) Water cylinder with bone and air inserts and (b) corresponding sinogram.

Sinogram

A sinogram is a two-dimensional, sampled representation of the data from a tomographic acquisition in two dimensions. The data from the projections at different angles are represented as a two-dimensional image, as a function of s and θ. The name "sinogram" comes from the fact that such a display of the projections of a Dirac impulse looks like a sinusoid, as shown on Figure 3.7.

3.2.2 Central-slice theorem

The central-slice theorem, also called Fourier-slice theorem, states the following: if $p_\theta(s)$ is the Radon transform of $f(x, y)$, then the 1D Fourier transform of p_θ equals the slice of the 2D Fourier transform of $f(x, y)$ at angle θ through its origin.

Let $P_{10}(\nu_s, \theta)$ be the 1D Fourier transform of $p_\theta(s)$, and $F_{11}(U, V)$ the 2D Fourier transform of $f(x, y)$, with the indices indicating that the parameters belong to the real (0) or frequency (1) domain. Then:

$$P_{10}(\nu_s, \theta) = \int_{-\infty}^{+\infty} p_\theta(s) \mathrm{e}^{-2i\pi\nu_s s} ds \tag{3.4}$$

$$= \int_{-\infty}^{+\infty} \int_{-\infty}^{+\infty} \int_{-\infty}^{+\infty} f\,(x, y)\, \delta\,(x\cos\theta + y\sin\theta - s)\, \mathrm{e}^{-2i\pi\nu_s s} dydxds \tag{3.5}$$

$$= \int_{-\infty}^{+\infty} \int_{-\infty}^{+\infty} f\,(x, y)\, \mathrm{e}^{-2i\pi\nu_s(x\cos\theta + y\sin\theta)} dxdy \tag{3.6}$$

And changing the polar to the Cartesian coordinate system with $U = \nu_s \cos\theta - \nu_t \sin\theta$ and $V = \nu_s \sin\theta + \nu_t \cos\theta$:

$$P_{10}(\nu, \theta) = F_{11}(U, V)|_{\nu_t = 0} \tag{3.7}$$

As a consequence, the Radon transform describes completely any object $f(x, y)$.

In a practical case, the exact reconstruction of the original object can only be realised if the frequency plane is known in every point. This induces the necessity of an infinity of projections. As the number of projections is limited, a limited number of radial lines representing the information on the frequency plane is available. This is illustrated on Figure 3.6(b), where the blue dots represent the sampled information. This generates an over-sampling of the low frequencies and a lack of information in the high-frequency domain. Moreover, the passage from the function $P_{10}(\nu, \theta)$ defined in the polar space to $F_{11}(U, V)$ defined in the Cartesian space requires interpolation.

3.2.3 Filtered Back-projection algorithm

The direct back-projection of each sinogram value onto the object space along the corresponding ray does not, however, allow to recover the object $f(x, y)$. Instead, it generates a blurred version of the object, called laminogram or layergram [Smith et al., 1973]. It is possible to deconvolve the laminogram by a cone filter in order to recover the original image: this is the backproject-filter method. It is also possible to apply the filter to the projections, before the back-projection operation: this is the filtered back-projection (FBP) method. We have:

$$f\left(x, y\right) = \int_{-\infty}^{+\infty} \int_{-\infty}^{+\infty} F_{11}\left(U, V\right) \mathrm{e}^{2i\pi(Ux+Vy)} dU dV \tag{3.8}$$

Changing from the Cartesian to the polar coordinate system with, as previously, $U = \nu \cos\theta$ and $V = \nu \sin\theta$ ($\nu_t = 0$, $\nu = \nu_s$), we obtain:

$$f\left(x, y\right) = \int_{0}^{\pi} \int_{-\infty}^{+\infty} F_{11}\left(\nu\cos\theta, \nu\sin\theta\right) \mathrm{e}^{2i\pi\nu(x\cos\theta+y\sin\theta)} |\nu| d\nu d\theta \tag{3.9}$$

$$= \int_{0}^{\pi} \left[\int_{-\infty}^{+\infty} P_{10}\left(\nu, \theta\right) \mathrm{e}^{2i\pi\nu(x\cos\theta+y\sin\theta)} |\nu| d\nu\right] d\theta \tag{3.10}$$

$$= \int_{0}^{\pi} \int_{-\infty}^{+\infty} p_{\theta}\left(s\right) h\left(x\cos\theta + y\sin\theta - s\right) ds d\theta \tag{3.11}$$

with h the inverse Fourier transform of the ramp function $|\nu|$.

As the introduction of the ramp filter amplifies high frequency noise, it is necessary to apodize the ramp filter using a 1D lowpass filter. However, as the sharp transition generated by a cut-off can lead to artefacts in the image, “smoother” apodizing filters are used, which further reduce the high frequencies.

3.2.4 Specificities

3.2.4.1 On the generation of projections

The listmode data acquisitions make it possible to know the exact position of interaction of each proton on every tracker plane. As mentioned in the previous chapter (Section 2.3.3.1), different possibilities exist for binning the data into projections. The question takes all its importance in proton imaging, more than in X-ray imaging, because of multiple scattering. For example, taking into account only the position of interaction at the entrance of the calorimeter results in a very poor spatial resolution of the reconstructed image. Whatever the binning procedure chosen, the straight line $\mathcal{L}(s, \theta)$ will only be an approximation of the particles path.

Different binning options were used throughout this work (detailed in Section 4.1.1). As the geometry used for this work is based on a parallel beam, the positions of entrance in the object will be the same than the positions of interaction on the upstream tracker plane (in the xy plane). Upon exit, however, as the particles will have acquired an angle, the position on the tracker planes will strongly depend on the position of the plane (in z, the distance to the object). For an object to image without lateral discontinuities in the path of the particles in the xy plane, the path approximation of a straight line from the upstream position will represent the average path of the particles. Therefore, this was used for the study of the scattering and transmission rate of the particles (presented in Chapter 5).

3.2.4.2 On the Filtered Back-projection algorithm implementation

The FBP algorithm used for this work had been previously implemented in the group. The three-dimensional reconstructed image is the concatenation of a series of two-dimensional image slices reconstructed with a 2D sinogram each.

For the apodization, a Hamming filter [Fessler, 2009] with a cut-off at the Nyquist frequency [Nyquist, 2002] was used.

3.3 Iterative reconstruction with the Algebraic Reconstruction Technique along the most likely path

Iterative reconstruction algorithms have the advantage of easily allowing a proton-by-proton reconstruction using the definition of curved projection and back-projection paths. Reconstructions using the data binned into projections as well as in listmode format can be performed, which may present an advantage in terms of spatial resolution for proton CT.

Algebraic reconstruction techniques are nowadays mainly used in the context of limited-angle tomography and sparse-view tomography [Intes et al., 2002; Sidky and Pan, 2008; Han et al., 2011]. Statistical algorithms for image reconstruction are often preferred in emission or transmission imaging modalities. The advantage of a statistical reconstruction algorithm is that it makes it possible to include statistical and physical models into the reconstruction [Vandenberghe et al., 2001]. However, an appropriate formulation of the pCT image reconstruction problem has not been developed yet. Nevertheless, it was shown that algebraic methods are adapted to the pCT image reconstruction problem [Penfold, 2010], leading to the choice of implementing the Algebraic Reconstruction Technique (ART) algorithm. In addition, a curved path estimation of the most likely path (MLP) for each proton in the reconstruction process was implemented.

3.3.1 The ART algorithm

The ART algorithm belongs to the class of "projection methods", as first proposed by Kaczmarz [1937] and further developed by Tanabe [1971].

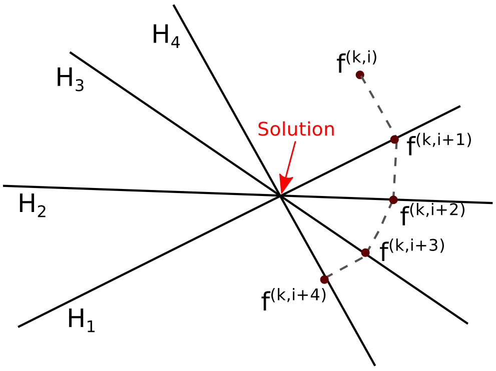

Figure 3.8: Hyperplanes intersecting at the point representing the solution. Consecutive projections on the different hyperplanes representing the convergence of ART towards the solution.

Let us re-write the projection along a proton trajectory, similar to the Equation 3.2:

$$p_i = \int_{\mathcal{L}_i} f(x,y)dl \tag{3.12}$$

with $\mathcal{L}_i$ the path of the ith proton, that can be chosen either to be a straight line orthogonal to the projection plane, or a trajectory estimated for a given proton (more details in Section 3.3.2). In a discrete formalism, adapted to image reconstruction, it can be expressed as:

$$p_i = \sum_{j=1}^{N} f_j a_{ij} \tag{3.13}$$

where f_j is the value of the j^{th} voxel of the image containing N voxels, and a_{ij} the intersection length of the i^{th} proton path with the j^{th} voxel.

The reconstruction problem then consists in solving the system of linear equations $A \cdot \vec{f} = \vec{p}$, where A is the MxN matrix of $\{a_{ij}\}$, $\vec{f} = \{f_1, f_2, ..., f_N\}$ represents the values of the N image voxels and $\vec{p} = \{p_1, p_2, ..., p_M\}$ is the vector of the measured WEPL of the M proton histories.

In a N-dimensional space, the image f is represented by a single point. Each linear equation to solve can be represented by a hyperplane in the same space. When a unique solution to these equations exist, the hyperplanes all intersect in one point which is the solution. This is illustrated on Figure 3.8.

Let k be the iteration number. The projection of $\vec{f}^{(k,i-1)}$ on the hyperplane represented by the i^{th} equation to yield $\vec{f}^{(k,i)}$ can be mathematically described by:

$$\vec{f}^{(k,i)} = \vec{f}^{(k,i-1)} - \frac{\vec{f}^{(k,i-1)} \cdot \vec{a_i} - p_i}{\vec{a_i} \cdot \vec{a_i}} \vec{a_i} \tag{3.14}$$

which can be re-formulated as [Gordon, 1974; Fessler, 2009]

$$f_j^{(k,i+1)} = f_j^{(k,i)} + \frac{p_i - q_{k,i}}{L_i} a_{ij} \tag{3.15}$$

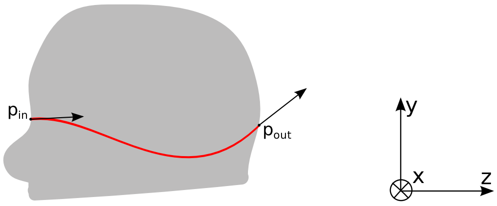

Figure 3.9: Illustration of a most likely path calculated from the entrance and exit vectors p_{in} and p_{out}.

where the projection operator is:

$$q_{k,i} = \sum_{j=1}^{N} f_j^{(k,i)} a_{ij} \tag{3.16}$$

and the normalization factor:

$$L_i = \sum_{j=1}^{N} a_{ij}^2 \tag{3.17}$$

The ART algorithm is intrinsically serial: the image is updated after each event is processed. As a consequence, the reconstruction process is rather slow. In order to improve timing performances, Penfold [2010] has investigated other algorithms, also based on projection methods and more adapted to parallel computing.

3.3.2 Most likely path

The most likely path of a charged particle in a uniform medium was derived ten years ago [Williams, 2004]. It was similar to the “most likely trajectory” derived by Schneider [1994], with a Chi-square formalism.

3.3.2.1 Maximum likelihood formalism

This section describes the computation of the most likely path using a maximum likelihood formalism, as proposed by Schulte et al. [2008].

In order to derive the most likely path of a particle in an uniform medium, two assumptions are made. The scattering due to MCS is assumed to be continuous, and can be approximated by a gaussian distribution; the energy loss is also continuous. The expression is derived in two dimensions. In order to obtain a 3-dimensional trajectory, the computation is performed both in the (xOz) and in the (yOz) planes (Figure 3.9). In the (yOz) plane for example, the position and direction of a particle at any depth can be given by a 2D parameter vector $p\,(y, \theta)$ with y the vertical coordinate and θ the angle between the direction of the particle and its direction of propagation (in this example, the z-axis).

With the assumptions stated previously, it is possible to approximate the scattering distribution with a formula such as the one of Equation 2.7. For a mono-energetic and unidirectional parallel beam, this expression gives the variance of the angular scattering for a thin object ($l \ll X_0$). Should one consider only one particle, this describes the variance of the Gaussian angular scattering probability distribution.

Let p_{in} and p_{out} be the two-dimensional parameter vectors characterizing the entrance and exit parameters of the particle, so that:

$$p_{in} = \begin{pmatrix} y_{in} \\ \theta_{in} \end{pmatrix} \qquad p_{out} = \begin{pmatrix} y_{out} \\ \theta_{out} \end{pmatrix}$$

with y_{in} and y_{out} the lateral coordinates at entrance (depth z_{in}) and exit (depth z_{out}), and θ_{in} and θ_{out} the angles upon entry and exit. Let p_1 be the 2D parameter vector characterizing the position and direction of the particle at depth z_1.

In the bayesian formalism, one can express the posterior likelihood of finding the particle in the state p_1 as:

$$L\left(p_1|p_{out}\right) = L\left(p_{out}|p_1\right) \frac{L\left(p_1\right)}{L\left(p_{out}\right)} \tag{3.18}$$

As we start with the knowledge that the particle did exit the object with p_{out} and entered it with p_{in}, this can be re-written as:

$$L\left(p_1|p_{out}\right) = L\left(p_{out}|p_1\right) L\left(p_1|p_{in}\right) \tag{3.19}$$

The most likely location and direction can be derived by finding the vector p_1 maximizing this likelihood. It can be put forward that $L\left(p_1|p_{in}\right)$ and $L\left(p_{out}|p_1\right)$ are determined by the scattering inside the object. As an example, one can write the likelihood of finding a proton with the parameters p_1 knowing $p_{in} = (0, 0)$ as:

$$L\left(p_1|p_{in} = \begin{pmatrix} 0 \\ 0 \end{pmatrix}\right) = \exp\left(-\frac{1}{2} p_1^T \Sigma_1^{-1} p_1\right) \tag{3.20}$$

where p^T denotes the transpose of p. Therefore, knowledge of the scattering matrices is required.

Let Σ_1 be the scattering matrix whose elements correspond to the variances and covariances of y_1 and θ_1 acquired between z_{in} and z_1 :

$$\Sigma_1 = \begin{pmatrix} \sigma^2_{y_1} & \sigma^2_{y_1\theta_1} \\ \sigma^2_{\theta_1 y_1} & \sigma^2_{\theta_1} \end{pmatrix} \tag{3.21}$$

The elements of this matrix are computed using Equation 2.7 from Lynch and Dahl [1991] presented in the previous chapter. However, the object can not be approximated by a "thin" object, and the order of magnitude of the distance traversed can go from a few millimetres to about 20 cm in the case of a head. Therefore, the previous formula needs to be integrated over the depth considered:

$$\sigma^2_{y_1}\left(z_{in}, z_1\right) = E_0^2 \left(1 + 0.038 \ln \frac{z_1 - z_{in}}{X_0}\right)^2 \times \int_{z_{in}}^{z_1} \frac{\left(z_1 - u\right)^2}{\beta^2\left(u\right) p^2\left(u\right)} \frac{du}{X_0} \tag{3.22}$$

$$\sigma^2_{\theta_1}\left(z_{in}, z_1\right) = E_0^2 \left(1 + 0.038 \ln \frac{z_1 - z_{in}}{X_0}\right)^2 \times \int_{z_{in}}^{z_1} \frac{1}{\beta^2\left(u\right) p^2\left(u\right)} \frac{du}{X_0} \tag{3.23}$$

$$\sigma^2_{y_1\theta_1}(z_{in}, z_1) = E_0^2 \left(1 + 0.038 \ln \frac{z_1 - z_{in}}{X_0}\right)^2 \times \int_{z_{in}}^{z_1} \frac{z_{in} - u}{\beta^2(u)\, p^2(u)} \frac{du}{X_0} \tag{3.24}$$

with X_0 the radiation length of the material (31.6 cm for water) and $E_0 = 13.6$ MeV. The equivalent Σ_2 can be computed for the scattering between z_1 and z_{out}.

In order to allow for the explicit evaluation of the integrals, the energy-loss term $\frac{1}{\beta^2 p^2}$ is approximated by a fifth-degree polynomial. This polynomial is obtained by fitting the energy loss of protons with the same characteristics as the beam used, in the material of interest – here water – using a Monte Carlo simulation.

Let R_{in} and R_1 be the matrices changing the local coordinates system of the incoming proton according to the location of the proton path at entry depth z_{in} and at depth z_1:

$$R_{in} = \begin{pmatrix} 1 & z_1 - z_{in} \\ 0 & 1 \end{pmatrix}, \qquad R_1 = \begin{pmatrix} 1 & z_{out} - z_1 \\ 0 & 1 \end{pmatrix} \tag{3.25}$$

The posterior likelihood of p_1 can then be written as:

$$\begin{aligned} L(p_1|p_{out}) = \exp\Big(-\frac{1}{2}\big[&\left(p_1^T - p_{in}^T R_{in}^T\right)\Sigma_1^{-1}(p_1 - R_{in}p_{in}) \\ &+ \left(p_{out}^T - p_1^T R_1^T\right)\Sigma_2^{-1}(p_{out} - R_1 p_1)\big]\Big) \qquad (3.26) \\ \equiv \exp\left(-\chi^2\right) \qquad (3.27) \end{aligned}$$

Differentiating the expression of χ^2 with respect to y_1 and θ_1, setting the result to zero and solving for p_1, one can obtain the maximum likelihood proton path formula:

$$p_{\mathrm{MLP}} = \left(\Sigma_1^{-1} + R_1^T \Sigma_2^{-1} R_1\right)^{-1} \left(\Sigma_1^{-1} R_{in} p_{in} + R_1^T \Sigma_2^{-1} p_{out}\right) \tag{3.28}$$

Uncertainty on the path

An advantage of this formulation is that it makes it possible to consider the error on this most likely path: a one-sigma envelope on the positions determined can be computed using the inverse of the curvature matrix. The error matrix is defined as:

$$\epsilon_{y_1\theta_1}(z_1) = 2\left(\Sigma_1^{-1} + R_1^T \Sigma_2^{-1} R_1\right)^{-1} \tag{3.29}$$

and the variance in the lateral displacement at depth z_1 is given by the element in the first row and first column of this matrix.

3.3.2.2 Implementation for parallel-beam geometry

The fifth-degree polynomial was calculated as described in [Schulte et al., 2008], using a Geant4 simulation of a mono-directional and mono-energetic 200 MeV proton beam, sent into a 20 cm deep cube of water. For each proton, the energy in each 1 mm-slice was recorded and the value of $\frac{1}{\beta^2 p^2}$ was calculated as:

$$\frac{1}{\beta^2(u) p^2(u)} = \frac{\left(E(u) + E_p\right)^2 c^2}{\left(E(u) + 2E_p\right)^2 E^2(u)} \tag{3.30}$$

Table 3.1: Coefficients of the fifth-degree polynomial of Equation 3.31, fitting $\frac{1}{\beta^2(u)p^2(u)}$, in c^2/MeV^2 divided by the appropriate powers of mm.

	Values	Values from Schulte et al.
a_0	$7.501 \cdot 10^{-6}$	$7.457 \cdot 10^{-6}$
a_1	$3.296 \cdot 10^{-8}$	$4.548 \cdot 10^{-8}$
a_2	$-8.696 \cdot 10^{-12}$	$-5.777 \cdot 10^{-10}$
a_3	$3.454 \cdot 10^{-12}$	$1.301 \cdot 10^{-11}$
a_4	$-2.821 \cdot 10^{-14}$	$9.228 \cdot 10^{-14}$
a_5	$1.218 \cdot 10^{-16}$	$2.697 \cdot 10^{-16}$

where $E(u)$ is the average energy at depth u and E_p is the proton rest energy.

The mean value of $\frac{1}{\beta^2 p^2}$ was recorded and fitted by a fifth-degree polynomial:

$$\frac{1}{\beta^2(u)p^2(u)} = a_0 + a_1 u + a_2 u^2 + a_3 u^3 + a_4 u^4 + a_5 u^5 \tag{3.31}$$

The coefficients of the polynomial are listed in Table 3.1, along with those obtained by Schulte et al. [2008]. Both polynomials are represented on Figure 3.10. There is very few differences between the polynomial from Schulte et al. [2008] and those found for a strictly parallel beam.

3.3.2.3 Validation

Figure 3.11 shows a proton track in water obtained by GEANT4 simulation, the corresponding MLP computed as well as the 1- and 3-σ envelopes associated.

As a Gaussian approximation to multiple scattering was used to derive the MLP computation, tracks of large-angle multiple scattering and nuclear scattering events are not well approximated by the MLP. In order to remove these events from the reconstruction process, Schulte et al. [2008] proposed the use of 3-σ cuts on the exit angle. This leads to a significant reduction of the root mean square error in the lateral position estimated, to about 0.5 mm at the center of the object, as shown on Figure 3.12. Note that the curve without cuts is significantly lower than that of Schulte et al. [2008] (0.8 mm instread of 1.4 mm at the maximum) because secondary protons were never considered.

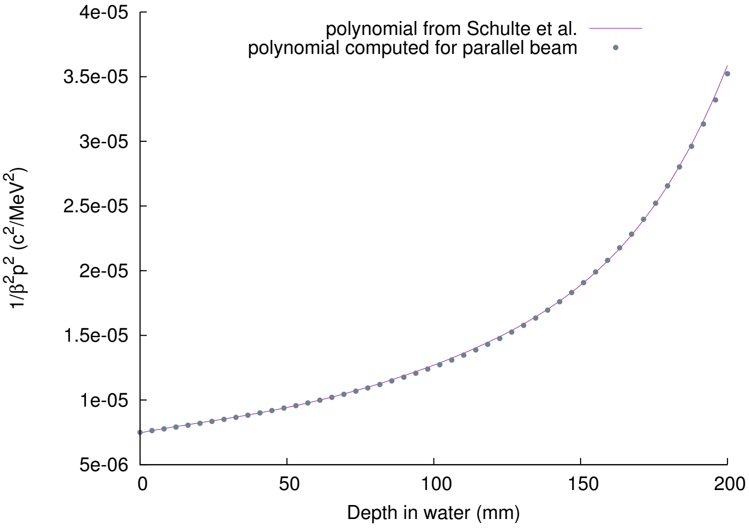

Figure 3.10: Polynomials described by the coefficients of Table 3.1

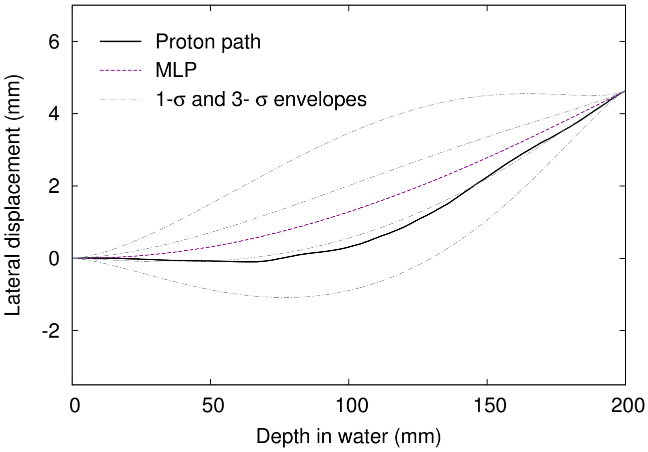

Figure 3.11: A proton trajectory in water, the path estimation and the 1- and 3-σ error envelope.

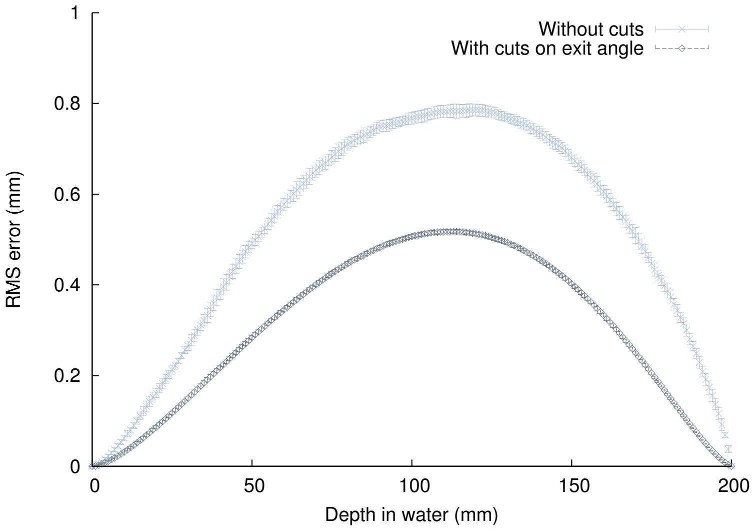

Figure 3.12: RMS error of lateral displacement with and without cuts

3.3.3 Implementation specificities

In addition to the basic reconstruction scheme and path estimation, the questions of data management and regularization for the ART were addressed. Proton-by-proton reconstruction also requires the knowledge of the length of intersection between each proton path and each voxel (noted a_{ij} in Equation 3.15). Furthermore, the knowledge of the border of the object is a prerequisite in order to consider that protons are not scattered outside the object and follow a curved trajectory inside.
The specificities of the implementation of ART, taking the MLP into account, are described in this section.

3.3.3.1 Data management

It has been recognized early in the use of ART for medical image reconstruction that data access ordering can *"have a significant effect on the practical performance of the algorithm"* [Herman, 2009]. It was shown that using a random order of the projections gave the best results [Herman and Meyer, 1993]. Throughout this work, whether the ART reconstruction was performed in listmode or using the data binned into projections, the order for treating the projections when using ART was chosen as random.

Moreover, in the case of proton-by-proton reconstruction, the data of one "projection" i.e. acquired at one detector angle is both redundant and noisy - due to the energy loss straggling. As a consequence, the consecutive projections on "close" hyperplanes (Section 3.3.1), that describe nearly the same path in our case, are not efficient to converge towards the solution. This is illustrated on Figures 3.13(a) and 3.13(b). After three updates of the image, the estimated image ($f^{(k,i+3)}$) is much closer to the solution (the intersection of the hyperplanes) for the case represented on Figure 3.13(b), for which the hyperplanes were more different.

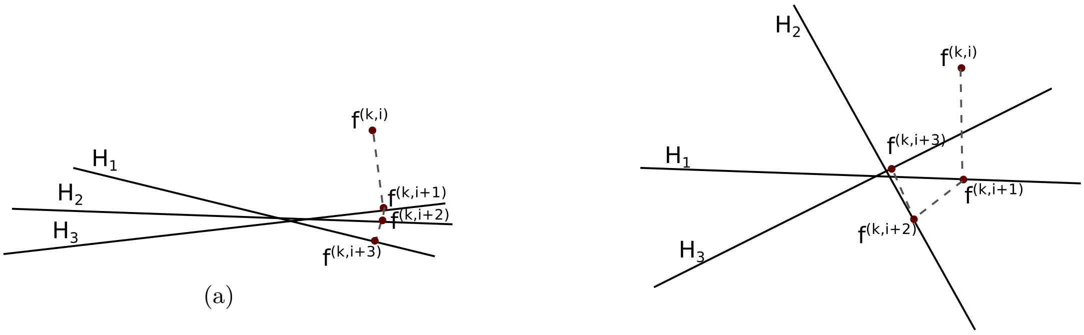

(a)

(b)

Figure 3.13: Illustration of projections onto hyperplans to converge towards the solution for one voxel with (a) data from "close" proton histories (i.e. from the same acquisition angle or consecutive projections for example) and (b) for more random proton histories.

In order to overcome this problem, the tomographic acquisition data was split into "blocks". Each block contains, on the average, the histories of one proton sent per square millimetre of the source, for all the projections - with the order of projections chosen randomly. Throughout this document, one "iteration" of ART will denote the correction of the image using once the M proton histories.

Due to the "embarrassingly parallel" execution of the simulations (Section 3.1.4), the concatenated listmode file was split into projections. As the source was chosen a plane source with a random position for the generation of the protons, further processing was needed in order to be able to select a statistic of one proton per square millimetre pixel of source. Therefore, an "index" file was associated to the listmode file. For each pixel of the source, the number of particles generated and their localization in the listmode file are stored. A third file was also generated, keeping record of whether each proton history should be kept or not in case cuts on the angle and energy are applied.

3.3.3.2 Regularization

ART reconstructions often suffer from salt and pepper noise, caused by the inconsistencies in the set of equations due to noise in the data or, in the case of proton-by-proton reconstruction for pCT, to the energy loss straggling. Indeed, Bethe-Bloch formula describes the average energy loss of the particles in matter. This generates the need for introducing a regularization scheme into the reconstruction.

Relaxation factor

The first form of regularization is the multiplication of the correction applied to each pixel of the image by a relaxation factor λ, giving the image update equation:

$$f_j^{(k,i+1)} = f_j^{(k,i)} + \lambda^{(k,i)} \frac{p_i - q_{k,i}}{L_i} a_{ij} \tag{3.32}$$

For better use and in order not to introduce noise, the relaxation factor can be changed and diminished as a function of the iterations. One consequence of this is however to slow down the convergence.

Total Variation

The use of a relaxation scheme in the form of a Total Variation (TV) minimization [Rudin et al., 1992] was also investigated. TV-based regularization schemes have been used for the reconstruction of CT data with low signal-to-noise ratio or incomplete, irregularly sampled or sparse projections [Defrise et al., 2011]. In the context of proton tomography, Penfold et al. [2010] have shown that inserting a total variation superiorization scheme to their projection-based DROP (Diagonally Relaxed Orthogonal Projection) algorithm [Censor et al., 2008] resulted in superior spatial and density resolution of the reconstructed images.

For this work, a TV-minimization scheme, previously implemented in the group for applications to limited angle tomography in pre-clinical X-ray imaging [Barquero and Brasse, 2012], was adapted to the listmode ART reconstruction for pCT. The TV descent scheme was implemented following the steepest-descent, proposed by Sidky and Pan [2008] in their ASD-POCS (Adaptive Steepest Descent - Projections Onto Convex Sets) algorithm. The POCS scheme represents ART with an additional constraint on the non-negativity of the voxels at the end of each iteration. The aim is to minimize the TV norm of the image by means of a steepest descent with an adaptive step-size. In contrast with the (ASD-)POCS, the constraint of non-negative voxels was applied after each event. Moreover, the relaxation scheme was inserted in the listmode ART reconstruction after each block of m events, giving rise to the following scheme:

```
for each iteration do
    for each block do
        for $i=1..m$ do
            Correct the image with ART
        end
        for $l=1..L$ do
            Proceed to TV norm minimization
        end
    end
end
```

with L the number of iterations of TV descent.

The TV norm can be calculated as:

$$\|\vec{f}\|_{TV} = \sum_{u,v,w} |\nabla f_{u,v,w}| \tag{3.33}$$

with the subscripts u, v and w indicating the three-dimensional coordinates of each voxel and $\nabla\vec{f}$ the gradient magnitude image of $\vec{f}$, defined as:

$$\nabla f_{u,v,w} = \sqrt{(f_{u+1,v,w} - f_{u,v,w})^2 + (f_{u,v+1,w} - f_{u,v,w})^2 + (f_{u,v,w+1} - f_{u,v,w})^2} \tag{3.34}$$

Figure 3.14: Illustration of a raytracing on a curved trajectory.

Let l denote the index of steepest descent iteration and k the index of the block. The steepest descent can then be described as:

$$f_{u,v,w}^{l+1,k} = f_{u,v,w}^{l,k} - w_1 \cdot w_2 \cdot \frac{\partial \|\vec{f}\|_{TV}}{\partial f_{u,v,w}^{l,k}} \tag{3.35}$$

Where w_1 is a weighting factor. In the ASD-POCS algorithm, the weight w_2 is determined by the norm of the difference between the image with and without the positivity constraint. As this constraint was applied after each event for the listmode ART reconstruction in the case of pCT, the weight was set to be proportional to the image correction generated by the ART loop of the block:

$$w_2 = \|\vec{f}^k - \vec{f}^{k-1}\| \tag{3.36}$$

3.3.3.3 Raytracing

As can be seen in Equation 3.15, the ART reconstruction makes use of the chord length of proton trajectories in voxels (a_{ij}). For this purpose, a fast Siddon raytracing algorithm [Siddon, 1985] was implemented on CPU, following the approach of Zhao and Reader [2003]. In the case of reconstruction using the MLP, the path was computed with steps corresponding to voxel boundaries, and the raytracing was performed in straight line for each interval, as illustrated on Figure 3.14.

This approach is computationally expensive. Many works using the ART have used averaged values for the a_{ij}. In the context of proton imaging, Penfold [2009] proposed the use of an "effective mean chord length", depending on the acquisition angle. Their results showed an important gain in reconstruction time by using the effective mean chord length, however the noise in the image was higher than when using the exact chord length. As timing performances were not of a priority throughout this work, the exact chord length was kept. Should it take more importance, it can be noted that the raytracing algorithm implemented on CPU can also be implemented on graphical processing usints (GPU) [Pratx and Chinn, 2009; Nassiri et al., 2012].

3.3.3.4 Boundary detection

Knowing the border of the object that is being reconstructed is of importance in proton CT as this *a priori* is needed for the computation of the MLP. Indeed, it is based on the assumption that the outside of the object does not scatter the protons, while the inside has the scattering and energy loss properties of water.

Different methods have been proposed in the literature in order to answer this problem without using the *a priori* knowledge of a phantom [Schultze et al., 2014]:

- Space carving by retro-projecting data that have been determined as not belonging to the object (i.e. protons that have lost very few to no energy for example). Different implementations can include counting the number of times a voxel was classified as outside of the object for example.
- Space modelling was also proposed. It consists in using the data that were determined (using the energy or angle of the particles) as having gone through the object. When counting the number of occurrences of a voxel being classified as inside or outside the object, one can use the gradient to determine the object border.
- Using a first image, reconstructed analytically (FBP), and applying a threshold to isolate the object. Downsides of this methods are mainly the presence of artefacts in the image, generating “lines” of pixels counted as belonging to the object while they are outside. Moreover, pixels inside a head, for example, may be classified as not belonging to the object. It has also been put forward that this method is more time-consuming than the alternatives listed above.

Zhao and Reader [2002] have proposed a modification of their raytracing algorithm adapted for PET imaging. In their algorithm, the raytracing starts from one point that is both on the projection line and in the object, and the projection is carried out from the internal point towards the outside of the object. In order to determine the object boundary, the opposite was done here. The raytracing is performed on each side of the object separately, starting from the point on the border of the image space and carried out inwards, knowing the direction of the particle. This was done on the phantom image for this work. When the raytracing reaches a point above a threshold, it exits the raytracing operation. Using the coordinate, as well as the yet unchanged direction on each side, the MLP is computed. This process is illustrated on Figure 3.15. Should no object be reached, the raytracing is performed in straight line between the two points on the border of the image space.

For the applications in this thesis, the use of a FBP image (the best produced, see Section 4.1) as a reference for the border detection gives the same result as using the phantom. This is explained by the fact that there are very few artefacts on the FBP image because a perfect detector is considered and the number of projections is rather high (256).

Moreover, the fact that using the FBP image is more time-consuming than the alternatives because of the need to bin the data into projections and perform the reconstruction may not be pertinent, as it was shown that starting with an analytical image for the iterative reconstruction process may be advantageous [Penfold, 2009].

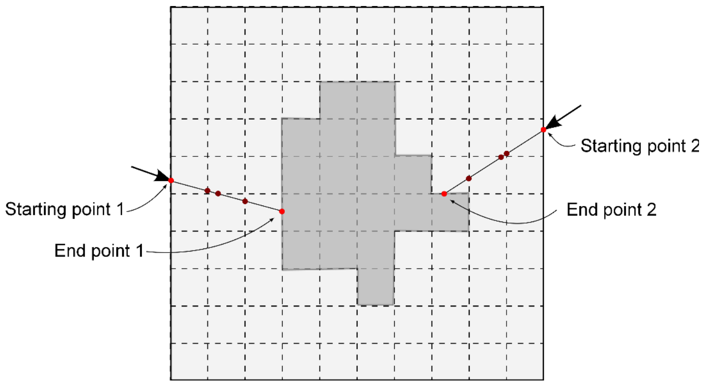

Figure 3.15: Raytracing using directions up to the object boundary.

Should a border detection method similar to the one used for this work be used, the voxels inside the object but under the threshold will not be a problem. Should another methodology be applied, for which it is necessary to mark the pixels inside the object but under the threshold as “in” the object, a simple region-growth algorithm could be used. The main disadvantage of using a FBP image is the potential artefacts that may be above a given threshold. Image processing techniques, such as edge-detection filters, as suggested by Penfold [2010], could overcome this problem.

Summary

- A Monte Carlo simulation of a proton scanner was set up using the GATE platform.
- An anthropomorphic phantom and a semi-anthropomorphic phantom were adapted to be implemented in the simulation.
- A dedicated reconstruction platform was set up: a proton-by-proton reconstruction algorithm (ART) was implemented. The required tools for image reconstruction taking into account the path of each particle were implemented as well (most likely path computation, raytracing, border detection).

CHAPTER 4

FURTHER STUDIES OF THE MOST LIKELY PATH APPROXIMATION

Contents

4.1 Preamble: image reconstruction of the relative stopping power

The data of a pCT acquisition of the Forbild phantom was simulated using the platform detailed in Section 3.1.2. A total of 256 projections with 100 protons/mm^2 were generated. Image reconstructions of the relative stopping power were carried out using the FBP algorithm (Section 3.2.3) and the ART algorithm (Section 3.3.1).

4.1.1 Analytical image reconstruction

As explained in the previous chapter, image reconstruction using the FBP algorithm relies on the use of the data binned into projections. As the data is recorded in listmode format, the binning can therefore be chosen. For the analytical reconstructions performed, the data was binned according to the 2D position on a tracker plane or at the entrance of the object. Projection pixels of 1×1 mm^2 were used, and the data on the WEPL was averaged on all proton histories belonging to the same pixel. Different binning options were investigated:

(a) binning according to the position on the first downstream tracker plane, as illustrated on Figure 4.1(a). This basically does not make use of the tracking system, and is equivalent to the very first pCT image reconstructions.

(b) binning according to the position upon exit of the object, illustrated on Figure 4.1(b). The information on each particle's direction from the downstream tracking system is used to find the projection of the proton path onto the object boundary.

(c) binning at the mean position in the object when approximating the proton path by a broken straight line, illustrated on Figure 4.1(c). This makes use of the directions given by the tracking systems upstream and downstream from the object.

(d) binning according to the position on the second upstream tracker plane (in this simulation geometry, the only one). As the beam is parallel and the trackers are perfect, this is the same position than upon entrance in the object. This is illustrated on Figure 4.1(d).

To evaluate the accuracy of the path estimations resulting from such binnings, a Geant4 simulation of a mono-energetic uni-directional beam of 200 MeV protons in a 20 cm deep cube of water was performed. Figure 4.2 shows the root mean square of the distance distribution between the true proton paths and the straight line approximations as a function of depth. The distance distributions were computed in a plane orthogonal to the direction of propagation of the beam for the approximations resulting from the binnings listed (b), (c) and (d). The first binning was not included as it depends highly on the distance between the exit face of the object and the detector and is known to generate very poor image quality because multiple scattering is totally neglected.

Figure 4.3 shows the reconstructed images for the four binning options listed above, and Figure 4.4 represents the RSP values profile in the phantom and reconstructed

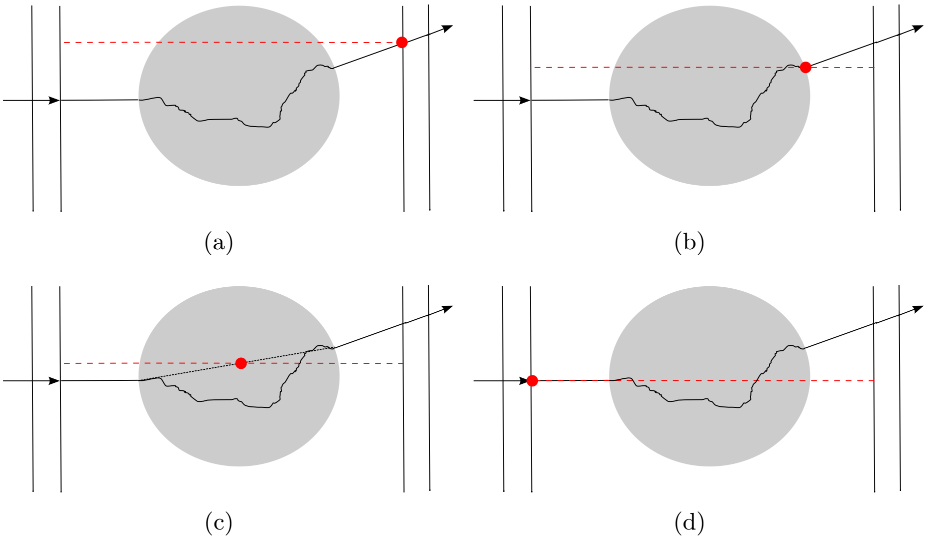

Figure 4.1: Different binning of projections used for FBP reconstruction: binning case (a) according to the position on the first downstream tracker; binning case (b) according to the position of exit of the object; binning case (c) according to the position at the middle of the object, supposing a straight line propagation inside; binning case (d) according to the position on the upstream tracking plane. In black is represented an example of proton path. The red dot represents the binning position and the red line is the horizontal back-projection path considered with FBP.

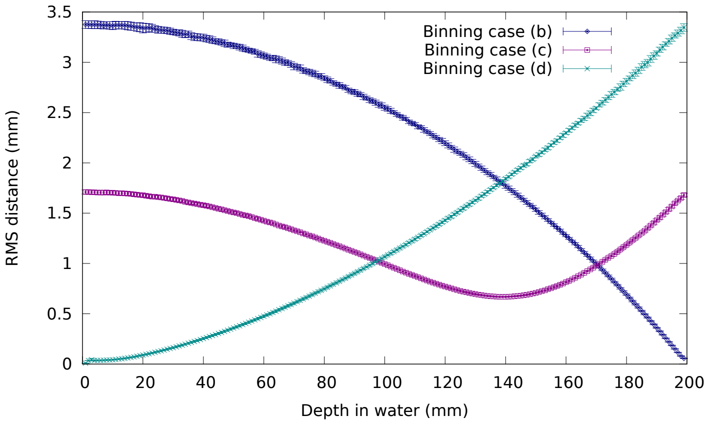

Figure 4.2: RMS error on the path estimation for the cases (b), (c) and (d) listed previously. The uncertainty was estimated using 10 simulations of 5000 proton histories.

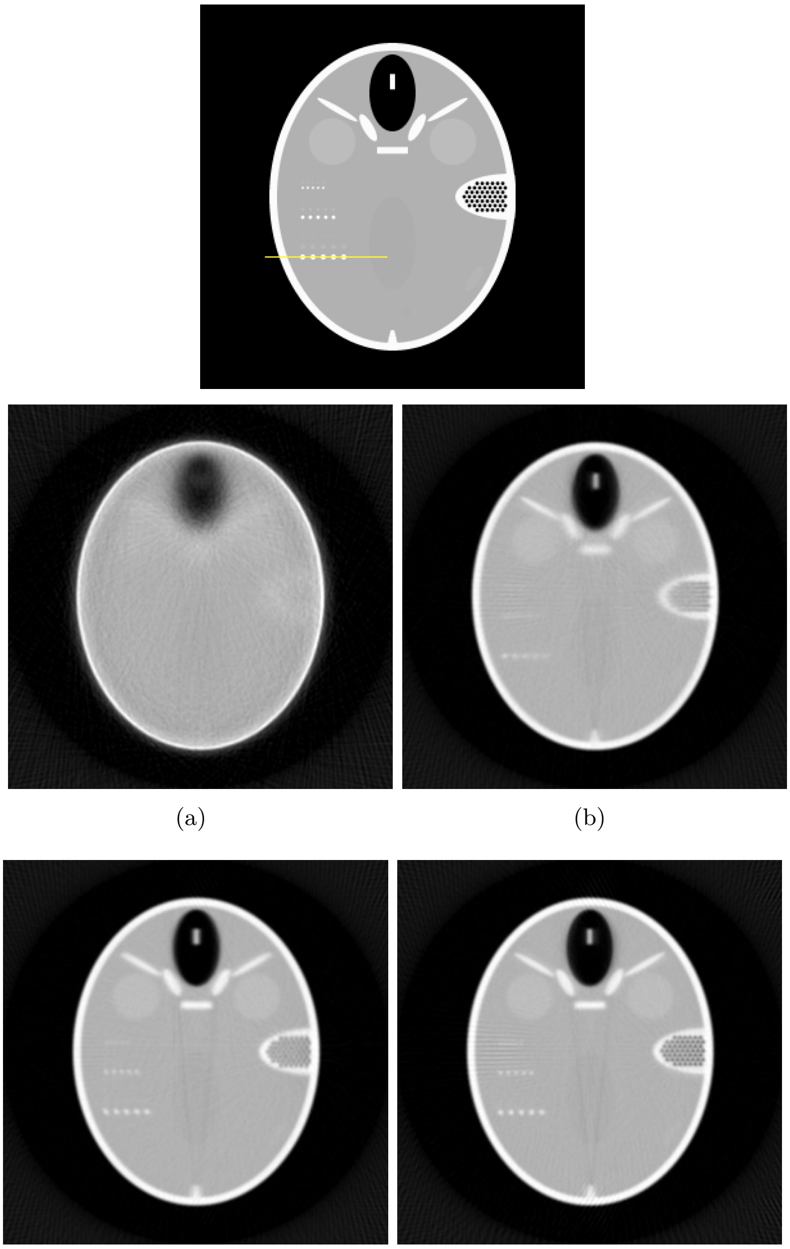

(a) (b)

(c) (d)

Figure 4.3: On top, the Forbild phantom. FBP reconstructions of the Forbild phantom with binning of the projections (a) on the downstream tracker plane (see Figure 4.1(a)), (b) using the position of the exit from the phantom (see Figure 4.1(b)), (c) at the middle of the broken straight line defining the proton's trajectory (see Figure 4.1(c)) and (d) using the position on the upstream tracker plane (see Figure 4.1(d)). The line on the phantom image represents the section used to generate the profiles shown on Figure 4.4 and Figure 4.7. Colour range of [0:1.5].

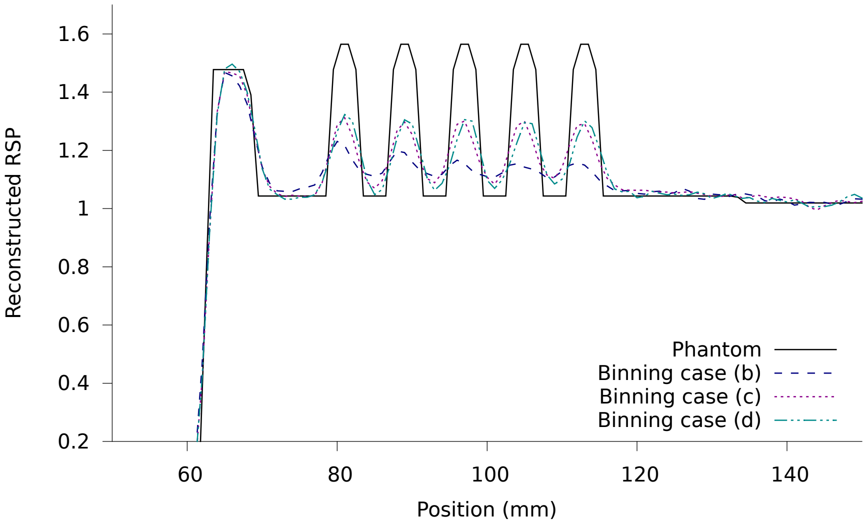

Figure 4.4: RSP profile through the line shown on the phantom in Figure 4.3 for the phantom and different images reconstructed using FBP.

images through the high-density inserts of the left ear modified pattern, shown by a line on the phantom.

The image reconstructed using the binning (a), shown on Figure 4.3(a), clearly suffers from the inappropriate path approximation.

The image reconstructed using the binning proposed in (b) is shown on Figure 4.3(b). In particular, it can be seen on the right and left ears spatial resolution patterns that the resolution is greatly degraded as we go towards the center of the object. This is well illustrated by the profile shown in Figure 4.4. It can be explained by the fact that even though the right position is considered upon exit, the horizontal direction that will approximate the path is far from the actual direction of the particles.

It can be seen from the reconstructed image using binning (c), shown in Figure 4.3(c), that the spatial resolution in the image is more homogeneous than in the previous case. However, the resolution towards the edges of the phantom do not seem to be improved. This method of binning was proposed by Vanzi et al. [2013]. The main difference between their system and the one considered here is the cone-beam geometry used for their work. Their acquired data is then binned in order to be reconstructed with a parallel-beam FBP algorithm.

The image reconstructed using binning (d), shown on Figure 4.3(d), shows that this solution seems to bear a rather good spatial resolution compared to the previous ones. Indeed, the parallel-beam geometry makes it so that the straight line approximation fits the position and global direction of the protons. It can be put forward that the parallel-beam geometry is convenient here, but the same result should be achievable with a cone-beam acquisition. The parallel-beam FBP reconstruction algorithm can be adapted to cone beam geometry, using a Feldkamp, Davis and Kress [Feldkamp et al., 1984] method for example.

Other methods that have not been implemented in this work have also been put forward to improve the spatial resolution of analytically reconstructed images.

One solution, to take into account the scattering of each proton as much as possible, is to rebin the proton history in a different projection according to the angle of the straight line segment inside the object [Penfold, 2010]. This solution is expected to give a good spatial resolution towards the edges of the object, and slightly less satisfying results towards the centre. However, when using a slice-based reconstruction algorithm such as FBP, only a two-dimensional rebinning can be performed (the ray will always be considered horizontal). The accuracy of the path estimation then depends on the slice thickness as well as the angular step between the projections.

In order to take the proton path into account as accurately as possible, it is also possible to perform cuts on the data to remove protons that exited with a lateral displacement greater than a given threshold (for example, 1 mm). It is also possible to use the information provided by the MLP in order to remove the proton histories for which any point in the most likely path showed a lateral displacement greater than the threshold [Cirrone et al., 2011]. This was shown to improve spatial resolution in the reconstructed images. However, as many proton histories are rejected, a greater number should be recorded during the acquisition.

Finally, the possiblity to account for a curved proton path (using the MLP) in a FBP algorithm has been put forward by Rit et al. [2013]. A distance-driven binning, associated to a voxel-specific backprojection has shown to provide a 30% improvement of the spatial resolution compared to the straight line approximation with the binning case (d). This method seems very promising but no comparison with iterative reconstructions has been provided yet.

4.1.2 Iterative image reconstruction

In order to be able to consider a more accurate path approximation (using the MLP), event-by-event reconstruction using the data in list-mode format was performed. The ART algorithm with an additional total variation (TV) minimization constraint was used, as detailed in Section 3.3.1. The main challenge in the reconstruction using this algorithm is the adjustment of the relaxation parameter (λ in Equation 3.32), the TV weighting (w_1 in Equation 3.35) and the number of iterations of TV descent. The main difficulty is that the optimal parameters depend on the noise in the data and on the considered object. This particular problem is a general problem of algebraic reconstruction techniques. In the case of proton imaging, for example, different algebraic image reconstruction algorithms have been tested by Penfold [2010] and each time the parameters need to be adjusted. The same problem can be found in limited angle X-ray tomography using ASD-POCS (described in Section 3.3.3.2) [Barquero and Brasse, 2012].

In order to determine the optimal image, two criteria were used. The first is the relative error between the reconstructed image and the phantom, defined as:

$$\mathrm{RE} = \frac{\sum_j |x_j^{ph} - x_j|}{\sum_j |x_j^{ph}|} \tag{4.1}$$

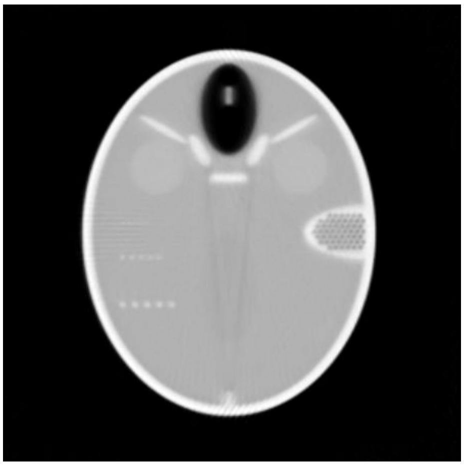

Figure 4.5: Image reconstruction of the Forbild phantom after 8 iterations of ART with the following parameters: $\lambda = 0.001$, $w_1 = 0.1$ and 2 iteration of TV descent. The image reconstructed using FBP with the binning case (d) was taken as initial estimate. Colour range of [0:1.5].

---

where x_j^{ph} is the value in the j^{th} voxel of the phantom and x_j the value of the same voxel in the reconstructed image. Note that this figure of merit is useful to compare different reconstructions of the same phantom but is not adapted to compare reconstructions of different objects. The second considered criterion was visual assessment of noise and detail in the images.

Parameters were tested and adjusted manually in an empirical fashion to find the "optimized" ones. For simplicity, the relaxation factor was kept constant throughout cycles and iterations. The data was always organized as 1 proton/mm^2 of source per projection for each cycle. A treatment of each proton history once represents an iteration of the algorithm. It was shown that starting the iterative reconstruction procedure with an initial estimate already close to the object, such as an analytically reconstructed image, accelerates the convergence of the algorithm [Penfold, 2009]. The starting point of the reconstruction was taken as the FBP image reconstructed using the data binned according to the position upon interaction on the upstream tracking plane (case (d) in the previous section, illustrated on Figure 4.3(d)).

Satisfactory results were found for a relaxation factor $\lambda = 0.001$, a TV weighting factor $w_1 = 0.1$ and two iterations of TV descent after each cycle. The reconstructed image after 8 iterations is shown on Figure 4.5. Figure 4.6 shows the relative error as a function of the iterations for this set of parameters. The point at 0 iteration represents the relative error of the FBP image used as initial estimate of the object.

It can be seen that the ART iterations over the FBP image allow to reduce the error and that the algorithm seems to converge. Figure 4.7 represents the reconstructed RSP profile through the biggest left ear resolution pattern, as drawn previously on the phantom in Figure 4.3.

While the relative error between the reconstructed image and the phantom is reduced by using the iterative algorithm, it can be noticed that the spatial resolution is not. This

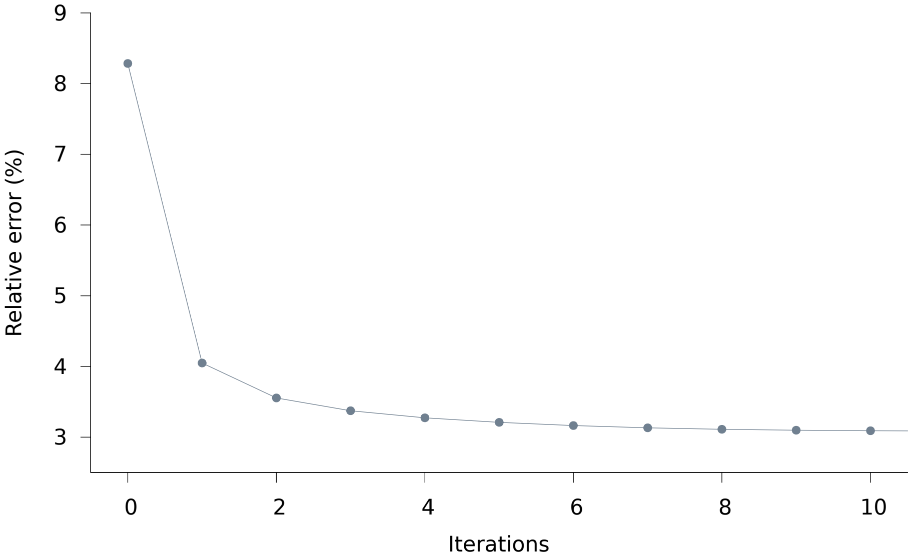

Figure 4.6: Relative error (RE) between the reconstructed image and the phantom as a function of the iterations. Reconstruction parameters were set to $\lambda = 0.001$, $w_1 = 0.1$ and 2 iteration of TV descent. The point at 0 iteration represents the relative error of the FBP image used as initial estimate of the object.

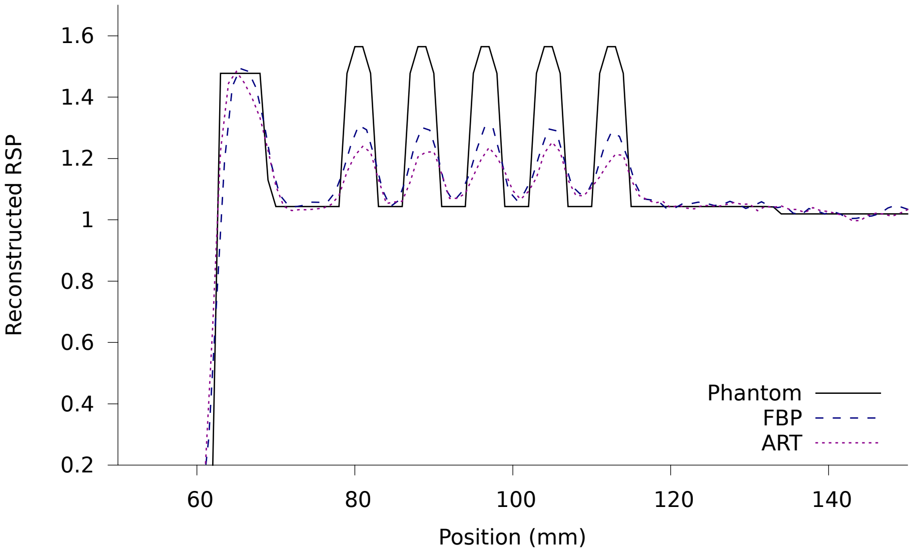

Figure 4.7: Profile through the left ear pattern of the phantom, FBP (binning case (d)) and ART reconstructions.

result is surprising because a more accurate path estimation would intuitively lead to a better spatial resolution. However, it can be explained by the fact that the weighting factor of the TV may not be optimal. As the TV minimisation results in a reduction of the gradients, inappropriate weighting may result in a blur.

Discussion

Because it will not impact the main conceptual arguments of this thesis work, the optimization of the parameters for the ART algorithm was not performed.
However, should such an optimization be of interest, two main things need to be considered. The first is the image used as a starting point, here the FBP image. It can be put forward that this image shows some streak artefacts which might affect the ART algorithm. The second thing to consider is the optimization of the parameters for the ART algorithm. The search for the optimized parameters could be performed automatically. This would require a set of figures of merit to test the different aspects of image quality. Indeed, the RE considered here represents a general criterion on the whole image, favouring the low frequencies, and is not indicative of the spatial resolution or noise. A comprehensive quantification of image quality would in addition need to consider noise, spatial resolution and potential artefacts. A huge amount of computation time will also be necessary to systematically test the possibilities. The reconstruction algorithm set-up here, in particular the ray-tracing and MLP computation, could be implemented for computation on graphical processing units (GPU). The gain in computation time would make it possible to consider such a systematic search. In order not to have to test all possibilities, a search following an experimental design could be performed, as can be done in experimental sciences. Furthermore, it needs to be considered that the optimized parameters determined on a simulation with perfect detectors and with such a semi-anthropomorphic phantom may be different from the ones required to optimize image quality in clinical conditions.

Nevertheless, the path approximation is of key importance in order to achieve the best spatial resolution possible with proton imaging. In this context, the MLP is the most accurate path approximation that has been proposed to this day. The sequel of this chapter aims at further investigating the MLP, from two different points of view. The computation of the MLP is performed assuming all materials have the scattering and energy loss properties of water. This is often the case for first approximations. However, in regions with important proportions of bone or air, such as the thorax or nasal cavity, this approximation may not be the most appropriate. Therefore, a MLP estimation in non-homogeneous medium consisting of slabs was derived and studied in Section 4.2. Section 4.3 aims at investigating the impact of the tracking system parameters (spatial resolution, material budget, positioning of the tracking planes) on the path estimation.

4.2 Improving spatial resolution? Most likely path in a non-uniform medium

The MLP, described in section 3.3.2, is computed assuming the medium has both the scattering and the energy-loss properties of water. This approximation may induce some error, should the materials be much more or much less dense (such as bone or air for example). It has been shown [Wong et al., 2009] that in a mixed-slab geometry, the root mean square error made on the estimation of the lateral displacement is increased by 20% compared to an homogeneous phantom.

The potential of improving trajectory estimation by taking inhomogeneities into account was investigated. A segmentation in three kind of materials is considered: water, bone and air. This can easily be done using thresholds on a first reconstructed image. This first image could be, for example, an analytical reconstruction used as the starting point for the iterative reconstruction using the MLP.

This section presents the investigation on a MLP formalism taking into account slabs of materials.

4.2.1 Scattering of particles in a non-uniform medium and implementation in the MLP

In order to compute this "slab" version of the most likely path of a proton, the scattering matrices (Σ_1 and Σ_2, detailed in Equation 3.21) need to be computed for a mixed-slab case.

Expressions of the scattering of charged particles in multi-material slabs geometries have been previously used for analytical modelling of beam propagation [Safai et al., 2008]. Consider a multi-slab, heterogeneous geometry consisting in N different slabs. Let i denote the index corresponding to a slab of thickness t_i and of radiation length $X_{0,i}$ with its upstream face at the depth z_{i-1} and its downstream face at depth z_i. Thus, $t_i = z_i - z_{i-1}$. Let the depth at which the path is computed be considered as exit boundary of the j^{th} slab, at position z_j. The elements of the variance-covariance matrix between z_{in} and z_j (Σ_1 in Equation 3.28) can then be computed as:

$$\sigma^2_{t_1}\left(z_{in}, z_j\right) = \sum_{i=1}^{j} E_0^2 \left(1 + 0.038 \ln \frac{t_i}{X_{0,i}}\right)^2 \times \int_{z^*_{i-1}}^{z^*_{i-1}+t_i} \frac{\left(z^*_j - u\right)^2}{\beta^2\left(u\right) p^2\left(u\right)} \frac{du}{X_{0,i}} \tag{4.2}$$

$$\sigma^2_{\theta_1}\left(z_{in}, z_j\right) = \sum_{i=1}^{j} E_0^2 \left(1 + 0.038 \ln \frac{t_i}{X_{0,i}}\right)^2 \times \int_{z^*_{i-1}}^{z^*_{i-1}+t_i} \frac{1}{\beta^2\left(u\right) p^2\left(u\right)} \frac{du}{X_{0,i}} \tag{4.3}$$

$$\sigma^2_{t_1\theta_1}\left(z_{in}, z_j\right) = \sum_{i=1}^{j} E_0^2 \left(1 + 0.038 \ln \frac{t_i}{X_{0,i}}\right)^2 \times \int_{z^*_{i-1}}^{z^*_{i-1}+t_i} \frac{z^*_j - u}{\beta^2\left(u\right) p^2\left(u\right)} \frac{du}{X_{0,i}} \tag{4.4}$$

The star represents the referential in terms of energy of the current slab. A particle enters the slab i at position z_{i-1} with a given energy. The depth z^*_{i-1} represents the depth of i^{th} material for which the particle would enter with the same energy. As a segmentation into three known materials is considered, this can be computed knowing the

Table 4.1: Coefficients of the fifth-degree polynomial fitting $\frac{1}{\beta^2(u)p^2(u)}$ in c^2/MeV^2 divided by the appropriate powers of mm for air and bone. The coefficients of the polynomial computed for water are shown on Table 3.1.

	Values for air	Values for bone
a_0	$7.516 \cdot 10^{-6}$	$7.450 \cdot 10^{-6}$
a_1	$3.303 \cdot 10^{-11}$	$4.992 \cdot 10^{-8}$
a_2	$1.487 \cdot 10^{-16}$	$-8.971 \cdot 10^{-11}$
a_3	$5.686 \cdot 10^{-22}$	$1.313 \cdot 10^{-11}$
a_4	–	$-1.532 \cdot 10^{-13}$
a_5	–	$9.164 \cdot 10^{-16}$

relative stopping powers of the materials. As an example, an object with two slabs can be considered: the first slab is made of material 1 with a RSP = RSP_1, the second is made of material 2 with a RSP = RSP_2. The entrance point of the second slab, at depth z_1 will correspond in the second material's referential to the depth $z_1^* = z_1 \cdot (\mathrm{RSP}_1/\mathrm{RSP}_2)$.

It can be noticed that, using this formulation, the sum of two slabs of the same material is not quite equal to the same depth in only one slab, because the common term to the three equations $\left(1 + 0.038 \ln \frac{t_i}{X_{0,i}}\right)^2$ differs. For our implementation, it was therefore chosen to replace t_i by the total depth $(z_j - z_{in})$. Nevertheless, both versions were tested. As the difference only affects the logarithmic correction term, the effect was not significant.

As mentioned previously, a segmentation in three materials was considered: water (the current approximation, kept for soft tissues), air and bone. The polynomials approximating the energy loss of protons in air and bone were computed based on a Geant4 simulation, as was done for water (Section 3.3.2.2). As the energy loss of protons of tens of MeV in air is very small, a third order polynomial was used for the fit. The coefficients of the polynomial fits for air and bone are reported in Table 4.1.

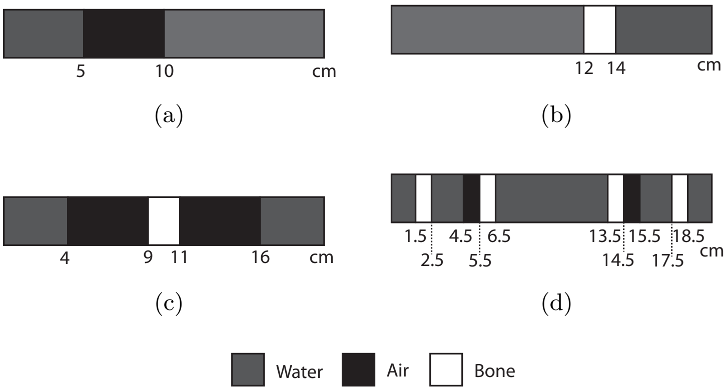

Figure 4.8: Sequences of materials in the different slabs geometries: (a) air gap in water, (b) bone insert in water, (c) air and bone in water for a nasal cavity ("nose") and (d) multi-slab geometry used in [Wong et al., 2009].

4.2.2 Results

The multi-slab MLP was tested for different combinations of air, bone and water slabs, namely: an air gap in water (Figure 4.8(a)), a bone insert in water (Figure 4.8(b)), a "nose" (Figure 4.8(c)) and the multi-slab geometry of Wong et al. [2009] (Figure 4.8(d)).

Geant4 simulations of a 200 MeV, unidirectional, proton beam in 20 cm of material for each slab combination was performed. It was shown that cuts on the exit angles of the data allowed the removal of particles that underwent nuclear scattering [Schulte et al., 2005]. In order to reduce computation time, nuclear scattering was not included in the simulations.

For the first 2000 events of each geometry, the MLP was computed (i) using the standard all-water approximation, (ii) knowing the position and composition of each slab, using the multi-slab formulation. An example of proton path with the computed MLP and "slab" MLP are represented on Figure 4.9 in the case of the air gap in water (Figure 4.8(a)). It can be seen that the path of the proton estimated using the "slab" version of the MLP is straight in the air slab. Nevertheless, the improvement in the path estimation seems minor.

Figure 4.10 shows the root mean square (RMS) of the displacement between the true proton path and the estimations using both MLP for the slab configurations detailed in Figure 4.8. It can be seen that for some cases, such as the air insert in the water (Figure 4.10(a)) or the "nose" configuration (Figure 4.10(c)), there is a slight improvement in the path approximation using the mixed slab MLP. In the other two cases, no improvement can be seen.

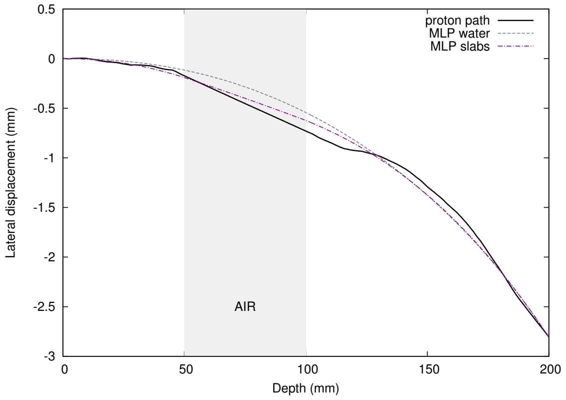

Figure 4.9: A proton path in a medium consisting of water, air and water and the MLP computed considering only water and considering the slab media.

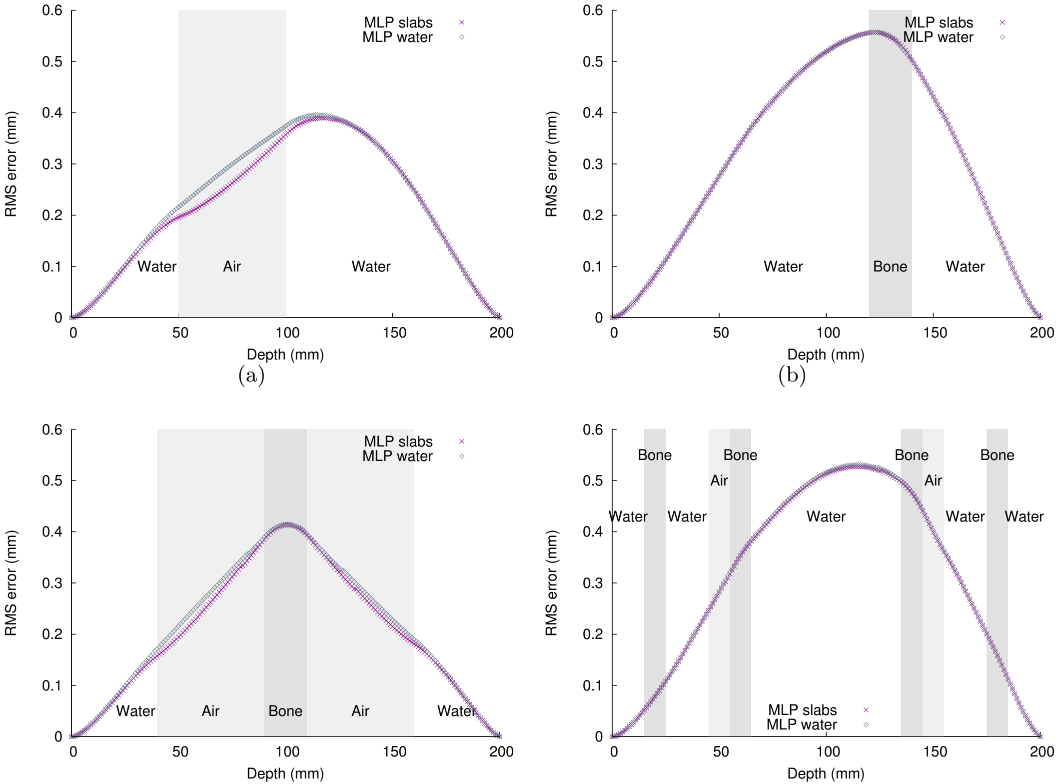

(a) (b)

(c) (d)

Figure 4.10: RMS error between the real and estimated proton paths using the MLP and slab-MLP for different configurations of slabs detailed in Figure 4.8.

4.2.3 Discussion

Results show that in some slab geometries, a slight improvement of the path approximation can be achieved by using the proposed multi-slab MLP. This is well illustrated by the cases with the bigger inserts, such as the air gap. This improvement seems however rather small (maximum 50 µm on the RMS error for the tested geometries). The significance of this improvement needs to be estimated with respect to the size of the voxels of the reconstructed image. For the reconstruction study presented previously (in section 4.1), cubic voxels of 1mm-side were chosen. In these conditions, such an improvement may not justify the additional computation time of the slab-MLP. However, different pCT image reconstruction studies have used smaller voxels (0.1 mm-side for Rit et al. [2013] for example), for which such an improvement may induce a difference in the reconstructed images. It can be noted that the 20% error increase in the "multi-slab" geometry [Wang et al., 2010] is not compensated by the slab implementation of the MLP. This may be an indication of the limitations of the most likely path approach: the most likely distribution is not very different in the presence of thin air or bone inserts, whereas the individual proton paths are.

The results shown here seem to indicate that, in the case of pCT imaging of a head, the gain in terms of path accuracy obtained with the slab MLP is limited. This assertion may need to be reassessed in other cases, should proton imaging be considered to produce images of a thorax for instance.

Finally, one disadvantage of the proposed multi-slab MLP is that it does not allow to take into account heterogeneities with a finite lateral dimension. One possibility to take into account the lateral dimensions of heterogeneities may be to perform this computation in an iterative fashion, computing depth at which a particle changes medium by already considering a curved trajectory.

4.3 Impact of the tracking system properties on the path estimation

This section aims at determining the impact of the tracking system properties on the most likely path estimation. The basic procedure for the computation of the MLP in the image reconstruction process is illustrated on Figure 4.11(a). First, the directions of each particle upstream and downstream of the object are determined using the impinging positions on the four tracker planes (1). Then, the object boundaries are determined (2). By projecting the directions on the object boundaries, the entry and exit position of each proton in the object are estimated (3). Then, the MLP is computed (4).

The precision in the determination of the positions of the particles as well as the subsequent calculation of their directions depends on the scanner characteristics: (i) the spatial resolution of the tracking system (R); (ii) the spacing between trackers on the same side of the object (d_{T-T}); (iii) the material budget of the inner trackers (x/X_0), namely the scattering that will generate an uncertainty on the direction of the particle; (iv) the distance between the inner trackers and the object (d_{T-O}), that leads to the amplification of the errors made on the determined positions and directions. As a consequence, the error on the path estimation for a proton is the quadratic sum of two contributions: the intrinsic uncertainty of the MLP derivation and the instrumental

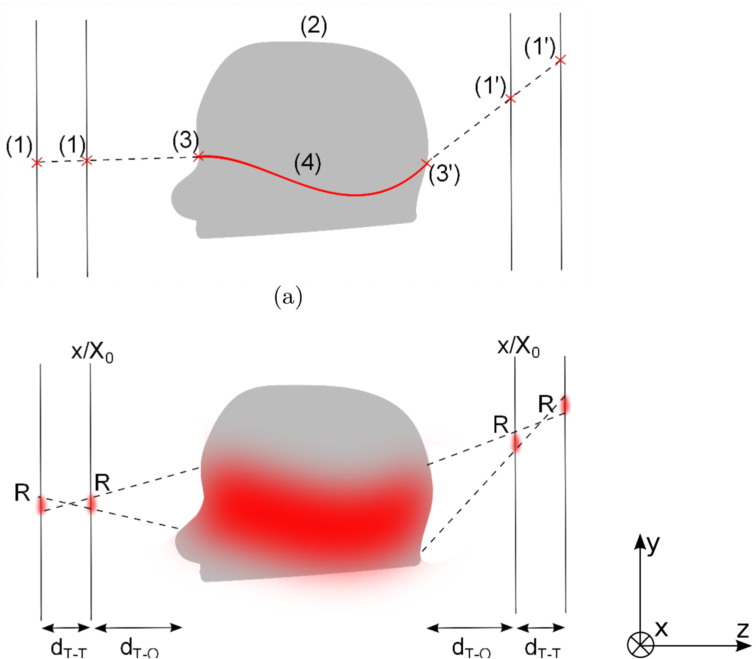

(a)

(b)

Figure 4.11: Illustration of the estimation of the most likely path with (a) exact data, and (b) taking into account uncertainties due to the tracking system. The numbers represent the steps in the MLP computation detailed in the text. The z-axis represents the direction of propagation of the particle at the given acquisition angle.

considerations. This second part is schematically illustrated on Figure 4.11(b).

Previous results demonstrate the improvement of image quality for a reduced distance between the inner trackers [Sadrozinski et al., 2013]. It was also shown for a specific system with a pitch of 228 µm, that increasing the distance between trackers d_{T-T} to more than 8 cm did not noticeably improve MLP accuracy [Penfold et al., 2011].
The impact of the material budget of the trackers was evaluated, specifically for silicon detectors [Sadrozinski et al., 2013; Civinini et al., 2012]. The first study advocates a reduction of the downstream inner tracker thickness from 400 µm to 200 µm; the second concludes that increasing tracker thickness from 200 µm to 320 µm has little impact on the error on the MLP, if the distance between the inner trackers and the object is neglected. However, the impact of all the parameters affecting the path estimation have not been evaluated systematically.

The error on the MLP estimation for one proton has two sources: one is the intrinsic uncertainty of the MLP derivation, the other is a consequence of the system considered that induces an uncertainty on the positions and directions used as inputs for the MLP estimation. The total error on the MLP is then the quadratic sum of these two errors. The aim of the work presented in this section is to evaluate the impact of the second part of the error due to the acquisition and aforementioned system parameters.

4.3.1 Materials and methods

4.3.1.1 Uncertainty propagation in the MLP

The computation of the MLP is described in Section 3.3.2. The Equation 3.28 to calculate the most likely position and direction of a particle at a given depth, knowing the entrance and exit parameters p_{in} and p_{out} can be re-written as:

$$p_{MLP} = Ap_{in} + Bp_{out} \tag{4.5}$$

where A and B are the compressed expressions of all factors multiplying p_{in} and p_{out} in Equation 3.28. Let Σ_{in} and Σ_{out} be the variance-covariance matrices representative of the uncertainties on p_{in} and p_{out} respectively:

$$\Sigma_{in} = \begin{pmatrix} \sigma^2_{y_{in}} & \sigma^2_{y_{in},\theta_{in}} \\ \sigma^2_{y_{in},\theta_{in}} & \sigma^2_{\theta_{in}} \end{pmatrix}, \quad \Sigma_{out} = \begin{pmatrix} \sigma^2_{y_{out}} & \sigma^2_{y_{out},\theta_{out}} \\ \sigma^2_{y_{out},\theta_{out}} & \sigma^2_{\theta_{out}} \end{pmatrix} \tag{4.6}$$

The uncertainty on y_{MLP} at a given depth can then be calculated as:

$$\Sigma_{\mathrm{MLP}} = A\Sigma_{in}A^T + B\Sigma_{out}B^T \tag{4.7}$$

The same uncertainty propagation can be computed in the orthogonal plane.

4.3.1.2 Uncertainties due to the acquisition system

The uncertainty matrices on the entrance and exit parameters can be split in two contributions: (i) the distance between the trackers and their intrinsic spatial resolution and (ii) the scattering inside the innermost detector. For a strictly symmetrical system, the first contribution will be the same on both sides of the object, while the second will not, as it depends on the energy of the particles. Moreover, both contributions need to be projected onto the surface of the object.

For a given system, the matrices can be computed by smearing multiple realizations of the same 'event'. Consider, for example for the upstream side of the (yOz) plane, a particle interacting on the first two tracker planes at the positions (y_1, z_1) and (y_2, z_2). These interaction points can be smeared using random values generated on a Gaussian distribution, of which the full-width at half maximum is given by the resolution of the trackers. The resolution of the trackers is defined here as 2.35 times the root mean square (RMS) error on the interaction position of one event, which is known *a priori.* The smeared positions (y_1', z_1) and (y_2', z_2) can be used to compute the incidence angle of the particle θ'. This angle is in turn smeared into θ_{in} using random values generated on a Gaussian distribution to account for the scattering due to the material of the second tracker plane. The RMS of this Gaussian distribution can be computed using a Gaussian approximation to multiple scattering, with the following empirical formula [Lynch and Dahl, 1991]:

$$\sigma(l, E) = \frac{13.6}{\beta(E)p(E)}\sqrt{\frac{x}{X_0}}\left[1 + 0.038 \cdot \ln\left(\frac{x}{X_0}\right)\right] \tag{4.8}$$

where E, β and p are the energy, scaled velocity and momentum of the proton, X_0 is the radiation length of the material and x its thickness. The material budget of different

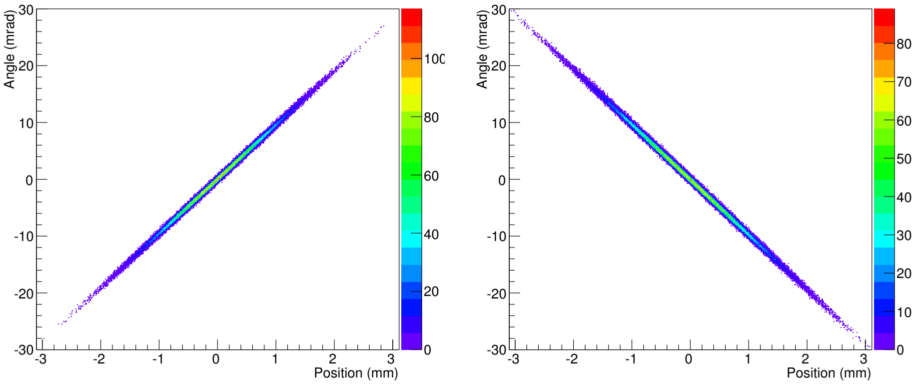

Figure 4.12: Phase space diagram of the particle distribution upon (a) entrance in the object and (b) exit from the object. The histograms were computed with 100000 events, for the following system parameters: d_{T-O} = 100 mm, d_{T-T} = 10 mm, R = 0.1 mm and x/X_0 = 0.5 %.

trackers can be expressed as x/X_0. This ratio describes the scattering properties of the tracker, making it possible to compare different depths of different materials.

Using the smeared position (y_2', z_2) and angle θ_{in}, the trajectory of the particle can be projected up to the object boundary. By repeating this procedure a statistically significant number of times, the variance of the position and angular distributions as well as their covariance can be computed. As an illustration, Figure 4.12 shows the position-direction histograms upon entrance and exit from the object for a system with d_{T-O} = 100 mm, d_{T-T} = 10 mm, R = 0.1 mm and x/X_0 = 0.5%. It can be noted that the correlation between the positions and directions is not linear, as can be seen in a rather "extreme" case (d_{T-O} = 100 mm, d_{T-T} = 10 mm, R = 5 mm and x/X_0 = 50%) on Figure 4.13.

4.3.1.3 Quantification of the uncertainty

The impact of three out of the four parameters affecting the uncertainties on the input vectors was investigated. Indeed, the distance between the inner trackers and the object amplifies the uncertainties, hence the advantage in keeping it as small as possible. Nevertheless, a clinical implementation of a pCT scanner requires a distance between the trackers and the patient's head of at least 10 cm [Schulte et al., 2004]. Therefore, this distance was set to 10 cm and the impact of the other parameters was evaluated. The study was performed for ranges of values that encompass what can be found in literature:

- a spatial resolution of the trackers (R) ranging from 0.01 mm to 1 mm,
- a distance between trackers ($d_{\text{T-T}}$) ranging from 1 mm to 100 mm,
- a material budget (x/X_0) of the innermost trackers ranging from 0.1% to 3%.

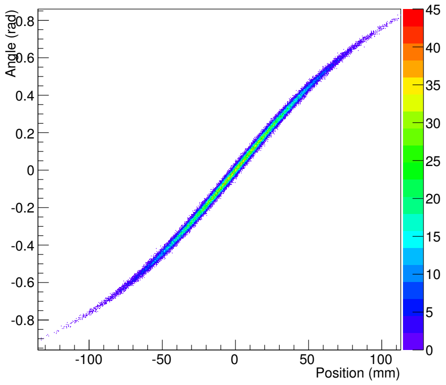

Figure 4.13: Phase space diagram of the particle distribution upon entrance of the object for a system with the following parameters: d_{T-O} = 100 mm, d_{T-T} = 10 mm, R = 5 mm and x/X_0 = 50 %.

For this study, a symmetrical geometric configuration of the detectors was considered, i.e. the distance between the two upstream and the two downstream trackers is the same, as are the resolution and material budget of each tracking plane. The object was a 20 cm thick cube. It was supposed, for the scattering calculations in the detectors, that the incoming protons have an energy of 200 MeV and the exiting protons of 80 MeV, which is the lowest exit energy of 200 MeV protons in the case of head imaging.

Each system configuration was characterized by the average of the RMS uncertainty on the position along the depth of the object.

4.3.2 Results

Figure 4.14 shows a plot of the contributions of the upstream and downstream tracking system in the uncertainty propagation in the MLP. The system illustrated here presents a distance between trackers d_{T-T} = 10 mm, a resolution on each tracking plane R = 0.1 mm, and the scattering in the detector is neglected. The average 1-sigma uncertainty amounts to 0.7 mm with a maximum of 0.77 mm around 5 cm depth.

Figure 4.15 shows the different contributions of the uncertainty sources, such as the detector positioning and resolution (also shown in Figure 4.14), the scattering inside the inner trackers, the intrinsic uncertainty on the MLP as well as root mean square of the quadratic sum of these contributions. The parameters of the system illustrated are set to d_{T-T} = 10 mm, R = 0.1 mm, with a material budget x/X_0 = 0.5%. For such a detector configuration, the overall RMS uncertainty (1-σ) exceeds 1 mm at the center of the object.

The average RMS uncertainty on the position estimation was then evaluated as a function of the three parameters.

Figure 4.16 represents the average distance of the root mean square of the uncertainty on the position as a function of the resolution of the tracking system, for d_{T-T} = 10 mm and x/X_0 = 0.5%.

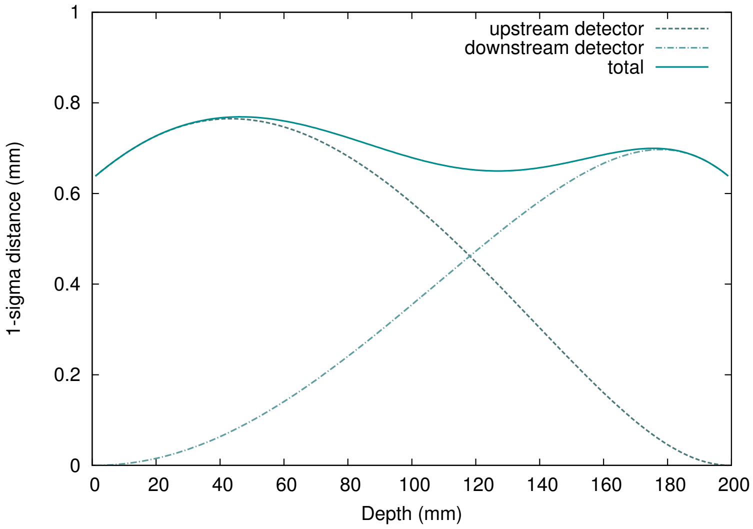

Figure 4.14: 1-σ error envelope as a function of the depth in the object. The curves represent the error due to the resolution, the positioning of the upstream and downstream detectors, as well as both. The system considered has R = 0.1 mm, d$_{T-T}$ = 10 mm.

Figure 4.17 shows the average error as a function of the distance between trackers, for $R = 0.1$ mm and $x/X_0 = 0.5\%$.
Figure 4.18 shows the average error as a function of the material budget of the inner trackers, for $R = 0.1$ mm and $d_{T-T} = 10$ mm.

A systematic study of the average error for the different configurations within the defined ranges was performed. The results of this multi-parametric study were stored into a 3D histogram, as a function of the three parameters. In order to make the results more legible, projections along the three axis were generated. Figure 4.19 represents the projection of this 3D histogram along the tracking system resolution, Figure 4.20 along the distance between trackers and Figure 4.21 along the material budget of the inner trackers.

4.3.3 Discussion on the acquisition system

The impact of the intrinsic spatial resolution of the tracking system, the distance between trackers and their material budget on the accuracy of the MLP estimation was investigated. The results demonstrate that these parameters have an influence on the estimation of the proton path due to the errors introduced on the positions and directions calculated at the entrance and exit of the object.

The system used as an example in the Figures 4.14 and 4.15 showed total average 1-σ uncertainty over 1 mm. While the example chosen is not representative of any actual system, it is not unreasonable: the distance of 10 mm between trackers is small, but could be justified for compactness purposes; the resolution R = 0.1 mm is better than that expected from current systems (a pitch of 220 µm corresponds to a resolution, as defined here of $2.35 \cdot 220\ \mu\text{m}/\sqrt{12} = 0.15$ mm); the material budget of 0.5% corresponds

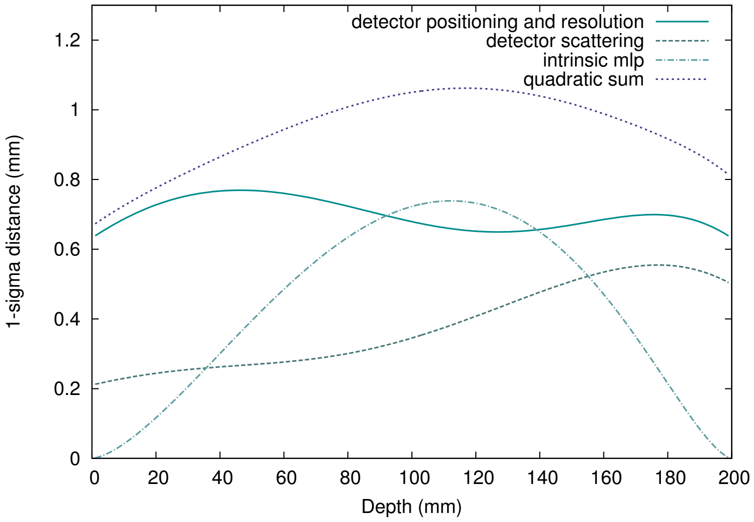

Figure 4.15: 1-σ error envelope as a function of the depth in the object given by the different contributions: resolution and positioning of the trackers, inner tracker material budget, intrinsic MLP uncertainty and quadratic sum of all uncertainties. The system considered has R = 0.1 mm, d_{T-T} = 10 mm and a material budget $x/X_0 = 0.5\%$.

---

to less than 500 µm of silicon, is a bit smaller than that of the triple-GEM detector [Amaldi et al., 2011], or corresponds to a bit more than 2 mm of scintillating fibres.

Thus, the tracking system parameters should not be neglected when considering building a new system or optimizing an existing one, in order to not jeopardize the spatial resolution of the reconstructed images.
As far as the distance between trackers is concerned, it can be seen from Figures 4.17, 4.19 and 4.21 that the accuracy of the path estimation is strongly affected by a too small distance (under 3 cm). However, once this distance is sufficient (more than 5 cm), the impact of this parameter is negligible.
The properties of the trackers, namely their spatial resolution and material budget are of utmost importance. It can be seen from Figures 4.16, 4.18 and 4.20 that a better resolution and a small material budget can greatly decrease the error on the trajectory estimation.

The results obtained by propagating analytically the uncertainties in the MLP computation can be compared to those obtained by Monte Carlo simulations. Penfold et al. [2011] performed a GEANT4 simulation of their system with a distance to the object of 10 cm, silicon trackers of 228 µm pitch and 400 µm thickness and using a 20 cm thick water cube as an object to record trajectories. They showed that for a distance between upstream trackers of 8 cm and between downstream trackers of 6 cm the RMS error on the estimated trajectory at the center of the object was of 0.802 mm, with no less than 0.8 mm when increasing the distance between the trackers. Using the analytical propagation with 8 cm separation between both upstream and downstream detector and considering the same tracking system (R = 0.155 mm and $x/X_0 = 0.423\%$) we find, at

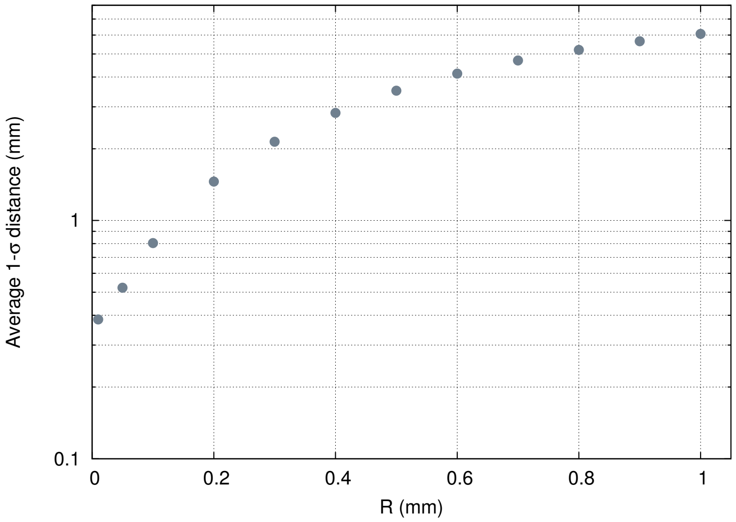

Figure 4.16: 1-σ as a function of the resolution, d$_{T-T}$=10 mm, $x/X_0 = 0.5\%$

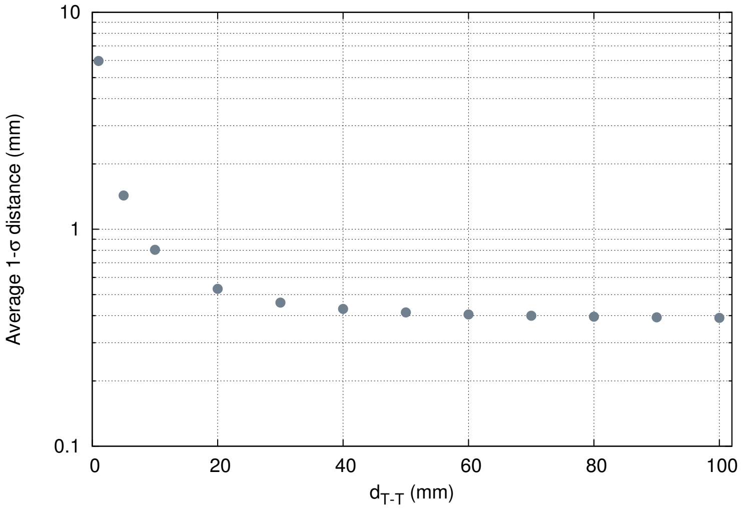

Figure 4.17: 1-σ as a function of the distance between trackers, R=0.1 mm , $x/X_0 = 0.5\%$

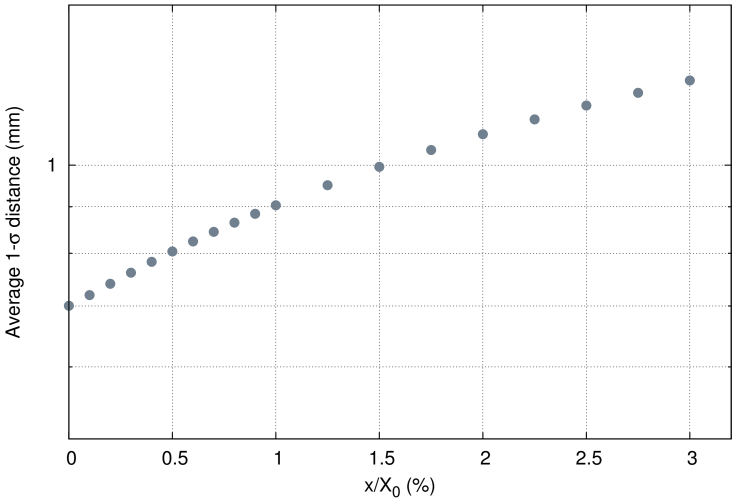

Figure 4.18: 1-σ as a function of the material budget, d$_{T-T}$=10 mm, R=0.1 mm

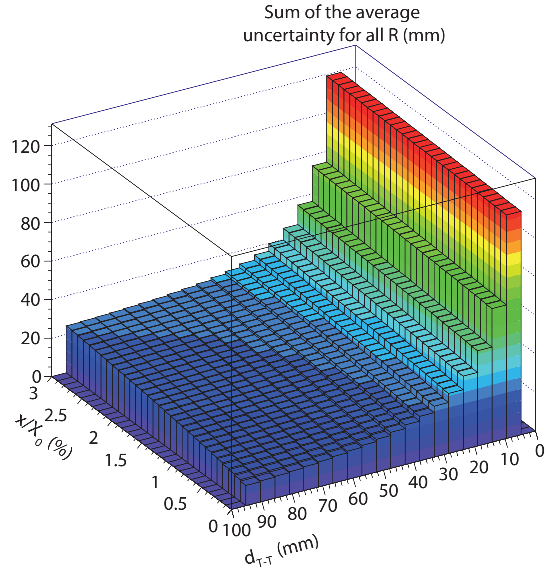

Figure 4.19: Projection of the average MLP uncertainty as a function of x/X_0, d$_{T-T}$ and R, along the axis of the resolution R.

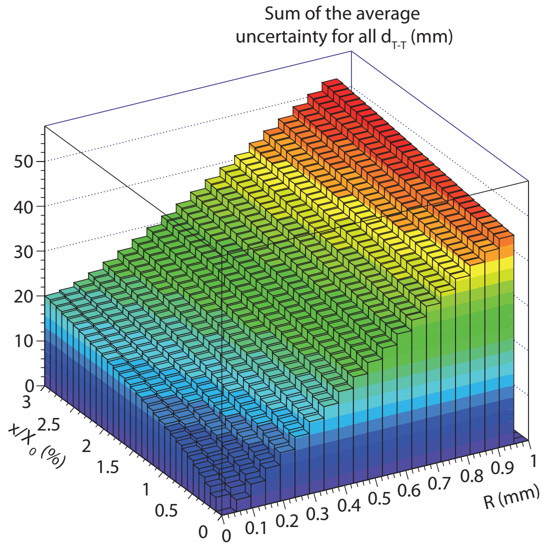

Figure 4.20: Projection of the average MLP uncertainty as a function of x/X_0, d_{T-T} and R, along the axis of the distance between trackers d_{T-T}.

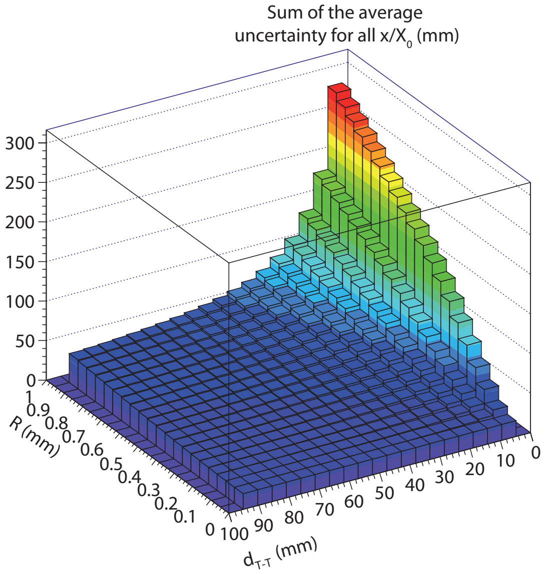

Figure 4.21: Projection of the average MLP uncertainty as a function of x/X_0, d_{T-T} and R, along the axis of the material budget x/X_0.

Table 4.2: Instrumental choices for pCT tracking system, parameters and RMS error on the MLP at the center of a 20 cm object. For comparison, the distance between trackers was set to 15 cm and the distance to the object to 10 cm.

Group	Tracker	R (mm)	x/X_0 (%)	System RMS (mm)	Total RMS (mm)	Reference
TERA	Triple-GEM	0.235	0.7	0.45	0.85	Amaldi et al. [2011]
PRIMA coll.	SSD	0.136	0.43	0.33	0.79	Scaringella et al. [2013]
LLU/UCSC/ NIU/CSUSB	SSD	0.155	0.43	0.33	0.80	Penfold et al. [2011]
NIU/FNAL	SciFi	0.62	0.45	0.54	0.90	Coutrakon et al. [2013]

the center of the object, an uncertainty of 0.723 mm due to computation of the MLP and of 0.356 mm due to the tracking system, giving a total uncertainty of 0.805 mm, which matches the results obtained by Monte Carlo.

The proposed methodology can then be used in order to compare different prototypes of proton CT systems. Different instrumental choices were made by the different groups [Sadrozinski et al., 2011] and are compared in Table 4.2. For the comparison, the distance to the object was set to 10 cm and the distance between trackers to 15 cm to maximize the accuracy on the direction estimation. The RMS uncertainty at 10 cm depth in an 20 cm-deep object due only to the acquisition system, as well as the quadratic sum with the intrinsic MLP uncertainty are shown. It can be seen that the systems exhibit a total RMS error between 0.79 mm and 0.9 mm. As the accuracy of the path estimation is indicative of the spatial resolution of the reconstructed images [Penfold et al., 2011; Erdelyi, 2009], this method can help estimate the overall system performances.

4.3.4 Conclusions and perspectives

A fast method to estimate the error made on the MLP for any proton CT tracking system is proposed. It makes it possible to optimize system parameters or compare different options without need for Monte Carlo simulations. The application of this method enabled the identification of the key points in the design of a tracking system for spatial resolution considerations: the resolution of the trackers as well as the material budget are of great importance. Nevertheless, for a system with a given set of trackers, the positions of the tracking planes can be optimized, limiting the error on the trajectory estimation.
This methodology could be used in an early research and development phase in order to compare possible choices of trackers.

In addition, other works have shown that image reconstruction considering a passage probability map for each particle and not just a line, in order to take into account the intrinsic uncertainty on the MLP is possible [Wang et al., 2010]. It would be possible to take the uncertainty due to the detector system into account as well. Whether this modelling of the uncertainty along the path could lead to the deconvolution of the effect of the detectors in the reconstruction process still needs to be investigated.

Summary

- A formulation of the most likely path computation taking into account slabs of different materials was investigated. A slight improvement compared to assuming all the object is made of water was noted.
- The impact of the tracking system properties (positioning, spatial resolution and material budget of the tracking planes) on the estimation of the most likely path was investigated:
    - The analytical propagation of the uncertainty in the path computation was established.
    - The resolution and material budget of the system are of key importance.
    - The methodology put forward was used to compare existing systems, and can be used in early development stages to compare technological choices.

CHAPTER 5

PROTON IMAGING BEYOND THE STOPPING POWER

Contents

As presented in the first chapter, uncertainties in hadron therapy treatments are of two kinds:

- the range uncertainty, mainly due to the use of X-ray images as a base for treatment planning (Section 1.2.2),
- the uncertainty on the delivered dose, due to the fact that we only have access to the CT numbers of the materials and not their exact composition and properties (Section 1.2.3).

Hitherto, proton imaging has been put forward as a way to directly map the RSP of the materials (Section 2.3). Nevertheless, the acquisition system of a pCT apparatus, as studied nowadays (described in Section 2.3.1, and illustrated in Figure 2.6), records not only the exit energy of each proton, but also its positions and direction upstream and downstream from the object allowing for the evaluation of the scattering it underwent. In addition, such a system makes it possible to access the transmission rate of the particles.

The aim of this study is to investigate the potential use of these outputs as sources of information on the tissue composition.

5.1 Preliminary study on the exploitation of the outputs

The preliminary study aimed at determining which information could be used and at identifying potential key points or limitations for their exploitation.

5.1.1 Description of the study

5.1.1.1 Definition of the observables

Physics processes of interactions between protons and matter are detailed in Section 2.1. After a given depth of material, an initially mono-energetic unidirectional proton beam exhibits an energy distribution (as illustrated on Figure 5.1(a)), a spatial and angular distribution (as illustrated on Figure 5.1(b)), as well as a reduction of fluence.

To investigate the potential information carried by these outputs, observables were chosen for this study:

- the average energy upon exit from the object,
- the root-mean square of the energy distribution upon exit of the object. It is representative of the energy loss straggling,
- the mean value of the non-projected angular distribution upon exit of the object,
- the transmission rate of the particles.

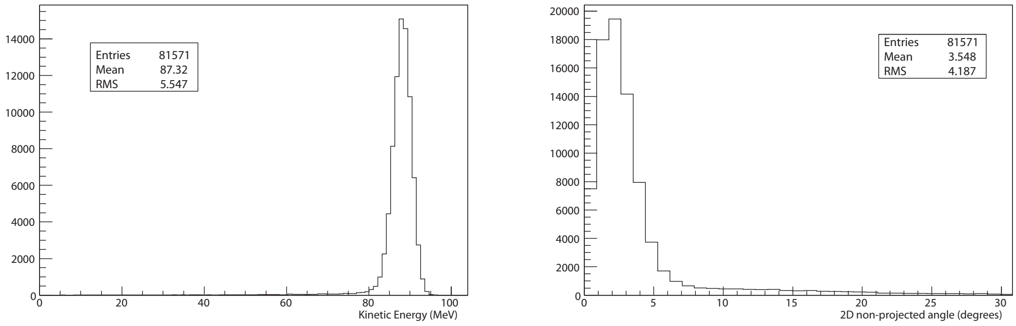

(a) (b)

Figure 5.1: (a) Energy distribution and (b) angular distribution of 200 MeV protons after 20 cm of water.

5.1.1.2 Monte Carlo simulation

A Geant4 simulation was performed in order to investigate the four observables. The study was performed in water, as well as in some human tissues such as adipose tissue, skeletal muscle, brain grey matter, brain white matter, carcinoma, brain... The compositions of these tissues were implemented based on different inputs [Woodard and White, 1986; Maughan et al., 1997; ICRU report 46, 1992] as well as the default material database of the GATE platform (Section 3.1.1.2). Modified versions of the brain and carcinoma materials were studied as well. These versions presented the same electron density as the original materials but a different chemical composition with a modified proportion of oxygen (10%, 20% or 30% less). A description of all the materials can be found in Appendix A.

A mono-energetic punctual and unidirectional proton beam was simulated. The 200 MeV protons were sent through a homogeneous cube of 20 cm depth of material that was segmented along the direction of propagation of the particles, so that the distribution of every observable could be studied in each 1-millimetre slice (Figure 5.2). For each material of interest, 10^7 protons were generated. A set of 10^5 protons was used for each simulation and 100 simulations were run per material. The value of each observable was recorded for each simulation. The distribution of these values was then used to calculate the average and the uncertainty on this average for the observables. All relevant physical processes were enabled, amongst which hadron ionisation and multiple scattering (standard models) as well as elastic and inelastic processes (low energy models). Secondary protons created from nuclear interactions were not considered in the analysis. In a realistic scan situation, most of those secondary protons can be identified and rejected because of their energies, lower than that of primary protons exiting [Schulte et al., 2005].

As an illustration, the behaviour with the depth of material of the four defined observables is represented in Figure 5.3 for 200 MeV protons going through a water cube.

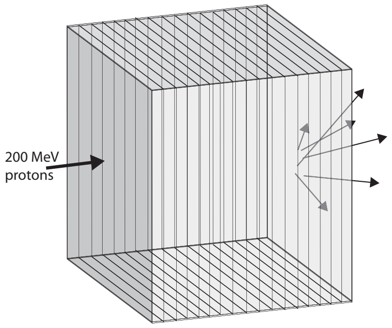

Figure 5.2: Representation of the cube of material simulated, segmented in 200 slices of 1 mm in its depth.

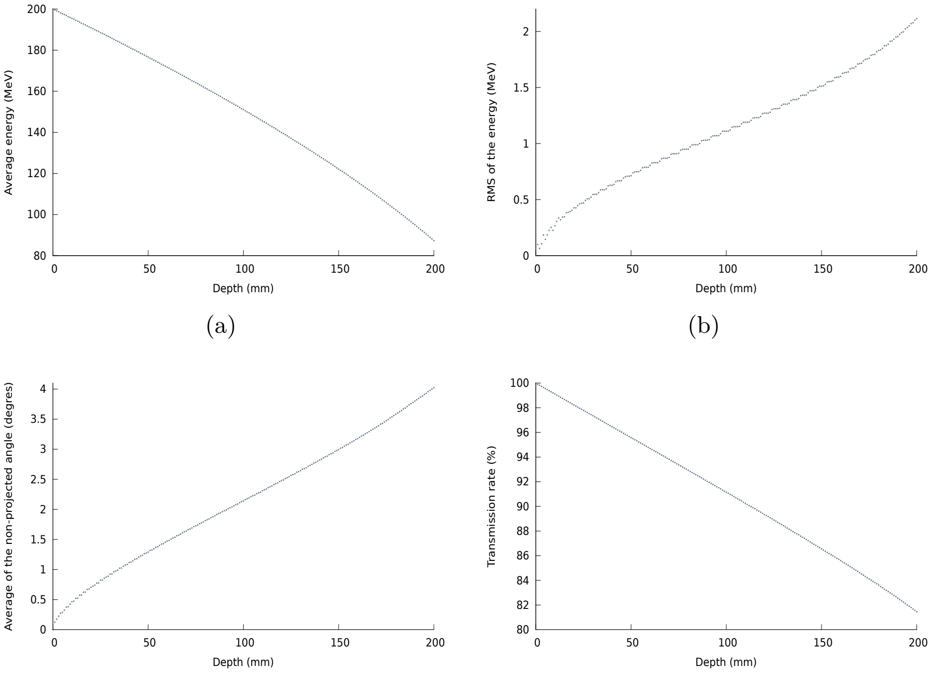

(a) (b)

(c) (d)

Figure 5.3: Behaviour of the defined observables with depth for 200 MeV protons in water: (a) average energy, (b) RMS of the energy, (c) average non-projected angular deviation and (d) transmission rate.

5.1.2 Influence of the chemical composition

5.1.2.1 Differentiation of materials

The possibility to differentiate materials using the observables defined was investigated. The variation of observables due to the oxygen concentration in the resulting values for the different observables at some depth was estimated for carcinoma. A normalized deviation D of the modified carcinoma to the reference material was used and defined as:

$$\mathrm{D} = \frac{\text{Reference carcinoma} - \text{Modified carcinoma}}{\text{Reference carcinoma}} \tag{5.1}$$

Table 5.1 shows, for each defined observable, the mean values and the associated errors after 20 cm of water, adipose tissue, skeletal muscle, brain grey matter and carcinoma.

The materials can be distinguished with all the observables. As far as the root mean square of the energy distribution is concerned, the variation between materials is less than 0.3 MeV for average energies approximately ranging between 79 and 91 MeV. The measurement of this observable would require an energy resolution of the calorimeter better than 0.1%. Due to this constraint, this observable was not studied any further. The mean angular deviation presents higher sensitivity to the relative differences between some materials than the information on the average energy. As an example, the relative difference between the values obtained for water and adipose tissue amounts to 4.5% when considering the energy, and 7.6% from the angular deviation standpoint. The differences in the percentage of transmission are slightly less substantial than the ones in the average energy.

It can be put forward that the different outputs exhibit different behaviour with the materials studied. For instance, water and carcinoma show very similar output energies (less than 0.2% difference). However, the output in terms of transmission rate shows more difference ($\sim$ 0.5%). The values of average transmission rate obtained for water and adipose tissue is much more similar (less than 0.07% difference). This result is encouraging, as it highlights that the outputs may bring different possibilities and sensitivity to distinguish materials.

Table 5.1: Average of the observables after 20 cm of material.

	Energy (MeV)	RMS Energy (MeV)	Deviation (°)	Transmission (%)
Water	87.323±0.002	2.116±0.001	4.023±0.002	81.45±0.01
Adipose tissue	91.381±0.002	2.008±0.001	3.717±0.002	81.50±0.01
Skeletal muscle	79.048±0.002	2.294±0.001	4.245±0.002	79.91±0.01
Brain grey matter	79.876±0.002	2.271±0.001	4.221±0.002	80.32±0.01
Carcinoma	87.476±0.002	2.101±0.001	4.001±0.002	81.04±0.01

5.1.2.2 Influence of the chemical composition for a fixed electron density

The influence on the observables of the oxygen concentration in the carcinoma with fixed electron density was studied. The modified carcinoma presented 10%, 20% and 30% less oxygen. Note that such change in the stoichiometric composition of the material is not, by far, an accurate modelling of hypoxia. However, as the aim of this section is to study the potential detectability of differences in the composition using the observable, rather great differences were chosen. The electron density was kept constant so that cases for which the energy loss properties are very similar can be studied.

After three to four centimetres in the cube, the carcinoma with different oxygen concentrations could be differentiated using the angular deviation and the transmission percentage. The information brought by the observables was compared at 15 cm depth. Table 5.2 shows the average values of the observables, the associated uncertainty as well as deviation of the modified carcinoma to the reference carcinoma as defined in Equation 5.1. As expected, small values of deviation D are found when considering the energy of the protons. This can be explained by the fact that the stopping power is predominantly dependent on the electron density. The small differences are the result of the dependence of the mean ionisation potential on the chemical composition. The angular deviation and transmission show a slightly larger values of D than the energy.

Table 5.2: Mean values and deviation D to reference carcinoma after 15 cm of material.

	Energy		Angular deviation		Transmission rate	
	Average	D	Average	D	Average	D
Reference	122.917±0.002	-	2.963±0.002	-	86.19±0.01	-
10% carcinoma	122.867±0.002	0.04%	2.948±0.002	0.51%	86.06±0.01	0.15%
20% carcinoma	122.666±0.002	0.20%	2.930±0.002	1.11%	85.92±0.01	0.31%
30% carcinoma	122.466±0.002	0.37%	2.919±0.002	1.50%	85.84±0.01	0.40%

This seems to indicate that these outputs, in particular the angular deviation, are sensitive to the composition change. However, this study was performed with a very high number of particles (10^7 protons for each material), so that the behaviour of the outputs could be investigated. The potential to distinguish materials on the basis of these outputs will also depend on the uncertainty on the measures.

5.1.3 Statistical uncertainty

The impact of the statistical uncertainty and subsequent resolution obtained for the observables was investigated in water. Distributions of 100 simulations of 100 protons each, and 100 simulations of 25000 protons each, were considered. The resolution was defined as:

$$\mathrm{R} = \frac{2.35 \times \sigma_{distribution}}{\mu_{distribution}} \tag{5.2}$$

where $\sigma_{distribution}$ and $\mu_{distribution}$ are the standard deviation and mean value of the distribution.

The dependence of the resolution of the observables as defined in Equation 5.2 on the number of protons is shown in Table 5.3. The values of resolution obtained for the transmission rate and the deviation are significantly higher than the ones obtained when considering the energy. Thus, for the same number of protons, a lower signal to noise ratio can be expected when studying the transmission or deviation of the particles.

This may be an indication that the use of these outputs will present more challenge in order to extract information than in the case of the energy, which would be a drawback of this approach.

Table 5.3: Resolution on the different observables for 100 and 25000 protons after 20 cm of water.

	100 protons	25000 protons
Energy	0.94%	0.059%
Angular deviation	50.76%	3.210%
Transmission rate	10.58%	0.670%

5.1.4 Conclusion

The results of the one-dimensional study of these observables have shown that the information on the dispersion of the energy loss would require a resolution of the calorimeter better than 0.1%, which is difficult to achieve nowadays. Moreover, this result was obtained with a perfectly mono-energetic beam, which would not be the case in a realistic situation. The granularity of the tracking system as well as the distance between trackers could be sufficient to measure the small differences in the average deviation angles. The differences in the percentage of transmission shown in Table 5.1 are slightly less than the ones in the average energy. Even though this does not seem favourable to the exploitation of this observable, the information brought should not be neglected. Since the observables are the results of different physical interactions, the information brought could be complementary. Table 5.2 shows that the different compositions of carcinoma studied have a slightly more important impact on the angular deviation and on the transmission rate of the particles than on the energy. This indicates that there may be some interest to investigate these outputs in order to help differentiate materials with close stopping power.

Nevertheless, one major drawback of the transmission rate and of the angular deviation of the particles is that the statistical uncertainty on the mean values of the distributions calculated is much higher than for the energy, as shown on Table 5.3. One way to compensate for this would be to use a large number of protons for a "one-dimensional" analysis as done here with one beam. This, however, implies a significant increase in the dose delivered to the tissues in the beam path, which is not optimal for clinical applications. In addition, the study of only one beam of particles as presented here means that the outputs are the result of the interactions of particles throughout their propagation in the medium. Information on the localization of heterogeneities for example could hardly be obtained this way.

A different solution is to consider an image reconstruction approach. By reconstructing images of the different outputs, it would be possible to study a voxel of the image or a region of interest. The information contained in this region is then representative of all protons that went through this volume. The higher statistical uncertainty on the scattering and transmission rate of the particles could then be taken into account by having a multi-scale approach: a voxel of the RSP image can be studied, whereas larger regions can be looked at when considering the other images. Assuming that this region is constituted of only one material, on the basis of the RSP image for example, the data reconstructed from a large number of particles can be studied without increasing the overall dose. The next section will present such a tomographic study.

In addition, it may be highlighted that all results and conclusions on the potential interest in the outputs presented in this work are obtained from Monte Carlo simulation data. It is an advantage in terms of conceptual study, as it allows for the investigation of the behaviour of particles without any experimental or detection effects. While it does not mean that the exact same results would be obtained in real conditions, Monte Carlo techniques and Geant4 in particular have been used for years in proton therapy and are more accurate than analytical dose calculations [Paganetti, 2012]. The Geant4 simulation code has been validated with experimental data for applications in proton imaging [Cuttone et al., 2005; Milhoretto et al., 2012].

5.2 Qualitative approach to image reconstruction using the scattering and transmission rate

In order to evaluate the potential of imaging using the scattering and transmission, image reconstruction studies were performed. The first approach taken was rather qualitative: if we reconstruct images, what can we get? As the results of the previous section highlighted, the statistical uncertainty on the measured outputs is quite significant. The first approach thus aims at answering the following question: may the information collected on the scattering and transmission be used to produce images that could be of importance?

5.2.1 Simulation and reconstruction process

Simulated pCT scan data of a modified version of the Zubal head phantom (Section 3.1.5.2) were generated using GATE (Sections 3.1.1.2 and 3.1.2). Two lesions were inserted inside the brain. They were assigned the composition of modified carcinoma, with the same electron density but with different proportions of oxygen. A description of the composition and properties of the two carcinoma and the brain region can be found in Appendix A.

In order to reduce simulation time and increase the number of particles studied, the data considered for this study were produced by only considering a 1.26 cm thick slice of the head. This is sufficient to get consistent results for the reconstruction of the central slice. As a head is comparable to a 20 cm-deep water object, this thickness encompasses more than 90% of the scattered particles.

The information gathered on the observables from the list-mode acquisition was binned depending on the emission position of the particles and put into projections in order to reconstruct the image using a FBP algorithm (Section 3.2.3) in an image volume with 1×1×1 mm^3 voxel size. This was done using a statistic of 100 protons/mm^2 and 1000 protons/mm^2. An acquisition of 256 projections using 100 protons/mm^2 gives a dose of 2.5 mGy at the center of the head phantom (estimated with the dose actor of GATE). Therefore, the number of protons was multiplied by 10; this is reasonable, as it results in a dose equivalent to that of an X-ray CT scan (estimated between 1.5 cGy and 3 cGy at the centre of a head-sized object by Islam et al. [2006]).

All the images were filtered with a three-dimensional median filter in order to reduce the noise.

Stopping power

As a reference, images of the RSP – making use of the information on the energy of the particles – were produced, with and without 3-σ cuts on the exit angle and energy of the protons.

Scattering

Images of the angular scattering were reconstructed using directly the mean values of the non-projected scattering angle in the projections described in Section 5.1.1.1. The quantity reconstructed in each voxel is representative of both the energy loss induced by the materials and the radiation length of the materials, as described in Equation 2.7. For this study, no attempt was made to deconvolve these two parts. Two images were produced for this observable: one with all the data and the other after performing 3-σ cuts on the exit energy and angles.

In addition, images using the cumulative scattering of each proton were also produced. The idea was that taking into account the difference in the direction of a particle between its entrance and exit of the object is not exactly representative, on an individual level, of the scattering it underwent. This is illustrated on Figure 5.4 where the two particles enter and exit the material with the same angle. However, the particle on the top was less scattered than the other one.

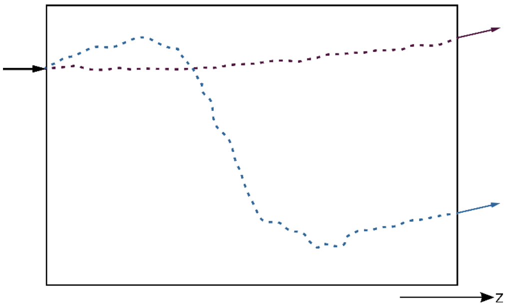

Figure 5.4: Paths of two protons with the same entrance parameters exiting an object with the same scattering angle but at different positions.

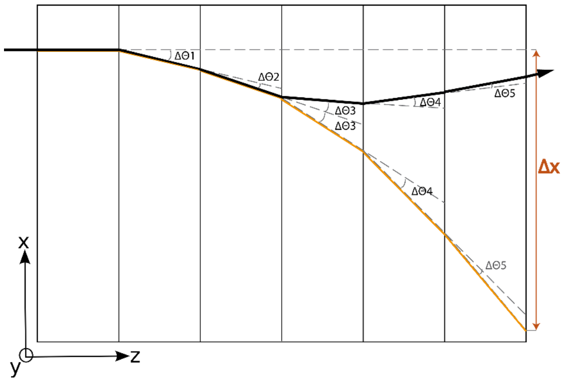

Figure 5.5: Cumulative scattering distance (Δx) for the angular scattering along the proton path. The black line represents the proton path estimation using the MLP.

Therefore, it was chosen to quantify the “cumulative scattering” of each proton by a distance, which would be the lateral displacement if the absolute value of its scattering angle was to be added along its propagation. This is illustrated on Figure 5.5. This procedure takes its sense when considering a curved trajectory for each particle; it was performed using the MLP. Two images were produced for this observable: one with all the data and the other after performing 3-σ cuts on the exit energy and angles.

Transmission rate

The image reconstruction using the transmission rate was performed in a similar fashion to the principle of X-ray CT image reconstruction. Each voxel of the reconstructed image represents an attenuation coefficient, directly proportional to the total macroscopic cross section for protons in the material represented by κ in Equation 2.10. The transmission rate was defined as the proportion of protons going through a 1×1 mm^2 pixel of the upstream tracking plane that are detected by the tracking system downstream from the object.

An alternative way to define the transmission rate is to consider a linear transmission rate. In that case, only the protons that were detected with a lateral displacement less than a value are considered as transmitted. This value was set to a 10 mm radius on the first downstream tracking plane: it makes it possible to consider a majority of the particles, while removing the most scattered ones. As a consequence, this linear transmission rate will depend both on the nuclear interactions and the MCS. Such a definition is for example used for high energy proton imaging [King et al., 1999].

5.2.2 Results

5.2.2.1 Image quality

Figures 5.6, 5.7, 5.8 and 5.9 show the reconstructed images of the RSP, of the scattering, of the cumulative scattering as well as of the transmission and linear transmission respectively. In addition, the phantom in RSP values is shown on Figure 5.6(a).

For easier inter-comparison, Figure 5.10 shows images reconstructed using the different observables using 1000 protons/mm^2/projection.

Visual assessment

Visual assessment of the images makes it possible to determine the following: the RSP images (Figure 5.6) seem to present a much higher quality than the images reconstructed using the other data. This is not surprising, as it was shown that proton imaging (of the RSP) makes it possible to reach a satisfactory density and spatial resolution to be used in a clinical setting. The effect of the 3-σ cuts on the data is not clearly visible, nor is the effect of the increase in the statistics. Indeed, as the statistical uncertainty on the measured energy (that is translated to noise in the projections and therefore in the images) is very low, using 1000 protons per square millimetre of projection is not necessary.

Nevertheless, the images reconstructed using the other observables all show some anatomical information.

In the case of the reconstructions using the scattering (Figure 5.7), it can be seen that the cuts help distinguish the tumours in the case of 100 protons/mm^2. The improvement in terms of reduction of noise in the image when using 1000 protons/mm^2 is considerable. The lesions can be clearly seen on the image of 1000 protons/mm^2 with cuts.

The images reconstructed using the cumulative scattering (Figure 5.8) exhibit interesting visual properties. Increasing the number of protons treated from 100 to 1000/mm^2 allows a much easier differentiation of the internal structures of the head. Moreover, the border of the two lesions appears clearly, in bright, allowing for a good detection. The images reconstructed using the transmission rate (Figures 5.9(a) and 5.9(b)) show an important level of noise, that is reduced with the increase in the number of particles studied. It can be seen that the images reconstructed using the linear transmission (Figures 5.9(c) and 5.9(d)) show a much greater contrast between the soft tissues and the bones than any other. However, for all the transmission images, the tumours can not be distinguished.

Signal to noise ratio

The signal to noise ratio (SNR) of the reconstructed images was evaluated. A number of $N = 10$ regions of interest (ROI) of 200 mm^3 each were drawn inside an area made of skeletal muscle (arrows in Figure 5.6(a)). The SNR was defined as:

$$\mathrm{SNR} = \frac{\frac{1}{N}\sum_{i=0}^{N}\mu_i}{\sqrt{\frac{1}{N}\sum_{i=0}^{N}\left(\mu_i - \frac{1}{N}\sum_{i=0}^{N}\mu_i\right)^2}} \tag{5.3}$$

with μ_i the mean value of the i^{th} ROI.

Results are presented in Table 5.4. As expected from the results shown in Table 5.3, the statistical uncertainty on the transmission rate and scattering induces a much lower SNR in the images reconstructed from these observables than from the RSP. Indeed, in the cases of the cumulative scattering and of the (linear) transmission, the SNR is an order of magnitude lower than for the images of the RSP.

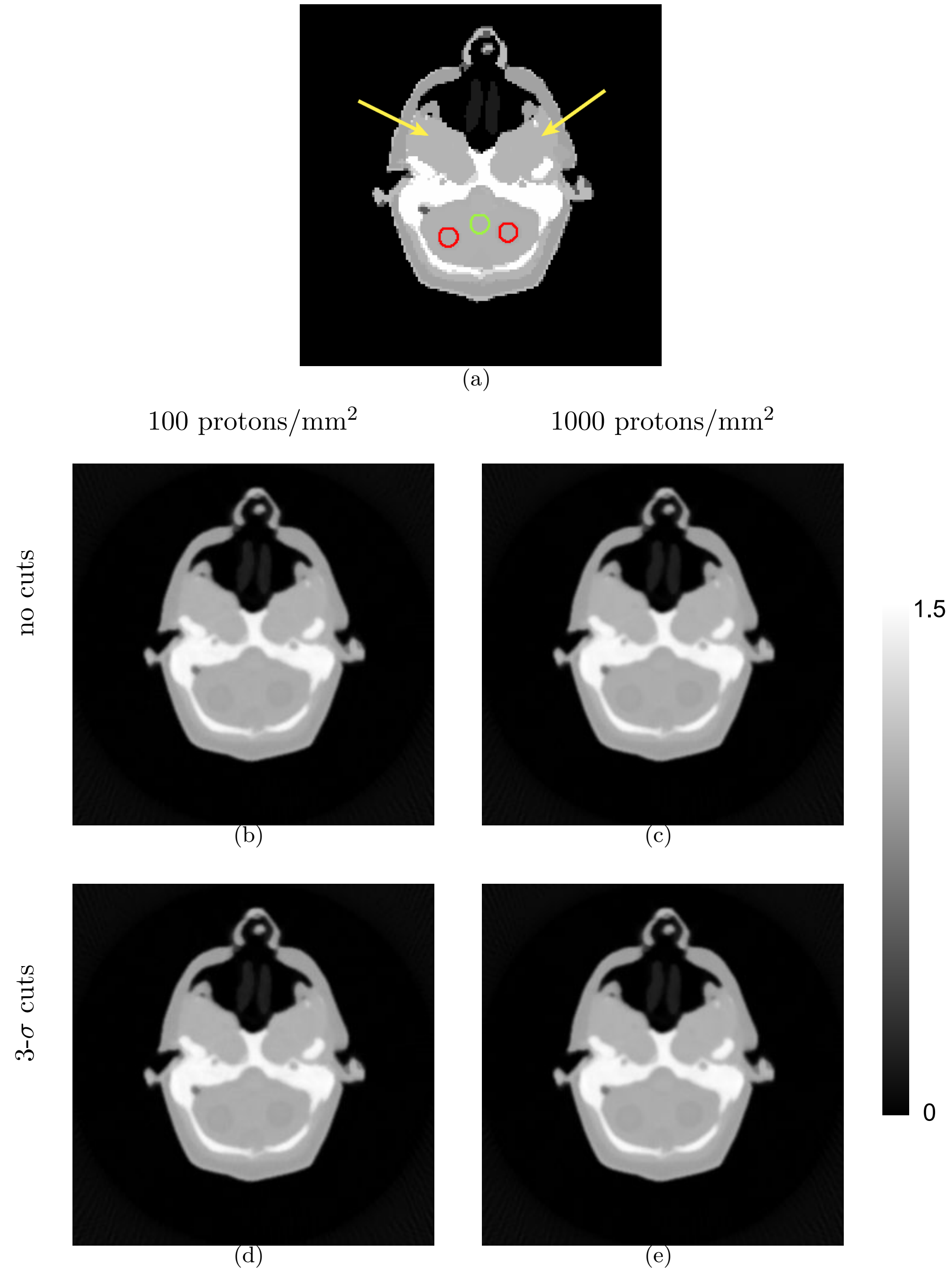

Figure 5.6: Transverse slices of (a) the RSP phantom, and of FBP reconstructions of the RSP for (b) 100 proton/mm^2 and (c) 1000 protons/mm^2 as well as reconstructions of the RSP with 3-σ cuts on the data for (d) 100 proton/mm^2 and (e) 1000 protons/mm^2. Images with [0:1.5] colour range window.
On (a), the colour circles indicate the ROI inside the carcinoma (bottom, red) and inside the brain tissue (top, green). The two arrows on the image of the phantom designate the areas of skeletal muscle in which the SNR (Equation 5.3) was calculated.

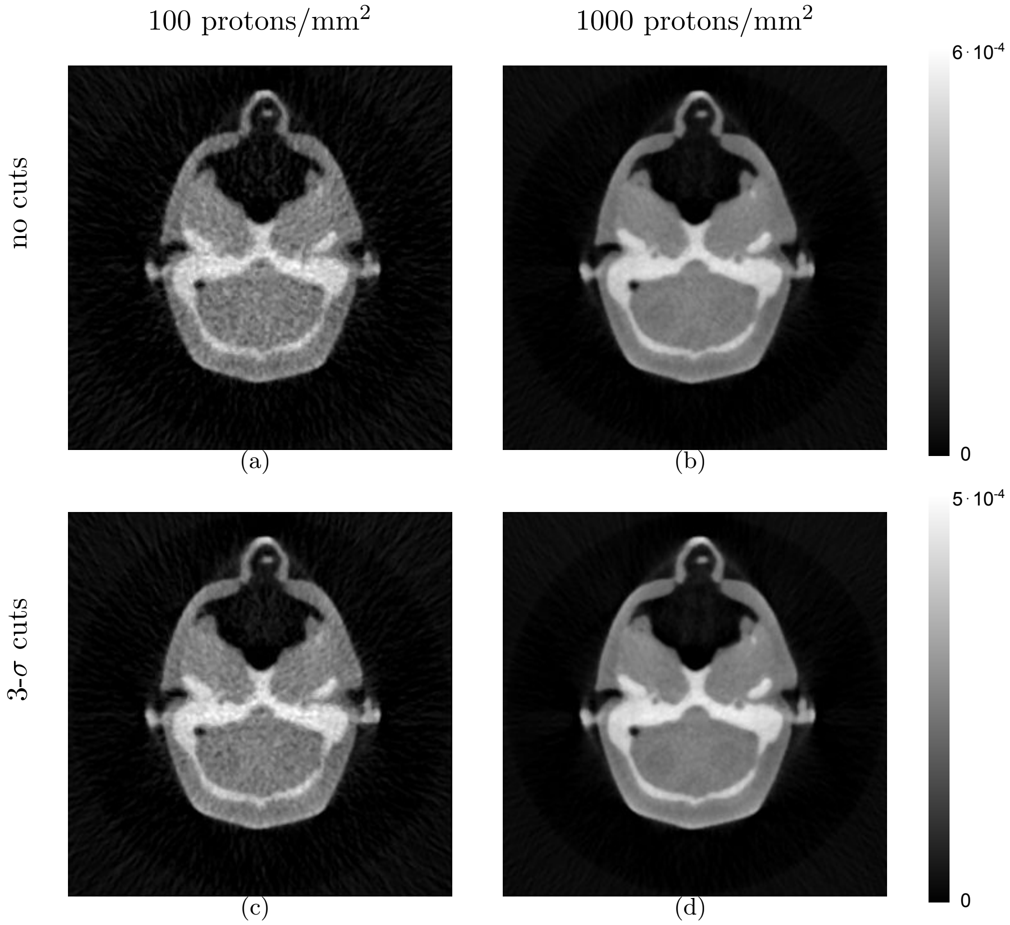

Figure 5.7: Transverse slices of FBP reconstructions of the scattering for (a) 100 proton/mm^2 and (b) 1000 protons/mm^2 with a colour window range of $[0{:}6 \cdot 10^{-4}]$. Reconstructions of the scattering with 3-σ cuts on the data for (c) 100 proton/mm^2 and (d) 1000 protons/mm^2 with a colour window range of $[0{:}5 \cdot 10^{-4}]$.

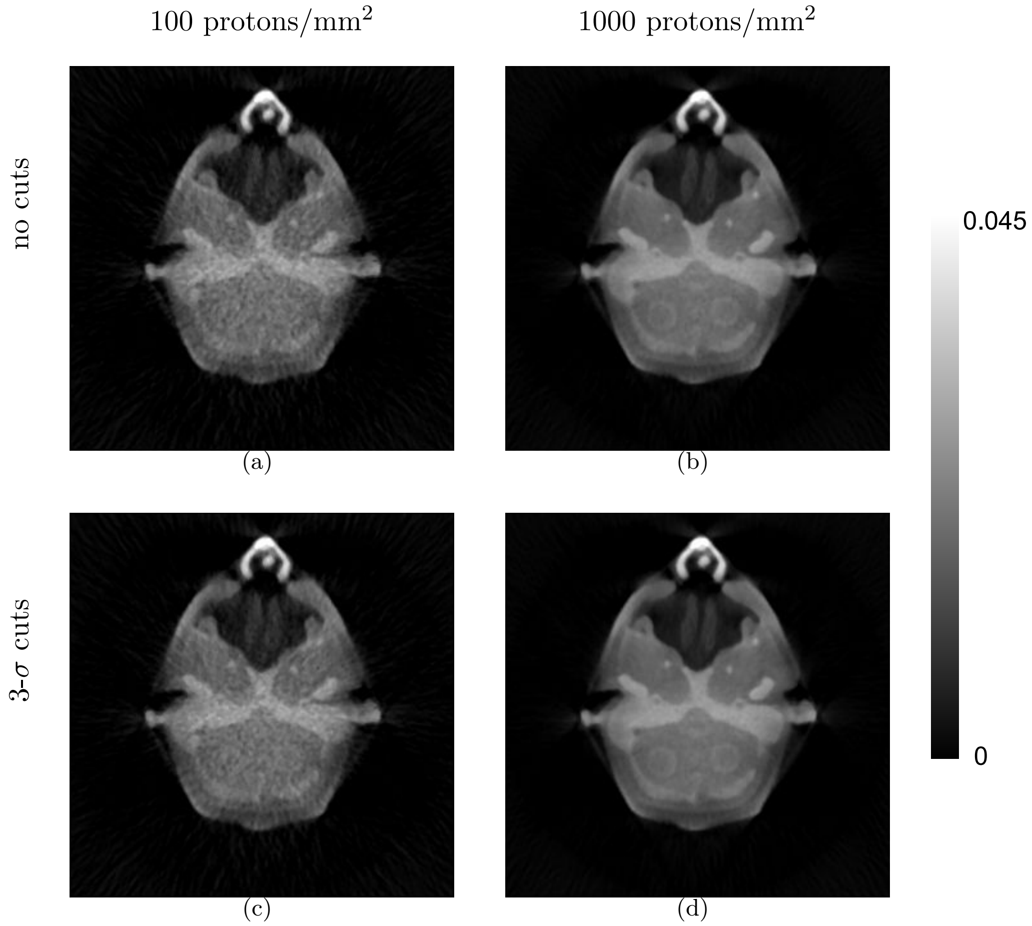

(a) (b) (c) (d)

Figure 5.8: Transverse slices of FBP reconstructions of the cumulative scattering on the MLP for (a) 100 proton/mm^2 and (b) 1000 protons/mm^2 as well as reconstructions of the cumulative scattering with 3-σ cuts on the data for (c) 100 proton/mm^2 and (d) 1000 protons/mm^2. Images with a colour window range of [0:0.045].

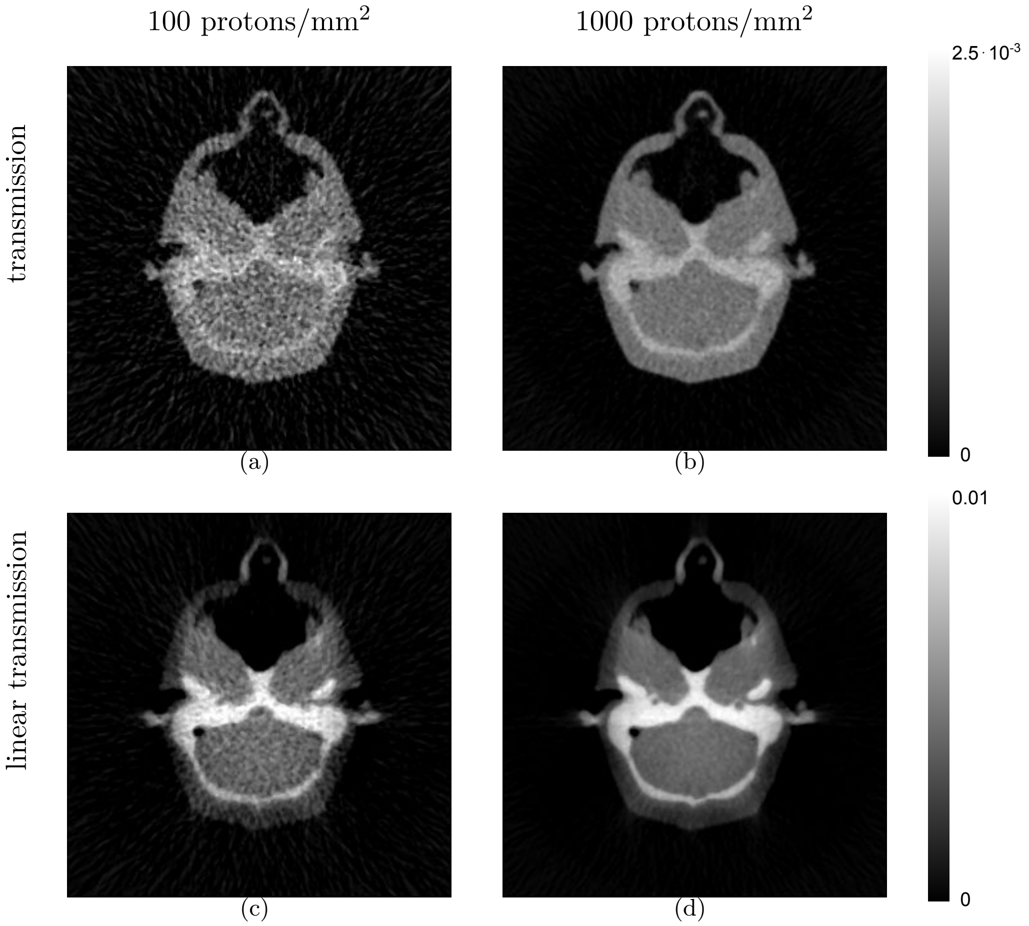

Figure 5.9: Transverse slices of FBP reconstructions using the transmission rate for (a) 100 proton/mm^2 and (b) 1000 protons/mm^2 using a colour window range of [0:0.0025]. Reconstructions using the linear transmission rate for (c) 100 proton/mm^2 and (d) 1000 protons/mm^2 using a colour range of [0:0.01].

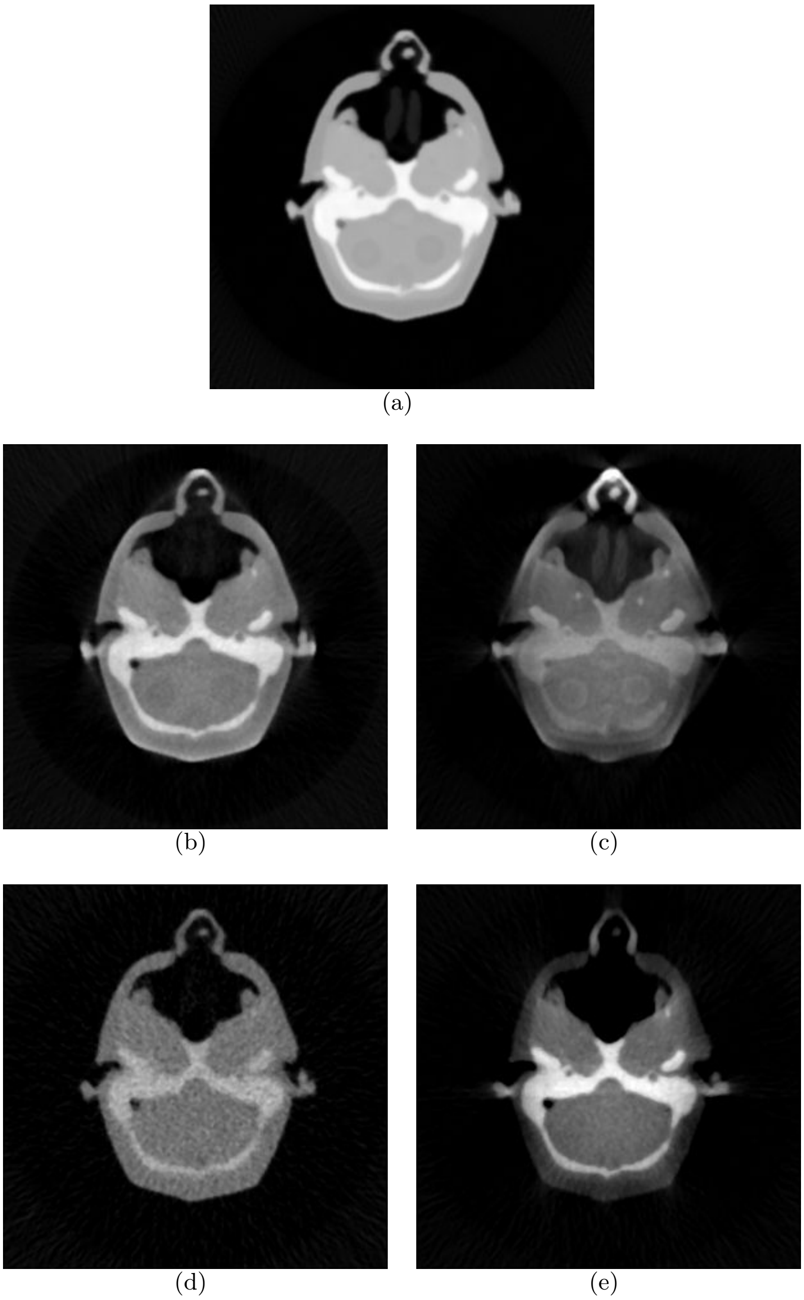

(a)

(b) (c)

(d) (e)

Figure 5.10: Transverse slices of the reconstructed images shown in the previous figures, with 1000 protons/mm^2/projection: (a) RSP image (Figure 5.6(e)); (b) image reconstructed from the scattering (Figure 5.7(d)); (c) image reconstructed from the cumulative scattering (Figure 5.8(d)); (d) image reconstructed from the transmission (Figure 5.9(b)); (e) image reconstructed from the linear transmission (Figure 5.9(d)).

Table 5.4: SNR of the different reconstructed images for 100 and 1000 protons/mm^2/projection

Image	100 protons/mm^2	1000 protons/mm^2
RSP	298	318
RSP - with cuts	300	320
Angular scattering	47	51
Angular scattering - with cuts	55	49
Cumulated scattering	19	19
Cumulated scattering - with cuts	22	20
Transmission	27	64
Linear transmission	23	20

Region of interest study

Three ROI were defined in the reconstructed images as follows: one inside each carcinoma and one in the brain tissue. Each 3D cylindrical ROI has a volume of 406 mm^3. They are represented by the circles on Figure 5.6(a). The study was performed on the images reconstructed using 1000 protons/mm^2.

It is possible to evaluate the accuracy of the reconstructed images in the case of the RSP and in the case of the transmission.
For the RSP, the expected values were computed analytically using the Bethe formula and knowing the stoichiometric composition of the materials simulated. Figure 5.11 shows the reconstructed values inside the three ROI, as well as the expected value for the RSP images. It can be seen that the values reconstructed in the ROI, for the images with and without the 3-σ cuts on the data, are quite close to the expected values.
Figure 5.12 shows the reconstructed values as well as the expected values for the transmission image. The expected values were calculated using the information on the transmission rate of protons inside an homogeneous cube of the materials (Section 5.1.1.2). While the reconstructed values are really close to the expected ones, the uncertainty on the average, represented on the histogram by the error bars, are significant.

The values in the reconstructed images using the scattering, cumulative scattering and linear transmission rate is difficult to interpret because they depend on multiple physics processes. As a consequence, no expected values could be determined for these images. Figures 5.13, 5.14 and 5.15 show the reconstructed values in the three ROI for the images produced from the scattering, cumulative scattering and linear transmission rate, respectively. It can be seen from Figure 5.13 that some difference between the three ROI can be distinguished. For both images, with and without the 3-σ cuts, the values in the carcinoma ROI can be set apart from the values in the brain ROI. As far as the cumulative scattering goes (Figure 5.14), the noise in the regions of interest results in the fact that the different ROI can not be well differentiated. Finally, in the case of

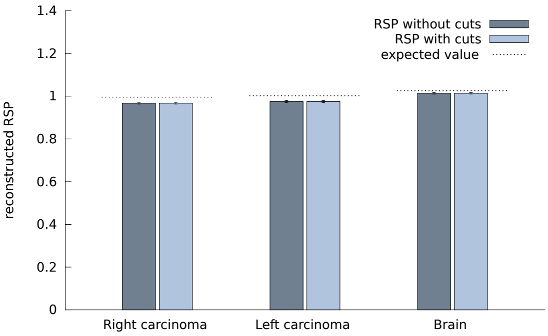

Figure 5.11: Values in the three ROI for the RSP reconstructions without and with cuts.

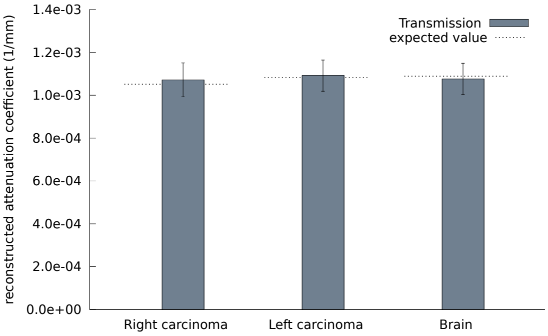

Figure 5.12: Values in the three ROI for the transmission image.

the image reconstructed from the linear transmission (Figure 5.15), it seems that some difference between the two carcinoma appears, but the noise may make them hardly distinguishable from the brain.

5.2.2.2 Contrast

In order to quantify the potential to differentiate the regions of interest and the possibility to distinguish the lesions, the contrast with the brain ROI was studied. To do so, the contrast between the mean value of the ROI in the brain μ_{Brain} and the mean value of the ROI in a carcinoma μ_{Lesion} was defined as:

$$C = \frac{\mu_{\text{Brain}} - \mu_{\text{Lesion}}}{\mu_{\text{Brain}} + \mu_{\text{Lesion}}} \tag{5.4}$$

The results are shown in Table 5.5. It can be seen that the contrast in the images of angular scattering is 1.5 to 2 times greater than in the images of the RSP. Images of the cumulative scattering show no contrast between the brain and left carcinoma, whereas between 1% and 2% contrast can be found between the brain and the right carcinoma. The linear transmission images seem to show a rather high contrast also. Interestingly,

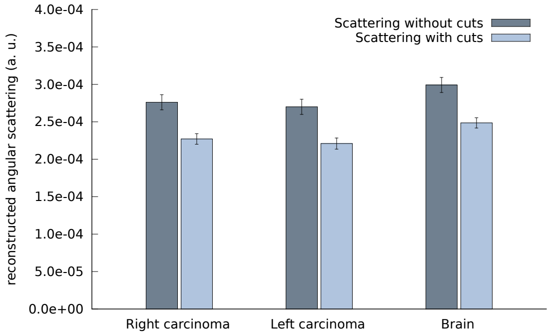

Figure 5.13: Values in the three ROI for the angular scattering reconstructions without and with cuts. The expected values are not defined.

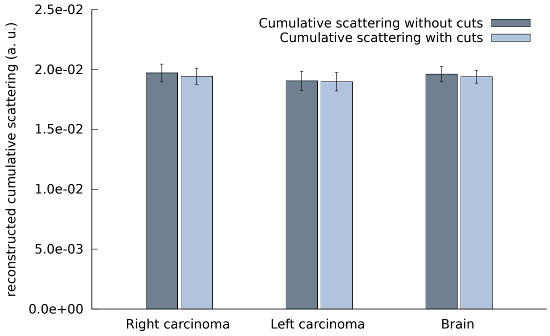

Figure 5.14: Values in the three ROI for the cumulative scattering reconstructions without and with cuts. The expected values are not defined.

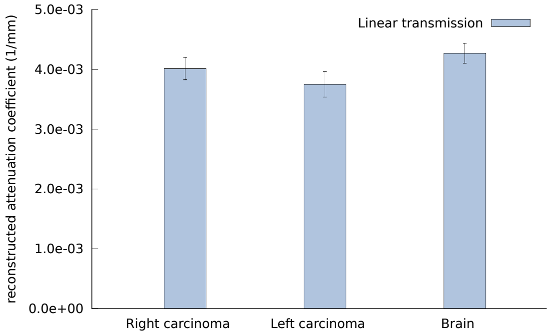

Figure 5.15: Values in the three ROI for the linear transmission image. The expected values are not defined.

Table 5.5: Contrast C between the mean values in the two carcinoma ROI and the brain ROI for the different reconstructed images

Image	Right carcinoma		Left carcinoma	
	100 p/mm^2	1000 p/mm^2	100 p/mm^2	1000 p/mm^2
RSP	2.35%	2.33%	1.97%	1.92%
RSP - with cuts	2.36%	2.33%	1.98%	1.92%
Angular scattering	3.55%	4.02%	4.33%	5.14%
Angular scattering - with cuts	3.70%	4.52%	5.70%	5.88%
Cumulated scattering	0.00%	-0.24%	2.03%	1.46%
Cumulated scattering - with cuts	-0.12%	-0.11%	1.09%	1.09%
Transmission	1.90%	0.21%	-4.02%	-0.71%
Linear transmission	4.00%	3.09%	5.00%	6.49%

the contrast values of the transmission images seem inconsistent: the contrast varies of more than 3% greatly when considering 100 and 1000 protons/mm^2.

This last result highlights the fact that a high contrast between the average values in the regions is not sufficient to distinguish the materials. Indeed, the noise in the image needs to be considered as well.

Therefore, in order to evaluate how significant this contrast is with respect to the noise in the images, the contrast to noise ratio (CNR) was considered as well. It was defined as [Soltanian-Zadeh et al., 1990]:

$$\mathrm{CNR} = \frac{\mu_{\mathrm{Brain}} - \mu_{\mathrm{Lesion}}}{\sqrt{\frac{1}{2}\left(\sigma^2_{\mathrm{Brain}} + \sigma^2_{\mathrm{Lesion}}\right)}} \tag{5.5}$$

where σ_{Brain} and σ_{Lesion} are the standard deviations calculated for the two considered ROI.

Results are shown in Table 5.6. As anticipated from the results of the contrast study, the CNR between the regions in the transmission image is very close to 0. Due to the low contrast between the regions, the images of the cumulative scattering also present very low CNR. Because they present a rather high contrast between the regions despite the level of noise, the images of the angular scattering and linear transmission present a higher CNR. However, it can be seen that even though the images of the RSP did not present the highest contrast between the regions, the low level of noise is a great asset in terms of CNR.

5.2.3 Discussion

As expected from the preliminary study of the previous section, the noise in the images of the RSP is much lower than in the other images. This is well illustrated by the SNR shown in Table 5.4. However, all the reconstructed images show information that may be of interest.

Table 5.6: CNR between the two carcinoma ROI and the brain ROI for the different reconstructed images

Image	Right carcinoma		Left carcinoma	
	100 p/mm^2	1000 p/mm^2	100 p/mm^2	1000 p/mm^2
RSP	9.00	11.71	7.12	9.19
RSP - with cuts	9.07	11.53	7.32	9.00
Angular scattering	0.63	2.30	0.77	2.89
Angular scattering - with cuts	0.90	3.10	1.29	3.87
Cumulated scattering	0.00	-0.13	0.48	0.78
Cumulated scattering - with cuts	-0.03	-0.07	0.27	0.64
Transmission	0.16	0.06	-0.37	-0.21
Linear transmission	0.58	1.45	0.74	2.72

As far as the RSP image reconstruction is concerned, the cuts on the data only slightly improve the accuracy and SNR of the reconstructed images. Indeed, the 3-σ cuts on the exit angle are most pertinent when using the MLP; it has been shown that more drastic cuts give more accurate results, as it fits better with the straight line approximation used for the reconstruction [Cirrone et al., 2011]. Moreover, the cuts on the exit energy have no effect here since secondary protons were not considered in the simulation. The contrast (Table 5.5) in the images of RSP is rather low (around 2%) for both carcinoma, however the low level of noise directly impacts the CNR value (Table 5.6). Two comments can be made about the reconstructed RSP images. The energy distribution of the beam in a realistic situation will increase the uncertainty on the results. Moreover, the RSP was reconstructed using FBP as a reference for the study. A more appropriate reconstruction process could give better results in terms of accuracy of the reconstructed values and spatial resolution [Li et al., 2006].

While the reconstructed images of the angular scattering, without and with cuts, have a much lower SNR than the RSP images, they also show a more important contrast. The CNR, however, is lower than that of the RSP image, though it is improved using 3-σ cuts on the exit angles that remove particles having undergone nuclear scattering [Schulte et al., 2008]. Nevertheless, the visual properties of the images, for example the one shown on Figure 5.7(d), seem interesting. With the increase in the number of protons, the two lesions can be distinguished. By looking at the approximation to multiple Coulomb scattering presented in Equation 2.7, it can be seen that these reconstructed images represent both the energy loss and the radiation length of the materials. This makes the interpretation of the reconstructed values very complex, as the contribution of the two properties are not deconvolved. This joint effect of different processes may explain the bright spot at the tip of the nose that can be seen on all images of Figure 5.7.

Reconstructed images of the cumulative scattering, estimated on the MLP, show a lower SNR than the images of the scattering used directly by a factor 2 at least. The contrast and CNR are accordingly unfavourable. Indeed, it can be seen on all images in

Figure 5.8 that this reconstruction process generated bright artefacts. The nose, on top of the images, presents very high intensity in the reconstructed images. This may be due to the path approximation used, as it induces an additional error in the reconstruction process, or because multiple physics processes are involved in the generation of the observable. However, while seemingly of low interest looking at the tabulated figures of merit, the cumulative scattering images present interesting visual characteristics. On Figure 5.8(b) for example, the two carcinoma can easily be seen: the reconstruction generated a bright outline around the lesions. This also explains the low contrast: an average value on the ROI was considered, and it can be clearly seen that the values reconstructed in the carcinoma are not homogeneous.

However, the visual interest of these images is even greater than this. Figure 5.16 shows an enlargement of an area of the reconstructed image using the cumulative scattering shown in Figure 5.8(d) and of the phantom in RSP for comparison. The two arrows on each image point towards small areas of blood in skeletal muscle. The two materials have very close RSP (less than 0.5% contrast: $\text{RSP}_{\text{blood}} \simeq 1.06$, $\text{RSP}_{\text{muscle}} \simeq 1.05$, data available in Appendix A). These areas are clearly visible in all the cumulative scattering images shown in Figure 5.8. This may be either because this reconstruction process generated here too a bright outline at the material interface, or because it presents a high sensitivity to a difference in the composition. Because the reconstructed values are difficult to interpret, further studies will be needed to explore further and test the limitations of this approach, which could be of great interest in diagnostics.

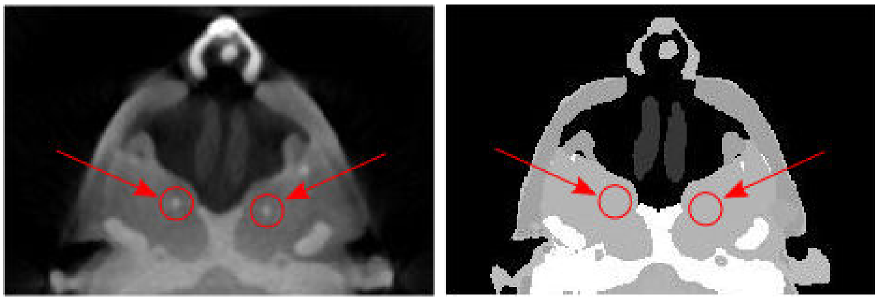
(a) (b)

Figure 5.16: Enlargements of (a) the cumulative scattering image of Figure 5.8(d) and (b) the phantom in values of the RSP shown in Figure 5.6(a). The two arrows on each figure point to areas of blood in skeletal muscle.

For the reconstructed total transmission image, the values in the ROI converge with the expected values (Figure 5.12). Nevertheless, the noise dominates the figures of merit, leading to a very low CNR. For the reconstructed images of the linear transmission, the high contrast still suffers from the important level of noise, leading to a small CNR. It can also be put forward that the 10 mm cut was set arbitrarily, and that a different choice of radius may impact all the figures of merit shown here. Moreover, the reconstructed attenuation coefficients depend at the same time on the nuclear interactions and the scattering – and thus also on the energy loss – which lead to a difficult quantification of the reconstructed values. A cut set arbitrarily as a distance may also not be the most representative in a physical sense; a proportion related to the scattering angle may be more pertinent.

5.2.4 Conclusion

This study lead to the reconstruction of images of the RSP as well as images using scattering, cumulative scattering and transmission rate. As expected from the preliminary study on the outputs of a pCT scan detailed in the previous section, the statistical uncertainty on the observables lead to an important noise in the reconstructed images. However, increasing the number of particles studied makes it possible to produce images with interesting visual attributes. The image of the linear transmission, for instance, shows an important contrast between the bone and soft tissues. Both lesions inserted in the brain can be distinguished in the images of the scattering. The images reconstructed using the cumulative scattering present even more interest in terms of qualitative information. The bright outline generated makes the lesions clearly visible. In addition, the small inserts of blood in skeletal muscle appear very brightly on this image, whereas the low contrast between these two materials in the image of RSP makes it impossible to separate them. This indicates that these images could present an interest in terms of diagnosis.

The fact remains that these images, in particular the scattering and cumulative scattering ones, are representative of the combination of different physical processes. Therefore, interpretation at this level can only be qualitative. The next section will present a method to reconstruct images using the information on the scattering and transmission rate of the particles, for which a physical interpretation of the values is provided.

5.3 Quantitative approach: a step towards stoichiometric composition?

As it was put forward in the previous section, the exploitation of information on the scattering and transmission rate of the protons may present interesting properties. However, no quantitative information on the reconstructed values were extracted. This section presents the investigation on a quantitative approach to the use of these data. The aim is to determine how much information on the composition of materials could be extracted from reconstructed images.

The reconstruction process using the transmission rate of the particles is very similar to X-ray CT image reconstruction. Therefore, the use of this information is rather straightforward, as will be shown in Section 5.3.1. The use of the information on the scattering, however, requires to pose the problem in a different fashion, in order to deconvolve the effect of the energy loss and the scattering. A possible reconstruction approach is investigated in Section 5.3.2. Finally, the potential use of all the data acquired to characterize a material is discussed.

5.3.1 Reconstruction using the transmission rate

As mentioned in Section 2.1.3, the attenuation of the proton flux follows a Beer-Lambert law (Equation 2.10), re-written here for convenience:

$$\Phi(l) = \Phi_0 \exp\left(-\int_l \kappa\left(x, y, z, E\right) \mathrm{d}l\right) \tag{5.6}$$

where $\kappa\left(x, y, z, E\right)$ is the macroscopic inelastic nuclear cross section for protons in the materials at energy E at each position (x, y, z) and l is depth of material.

This formulation is very similar to the expression of the attenuation of a photon flux, used in X-ray imaging. As put forward in the previous section (Section 5.2.1), it is possible to reconstruct images of the “attenuation coefficient” in a similar way to X-ray CT (Section 1.2.1.1).

For an element, the macroscopic cross section is defined as:

$$\kappa = N \cdot \sigma \tag{5.7}$$

with N the atomic density of the target, and σ the microscopic nuclear cross-section. Therefore, it can be re-written as:

$$\kappa = \rho \left(\frac{\mathcal{N}_A}{A}\right) \cdot \sigma \tag{5.8}$$

with ρ the target volumetric mass density, $\mathcal{N}_A$ the Avogadro number and A the target atomic number.

For a material constituted of i elements of mass proportions w_i, this can be generalized as:

$$\kappa = \rho \mathcal{N}_A \sum_i w_i \frac{1}{A_i} \sigma_i \tag{5.9}$$

The behaviour of κ as a function of the energy is shown on Figure 2.3 for different elements. It can be seen that for the energies considered in pCT (80-250 MeV), the inelastic nuclear interaction cross-sections of protons in light elements (oxygen and under) are in a “plateau” region. This is not the case for calcium for example, for which the plateau behaviour is found at energies superior to 150 MeV.

As a first approximation, the energy-dependence of the cross-sections is neglected. As a result, a bias can be expected in the regions of materials that have a significant proportion of elements heavier than oxygen such as bone. However, this makes it possible to use a straightforward reconstruction algorithm. Indeed, images reconstructed this way are shown in the previous section, on Figures 5.9(a) and 5.9(b).

Therefore, each voxel of the transmission images reconstructed in the previous section represents the total macroscopic inelastic nuclear cross-section of the material. Moreover, the interaction cross sections σ_i (Equation 5.9) can be measured experimentally and tabulated. Thanks to this, and in light of Equation 5.9, information on the composition of a material (i.e. its density and the mass proportion of each element) can be extracted.

5.3.2 Reconstruction using the scattering

Many approximations to multiple Coulomb scattering exist, amongst which the one used for the most likely path computation for example. Gottschalk [2009] reviewed these approximations of the scattering power used in proton transport calculations. The scattering power T is a differential description of the Gaussian approximation to multiple scattering, with:

$$T \equiv \frac{d\left\langle \theta^2 \right\rangle}{dx} \tag{5.10}$$

where $\left\langle \theta^2 \right\rangle$ represents the variance of the projected angular distribution (previously denoted σ^2 in Equation 2.7). The advantage of such a differential formulation is that it takes a similar form to that of the stopping power $S \equiv -\frac{dE}{dx}$, or more generally, to the formulation of the line integrals. As a consequence, the problem becomes particularly well-adapted to image reconstruction. However, an accurate formula for T must take into account the "history" of the protons, i.e. the competition between the Gaussian core and the single scattering tail of the distributions that will affect the rate of change of the Gaussian width. Thus, T should be non-local: it should not depend only on the local variables such as the mean proton energy, atomic properties and stopping power.

Different functions for T have been proposed, that recover more or less the Molière scattering angle if integrated over x for any slab [Gottschalk, 2009]. In the paper, Gottschalk reviews three local formulas:

- T_{FR}: Fermi-Rossi approximation ,
- T_{IC}: based on ICRU report 35,
- T_{LD}: based on the Linear displacement ,

and two non-local formulas

- $T_{ØS}$: Øversås and Schneider ,
- T_{dH}: differential Highland.

A new approximation is also proposed by Gottschalk [2009], named differential Molière (T_{dM}). Details of the approximations are given in Appendix B.

5.3.2.1 Reconstruction principle

The variance of the exit scattering angle of an initially parallel beam, after a slab of material of thickness x can be written as:

$$\theta^2_{proj} \simeq \int_0^x T\left(x'\right) dx' \tag{5.11}$$

All formulas listed previously except the Øversås and Schneider approximation can be re-written as $T = f(E)\frac{1}{X}$ with X the radiation length (X_0), or the scattering length (X_S), and $f(E)$ a function of the energy of the protons. This makes it possible to isolate the $\frac{1}{X}$ term. The energy-dependent term $f(E)$ can be evaluated for each depth in the object by making use of the image of the RSP. As the term X_0 is present many times in the formula of the Øversås and Schneider approximation, it is very inconvenient to isolate it. Therefore, this approximation was not further considered.

By comparing the estimated variance of the angular scattering using a formula and the one obtained in the data, and knowing the energy loss properties of the materials, one can estimate the scattering or radiation length in each voxel. The reconstruction process goes as follows:

(i) Estimation of a trajectory. As the RMS of the scattering angle is considered, an average straight line path can be considered.

(ii) Computation of the $f(E)$ term. For each voxel in the path, the average energy (or impulsion, or residual range) of the protons can be computed, knowing the initial energy and using the RSP image.

(iii) Reconstruction of the $\frac{1}{X}$ term.

This process can be performed through an iterative reconstruction algorithm.

5.3.2.2 Model validation

In order to determine the most appropriate model, the five models with $\frac{1}{X}$ term that can be isolated were compared to the GATE simulation data. It is possible to change the model used for multiple scattering in GEANT4. GATE, however, only takes the default Urban simulation model [Urban, 2006]. The Urban model is a condensed multiple Coulomb scattering model (Section 3.1.1.1). It is, however, much more complex than the approximations to multiple scattering listed previously, as it does not aim at only reproducing the Gaussian part of the MCS distribution, but also the tail. Gottschalk [2009] concludes that the differential Molière formula is the best fit to real data. However, as this section aims at showing a proof of concept of the reconstruction principle, the model that is closest to the simulation data should be used.

Figure 5.17 shows the variance of the angular distribution after different depths in water, for the five models studied and the GATE simulation data.

For easier evaluation of the agreement between the models and the simulation, Figure 5.18 shows the normalized difference D between the calculated θ^2_{proj} and the variance obtained by Monte Carlo simulation for different depths in water, defined as:

$$D = \frac{\langle\theta^2_{simulation}\rangle - \langle\theta^2_{model}\rangle}{\langle\theta^2_{simulation}\rangle} \tag{5.12}$$

for the five models. $\langle\theta^2_{simulation}\rangle$ and the associated uncertainty was estimated using 100 simulations of 10000 protons for each depth.

The model which shows the best agreement with the simulation data is the differential Molière. However, the discrepancies for thin objects (less that 5 cm depth) may induce some additional inconsistencies in the image reconstruction process. This behaviour was found to be the same for different materials tested, as illustrated on Figure 5.19 for water, adipose tissue, skull bone and muscle.

Furthermore, a high number of particles (10^6 protons) were used to test the agreement between the models and simulation, in order not to be affected by the statistical

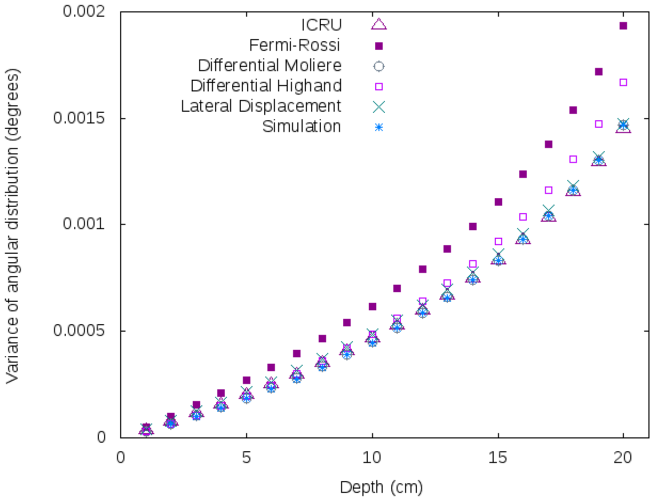

Figure 5.17: Scattering evaluation of the different models and the simulation for different thickness of water.

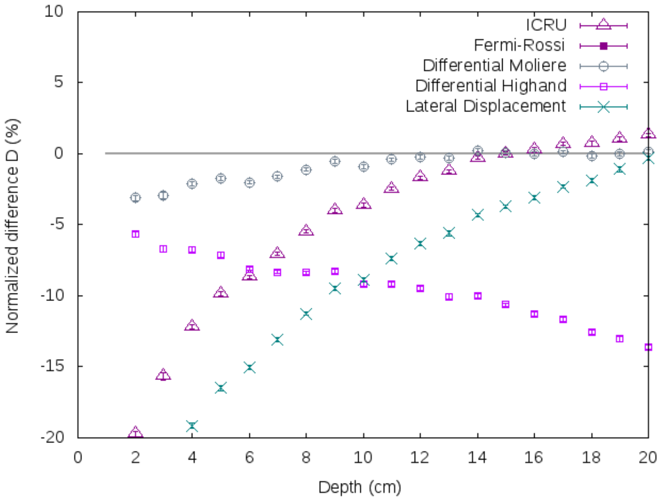

Figure 5.18: Normalized difference between models and the simulation for different thickness of water. The difference for the Fermi-Rossi approximation exceeds the range shown here for all thicknesses.

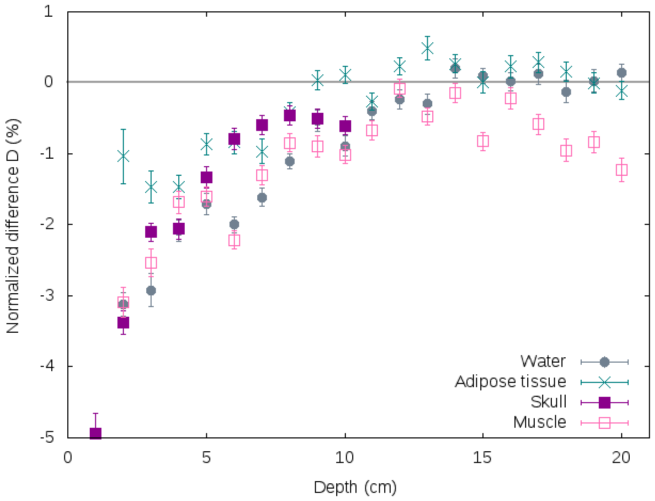

Figure 5.19: Comparison between the differential Molière model and the simulation for different thickness of water, adipose tissue, skull bone and muscle.

uncertainty. In a realistic scan situation, between 100 and 1000 protons can be used per square millimetre of projection. Therefore the measures will be greatly affected by the statistical uncertainty: the statistical uncertainty on a measure of $\langle\theta^2_{simulation}\rangle$ from 1000 protons is of the order of 4%. As a consequence, a rather high level of noise can be expected in the reconstructed images.

5.3.2.3 Reconstruction of the scattering length

Images of the inverse scattering length ($1/X_S$) of the modified Zubal head phantom (Section 3.1.5.2) were reconstructed with an ART algorithm using the data binned into projections. 1000 protons/mm^2 of projection and 256 projections were used to reconstruct images of $1{\times}1{\times}1$ mm^3 voxels. As the distribution of the angular scattering is fitted for each pixel in order to obtain the value of $\langle\theta^2\rangle$, the projections were naturally binned according to the positions of the particles upstream from the object.

Figure 5.20 shows a transverse view of (a) the FBP image of the RSP (b) expected inverse Xs and (c) reconstructed inverse Xs.

It can be seen that, as anticipated, the inverse scattering length image shows a high level of noise. Both the noise and spatial resolution seem degraded compared to the image produced using the scattering without any deconvolution of the energy contribution shown on Figure 5.7(d)). Nevertheless, the two carcinoma can be distinguished from the brain, indicating a rather good contrast between the soft tissues.

The advantage of this reconstruction method rather than just using the scattering in a qualitative way (as was done in the previous section) is that it gives access to quantitative information on the materials. In order to evaluate the accuracy of this reconstruction, regions of interest (ROI) were drawn in the carcinoma, brain and in

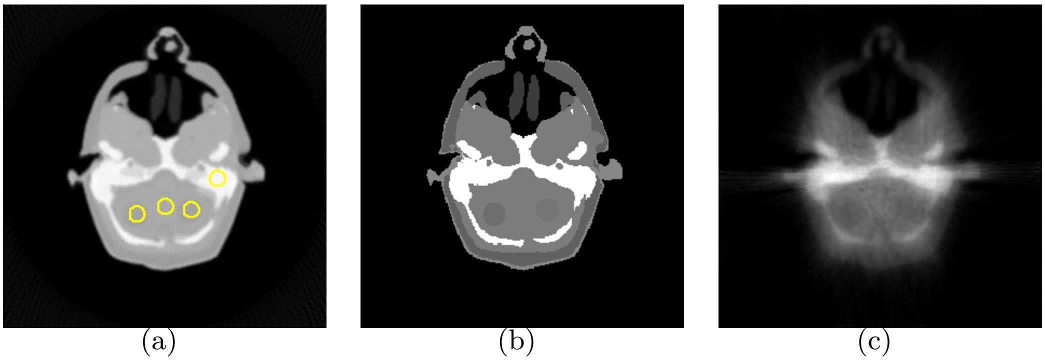

Figure 5.20: Transverse slice of (a) the FBP image of the RSP, (b) the phantom in inverse scattering length and (c) the reconstructed image in inverse scattering length. The regions of interest studied are drawn on figure (a). Colour range of [0:1.5] for the RSP image, and of $[0{:}4.5\cdot10^{-3}]$ for the inverse scattering length images (in mm^{-1}).

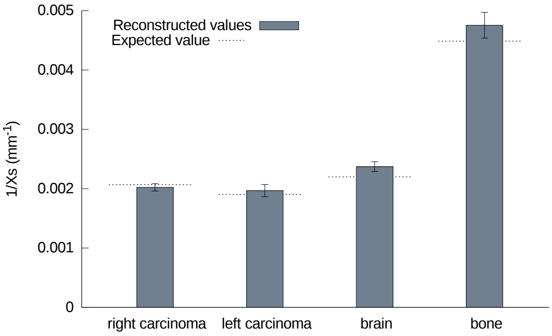

Figure 5.21: Expected and reconstructed values in the ROIs.

the skull (see Figure 5.20(a)). Figure 5.21 shows the reconstructed values as well as the expected value for each ROI. The reconstructed values for the bone and brain regions are overestimated, whereas the two carcinoma regions seem to be accurately reconstructed. This may be due either to the model used for the reconstruction or to the statistical uncertainty that introduces inconsistencies in the reconstruction algorithm.

5.3.2.4 Conclusion

These results show that quantitative image reconstruction of scattering length using a proton scanner is feasible. The use of the RSP image to estimate the energy of the protons make it possible to deconvolve the two contributions, and gives access to information directly related to the composition of the materials.

The statistical uncertainty on the measured $\langle\theta^2\rangle$ generates a high level of noise in the reconstructed image. The spatial resolution of the inverse scattering length image

appears to be limited, which is most probably due to the straight line path approximation used for image reconstruction in this work.
The ROI study shows that the method is viable. The accuracy is currently limited to a few percent, which may be due to the differences between the models used for simulation and reconstruction introducing additional inconsistencies in the reconstruction process. The use of a different reconstruction algorithm or the addition of a regularization scheme, such as the total variation (Section 3.3.3.2), could probably help improve results.

5.3.3 Towards the stoichiometric composition?

The data acquired with a pCT scanner as studied nowadays can obviously be used to reconstruct images of the RSP. Sections 5.3.1 and 5.3.2 showed that using the recorded information on the transmission rate and scattering of the particles make it possible to reconstruct images of the total macroscopic inelastic cross-section and scattering length of the materials as well. Therefore, we have three key pieces of information:

- the RSP of the materials
- the scattering length of the materials
- the total macroscopic inelastic cross-section of the materials

Each of these pieces of information is representative in a way of the chemical composition of the materials. Subsequently, the following question arises: once these data obtained, how much knowledge on the composition of materials can be extracted?

In order to define the stoichiometric composition of a material, its mass density ρ and the mass proportions w_i of the i elements involved in its composition need to be determined. This section presents the first step to answer this question. The information gathered will first be reviewed, then discussed.

5.3.3.1 Overview of the information

- Relative stopping power

  The RSP is the ratio of the stopping power of the material to that of water, i.e.:

$$RSP = \frac{S_{mat}}{S_w} = \frac{\frac{4\pi n_{mat}}{m_e c^2 \beta^2}\left(\frac{e^2}{4\pi\epsilon_0}\right)^2\left[\ln\left(\frac{2m_e c^2\beta^2}{I_{mat}(1-\beta^2)}\right)-\beta^2\right]}{\frac{4\pi n_w}{m_e c^2 \beta^2}\left(\frac{e^2}{4\pi\epsilon_0}\right)^2\left[\ln\left(\frac{2m_e c^2\beta^2}{I_w(1-\beta^2)}\right)-\beta^2\right]} \tag{5.13}$$

  with n_{mat} the density of electrons in the material of density ρ and i components of mass proportions w_i, that can be expressed as:

$$n_{mat} = \rho_{mat}\sum_i w_i \frac{\mathcal{N}_A \cdot Z_i}{A_i \cdot \mathcal{M}_u} \tag{5.14}$$

  where Z and A are the elements atomic and mass numbers, $\mathcal{N}_A$ is the Avogadro number and $\mathcal{M}_u$ the molar mass constant.

Let us make the approximation that the material presents the ionization potential of water. This makes it possible to simplify equation 5.13 to:

$$RSP \simeq \frac{n_{mat}}{n_w} \tag{5.15}$$

which we can re-write as:

$$RSP \simeq \frac{1}{n_w} \cdot \frac{\mathcal{N}_A}{\mathcal{M}_u} \rho_{mat} \sum_i w_i \frac{Z_i}{A_i} \tag{5.16}$$

where n_w can be calculated, $\mathcal{N}_A/\mathcal{M}_u$ is known and $\mathcal{F}_i = Z_i/A_i$ can be computed for each element i, thus giving:

$$RSP = f_{RSP} \cdot \rho_{mat} \sum_i w_i \cdot \mathcal{F}_i \tag{5.17}$$

where $f_{RSP} = \frac{1}{n_w} \cdot \frac{\mathcal{N}_A}{\mathcal{M}_u}$.

– Inverse scattering length

The inverse scattering length that can be reconstructed using the information on the exit angle of the particles is calculated for a material as:

$$\frac{1}{X_s} = \rho_{mat} \sum_i w_i \left(\alpha \mathcal{N}_A r_e^2 \frac{Z_i^2}{A_i} \left[2 \log \left(33219 \left(A_i Z_i \right)^{-1/3} \right) - 1 \right] \right) \tag{5.18}$$

which can be re-written as:

$$\frac{1}{X_s} = \rho_{mat} \sum_i w_i \cdot \mathcal{G}_i \tag{5.19}$$

where $\mathcal{G}_i$ can be computed and tabulated for each element i.

– Macroscopic nuclear cross-section

The macroscopic nuclear cross-section can be written as:

$$\kappa = \rho_{mat} \sum_i w_i \frac{\mathcal{N}_A}{A_i} \sigma_i \tag{5.20}$$

which can be re-written as:

$$\kappa = \rho_{mat} \sum_i w_i \cdot \mathcal{H}_i \tag{5.21}$$

with $\sigma_i \cdot \mathcal{N}_A/A_i = \mathcal{H}_i$, a function that can be computed for each element for which the cross-section has been measured in the plateau region.

5.3.3.2 Discussion

Putting all three results together, a system of three equations is obtained:

$$\begin{cases} RSP = f_{RSP} \cdot \rho_{mat} \sum_i w_i \cdot \mathcal{F}_i \\ \frac{1}{X_s} = \rho_{mat} \sum_i w_i \cdot \mathcal{G}_i \\ \kappa = \rho_{mat} \sum_i w_i \cdot \mathcal{H}_i \end{cases} \tag{5.22}$$

To this set of equations, an additional constraint can be added on the sum of the mass proportions:

$$\sum_i w_i = 1 \tag{5.23}$$

The element f_{RSP} can be known and $\mathcal{F}_i$, $\mathcal{G}_i$ as well as $\mathcal{H}_i$ can be computed or measured and tabulated. Therefore, the unknowns of the system are ρ_{mat} and w_i for each element i.

A straightforward approach for solving the problem indicates that this system of equations can be solved for a number of elements involved in the composition inferior or equal to three. This method could be used to analyse simple materials such as water or PMMA. For biological tissues composed of Hydrogen, Carbon, Nitrogen, Oxygen, Calcium, ... the system to solve would be greatly under-determined.

A different approach may be not to rely on these information to fully determine the composition of the tissues, but to use them as additional constraints. Indeed, the biological materials of interest are not completely unknown, and *a priori* knowledge is available. What is currently done for treatment planning is to convert X-ray CT images into material compositions [Schneider et al., 1996]. The same kind of procedure could be performed using proton RSP images as a basis. Then, to refine the composition, the additional information on the scattering length and nuclear interaction cross-section could be used.

5.3.3.3 Conclusion

The different data recorded during a pCT scan make it possible to provide additional qualitative information on the materials (Section 5.2). In addition, these pieces of information can be used to reconstruct images of materials properties: inelastic nuclear cross-sections and scattering length (Section 5.3). This quantitative information, in turn, is indicative of the stoichiometric composition of the tissues. However, as three pieces of information are available, for the three quantitative images that can be reconstructed, the direct assessment of the composition of biological tissues will not be possible. Nevertheless, this information may be used as constraints to distinguish materials with close RSP.

Further investigations are required to determine the precision in the measurements of the scattering length and macroscopic cross-sections that can be reached with optimized image reconstruction. The approximation between RSP and electron density in Equation 5.15, as well as the consistency between the differential Molière scattering model and real data may also introduce a bias.

Summary

- Information on the materials is recorded through the scattering and transmission rate of the particles.
- It is possible to reconstruct images using these data.
- Qualitative image reconstructions make it possible to enhance the contrast between regions of similar stopping powers, which may be of use in diagnostics. The cumulative scattering image presents particularly interesting characteristics that could help differentiate tissues.
- These data can be used to reconstruct quantitative images of the inverse scattering length, and of inelastic nuclear cross-sections of protons in the materials.
- While the direct determination of the stoichiometric using all this data is not possible, the information gathered gives indication on the composition that may be used to refine the conversion.

CONCLUSIONS AND PERSPECTIVES

The principle of proton imaging as studied nowadays is to use the information on the energy loss of protons to map the stopping powers of the materials. To be of interest in treatment planning, there is need for a resolution on the relative stopping power less than 1%. The main challenge of proton imaging is to reach satisfactory (≤ 1 mm) spatial resolution. Indeed, as protons scatter in the materials, the individual path of each particle needs to be estimated during the image reconstruction process. Up to now, the most accurate path estimation available consists in computing the most likely path (MLP) of the particle assuming the object has the scattering and energy loss properties of water. This computation is based on the positions and directions of the particles upstream and downstream of the object. Therefore, the most common design of proton scanner consists in (i) a tracking system made of two sets of (at least) two tracker planes and (ii) a calorimeter or range-meter.

This setup gives access to data on the transmission rate and on the scattering of the particles, that are not currently exploited as sources of information on the materials. The main objective of this thesis work was to investigate the potential use of all the information gathered during a proton scan, and to determine whether or not more information on tissue composition could be acquired.

In order to study such a proton imaging system, a Monte Carlo simulation platform using GATE as well as a dedicated image reconstruction platform were set up.

A preliminary one-dimensional study, presented in Section 5.1, has shown that there is information in the scattering and transmission rate of the protons. Moreover, the results indicate that this information can help distinguish materials with close stopping powers. This work allowed to point out that the major drawback to the use of these data is the statistical uncertainty on the measurements of the scattering and transmission rate, which is much higher than that on the measured energy (or residual range). In order to consider a higher statistic in a region of the phantom, tomographic acquisitions of a proton scanner were simulated.

The qualitative reconstruction study presented in Section 5.2 showed that the use of "extra" information can indeed improve the contrast in some regions of close stopping power. The different images, reconstructed by making use of the scattering, cumulative scattering, transmission rate and linear transmission rate of the particles, make it possible to highlight some differences in the composition of tissues. The distinctive characteristics of the reconstructed images, in particular the bright outlines at tissue interfaces in the cumulative scattering image, could bring information of use in terms of diagnostics. While the use of proton imaging as a diagnostic tool is not currently a major research axis, these results could be an incentive to reconsider.

However, the images which present the most interesting visual properties in terms of contrast and detectability of the lesions are also the most difficult to interpret in a quantitative manner, as they are the result of a combination of physical processes. To reach a quantification of the values reconstructed in the image, the physical processes involved were more closely examined in Section 5.3:

- The transmission rate of the particles in a medium is representative of the inelastic nuclear interactions, which depend on the energy of the protons. The approximation that the inelastic nuclear cross-sections of interaction between protons and tissues are in the plateau region is reasonable at the energies considered in proton imaging. Therefore, a reconstruction of the “attenuation coefficient”, in a similar fashion to X-ray tomography, was performed, giving access to a map of the total macroscopic inelastic nuclear cross sections.

- The scattering of charged particles in a medium depends on the scattering properties of the medium and on the energy of the particles. As a result, the information on the scattering of the protons, gathered at the exit of the object that is imaged, is the result of these two properties. To isolate the effect of the scattering properties of the materials, an estimation of the energy loss of the particles is therefore mandatory. This information can be obtained by making use of the reconstructed image of the relative stopping powers. This makes it possible to reconstruct a map of the scattering properties of the materials, represented here by the scattering length.

The results presented in this work constitute a proof of concept that quantitative imaging using the transmission rate and scattering of the protons is possible. In the context of particle beam therapy treatment planning, two possible applications can be foreseen: the first is to directly makes use of these images to include the scattering and nuclear interactions of the beam in analytical treatment plans; the second option is to extract information on the stoichiometric composition of the tissues from the reconstructed images. The results obtained in the last section of this thesis indicate that the gathered information is not sufficient to determine directly the composition of the materials. Nevertheless, the additional pieces of information could be used as constraints, refining the conversion from relative stopping power to stoichiometric composition that would be used for Monte Carlo treatment planning.

The limitations of these two approaches in order to enable more accurate treatment planning will depend on the accuracy of the reconstructed images. Several perspectives to optimize the reconstruction processes can be considered, and are detailed for both transmission and scattering imaging in the following two pages.

Transmission imaging

Though the reconstruction using the transmission rate of the particles is quite straightforward, the accuracy is limited by the statistical uncertainty on the measured rate and by the scattering of the protons. Different solutions towards improved transmission images can be considered:

- Increasing the number of protons studied to more than 1000 protons per square millimetre of projection will not be considered because it would result in a dose higher than that of an X-ray CT scan. However, it may be that increasing the number of particles per projection and decreasing the number of projections could reduce the noise in the image. A compromise between the statistical uncertainty (and therefore noise in the projections) and the effect of fewer projections in terms of image reconstruction may need to be found. Such optimization work can be found in the literature for X-ray CT imaging for example.

- In this work, the image reconstructions of the total macroscopic nuclear cross sections were performed using FBP with the data binned upstream of the object. However, it may be considered that even the protons that were stopped in the object underwent some scattering. While no event-by-event reconstruction can be performed, a projection/back-projection path in the reconstruction algorithm that would take the scattering into account could be considered. Instead of considering a straight line, one could consider a probability of passage of the "beam" defined by the impinging particles from the same projection beam, that would be spread laterally along the propagation according to the scattering. As a first approximation, the medium could be considered to have the scattering properties of water for example. Then, the image reconstruction of the scattering length may also be used to estimate the spread of the particle beam with its propagation.

- The constant interaction cross-section assumption, justified by the plateau in the cross-section values as a function of the energy, is a good approximation for most elements at the energies considered in proton imaging. However, it is less appropriate for heavier elements, such as Calcium, present mostly in the bones. To refine this approximation, a more complex image reconstruction procedure could be considered. The areas of bone can be segmented, from an image of the relative stopping power for example, and the quantity of "heavier" elements can be estimated. The image of the relative stopping power could then be used to compute the average energy of the particles considered and an energy-dependent correction could be applied.

- Post-processing techniques could be of use to reduce the level of noise in the image and gather more representative values.

Scattering imaging

The reconstructed images of the inverse scattering length of the materials also suffer from the statistical uncertainty and scattering of the particles (the reconstructions assuming a straight line path). The following axes for improvement of the reconstructed images can be put forward:

- Considering the statistical uncertainty on the variance of the measured angular distribution, a re-arrangement of the number of particles per projections and number of projections might reduce this effect.

- Event-by-event path estimation and image reconstruction is possible when considering scattering imaging. Following a reconstruction approach that takes into account the MLP could be advantageous in terms of spatial resolution, as it does in the case of image reconstruction of the relative stopping power.
  In a totally different application, event-by-event reconstruction of the information on scattering is performed in the context of muon imaging. Muon imaging is considered in applications aiming at detecting materials with high atomic numbers: for homeland security, to detect uranium in containers or to image nuclear reactors [Perry, 2013]. A muon imaging device consists in two sets of multiple tracker planes on two sides of the object. Through the information on the scattering of cosmic muons, images of the “scattering density” of materials (proportional to the inverse of the radiation length for a nominal muon energy) are reconstructed. Schultz et al. [2007] have shown that a maximum likelihood-based image reconstruction algorithm could be used on this data. The difference of energy between the impinging muons is taken into account by the ratio of the nominal muon energy to the effective muon energy, estimated using the scattering of the particle inside a tracking plane. As the stopping power of cosmic muons in materials is at least ten times less than that of protons (for an average energy of cosmic muons of 4 GeV at the surface of the Earth), the energy loss inside the materials can be neglected in the case of muon imaging. This can not be the case for proton imaging.
  However, the methodology proposed in the last chapter makes it possible to overcome this problem by estimating the energy of the particles by using the relative stopping power. Therefore, a maximum likelihood - expectation maximization type algorithm for event-by-event reconstruction of the scattering length on the MLP could be considered.

While the image reconstructions of the different physical processes were performed in a separate way, a paragon of image reconstruction algorithm for proton tomography would be multi-parametric, in order to make use of all the information at the same time. A statistical algorithm which aim would be to maximize the likelihood of detecting a given set of:

$$\{\text{water equivalent path length, transmission rate, scattering}\}$$

for each particle or group of particles can be foreseen as a good candidate.

It can be highlighted that such perspectives are not unique to proton imaging and the same studies could be performed for carbon imaging for example. In a really similar fashion to proton imaging, carbon imaging makes it possible to reconstruct the relative stopping power of carbon ions in the tissues by using the information on the energy loss of carbon ions. The scattering of carbon ions in matter is less important than that of protons. This is a definite advantage in terms of simplicity for path approximation in reconstruction of the relative scattering power. However, it may be possible to record the scattering of the particles anyway and investigate the potential of using this information as well as the information on the transmission rate of carbon ions.

The work described in this thesis was performed on the basis of Monte Carlo simulations. Therefore, in addition to the optimization of the reconstruction process using the different information, validation on experimental data is necessary before drawing a conclusion on the practical potential of this approach.

In clinical conditions, two additional factors need to be considered: the beam characteristics and the detector characteristics. The beam properties in terms of energy spread and spatial and angular distribution will have an impact on the results. Initial spread of the beam energy will mostly impact the reconstructed image of the relative stopping power, which was not the main focus of this work. The spatial and angular spread of the beam however, will impact the accuracy of the path approximation in the reconstruction algorithm when using the data binned into projections, as was done in this work for the scattering and transmission rate images. An event-by-event image reconstruction, at least for the scattering of the protons, may reduce this impact.
The characteristics of the tracking system will play an essential role in the potential for imaging using the transmission rate and scattering of the particles. As far as the transmission imaging is concerned, the detection efficiency of the tracking system will be essential, inasmuch as an additional uncertainty can be expected if not all the protons are detected.
The effect of the tracking system properties, i.e. spatial resolution, material budget and positioning, on the trajectory estimation using the MLP was evaluated in section 4.3. This study presents the analytical propagation of the uncertainty due to the tracking system in the MLP. However, as this uncertainty concerns the estimation of the positions and directions of the protons, the tracking system will have a great impact on the scattering imaging as well. Should enough interest in the scattering imaging be found to impact the choice of detector, tracker planes with a pixel pitch less than that of the current prototypes might be preferred.

The requirements of a proton system in terms of particle rate to detect is also representative of the instrumental challenges of a proton tomography system. While it does not impact the quality of the reconstructed images, it is of key importance before a proton tomograph can be set up and used in clinical routine. The prototype with the fastest acquisition rate currently reaches a rate of 2 MHz (Section 2.3.2.1). The requirements sheet for a proton tomograph put forward by Schulte et al. [2004] (Table 2.1) indicates the aim of a scan time of 5 minutes. Sadrozinski et al. [2011] indicate that for a satisfying resolution on the reconstructed relative stopping power, the ratio between the number of protons used in the image reconstruction process and the number of voxels in the image should be of 100. This is consistent with all the works in the literature. Considering an average of 20% loss of particles due to nuclear interaction, this results in the need for a ratio of 125. Let us now consider the image of a head, of dimensions 300×300×200 mm^3 with 1×1×1 mm^3 voxels. This is slightly smaller than the images reconstructed during this work, but would be sufficient for the image of a head. The resulting acquisition rate is about 7.5 MHz.

This requirement needs to be considered along with the accelerator beam structure. The cyclotron of the proton therapy facility in Orsay is a IBA Proteus 235. The isochronous cyclotron beam is a continuous beam on a macroscopic scale, but consists in 3.2 ns bunches of particles every 9.37 ns [Richard, 2012]. This does not in itself challenge the detectors in terms of particle rate. The new synchrocyclotron of the proton therapy facility in Nice is the IBA S2C2, which presents a beam structure of 50 µs-bunches every 1 ms [Conjat et al., 2013]. Therefore, to reach an average particle rate of 7.5 MHz, the particle rate to detect during a bunch is about 150 MHz.

The current prototypes are either limited because of the residual energy/range measurement [Johnson et al., 2013] or the tracking system [Bucciantonio et al., 2013].

It may be further considered that the average rate of 7.5 MHz corresponds to a beam intensity of 1.2 pA. It can be found in the literature concerning medical cyclotrons that the lower limit for stable beam current is of 0.1 nA [Olko and Jezabek, 2012; Denker et al., 2012]. Indeed, in the context of treatment, intensities of the order of the nA or tens of nA are more of interest. Should an intensity of 0.1 nA be considered for imaging purposes, the required detector rate would be more than 600 MHz (though the acquisition would last less than 4 seconds). Therefore, to reach such a low intensity, the beam line will need to be adapted, with the insertion of collimators or pepper pots for example.

Handling such particle rates remains an instrumental challenge nevertheless, and fast plastic scintillator range-meters will probably be preferred to crystal calorimeters in the next generations of prototypes. In this line of thought, encouraging first results of a new prototype were very recently published by Lo Presti et al. [2014]. The proposed system is exclusively based in scintillating fibers, for both the tracking system and the residual range detector, and should be able to handle a particle rate up to 10 MHz.

Proton imaging is a rather exceptional modality, in the sense that each particle undergoes a long series of physical interactions, and each interaction is a source of information on the materials encountered. This generates great challenges, for example in terms of data management, image reconstruction and analysis, but it also allows for a great wealth in terms of information gathered during a scan. In light of the results presented in this work, the use of the scattering and transmission rate of the particles to obtain qualitative and hopefully quantitative information could be of interest in diagnostics. The images produced using the cumulative scattering, in particular, make it possible to distinguish the interfaces between the tissues, here the lesions in the brain, in a very distinctive way.

In the context of particle beam therapy, two applications of proton imaging have been put forward. One is portal imaging, to verify patient positioning with radiography or use the proton beam as a range probe, to validate the treatment planning just before the irradiation. The other is the use of proton tomography as a basis for treatment planning. For analytical treatment planning, proton computed tomography for imaging the relative stopping power of the materials will help reduce the range uncertainty. In addition, the quantitative information obtained through the reconstructed images using the scattering and the transmission rate could help improve the accuracy in terms of dose deposit of the treatment plan. However, the space taken by Monte Carlo treatment planning is more and more important, and the reduction of computation time using graphical processing units will probably increase this trend. For Monte Carlo treatment planning, the images of the relative stopping power will bring an information on one property of the materials, just like X-ray CT imaging. The conversion from this value to stoichiometric composition will still be required. Where proton imaging presents an advantage over X-ray imaging is that the relative stopping power is not the only information that can be exploited from a tomographic acquisition. The last section of this thesis (Section 5.3.3) presents the first step towards the use of these information to characterize the stoichiometric composition of the tissues. While the direct use of these data will not provide enough knowledge to fully characterize a tissue, the additional constraints provided by the image reconstructions of the inverse scattering length and macroscopic inelastic nuclear cross-section could very well be used to reduce the uncertainty on the decomposition in elements from the relative stopping power value alone. This, in turn, could help improve the accuracy of the conversion to material composition, and therefore of the treatment plan, both in terms of range and dose deposit predictions. Further work on this topic should explore the limits of the multi-parametric approach to image reconstruction presented in this work. The greatest challenge may be to reach a satisfactory accuracy on the data obtained from the transmission and scattering despite the statistical uncertainty on the measures. An increase in the number of particles studied by a factor 10 would be welcome in order to do so. Therefore, a full study on the potential improvement of treatment planning accuracy will be needed before determining if additional instrumental developments would be worthwhile.

Appendix A

Materials and properties

The materials used in the Monte Carlo studies were taken from different sources: Woodard and White [1986]; Maughan et al. [1997]; Batin [2008]; Opengate collaboration [n.d.].

Table A.1 (on the next page) shows the compositions and properties of the materials used. The letters in the last column designates the phantom(s) in which the materials were used: (F) for the Forbild phantom, (Z) for the Zubal phantom. All materials were tested for the preliminary study on the cube presented in Section 5.1.

Table A.1: Materials used in the Monte Carlo simulations.

Material	ρ (g/cm^3)	Mass proportion of elements (%)													RSP (I$_{\text{water}}$=75 eV)	I (eV)	X$_0$ (cm)	X$_S$ (cm)	Phantom
		H	C	N	O	Na	Mg	P	S	Cl	Ar	K	Ca	Fe					
Adipose tissue	0.95	11.4	59.8	0.7	27.8	0.1	-	-	0.1	0.1	-	-	-	-	0.94	80.82	43.40	58.18	(Z)
Air	0.0012	-	0.01	75.5	23.2	-	-	-	-	-	1.3	-	-	-	0.00	85.62	283.9	$> 10^3$	(Z)(F)
Blood	1.06	10.2	11.0	3.3	74.5	0.1	-	0.1	0.2	0.3	-	0.2	-	0.1	1.06	71.28	34.50	45.00	(Z)
Brain	1.04	10.7	14.5	2.2	71.2	0.2	-	0.4	0.2	0.3	-	0.3	-	-	1.04	70.21	35.41	46.14	(Z)(F)
Brain grey matter	1.04	10.7	9.5	1.8	76.7	0.2	-	0.3	0.2	0.3	-	0.3	-	-	1.04	70.85	35.04	45.58	(Z)
Brain white matter	1.04	10.6	19.4	2.5	66.1	0.2	-	0.4	0.2	0.3	-	0.3	-	-	1.04	69.72	35.78	46.73	(Z)
Carcinoma	1.00	10.0	18.5	4.2	65.9	0.2	-	0.3	0.4	0.2	-	0.3	-	-	1.00	70.69	37.08	48.34	(Z)
Carcinoma -10%	1.00	10.0	29.4	4.2	55.0	0.2	-	0.3	0.4	0.2	-	0.3	-	-	1.00	69.21	37.96	49.76	
Carcinoma -20%	1.00	10.0	39.4	4.2	45.0	0.2	-	0.3	0.4	0.2	-	0.3	-	-	1.00	68.06	38.81	51.13	
Carcinoma -30%	1.00	10.0	49.4	4.2	35.0	0.2	-	0.3	0.4	0.2	-	0.3	-	-	1.00	66.83	39.71	52.59	(Z)
Cerebellum	1.04	9.3	11.1	2.2	76.6	0.3	0.2	-	-	0.4	-	-	-	-	1.03	72.96	35.03	45.50	(Z)
Cerebral fluid	1.01	11.1	-	-	88.0	0.5	-	-	-	0.4	-	-	-	-	1.01	71.36	35.56	46.13	(Z)
Connective tissue	1.12	9.5	20.7	6.2	62.2	0.6	-	-	0.6	0.3	-	-	-	-	1.11	71.22	33.30	43.42	(Z)
C4 without cartilage	1.42	6.3	26.1	3.9	43.6	0.1	0.1	6.1	0.3	0.1	-	0.1	13.3	-	1.33	85.86	21.79	27.30	(Z)
Eye lens	1.07	9.6	19.5	5.7	64.6	0.1	-	0.1	0.3	0.1	-	-	-	-	1.06	70.79	34.95	45.62	(Z)(F)
Skeletal muscle	1.05	10.2	14.3	3.4	71.0	0.1	-	0.2	0.3	0.1	-	0.4	-	-	1.05	70.87	35.06	45.66	(Z)
Skeleton-Cartilage	1.10	9.6	9.9	2.2	74.4	0.5	-	2.2	0.9	0.3	-	-	-	-	1.09	73.62	32.49	42.00	(Z)
Skin	1.09	10.0	20.4	4.2	64.5	0.2	-	0.1	0.2	0.3	-	0.1	-	-	1.09	70.24	34.31	44.82	(Z)
Skull	1.61	5.0	21.1	4.0	43.5	0.1	0.2	8.1	0.3	-	-	-	17.6	-	1.48	93.31	18.00	22.29	(Z)(F)
Turbinates	0.35	4.7	14.4	4.2	44.6	-	0.2	10.5	0.3	-	-	-	21.0	-	0.32	98.71	78.33	96.19	(Z)
Water	1.00	11.2	-	-	88.8	-	-	-	-	-	-	-	-	-	0.99	80.82	35.20	46.89	(Z)(F)

APPENDIX B

DIFFERENTIAL APPROXIMATIONS TO MULTIPLE COULOMB SCATTERING

Brief overview of the scattering approximations found in [Gottschalk, 2009]:

Fermi-Rossi approximation (local)

$$T_{FR} = \left(\frac{E_s}{pv}\right)^2 \frac{1}{X_0} \tag{B.1}$$

with X_0 the radiation length of the material (detailed in Section 2.1.2), pv the product of the particles speed and momentum and:

$$E_s = \left(\frac{2\pi}{\alpha}\right)^{1/2} m_e c^2 = 15\ \text{MeV} \tag{B.2}$$

ICRU report 35 (local)

$$T_{IC} = \left(\frac{E_s}{pv}\right)^2 \frac{1}{X_S} \tag{B.3}$$

where, at the difference of the previous expression, X_S represents the scattering length of the material. The scattering length for an element is defined as:

$$\frac{1}{\rho X_S} \equiv \alpha \mathcal{N}_A r_e^2 \frac{Z^2}{A} \left[2 \log\left(33219\,(AZ)^{-1/3}\right) - 1\right] \tag{B.4}$$

with $\mathcal{N}_A$ Avogadro's number and Z, A and ρ the atomic number, weight and density of the target material. For compounds or mixtures, a Bragg rule can be applied as for the radiation length, leading to:

$$\frac{1}{\rho X_S} = \sum_i w_i \left(\frac{1}{\rho X_S}\right)_i \tag{B.5}$$

Linear displacement (local)

$$T_{LD} = 10^{-3} \cdot \frac{\rho_x}{R_{\text{water}}} \tag{B.6}$$

where

$$\rho_x = \frac{X_{0_{\text{material}}}}{X_{0_{\text{water}}}} \tag{B.7}$$

and R_{water} is the proton's residual range in water.

Øversås and Schneider (non-local)

$$T_{ØS} = \left(\frac{19.9 \text{ MeV}}{p_1 v_1}\right)^2 \frac{1}{X_0} (1-t)^{-(1+k)} \left[c_0 + c_1 \left(t - \frac{1}{2}\right)^4 + \frac{4c_1}{k}\left(t - \frac{1}{2}\right)^3 (1-t)\left(1-(1-t)^k\right)\right] \tag{B.8}$$

with $p_1 v_1$ the product of the particles initial speed and momentum, c_0 and c_1 such as:

$$c_0 = \tfrac{201}{200} - \tfrac{23}{5000}\rho X_0 \tag{B.9}$$

$$c_1 = -\tfrac{11}{2} + \tfrac{43}{1000}\rho X_0 \tag{B.10}$$

with ρX_0 the mass radiation length of the current material and

$$t\,(x) \equiv \frac{x}{R\,(E_1, M\,(x))} \tag{B.11}$$

where E_1 is the particles initial energy and $M(x)$ the current material.

Differential Highland (non-local)

$$T_{dH} = f_{dH}\,(l)\left(\frac{E_s}{pv}\right)^2 \frac{1}{X_0} \tag{B.12}$$

with the non-local correction factor:

$$f_{dH} = 0.97\left(1 + \frac{\ln l}{20.7}\right)\left(1 + \frac{\ln l}{22.7}\right) \tag{B.13}$$

and using l, defined as the radiative path length:

$$l\,(x) \equiv \int_0^x \frac{dx'}{X_0\,(x')} \tag{B.14}$$

Differential Molière (non-local)

$$T_{dM} = f_{dM}\left(pv, p_1 v_1\right)\left(\frac{E_s}{pv}\right)^2 \frac{1}{X_S} \tag{B.15}$$

where

$$\begin{aligned} f_{dM} \equiv 0.5244 + 0.1975 \log\left(1 - \left(\frac{pv}{p_1 v_1}\right)^2\right) + 0.2320 \log\left(pv\right) \\ - 0.0098 \log\left(pv\right) \log\left(1 - \left(\frac{pv}{p_1 v_1}\right)^2\right) \end{aligned} \tag{B.16}$$

BIBLIOGRAPHY

Abdoli, M., Dierckx, R. a. J. O. and Zaidi, H. [2012], 'Metal artifact reduction strategies for improved attenuation correction in hybrid PET/CT imaging.', *Medical physics* **39**(6), 3343–60. 29

Agostinelli, S., Allison, J. and Amako, K. [2003], 'GEANT4 - a simulation toolkit', *Nuclear Instruments and Methods in Physics Research Section A: Accelerators, Spectrometers, Detectors and Associated Equipment* **506**(3), 250–303. xiii, 57

Albertini, F., Hug, E. B. and Lomax, a. J. [2011], 'Is it necessary to plan with safety margins for actively scanned proton therapy?', *Physics in medicine and biology* **56**(14), 4399–413. 29

Alvarez, R. E. and Macovski, a. [1976], 'Energy-selective reconstructions in X-ray computerized tomography.', *Physics in medicine and biology* **21**(5), 733–44. 30

Amaldi, U., Bianchi, A., Chang, Y.-H., Go, A., Hajdas, W., Malakhov, N., Samarati, J., Sauli, F. and Watts, D. [2011], 'Construction, test and operation of a proton range radiography system', *Nuclear Instruments and Methods in Physics Research Section A: Accelerators, Spectrometers, Detectors and Associated Equipment* **629**(1), 337–344. xii, 48, 49, 51, 52, 98, 102

Amaldi, U., Hajdas, W., Iliescu, S., Malakhov, N., Samarati, J., Sauli, F. and Watts, D. [2010], 'Advanced Quality Assurance for CNAO', *Nuclear Instruments and Methods in Physics Research Section A: Accelerators, Spectrometers, Detectors and Associated Equipment* **617**(1-3), 248–249. 25

Amaldi, U. and Kraft, G. [2006], 'Particle accelerators take up the fight against cancer', *CERN Courier* **18**(1). 2

ARCHADE [n.d.], 'Advanced ressource centre for hadrontherapy in europe'.
URL: *archade.fr* ix, 2

Aso, T., Kawashima, K., Nishio, T., Lee, S. B. and Sasaki, T. [2012], 'A study on multiplex proton imaging using GEANT4', *2012 IEEE Nuclear Science Symposium and Medical Imaging Conference Record (NSS/MIC)* pp. 1717–1719. 52, 57

Barendsen, G., Walter, H., Fowler, J. F. and Bewley, D. K. [1963], 'Effects of different ionizing radiations on human cells in tissue culture: III. Experiments with cyclotron-accelerated alpha-particles and deuterons', *Radiation research* **19**(1), 106–119. 13

Barquero, H. and Brasse, D. [2012], 'Limited angle geometries applied to small animal X-ray imaging', *2012 IEEE Nuclear Science Symposium and Medical Imaging Conference Record (NSS/MIC)* pp. 3635–3640. 75, 84

Bassler, N., Jäkel, O., Sø ndergaard, C. S. and Petersen, J. r. B. [2010], 'Dose- and LET-painting with particle therapy.', *Acta oncologica (Stockholm, Sweden)* **49**(7), 1170–6. 28

Batin, E. [2008], Influence de la composition chimique des tissus humains sur les dépôts de dose en hadronthérapie, PhD thesis. x, 147

Beer, A. [1852], 'Bestimmung der Absorptioin des rothen Lichts in farbigen Glussigkeiten', *Annalen der Physik und Chemie* . 7

Bennett, G., Archambeau, J., Archambeau, B., Meltzer, J. and Wingate, C. [1978], 'Visualization and transport of positron emission from proton activation in vivo', *Science* **200**(June), 1–3. 24

Berger, J. and Duchazeaubeneix, J. [1978], 'Nuclear scattering radiography of the spine and sphenoid bone', *Journal of computer assisted tomography* **2**, 488–498. xi, 42

Besemer, A., Paganetti, H. and Bednarz, B. [2013], 'The clinical impact of uncertainties in the mean excitation energy of human tissues during proton therapy.', *Physics in medicine and biology* **58**(4), 887–902. 36

Bethe, H. [1930], 'Zur theorie des durchgangs schneller korpuskularstrahlen durch materie', *Annalen der Physik* **397**(3), 325–400. 34

Bethe, H. [1953], 'Moliere's theory of multiple scattering', *Physical Review* **634**. 37

Bloch, F. [1933], 'Zur Bremsung rasch bewegter Teilchen beim Durchgang durch Materie', *Annalen der Physik* **408**(3). 34

Bohr, N. [1948], *The Penetration of Atomic Particles Through Matter*, munksgaard edn, Copenhagen. 36

Bom, V., Joulaeizadeh, L. and Beekman, F. [2012], 'Real-time prompt γ monitoring in spot-scanning proton therapy using imaging through a knife-edge-shaped slit.', *Physics in medicine and biology* **57**(2), 297–308. 25

Brard, E. [2013], La tomographie à émission de positrons à géométrie axiale : de l'imagerie de la souris au cerveau humain, PhD thesis. 60

Bravin, A., Coan, P. and Suortti, P. [2013], 'X-ray phase-contrast imaging: from pre-clinical applications towards clinics.', *Physics in medicine and biology* **58**(1), R1–35. 31

Bucciantonio, M., Amaldi, U. and Kieffer, R. [2013], 'Development of a fast proton range radiography system for quality assurance in hadrontherapy', *Nuclear Instruments and methods A* pp. 1–4. 49, 144

Butts, J. J. and Katz, R. [1967], 'Theory of RBE for heavy ion bombardment of dry enzymes and viruses.', *Radiation research* **30**(4), 855–71. 9

Carabe, A., Moteabbed, M., Depauw, N., Schuemann, J. and Paganetti, H. [2012], 'Range uncertainty in proton therapy due to variable biological effectiveness.', *Physics in medicine and biology* **57**(5), 1159–72. 21

Censor, Y., Elfving, T., Herman, G. and Nikazad, T. [2008], 'On diagonally relaxed orthogonal projection methods', *SIAM Journal on Scientific Computing* pp. 1–40. 75

Charpak, G., Guillerminet, B., Leopold, M., Melchart, G., Odyniec, G., Perrin, Y. and Sauli, F. [1979], 'Progress in Nuclear Scattering Radiography', *IEEE Transactions on Nuclear Science* **26**(1), 654–657. xi, 42

Charpak, G., Majewski, S., Perrin, Y., Saudinos, J., Sauli, F., Towensend, D. and Vinciarelli, J. [1976], 'Further results in nuclear scattering radiography.', *Physics in medicine and biology* **21**(6), 941–8. xi, 42

Chen, W., Unkelbach, J., Trofimov, A., Madden, T., Kooy, H., Bortfeld, T. and Craft, D. [2012], 'Including robustness in multi-criteria optimization for intensity-modulated proton therapy.', *Physics in medicine and biology* **57**(3), 591–608. 29

Chvetsov, A. V. and Paige, S. L. [2010], 'The influence of CT image noise on proton range calculation in radiotherapy planning.', *Physics in medicine and biology* **55**(6), N141–9. x, 21

Cirrone, G., Bucciolini, M., Bruzzi, M., Candiano, G., Civinini, C., Cuttone, G., Guarino, P., Lo Presti, D., Mazzaglia, S., Pallotta, S., Randazzo, N., Sipala, V., Stancampiano, C. and Talamonti, C. [2011], 'Monte Carlo evaluation of the Filtered Back Projection method for image reconstruction in proton computed tomography', *Nuclear Instruments and Methods in Physics Research Section A: Accelerators, Spectrometers, Detectors and Associated Equipment* **658**(1), 78–83. 51, 84, 125

Cirrone, G., Cuttone, G., Candiano, G., Rosa, F. D., Nigro, S. L., Presti, D. L., Randazzo, N., Sipala, V., Bruzzi, M., Menichelli, D., Scaringella, M., Bashkirov, V., DavidWilliams, R., Sadrozinski, H. F.-W., Heimann, J., Feldt, J., Blumenkrantz, N., Talamonti, C. and Schulte, R. W. [2007], 'Monte Carlo studies of a proton computed tomography system', *IEEE Transactions on Nuclear Science* **54**(5), 1487–1491. 57

Civinini, C., B.-M. B. M. B. M. C. M. C. G. a. P. C. G. L. D., Pallotta, S., Pugliatti, C., Randazzo, N., Romano, F., S.-M., Sipala, V., Stancampiano, C., Talamonti, C., Tesi, M. and Vanzi, E., Z.-M. [2012], 'Development of a Proton Computed Tomography system for pre-clinical tests', *2012 IEEE Nuclear Science Symposium and Medical Imaging Conference Record (NSS/MIC)* pp. 1279–1283. 93

Civinini, C., Bruzzi, M., Bucciolini, M., Carpinelli, M., Cirrone, G., Cuttone, G., Lo Presti, D., Pallotta, S., Pugliatti, C., Randazzo, N., Romano, F., Scaringella, M., Sipala, V., Stancampiano, C., Talamonti, C., Vanzi, E. and Zani, M. [2013], 'Recent results on the development of a proton computed tomography system', *Nuclear Instruments and Methods in Physics Research Section A: Accelerators, Spectrometers, Detectors and Associated Equipment* **732**, 573–576. xii, 48, 49

Conjat, M., Mandrillon, P. and Mandrillon, J. [2013], 'The future protontherapy facility of the Centre Antoine Lacassagne'.
URL: *https://indico.in2p3.fr/getFile.py/access?sessionId=5&resId=0&materialId=0&confId=8162* xviii, 144

Cookson, J. [1974], 'Radiography with protons', *Naturwissenschaften* **194**. 43

Cookson, J. A., Armitage, B. H. and Ferguson, A. T. G. [1972], 'Proton radiography', *Non-destructive testing* (August), 225–228. 39

Cormack, a. M. [1963], 'Representation of a Function by Its Line Integrals, with Some Radiological Applications', *Journal of Applied Physics* **34**(9), 2722. xi, 39

Cormack, a. M. [1964], 'Representation of a Function by Its Line Integrals, with Some Radiological Applications. II', *Journal of Applied Physics* **35**(10), 2908. xi, 39

Cormack, A. M. and Koehler, a. M. [1976], 'Quantitative proton tomography: preliminary experiments.', *Physics in medicine and biology* **21**(4), 560–9. xi, 39

Coutrakon, G., Blazey, G., Boi, S., Dychkant, A., Erdelyi, B., Gearhart, A., Hedin, D., Rykalin, V., Uzunyan, S., Zutshi, V., Krider, J., Sellberg, G., Rauch, J. E., Roman, M., Rubinov, P., Wilson, P. and National, F. [2013], 'A new proton CT detector', *proceedings AccApp* . 52, 102

Crowe, K. M., Budiriger, T. F., Cahoon, J. L., Elischer, V. P., Huesman, R. H. and Kanstein, L. L. [1975], 'Axial scanning with 900 MeV alpha partivles', *IEEE Transactions on Nuclear Science* **22**(3), 1752–1754. 39

Cuttone, G., Cirrone, G., Candiano, G., Di Rosa, F., Russo, G., Randazzo, N., Sipala, V., Lo Nigro, S., Lo Presti, D., Feldt, J., Heimann, J., Sadrozinski, H.-W., Seiden, A., Williams, D., Bashkirov, V., Schulte, R. W., Bruzzi, M., Menichelli, D. and Scaringella, M. [2005], 'Detailed Monte Carlo Investigation of a Proton Computed Tomography System', *IEEE Nuclear Science Symposium Conference Record, 2005* **5**, 2873–2875. 112

Dale, R. G., Jones, B. and Cárabe-Fernández, a. [2009], 'Why more needs to be known about RBE effects in modern radiotherapy.', *Applied radiation and isotopes : including data, instrumentation and methods for use in agriculture, industry and medicine* **67**(3), 387–92. 12, 14, 26

Defrise, M., Vanhove, C. and Liu, X. [2011], 'An algorithm for total variation regularization in high-dimensional linear problems', *Inverse Problems* **27**(6), 065002. 75

Denker, A., Bundesmann, J. and Damerow, T. [2012], 'Status of the HZB cyclotron', *accelconf.web.cern.ch* pp. 31–33. 144

Denyak, V., Paschuk, S., Schelin, H. R., Rocha, R., Setti, J., Klock, M., Evseev, I. and Yevseyeva, O. [2011], 'Dose energy dependence in proton imaging', *Nuclear Instruments and Methods in Physics Research Section A: Accelerators, Spectrometers, Detectors and Associated Equipment* **652**(1), 747–750. 52

Duchazeaubeneix, J., Faivre, J., Garreta, D., Guillerminet, B., Rouger, M., Saudinos, J., Palmieri, C., Raybaud, C., Salamon, G., Charpak, G., Melchart, G., Perrin, Y., Santiard, J. and Sauli, F. [1980], 'Nuclear Scattering Radiography', *journal of computer assisted tomogrpahy* . 42

Dudouet, J., Juliani, D., Labalme, M., Cussol, D., Angélique, J. C., Braunn, B., Colin, J., Finck, C., Fontbonne, J. M., Guérin, H., Henriquet, P., Krimmer, J., Rousseau, M., Saint-Laurent, M. G. and Salvador, S. [2013], 'Double-differential fragmentation cross-section measurements of 95 MeV/nucleon ^{12}C beams on thin targets for hadron therapy', *Physical Review C* **88**(2), 024606. 38

Eekers, D. [2014], 'The maastricht protontherapy project: Zon-ptc'.
URL: *bhtc.sckcen.be/~/media/Files/Bhtc/Documents /Eekers_The Maastro Protontherapy Project.pdf* 16

Efstathiou, J. a., Gray, P. J. and Zietman, a. L. [2013], 'Proton beam therapy and localised prostate cancer: current status and controversies.', *British journal of cancer* **108**(6), 1225–30. 7, 14, 15

Enghardt, W., C. P. F. F. H. R. P. K. P. J. P. F. [2004*a*], 'Charged hadron tumour therapy monitoring by means of PET', *Nuclear Instruments and Methods in Physics Research Section A: Accelerators, Spectrometers, Detectors and Associated Equipment* **525**(1-2), 284–288. 24

Enghardt, W., P. K. C. P. F. F. P. J. P. F. [2004*b*], 'Dose quantification from in-beam positron emission tomography', *Radiotherapy and Oncology* **73**, S96–98. 24

Erdelyi, B. [2009], 'A comprehensive study of the most likely path formalism for proton-computed tomography.', *Physics in Medicine and Biology* **54**(20), 6095–122. 102

Erdelyi, B. [2010], 'Electron density uncertainties in proton computed tomography.', *Physics in medicine and biology* **55**(23), 7121–34. xii, 52

España, S. and Paganetti, H. [2011], 'Uncertainties in planned dose due to the limited voxel size of the planning CT when treating lung tumors with proton therapy.', *Physics in medicine and biology* **56**(13), 3843–56. x, 21

ETOILE [n.d.], 'Centre ETOILE'.
URL: *centre-etoile.org* ix, 2

Feldkamp, L., Davis, L. and Kress, J. [1984], 'Practical cone-beam algorithm', *JOSA A* **1**(6), 612–619. 83

Fessler, J. [2009], Analytical tomographic image reconstruction methods, *in* 'Image Reconstruction: Algorithms and Analysis'. 66, 67

Fidorra, J. and Linden, W. a. [1977], 'Radiosensitivity and recovery of mouse L cells during the cell cycle.', *Radiation and environmental biophysics* **14**(4), 285–94. 13

Fokas, E., Kraft, G., An, H. and Engenhart-Cabillic, R. [2009], 'Ion beam radiobiology and cancer: time to update ourselves.', *Biochimica et biophysica acta* **1796**(2), 216–29. 9, 10, 11

Fournier, C. and Taucher-Scholz, G. [2004], 'Radiation induced cell cycle arrest: an overview of specific effects following high-LET exposure', *Radiotherapy and Oncology* **73**(supplement 2), 119–122. 13

Geant4 website [n.d.].
URL: *geant4.cern.ch* 57

Gearhart, A., Johnson, E., Medvedev, V., Ronzhin, A. and Rykalin, V. [2012], 'Silicon Photomultiplier Choice for the Scintillating Fiber Tracker in Second Generation Proton Computed Tomography Scanner', pp. 1–14. xii, 48

Gensheimer, M. F., Yock, T. I., Liebsch, N. J., Sharp, G. C., Paganetti, H., Madan, N., Grant, P. E. and Bortfeld, T. [2010], 'In vivo proton beam range verification using spine MRI changes.', *International journal of radiation oncology, biology, physics* **78**(1), 268–75. 25

Giantsoudi, D., Grassberger, C., Craft, D., Niemierko, A., Trofimov, A. and Paganetti, H. [2013], 'Linear energy transfer-guided optimization in intensity modulated proton therapy: feasibility study and clinical potential.', *International journal of radiation oncology, biology, physics* **87**(1), 216–22. 28

Giersch, J., Firsching, M., Niederlöhner, D. and Anton, G. [2005], 'Material reconstruction with spectroscopic pixel X-ray detectors', *Nuclear Instruments and Methods in Physics Research Section A: Accelerators, Spectrometers, Detectors and Associated Equipment* **546**(1-2), 125–130. 31

Glimelius, B. and Montelius, A. [2007], 'Proton beam therapy - do we need the randomised trials and can we do them?', *Radiotherapy and oncology : journal of the European Society for Therapeutic Radiology and Oncology* **83**(2), 105–9. 15

Glynn, P. and Heidelberger, P. [1991], 'Analysis of parallel, replicated simulations under a completion time constraint', *ACM Transactions on Modeling and Computer Simulation* **1**(1), 3–23. 60

Goitein, M. [1972], 'Three-dimensional density reconstruction from a series of two-dimensional projections', *Nuclear Instruments and Methods* pp. 509–518. 39

Goitein, M. [2010], 'Trials and tribulations in charged particle radiotherapy.', *Radiotherapy and oncology : journal of the European Society for Therapeutic Radiology and Oncology* **95**(1), 23–31. 6, 14, 15

Goitein, M. and Cox, J. D. [2008], 'Should randomized clinical trials be required for proton radiotherapy?', *Journal of clinical oncology : official journal of the American Society of Clinical Oncology* **26**(2), 175–6. 15

Goitein, M. and Jermann, M. [2003], 'The Relative Costs of Proton and X-ray Radiation Therapy', *Clinical Oncology* **15**(1), S37–S50. 16

Gordon, R. [1974], 'A tutorial on ART', *IEEE Transactions on Nuclear Science* **21**. 67

Gottschalk, B. [2009], 'On the scattering power of radiotherapy protons', *Medical Physics* **37**(1), 352–367. 37, 129, 130, 149

Gottschalk, B., Tang, S., Bentefour, E. H., Cascio, E. W., Prieels, D. and Lu, H.-M. [2011], 'Water equivalent path length measurement in proton radiotherapy using time resolved diode dosimetry', *Medical Physics* **38**(4), 2282. 24

Graffman, S. and Jung, B. [1975], '11C and 15O induced in the mouse by 175 MeV protons', *Acta Oncologica* **14**(October 1974). 24

Grassberger, C. and Paganetti, H. [2011], 'Elevated LET components in clinical proton beams.', *Physics in medicine and biology* **56**(20), 6677–91. 28

Grosclaude, P., Danzon, A. and Bossard, N. [2013], 'Survie des personnes atteintes de cancer en France'. 1

Grün, R., Friedrich, T., Elsässer, T., Krämer, M., Zink, K., Karger, C. P., Durante, M., Engenhart-Cabillic, R. and Scholz, M. [2012], 'Impact of enhancements in the local effect model (LEM) on the predicted RBE-weighted target dose distribution in carbon ion therapy.', *Physics in medicine and biology* **57**(22), 7261–74. 12

Grusell, E., Montelius, a., Brahme, a., Rikner, G. and Russell, K. [1994], 'A general solution to charged particle beam flattening using an optimized dual-scattering-foil technique, with application to proton therapy beams.', *Physics in medicine and biology* **39**(12), 2201–16. 8

Hagiwara, K. e. a. [2002], 'Review of Particle Physics', *Physical Review D* **66**. 37

Hall, E. J. and Giaccia, A. J. [2012], *Radiobiology for the radiobioogist*, Lippincott Williams & Wilkins. 13

Hall, E. J. and Hei, T. K. [2003], 'Genomic instability and bystander effects induced by high-LET radiation.', *Oncogene* **22**(45), 7034–42. 11

Hammersberg, P. and Mångård, M. [1998], 'Correction for beam hardening artefacts in computerised tomography.', *Journal of X-ray science and technology* **8**(1), 75–93. 29

Han, X., Bian, J. and Eaker, D. [2011], 'Algorithm-enabled low-dose micro-CT imaging', *Medical Imaging, . . .* **30**(3), 606–620. 66

Hansen Ree, A., Stokke, T., Bratland, A., Patzke, S., Nome, R. V., Folkvord, S., Meza-zepeda, L. A., Flatmark, K., Fodstad, O. and Andersson, Y. [2006], 'DNA damage responses in cell cycle G2 phase and mitosis-tracking and targeting', *Anticancer Research* **26**(3A), 1909–16. 13

Hanson, K., Bradbury, J. and Cannon, T. [1978], 'The application of protons to computed tomography', *IEEE Transactions on Nuclear Science* **25**(1), 657–660. xi, 39, 44

Hanson, K. M. [1979], 'Proton Computed Tomography', *IEEE Transactions on Nuclear Science* **26**(1), 1635–1640. 40

Hanson, K. M., Bradbury, J. N., Cannon, T. M., Hutson, R. L., Laubacher, D. B., Macek, R. J., Paciotti, M. a. and Taylor, C. a. [1981], 'Computed tomography using proton energy loss.', *Physics in medicine and biology* **26**(6), 965–83. 40, 50, 51

Hanson, K. M., Bradbury, J. N., Koeppe, R. a., Macek, R. J., Machen, D. R., Morgado, R., Paciotti, M. a., Sandford, S. a. and Steward, V. W. [1982], 'Proton computed tomography of human specimens.', *Physics in medicine and biology* **27**(1), 25–36. 40, 44

Henriquet, P., Testa, E., Chevallier, M., Dauvergne, D., Dedes, G., Freud, N., Krimmer, J., Létang, J. M., Ray, C., Richard, M.-H. and Sauli, F. [2012], 'Interaction vertex imaging (IVI) for carbon ion therapy monitoring: a feasibility study.', *Physics in medicine and biology* **57**(14), 4655–69. 25

Herman, G. and Meyer, L. [1993], 'Algebraic reconstruction techniques can be made computationally efficient', *Medical Imaging, IEEE Transactions on* **12**(3). 73

Herman, G. T. [1979], 'Correction for beam hardening in computed tomography.', *Physics in medicine and biology* **24**(1), 81–106. 29

Herman, G. T. [2009], *Fundamentals of computerized tomography: image reconstruction from projections*, Springer. 73

Hünemohr, N., Krauss, B., Dinkel, J., Gillmann, C., Ackermann, B., Jäkel, O. and Greilich, S. [2013], 'Ion range estimation by using dual energy computed tomography.', *Zeitschrift fur medizinische Physik* . 30

Hurley, R. F., Schulte, R. W., Bashkirov, V. a., Wroe, a. J., Ghebremedhin, a., Sadrozinski, H. F.-W., Rykalin, V., Coutrakon, G., Koss, P. and Patyal, B. [2012], 'Water-equivalent path length calibration of a prototype proton CT scanner.', *Medical physics* **39**(5), 2438–46. xii, 45, 49

IAEA [2013], 'Directory of radiotherapy centres'.
URL: *www-naweb.iaea.org/nahu/dirac* 2

IAEA and ICRU [2008], Relative Biological Effectiveness in Ion Beam Therapy, Technical Report 46. 9

ICRU report 37 [1984], *Stopping Powers for Electrons and Positrons.* 36

ICRU report 46 [1992], *Photon, Electron, Proton and Neutron Interaction Data for Body Tissues.* 107

ICRU report 48 [1994], *Stopping Power and Ranges for Protons and Alpha Particles.* 36

ICRU report 60 [1998], *Fundamental quantities and units for ionizing radiation.* 8

International Agency for Research on Cancer [2008], 'Globalcan 2008'.
URL: *globalcan.iarc.fr* ix, 1

Intes, X., Ntziachristos, V., Culver, J. P., Yodh, A. and Chance, B. [2002], 'Projection access order in algebraic reconstruction technique for diffuse optical tomography.', *Physics in medicine and biology* **47**(1), N1–10.
URL: *http://www.ncbi.nlm.nih.gov/pubmed/11814231* 66

IPHC computational grid [n.d.].
URL: *www.iphc.cnrs.fr/Infrastructure-de-Calcul-Grid.html* 60

Islam, M. K., Purdie, T. G., Norrlinger, B. D., Alasti, H., Moseley, D. J., Sharpe, M. B., Siewerdsen, J. H. and Jaffray, D. a. [2006], 'Patient dose from kilovoltage cone beam computed tomography imaging in radiation therapy', *Medical Physics* **33**(6), 1573. 113

Ivanchenko, V. N., Kadri, O., Maire, M. and Urban, L. [2010], 'Geant4 models for simulation of multiple scattering', *Journal of Physics: Conference Series* **219**(3), 032045. 57

Jackson, D. and Hawkes, D. [1981], 'X-ray attenuation coefficients of elements and mixtures', *Physics Reports* . 18

Jäkel, O., Land, B., Combs, S. E., Schulz-Ertner, D. and Debus, J. [2007], 'On the cost-effectiveness of Carbon ion radiation therapy for skull base chordoma.', *Radiotherapy and oncology : journal of the European Society for Therapeutic Radiology and Oncology* **83**(2), 133–8. x, 16

Jäkel, O. and Reiss, P. [2007], 'The influence of metal artefacts on the range of ion beams.', *Physics in medicine and biology* **52**(3), 635–44. 22

Jan, S., Benoit, D., Becheva, E., Carlier, T., Cassol, F., Descourt, P., Frisson, T., Grevillot, L., Guigues, L., Maigne, L., Morel, C., Perrot, Y., Rehfeld, N., Sarrut, D., Schaart, D. R., Stute, S., Pietrzyk, U., Visvikis, D., Zahra, N. and Buvat, I. [2011], 'GATE V6: a major enhancement of the GATE simulation platform enabling modelling of CT and radiotherapy.', *Physics in medicine and biology* **56**(4), 881–901. xiii, 57

Jiang, H., Seco, J. and Paganetti, H. [2007], 'Effects of Hounsfield number conversion on CT based proton Monte Carlo dose calculations', *Medical physics* **34**(4), 1439–1449. x, 18, 22

Johns, H. [1983], 'The physics of radiology'. 30

Johnson, L., Keeney, B., Ross, G., Sadrozinski, H.-W., Seiden, A., Williams, D., Zhang, L., Bashkirov, V., Schulte, R. and Shahnazi, K. [2003], 'Initial studies on proton computed tomography using a silicon strip detector telescope', *Nuclear Instruments and Methods in Physics Research Section A: Accelerators, Spectrometers, Detectors and Associated Equipment* **514**(1-3), 215–223. 46

Johnson, R. P., Dewitt, J., Holcomb, C., Macafee, S., Sadrozinski, H. F., Member, S. and Steinberg, D. [2013], 'Tracker Readout ASIC for Proton Computed Tomography Data Acquisition', *IEEE Transactions on Nuclear Science* pp. 1–8. xviii, 49, 144

Johnson, R. P., Dewitt, J., Macafee, S., Sadrozinski, H. F., Steinberg, D. and Zatserklyaniy, A. [2012], 'A fast tracker data acquisition system for pCT', *2012 IEEE Nuclear Science Symposiwn and Medical Imaging Conference Record (NSS/MIC)* pp. 2529–2531. 49

Jones, B., Underwood, T. S. a. and Dale, R. G. [2011], 'The potential impact of relative biological effectiveness uncertainty on charged particle treatment prescriptions.', *The British journal of radiology* **84 Spec No**, S61–9. 12, 26

Kachelrieß , M., Sourbelle, K. and Kalender, W. a. [2006], 'Empirical cupping correction: A first-order raw data precorrection for cone-beam computed tomography', *Medical Physics* **33**(5), 1269. 29

Kaczmarz, S. [1937], 'Angenäherte auflösung von systemen linearer gleichungen', *Bulletin International de l'Academie Polonaise des Sciences et des Lettres* **35**, 355–357. 66

Kanai, T., Endo, M., Minohara, S., Miyahara, N., Koyama-ito, H., Tomura, H., Matsufuji, N., Futami, Y., Fukumura, A., Hiraoka, T., Furusawa, Y., Ando, K., Suzuki, M., Soga, F. and Kawachi, K. [1999], 'Biophysical characteristics of HIMAC clinical irradiation system for heavy-ion radiation therapy.', *International journal of radiation oncology, biology, physics* **44**(1), 201–10. 12

Kanai, T., Kawachi, K. and Kumamoto, Y. [1980], 'Spot scanning system for proton radiotherapy', *Medical physics* . 8

Kanematsu, N. [2008], 'Alternative scattering power for Gaussian beam model of heavy charged particles', *Nuclear Instruments and Methods in Physics Research Section B: Beam Interactions with Materials and Atoms* **266**(23), 5056–5062. 37

Kanematsu, N., Inaniwa, T. and Koba, Y. [2012], 'Relationship between electron density and effective densities of body tissues for stopping, scattering, and nuclear interactions of proton and ion beams', *Medical Physics* **1016**. 27

Kanematsu, N. and Matsufuji, N. [2003], 'A CT calibration method based on the polybinary tissue model for radiotherapy treatment planning', *Physics in medicine and biology* **1053**. 18

Katz, R., Ackerson, B., Homayoonfar, M. and Sharma, S. C. [1971], 'Inactivation of Cells by Heavy Ion Bombardment', *Radiation research* **47**(2), 402–425. 12

Katz, R. and Cucinotta, F. [1999], 'Tracks to therapy', *Radiation measurements* **31**, 379–388. 12

King, N. et al. [1999], 'An 800-mev proton radiography facility for dynamic experiments', *Nucl. Instrum. Methods A* **424**(1), 84 – 91. 114

Knopf, A.-C. and Lomax, A. [2013], 'In vivo proton range verification: a review.', *Physics in medicine and biology* **58**(15), R131–60. 23

Koehler, A. [1968], 'Proton radiography.', pp. 9–10. xi, 41

Koehler, A., Schneider, R. and Sisterson, J. [1977], 'Flattening of proton dose distributions for large-field radiotherapy', *Medical Physics* . 8

Kormoll, T., Fiedler, F., Schöne, S., Wüstemann, J., Zuber, K. and Enghardt, W. [2011], 'A Compton imager for in-vivo dosimetry of proton beamsâĂŤA design study', *Nuclear Instruments and Methods in Physics Research Section A: Accelerators, Spectrometers, Detectors and Associated Equipment* **626-627**, 114–119. 25

Koybasi, O., Goulet, M., Depauw, N., Gingras, L., Archambault, L., Beaulieu, L. and Seco, J. [2012], 'Development of a 2D scintillating fiber detector for proton radiography', *2012 IEEE Nuclear Science Symposium and Medical Imaging Conference Record (NSS/MIC)* pp. 4318–4323. 48

Kraft, G. [2000], 'Tumortherapy with ion beams', *Nuclear Instruments and Methods in Physics Research Section A: Accelerators, Spectrometers, Detectors and Associated Equipment* **454**(1), 1–10. 8

Krimmel, S., Stephan, J. and Baumann, J. [2005], '3D computed tomography using a microfocus X-ray source: Analysis of artifact formation in the reconstructed images using simulated as well as experimental projection data', *Nuclear Instruments and Methods in Physics Research Section A: Accelerators, Spectrometers, Detectors and Associated Equipment* **542**(1-3), 399–407. 29

Krishna, M. C., Subramanian, S., Kuppusamy, P. and Mitchell, J. B. [2001], 'Magnetic resonance imaging for in vivo assessment of tissue oxygen concentration.', *Seminars in radiation oncology* **11**(1), 58–69. 13

Lambert, J. [1760], 'Photometria, sive de mensura et gradinus luminis, colorum et umbrae', *Annalen der Physik und Chemie* . 7

Lauritsch, G. and Bruder, H. [n.d.], 'Forbild head phantom'.
URL: *www.imp.uni-erlanger.de/forbild/deutsch/results/head/head.html* 60, 61

Li, T., Liang, Z., Mueller, K., Heimann, J., Johnson, L., Sadrozinski, H., Seiden, A., Williams, D., Zhang, L., Peggs, S., Satogata, T., Bashkirov, V. and Schulte, R. W. [2004], 'Reconstruction for proton computed tomography: a Monte Carlo study', *2003 IEEE Nuclear Science Symposium. Conference Record (IEEE Cat. No.03CH37515)* pp. 2767–2770. 50, 57

Li, T., Liang, Z. and Singanallur, J. [2006], 'Reconstruction for proton computed tomography by tracing proton trajectories: A Monte Carlo study', *Medical ...* **33**(3), 699–706. 51, 125

Linz, U. [2012], *Ion-beam Therapy.* 6

Little, J. B. [2003], 'Genomic instability and bystander effects: a historical perspective.', *Oncogene* **22**(45), 6978–87. 11

Litzenberg, D. and Bajema, J. [1992], 'On-line monitoring and PET imaging of proton radiotherapy beams', *1992 IEEE Nuclear Science Symposium and Medical Imaging Conference Record (NSS/MIC)* pp. 954–956. 24

Lo Presti, D., Bonanno, D., Longhitano, F., Pugliatti, C., Aiello, S., Cirrone, G., Giordano, V., Leonora, E., Randazzo, N., Romano, F., Russo, G., Sipala, V., Stancampiano, C. and Ventura, C. [2014], 'A real-time, large area, high space resolution particle radiography system', *Journal of Instrumentation* **9**(06), C06012–C06012. xviii, 144

Lodge, M., Pijls-Johannesma, M., Stirk, L., Munro, A. J., De Ruysscher, D. and Jefferson, T. [2007], 'A systematic literature review of the clinical and cost-effectiveness of hadron therapy in cancer.', *Radiotherapy and oncology : journal of the European Society for Therapeutic Radiology and Oncology* **83**(2), 110–22. 16

Loeffler, J. and Durante, M. [2013], 'Charged particle therapy – optimization, challenges and future directions', *Nature Reviews Clinical Oncology* **10**, 411–424. 10

Lomax, a. J., Bortfeld, T., Goitein, G., Debus, J., Dykstra, C., Tercier, P. a., Coucke, P. a. and Mirimanoff, R. O. [1999], 'A treatment planning inter-comparison of proton and intensity modulated photon radiotherapy.', *Radiotherapy and oncology : journal of the European Society for Therapeutic Radiology and Oncology* **51**(3), 257–71. 8

Lu, H.-M. [2008*a*], 'A point dose method for in vivo range verification in proton therapy.', *Physics in medicine and biology* **53**(23), N415–22. 24

Lu, H.-M. [2008*b*], 'A potential method for in vivo range verification in proton therapy treatment.', *Physics in medicine and biology* **53**(5), 1413–24. 24

Lu, H.-M. [2009], 'A Method for Intra Fractional Beam Range Control in Proton Therapy Treatment', *Medical physics* **36**(6), 2573. 24

Lundkvist, J., Ekman, M., Ericsson, S. R., Jönsson, B. and Glimelius, B. [2005], 'Proton therapy of cancer: potential clinical advantages and cost-effectiveness.', *Acta oncologica (Stockholm, Sweden)* **44**(8), 850–61. 16

Lynch, G. and Dahl, O. [1991], 'Approximations to multiple Coulomb scattering', *Nuclear Instruments and Methods in Physics Research B* **58**(7991), 6–10. 37, 69, 94

Lynga, H., Sundf, K. and Rofstad, E. K. [1997], 'Oxygen tension in human tumours measured with polarographic needle electrodes and its relationship to vascular density , necrosis and hypoxia', **44**, 163–169. 12

Man, B. D., Member, S., Nuyts, J., Dupont, P., Marchal, G. and Suetens, P. [2000], 'Reduction of metal streak artifacts in x-ray computed tomography using a transmission maximum a posteriori algorithm', **47**(3), 977–981. 29

Matsufuji, N. and Tomura, H. [1998], ‘Relationship between CT number and electron density, scatter angle and nuclear reaction for hadron-therapy treatment planning’, *Physics in medicine and biology* **3261**. 26, 27

Matsumoto, M. and Nishimura, T. [1998], ‘Mersenne twister: a 623-dimensionally equidistributed uniform pseudo-random number generator’, *ACM Transactions on Modeling and Computer Simulation* **8**(1), 3–30. 60

Maughan, R. L., Chuba, P. J., Porter, A. T., Ben-Josef, E. and Lucas, D. R. [1997], ‘The elemental composition of tumors: Kerma data for neutrons’, *Med. Phys.* **24**, 1241. 107, 147

McGowan, S. E., Burnet, N. G. and Lomax, a. J. [2013], ‘Treatment planning optimisation in proton therapy.’, *The British journal of radiology* **86**(1021), 20120288. 20, 27, 29

Metropolis, N. and Ulam, S. [1949], ‘The monte carlo method’, *Journal of the American statistical association* **44**(247), 335–341. 56

Milhoretto, E., Schelin, H. R., Evseev, I., Paschuk, S. a., Setti, J. a., Junior, S. R., Silva, F. L., Lourenso, J. C., Denyak, V., de Assis, J., Yevseyeva, O., Lopes, R., Hurley, F. and Schulte, R. W. [2012], ‘Comparison of Geant4 version 9.3 simulations with experimental results from a prototype proton CT scanner’, *2012 IEEE Nuclear Science Symposium and Medical Imaging Conference Record (NSS/MIC)* pp. 1000–1002. 57, 112

Min, C.-H., Kim, C. H., Youn, M.-Y. and Kim, J.-W. [2006], ‘Prompt gamma measurements for locating the dose falloff region in the proton therapy’, *Applied Physics Letters* **89**(18), 183517. 25

Mobaraki, A., Ohno, T., Yamada, S., Sakurai, H. and Nakano, T. [2010], ‘Cost-effectiveness of carbon ion radiation therapy for locally recurrent rectal cancer.’, *Cancer science* **101**(8), 1834–9. 16

Molière, G. [1947], ‘Theorie der Streuung schneller geladener Teilchen I’, **2**(a), 133. 37

Molière, G. [1948], ‘Theorie der streuung schneller geladener teilchen II. Mehrfach-und vielfachstreuung’, *Zeitschrift Naturforschung Teil A* **3**(a), 78. 37

Momose, A., Takeda, T., Itai, Y. and Hirano, K. [1996], ‘Phase-contrast X-ray computed tomography for observing biological soft tissues’, *Nature medicine* . 31

Moteabbed, M., España, S. and Paganetti, H. [2011], ‘Monte Carlo patient study on the comparison of prompt gamma and PET imaging for range verification in proton therapy.’, *Physics in medicine and biology* **56**(4), 1063–82. 25

Mothersill, C. and Seymour, C. B. [2006], ‘Radiation-induced bystander effects and the DNA paradigm: an ”out of field” perspective.’, *Mutation research* **597**(1-2), 5–10. 11

Moulder, J. E. and Rockwell, S. [1987], 'Tumor hypoxia: its impact on cancer therapy.', *Cancer metastasis reviews* **5**(4), 313–41. 13

Mumot, M., Algranati, C., Hartmann, M., Schippers, J. M., Hug, E. and Lomax, a. J. [2010], 'Proton range verification using a range probe: definition of concept and initial analysis.', *Physics in medicine and biology* **55**(16), 4771–82. 23, 24

Mustafa, a. a. and Jackson, D. F. [1983], 'The relation between X-ray CT numbers and charged particle stopping powers and its significance for radiotherapy treatment planning.', *Physics in medicine and biology* **28**(2), 169–76. 18

Nalcioglu, O. and Lou, R. Y. [1979], 'Post-reconstruction method for beam hardening in computerised tomography.', *Physics in medicine and biology* **24**(2), 330–40. 29

Nassiri, M. A., Hissoiny, S., Carrier, J.-F. and Després, P. [2012], 'Fast GPU-based computation of the sensitivity matrix for a PET list-mode OSEM algorithm.', *Physics in medicine and biology* **57**(19), 6279–93. 76

Newhauser, W. D., Giebeler, A., Langen, K. M., Mirkovic, D. and Mohan, R. [2008], 'Can megavoltage computed tomography reduce proton range uncertainties in treatment plans for patients with large metal implants?', *Physics in medicine and biology* **53**(9), 2327–44. 29, 30

NIST [2014], 'Pstar database'.
URL: *physics.nist.gov/PhysRefData/Star/Text/PSTAR.html* 35

Nyquist, H. [2002], 'Certain topics in telegraph transmission theory', *Proceedings of the IEEE* **90**(2), 280–305.
URL: *http://ieeexplore.ieee.org/lpdocs/epic03/wrapper.htm?arnumber=989875* 66

Ohno, Y., Kohno, T., Matsufuji, N. and Kanai, T. [2004], 'Measurement of electron density distribution using heavy ion CT', *Nuclear Instruments and Methods in Physics Research Section A: Accelerators, Spectrometers, Detectors and Associated Equipment* **525**(1-2), 279–283. 24, 50

Olko, P. and Jezabek, M. [2012], 'Hadron radiotherapy in poland – where are we going?', *2nd COPIGAL workshop on studies of exotic nuclei* .
URL: *copigal.ifj.edu.pl/download/Tuesday/22_copigal_olko.pdf* 144

Olsen, D. R., Bruland, O. S., Frykholm, G. and Norderhaug, I. N. [2007], 'Proton therapy - a systematic review of clinical effectiveness.', *Radiotherapy and oncology : journal of the European Society for Therapeutic Radiology and Oncology* **83**(2), 123–32. 14, 15

Olson, E., Han, K. and Pisano, D. [1981], 'CT reprojection polychromaticity correction for three attenuators', *IEEE transactions on Nuclear Science* **28**(4). 29

Opengate collaboration [n.d.].
URL: *www.opengatecollaboration.org* 57, 147

Opengate collaboration wiki [n.d.].
URL: *wiki.opengatecollaboration.org/index.php/User_Guide_V7.0* 60

Paganetti, H. [2012], ‘Range uncertainties in proton therapy and the role of Monte Carlo simulations’, *Physics in medicine and biology* **57**(11). x, 22, 23, 112

Paganetti, H., Athar, B. S., Moteabbed, M., A Adams, J., Schneider, U. and Yock, T. I. [2012], ‘Assessment of radiation-induced second cancer risks in proton therapy and IMRT for organs inside the primary radiation field.’, *Physics in medicine and biology* **57**(19), 6047–61. 8

Paganetti, H., Niemierko, A., Ancukiewicz, M., Gerweck, L. E., Goitein, M., Loeffler, J. S. and Suit, H. D. [2002], ‘Relative biological effectiveness (RBE) values for proton beam therapy.’, *International journal of radiation oncology, biology, physics* **53**(2), 407–21. 9, 11, 12, 21

Paiva, R. F. D., Lynch, J., Rosenberg, E., Bisiaux, M. and Fran, I. [1998], ‘A beam hardening correction for X-ray microtomography’, **31**(1), 17–22. 29

Palmans, H. and Verhaegen, F. [2005], ‘Assigning nonelastic nuclear interaction cross sections to Hounsfield units for Monte Carlo treatment planning of proton beams.’, *Physics in medicine and biology* **50**(5), 991–1000. x, 27

Park, P. C., Zhu, X. R., Lee, A. K., Sahoo, N., Melancon, A. D., Zhang, L. and Dong, L. [2012], ‘A beam-specific planning target volume (PTV) design for proton therapy to account for setup and range uncertainties.’, *International journal of radiation oncology, biology, physics* **82**(2), e329–36. 29

Parodi, K. [2012], ‘PET monitoring of hadrontherapy’, *Nuclear Medicine Review* pp. 37–42. 25, 26

Parodi, K. [2014], ‘Heavy ion radiography and tomography.’, *Physica medica* **30**(5), 539–43. 24, 50

Parodi, K., Crespo, P., Eickhoff, H., Haberer, T., Pawelke, J., Schardt, D. and Enghardt, W. [2005], ‘Random coincidences during in-beam PET measurements at microbunched therapeutic ion beams’, *Nuclear Instruments and Methods in Physics Research Section A: Accelerators, Spectrometers, Detectors and Associated Equipment* **545**(1-2), 446–458. 25

Particle Therapy Cooperative Group [2014], ‘PTCOG’.
URL: *ptcog.ch* 2, 52

Particle Therapy Cooperative Group [n.d.], ‘PTCOG’.
URL: *ptcog.ch/index.php/clinical-protocols* 15

Pedroni, E., Bacher, R. and Blattmann, H. [1995], ‘The 200-MeV proton therapy project at the Paul Scherrer Institute: conceptual design and practical realization’, *Medical Physics* . 8

Peeters, A., Grutters, J. P. C., Pijls-Johannesma, M., Reimoser, S., De Ruysscher, D., Severens, J. L., Joore, M. a. and Lambin, P. [2010], 'How costly is particle therapy? Cost analysis of external beam radiotherapy with carbon-ions, protons and photons.', *Radiotherapy and oncology : journal of the European Society for Therapeutic Radiology and Oncology* **95**(1), 45–53. 16, 17

Pemler, P., Besserer, J., Boer, J. D., Dellert, M., Gahn, C., Moosburger, M., Schneider, U., Pedroni, E. and Sta, H. [1999], 'A detector system for proton radiography on the gantry of the', *Nuclear Instruments and Methods in Physics Research Section A: Accelerators, Spectrometers, Detectors and Associated Equipment* **432**, 483–495. xii, 48, 49, 50

Penfold, S., a.B. Rosenfeld, Schulte, R. and Sadrozinksi, H.-F. [2011], 'Geometrical optimization of a particle tracking system for proton computed tomography', *Radiation Measurements* **46**(12), 2069–2072. 93, 98, 102

Penfold, S. N. [2010], Image reconstruction and Monte Carlo simulations in the development of proton computed tomography for applications in proton radiation therapy, PhD thesis. 57, 66, 68, 78, 84

Penfold, S. N., Schulte, R. W., Censor, Y. and Rosenfeld, a. B. [2010], 'Total variation superiorization schemes in proton computed tomography image reconstruction', *Medical Physics* **37**(11), 5887. xii, 75

Penfold, Scott Nicholas, S. R. C. Y. B. V. R. A. B. [2009], 'Characteristics of proton ct images reconstructed with filtered backprojection and iterative projection algorithms', *2009 IEEE Nuclear Science Symposium Conference Record (NSS/MIC)* pp. 4176–4180. 51, 76, 77, 85

Perry, J. [2013], Advanced applications of cosmic-ray muon radiography, PhD thesis. xvi, 142

Pflugfelder, D., Wilkens, J. J. and Oelfke, U. [2008], 'Worst case optimization: a method to account for uncertainties in the optimization of intensity modulated proton therapy.', *Physics in medicine and biology* **53**(6), 1689–700. 29

Pijls-Johannesma, M., Pommier, P. and Lievens, Y. [2008], 'Cost-effectiveness of particle therapy: current evidence and future needs.', *Radiotherapy and oncology : journal of the European Society for Therapeutic Radiology and Oncology* **89**(2), 127–34. 16

Plautz, T., Bashkirov, V., Feng, V., Hurley, F., Johnson, R., Leary, C., Macafee, S., Plumb, A., Sadrozinski, H., Schubert, K. E., Schultze, R., Steinberg, D., Witt, M. and Zatserklyaniy, A. [2012], '200 MeV proton radiography studies with a hand phantom using a prototype proton CT scanner', *2012 IEEE Nuclear Science Symposium and Medical Imaging Conference Record (NSS/MIC)* pp. 4113–4117. 52

Polf, J. C., Peterson, S., Ciangaru, G., Gillin, M. and Beddar, S. [2009], 'Prompt gamma-ray emission from biological tissues during proton irradiation: a preliminary study.', *Physics in medicine and biology* **54**(3), 731–43. 25

Poludniowski, G., Allinson, N. M., Anaxagoras, T., Esposito, M., Green, S., Manolopoulos, S., Nieto-Camero, J., Parker, D. J., Price, T. and Evans, P. M. [2014], ‘Proton-counting radiography for proton therapy: a proof of principle using CMOS APS technology’, *Physics in Medicine and Biology* **59**(11), 2569–2581. 48

Pratx, G. and Chinn, G. [2009], ‘Fast, accurate and shift-varying line projections for iterative reconstruction using the GPU’, *Medical Imaging, IEEE Transactions on* **28**(3), 435–445. 76

Qi, Z., Zambelli, J., Bevins, N. and Chen, G.-H. [2010], ‘Quantitative imaging of electron density and effective atomic number using phase contrast CT.’, *Physics in medicine and biology* **55**(9), 2669–77. 31

Radon, J. [1986], ‘On the determination of functions from their integral values along certain manifolds’, *Medical Imaging, IEEE Transactions on* **MI-5**(4), 170–176. 63

Raeside, D. E. [1976], ‘Monte Carlo principles and applications.’, *Physics in medicine and biology* **21**(2), 181–97. 57

Ramaekers, B. [2013], *Acknowledging Patient Heterogeneity in Health Technology Assessment Towards Personalized Decisions in Innovative Radiotherapy Treatments.* 16

Rank, C. M., Tremmel, C., Hünemohr, N., Nagel, A. M., Jäkel, O. and Greilich, S. [2013], ‘MRI-based treatment plan simulation and adaptation for ion radiotherapy using a classification-based approach.’, *Radiation oncology (London, England)* **8**, 51. 17

Raytchev, M. and Seco, J. [2013], ‘Proton radiography in three dimensions: a proof of principle of a new technique.’, *Medical physics* **40**(10), 101917. 52

Rescigno, R., Finck, C., Juliani, D., Baudot, J., Dauvergne, D., Dedes, G., Krimmer, J., Ray, C., Reithinger, V., Rousseau, M., Testa, E. and Winter, M. [2014], ‘Simulation toolkit with CMOS detector in the framework of hadrontherapy’, *EPJ Web of Conferences* **66**, 10013. 25

Richard, M.-H. [2012], Design and study of a compton camera for prompt-gamma imaging during ion beam therapy, PhD thesis, Universite de Lyon. xviii, 144

Rinaldi, I., Brons, S., Gordon, J., Panse, R., Voss, B., Jäkel, O. and Parodi, K. [2013], ‘Experimental characterization of a prototype detector system for carbon ion radiography and tomography.’, *Physics in medicine and biology* **58**(3), 413–27. 50

Rit, S., Dedes, G., Freud, N., Sarrut, D. and Létang, J. M. [2013], ‘Filtered backprojection proton CT reconstruction along most likely paths.’, *Medical physics* **40**(3), 031103. xii, 51, 84, 92

Roellinghoff, F., Richard, M.-H., Chevallier, M., Constanzo, J., Dauvergne, D., Freud, N., Henriquet, P., Le Foulher, F., Létang, J., Montarou, G., Ray, C., Testa, E., Testa, M. and a.H. Walenta [2011], ‘Design of a Compton camera for 3D prompt-imaging during ion beam therapy', *Nuclear Instruments and Methods in Physics Research Section A: Accelerators, Spectrometers, Detectors and Associated Equipment* **648**, S20–S23. 25

Romero, J., Osborne, J., Brady, F., Caskey, W., Cebra, D., Partlan, M., Kusko, B., King, R., Mirshad, I., Kubo, H., Daftari, I. and Chu, W. [1995], 'Patient positioning for protontherapy using a proton range telescope', *Nuclear Instruments and Methods in Physics Research Section A: Accelerators, Spectrometers, Detectors and Associated Equipment* **356**(2-3), 558–565. 23

Rudin, L., Osher, S. and Fatemi, E. [1992], 'Nonlinear total variation based noise removal algorithms', *Physica D: Nonlinear Phenomena* **60**, 259–268. 75

Sadrozinski, H. F.-W., Bashkirov, V., Colby, B., Coutrakon, G., Erdelyi, B., Fusi, D., Hurley, F., Johnson, R. P., Kashiguine, S., McAllister, S., Martinez-McKinney, F., Missaghian, J., Scaringella, M., Penfold, S. N., Rykalin, V., Schulte, R., Schubert, K., Steinberg, D. and Zatserklaniy, A. [2011], 'Detector development for Proton Computed Tomography (pCT)', *2011 IEEE Nuclear Science Symposium Conference Record* pp. 4457–4461. xvii, 49, 50, 52, 102, 143

Sadrozinski, H. F.-W., Johnson, R. P., Macafee, S., Plumb, A., Steinberg, D., Zatserklyaniy, A., Hurley, V. B. F. and Schulte, R. [2013], 'Development of a Head Scanner for Proton CT.', *Nuclear instruments and methods in physics research. Section A, Accelerators, spectrometers, detectors and associated equipment* **699**, 205–210. xii, 48, 49, 50, 52, 93

Safai, S., Bortfeld, T. and Engelsman, M. [2008], 'Comparison between the lateral penumbra of a collimated double-scattered beam and uncollimated scanning beam in proton radiotherapy.', *Physics in medicine and biology* **53**(6), 1729–50. 88

Sakama, M., Kanai, T., Kase, Y., Yusa, K., Tashiro, M., Torikai, K., Shimada, H., Yamada, S., Ohno, T. and Nakano, T. [2012], 'Design of ridge filters for spread-out Bragg peaks with Monte Carlo simulation in carbon ion therapy', *Physics in Medicine and Biology* **57**(20), 6615. 12

Sakurai, H., Robert Lee, W. and Orton, C. G. [2012], 'Point/counterpoint: we do not need randomized clinical trials to demonstrate the superiority of proton therapy.', *Medical physics* **39**(4), 1685–7. 14

Saraya, Y., Izumikawa, T., Goto, J., Kawasaki, T. and Kimura, T. [2013], 'Study of spatial resolution of proton computed tomography using a silicon strip detector', *Nuclear Instruments and Methods in Physics Research Section A: Accelerators, Spectrometers, Detectors and Associated Equipment* pp. 1–5. xii, 48, 49, 51

Satogata, T., Sadrozinski, H.-W. F., Dilmanian, A., Peggs, S., Ruggiero, A., Ny, U. and Member, H. F. S. [2003], 'Dose/sensitivity in proton computed tomography', *2003 IEEE Nuclear Science Symposium Conference Record I* (2), 3667–3671. 52

Saudinos, J., Charpak, G., Sauli, F., Townsend, D. and Vinciarelli, J. [1975], 'Nuclear scattering applied to radiography.', *Physics in medicine and biology* **20**(6), 890–905. xi, 41

Scaringella, M., Brianzi, M., Bruzzi, M., Bucciolini, M., Carpinelli, M., Cirrone, G., Civinini, C., Cuttone, G., Lo Presti, D., Pallotta, S., Pugliatti, C., Randazzo, N., Romano, F., Sipala, V., Stancampiano, C., Talamonti, C., Tesi, M., Vanzi, E. and Zani, M. [2013], 'The PRIMA (PRoton IMAging) collaboration: Development of a proton Computed Tomography apparatus', *Nuclear Instruments and Methods in Physics Research Section A: Accelerators, Spectrometers, Detectors and Associated Equipment* **730**, 178–183. 102

Schaffner, B. and Pedroni, E. [1998], 'precision of proton range calculations in proton radiotherapy treatment planning: experimental verification of the relation between CT-HU and proton stopping power', *Physics in medicine and biology* **1579**. x, 21

Schardt, D., Elsässer, T. and Schulz-Ertner, D. [2010], 'Heavy-ion tumor therapy: Physical and radiobiological benefits', *Reviews of Modern Physics* **82**(1), 383–425. 6, 24

Schneider, U. [1994], Proton Radiography : in proton quality control, PhD thesis. 44, 68

Schneider, U. and Pedroni, E. [1995], 'Proton radiography as a tool for quality control in proton therapy', *Medical physics* **22**(4), 353–363. 24

Schneider, U., Pedroni, E. and Lomax, a. [1996], 'The calibration of CT Hounsfield units for radiotherapy treatment planning.', *Physics in medicine and biology* **41**(1), 111–24. 18, 19, 27, 136

Schneider, U., Pemler, P., Besserer, J., Pedroni, E., Lomax, A. and Kaser-Hotz, B. [2005], 'Patient specific optimization of the relation between CT-Hounsfield units and proton stopping power with proton radiography', *Medical physics* **32**(1), 195–199. 18

Schneider, W. [2000], 'Correlation between CT numbers and tissue parameters needed for Monte Carlo simulations of clinical dose distributions', *Physics in medicine and biology* **459**. 18

Scholz, M. and Elsässer, T. [2007], 'Biophysical models in ion beam radiotherapy', *Advances in Space Research* **40**(9), 1381–1391. 12

Schulte, R., Bashkirov, V., Mueller, K., Heimann, J., Johnson, L., Keeney, B., Sadrozinski, H.-W., Seiden, a., Williams, D., Peggs, S., Satogata, T. and Woody, C. [2004], 'Conceptual design of a proton computed tomography system for applications in proton radiation therapy', *IEEE Transactions on Nuclear Science* **51**(3), 866–872. xii, xvii, xxv, 46, 47, 95, 143

Schulte, R. W., Bashkirov, V., Klock, M. C. L., Li, T., Wroe, A. J., Evseev, I., Williams, D. C. and Satogata, T. [2005], 'Density resolution of proton computed tomography.', *Medical physics* **32**(4), 1035–46. xii, 36, 52, 59, 90, 107

Schulte, R. W., Penfold, S. N., Tafas, J. T. and Schubert, K. E. [2008], 'A maximum likelihood proton path formalism for application in proton computed tomography', *Medical Physics* **35**(11), 4849. xiii, 68, 70, 71, 125

Schultz, L. J., Blanpied, G. S., Borozdin, K. N., Fraser, A. M., Member, S., Hengartner, N. W., Klimenko, A. V., Morris, C. L., Orum, C. and Sossong, M. J. [2007], 'Statistical Reconstruction for Cosmic Ray Muon Tomography', *IEEE transactions on image processing* **16**(8), 1985–1993. xvi, 142

Schultze, B., Witt, M., Censor, Y., Schulte, R. W. and Schubert, K. E. [2014], 'Performance of Hull-Detection Algorithms For Proton Computed Tomography Reconstruction', *arXiv preprint* (arXiv1402.1720), 1–14. 77

Schulz-Ertner, D., Jäkel, O. and Schlegel, W. [2006], 'Radiation therapy with charged particles.', *Seminars in radiation oncology* **16**(4), 249–59. 21

Scifoni, E., Tinganelli, W., Weyrather, W. K., Durante, M., Maier, A. and Krämer, M. [2013], 'Including oxygen enhancement ratio in ion beam treatment planning: model implementation and experimental verification.', *Physics in medicine and biology* **58**(11), 3871–95. 12

Seco, J. and Depauw, N. [2011], 'Proof of principle study of the use of a CMOS active pixel sensor for proton radiography.', *Medical physics* **38**, 622–623. 48

Segrè, E. [1964], *Nuclei and particles*, benjamin edn, New York. 38

Shikhaliev, P. M. and Fritz, S. G. [2011], 'Photon counting spectral CT versus conventional CT: comparative evaluation for breast imaging application.', *Physics in medicine and biology* **56**(7), 1905–30. 31

Shinoda, H., Kanai, T. and Kohno, T. [2006], 'Application of heavy-ion CT.', *Physics in medicine and biology* **51**(16), 4073–81. 24, 50

Siddon, R. [1985], 'Fast calculation of the exact radiological path for a threeâĂŘdimensional CT array', *Medical physics* . 76

Sidky, E. and Pan, X. [2008], 'Image reconstruction in circular cone-beam computed tomography by constrained, total-variation minimization', *Physics in medicine and biology* **53**(17), 4777–4807. 66, 75

Skarsgard, L. [1998], 'Radiobiology with heavy charged particles: a historical review.', *Physica medica: PM: an international journal devoted to the applications of physics to medicine and biology: official journal of the Italian Association of Biomedical Physics (AIFB)* **14**, 1. 2, 14

Smeets, J., Roellinghoff, F., Prieels, D., Stichelbaut, F., Benilov, a., Busca, P., Fiorini, C., Peloso, R., Basilavecchia, M., Frizzi, T., Dehaes, J. C. and Dubus, a. [2012], 'Prompt gamma imaging with a slit camera for real-time range control in proton therapy.', *Physics in medicine and biology* **57**(11), 3371–405. 25

Smith, P., Peters, T. and Bates, R. [1973], 'Image reconstruction from finite numbers of projections', *Journal of Physics A: Mathematical, Nuclear and General* **6**(3). 65

Soltanian-Zadeh, H., Windham, J. and Jenkins, J. [1990], 'Error propagation in eigenimage filtering', *IEEE Trans. Med. Img.* **9**(4), 405–420. 124

Song, E., Ryu, H., Lee, J. and Kim, J. [2008], 'Image resolution of proton radiography by using a range modulation technique', **52**(3), 904–907. 51

Steinberg, D., Bashkirov, V., Feng, V., Hurley, R. F., Johnson, R. P., Macafee, S., Plautz, T., Sadrozinski, H. F.-W., Schulte, R. W. and Zatserklyaniy, A. [2012], 'Monte Carlo simulations for the development a clinical proton CT scanner', *2012 IEEE Nuclear Science Symposium and Medical Imaging Conference Record (NSS/MIC)* pp. 1311–1315. 49, 57

Steward, V. [1976], 'Proton (and other heavy charged particle) radiography in medical diagnosis', *Nuclear Science, IEEE Transactions on* **23**(1), 577–583. xi, 41

Steward, V. [1979], 'Proton (Heavy Ion) Radiography in Medical Diagnosis', *Nuclear Science, IEEE Transactions on* **26**(2), 2257–2261. 41

Steward, V. W. and Koehler, A. [1973*a*], 'Proton radiographic detection of strokes', *Nature* **245**. xi, 41

Steward, V. W. and Koehler, A. [1974], 'Proton radiography in the diagnosis of breast carcinoma', *Radiology* **1**(110), 217–221. xi, 41

Steward, V. W. and Koehler, A. M. [1973*b*], 'Proton beam radiography in tumor detection.', *Science (New York, N.Y.)* **179**(4076), 913–4. xi, 41

Suit, H., Kooy, H., Trofimov, A., Farr, J., Munzenrider, J., DeLaney, T., Loeffler, J., Clasie, B., Safai, S. and Paganetti, H. [2008], 'Should positive phase III clinical trial data be required before proton beam therapy is more widely adopted? No.', *Radiotherapy and oncology : journal of the European Society for Therapeutic Radiology and Oncology* **86**(2), 148–53. 15

Szymanowski, H. and Oelfke, U. [2003], 'CT calibration for two-dimensional scaling of proton pencil beams', *Physics in medicine and biology* **861**. x, 27, 28

Tanabe, K. [1971], 'Projection method for solving a singular system of linear equations and its applications', *Numerische Mathematik* **17**(3), 203–214. 66

Telsemeyer, J., Jäkel, O. and Martišíková, M. [2012], 'Quantitative carbon ion beam radiography and tomography with a flat-panel detector.', *Physics in medicine and biology* **57**(23), 7957–71. 50

Testa, E., Bajard, M., Chevallier, M., Dauvergne, D., Le Foulher, F., Freud, N., Létang, J.-M., Poizat, J.-C., Ray, C. and Testa, M. [2008], 'Monitoring the Bragg peak location of 73 MeV/u carbon ions by means of prompt γ-ray measurements', *Applied Physics Letters* **93**(9). 25

Thomas, S. J. [2006], 'Margins for treatment planning of proton therapy.', *Physics in medicine and biology* **51**(6), 1491–501. 28

Tilly, N., Johansson, J., Isacsson, U., Medin, J., Blomquist, E., Grusell, E. and Glimelius, B. [2005], 'The influence of RBE variations in a clinical proton treatment plan for a hypopharynx cancer.', *Physics in medicine and biology* **50**(12), 2765–77. 28

Tschalär, C. [1968*a*], 'Straggling distributions of extremely large energy losses', *Nuclear Instruments and Methods* **64**(October), 237–243. 36

Tschalär, C. [1968*b*], 'Straggling distributions of large energy losses', *Nuclear Instruments and Methods* **61**, 141–156. 36

Ulmer, W. and Matsinos, E. [2010], 'Theoretical methods for the calculation of Bragg curves and 3D distributions of proton beams', *The European Physical Journal Special Topics* **190**(1), 1–81. 38

Unkelbach, J., Chan, T. C. Y. and Bortfeld, T. [2007], 'Accounting for range uncertainties in the optimization of intensity modulated proton therapy.', *Physics in medicine and biology* **52**(10), 2755–73. 29

Urban, L. [2006], 'A multiple scattering model in Geant4', *Preprint CERNOPEN-2006-077, Dec* pp. 1–14. 57, 130

US National Institute of Health [2014], 'US clinical trials'.
URL: *clinicaltrials.gov* 15, 16

Vandenberghe, S., D'Asseler, Y., Van de Walle, R., Kauppinen, T., Koole, M., Bouwens, L., Van Laere, K., Lemahieu, I. and Dierckx, R. a. [2001], 'Iterative reconstruction algorithms in nuclear medicine.', *Computerized medical imaging and graphics : the official journal of the Computerized Medical Imaging Society* **25**(2), 105–11. 66

Vanzi, E., Bruzzi, M., Bucciolini, M., Cirrone, G. P., Civinini, C., Cuttone, G., Lo Presti, D., Pallotta, S., Pugliatti, C., Randazzo, N., Romano, F., Scaringella, M., Sipala, V., Stancampiano, C., Talamonti, C. and Zani, M. [2013], 'The PRIMA collaboration: Preliminary results in FBP reconstruction of pCT data', *Nuclear Instruments and Methods in Physics Research Section A: Accelerators, Spectrometers, Detectors and Associated Equipment* **730**, 184–190. 50, 51, 83

Wambersie, A. [1999], 'RBE, reference RBE and clinical RBE: applications of these concepts in hadron therapy', *Strahlentherapie und Onkologie* pp. 39–43. 12

Wambersie, A., DeLuca, P., Andreo, P. and Hendry, J. [2004], "'light" or "heavy" ions: a debate of terminology?', *Radiotherapy and Oncology* **73**, iiii. 3, 13

Wang, D., Mackie, T. R. and TomeÌĄ, W. a. [2010], 'On the use of a proton path probability map for proton computed tomography reconstruction', *Medical Physics* **37**(8), 4138. 92, 102

Watts, D., Amaldi, U., Go, a., Chang, Y.-H., Hajdas, W., Iliescu, S., Malakhov, N., Samarati, J. and Sauli, F. [2009], 'A proton range telescope for quality assurance in hadrontherapy', *2009 IEEE Nuclear Science Symposium Conference Record (NSS/MIC)* pp. 4163–4166. 23

Wei, J., Sandison, G. a., Hsi, W.-C., Ringor, M. and Lu, X. [2006], 'Dosimetric impact of a CT metal artefact suppression algorithm for proton, electron and photon therapies.', *Physics in medicine and biology* **51**(20), 5183–97. x, 22, 29

West, D. [1975], 'The potential of proton radiography.', *Experientia. Supplementum* pp. 503–506. xii, 43

West, D. and Sherwood, A. C. [1972], 'Radiography with 160 MeV protons', *Nature* **239**. xii, 42

Weyrather, W. and Kraft, G. [2004], 'RBE of carbon ions: experimental data and the strategy of RBE calculation for treatment planning', *Radiotherapy and Oncology* pp. 161–169. 9, 14

Williams, D. C. [2004], 'The most likely path of an energetic charged particle through a uniform medium', *Physics in Medicine and Biology* **49**(13), 2899–2911. xiii, 51, 57, 68

Wilson, R. R. [1946], 'Radiological use of fast protons.', *Radiology* **47**(5), 487–91. ix, 2

Wong, K., Erdelyi, B., Schulte, R. W., Bashkirov, V., Coutrakon, G., Sadrozinski, H., Penfold, S. N., Rosenfeld, A., McDaniel, F. D. and Doyle, B. L. [2009], 'The Effect of Tissue Inhomogeneities on the Accuracy of Proton Path Reconstruction for Proton Computed Tomography', *AIP Conference Proceedings* (1), 476–480. 88, 90

Woodard, H. and White, D. [1986], 'The composition of body tissues', *British journal of radiology* **59**(708), 1209–1218. 107, 147

Xu, Q., Yu, H., Bennett, J., He, P., Zainon, R., Doesburg, R., Opie, A., Walsh, M., Shen, H., Butler, A., Butler, P., Mou, X. and Wang, G. [2012], 'Image reconstruction for hybrid true-color micro-CT.', *IEEE transactions on bio-medical engineering* **59**(6), 1711–9. 31

Yang, M., Virshup, G., Clayton, J., Zhu, X. R., Mohan, R. and Dong, L. [2010], 'Theoretical variance analysis of single- and dual-energy computed tomography methods for calculating proton stopping power ratios of biological tissues.', *Physics in medicine and biology* **55**(5), 1343–62. 30

Yang, M., Virshup, G., Clayton, J., Zhu, X. R., Mohan, R. and Dong, L. [2011], 'Does kV-MV dual-energy computed tomography have an advantage in determining proton stopping power ratios in patients?', *Physics in medicine and biology* **56**(14), 4499–515. 30

Yang, M., Zhu, X. R., Park, P. C., Titt, U., Mohan, R., Virshup, G., Clayton, J. E. and Dong, L. [2012], 'Comprehensive analysis of proton range uncertainties related to patient stopping-power-ratio estimation using the stoichiometric calibration.', *Physics in medicine and biology* **57**(13), 4095–115. x, 21, 22

Zatserklyaniy, A., Feng, V., Johnson, R. P., Lustig-Jaeger, J., Macafee, S., Plautz, T., Plumb, A., Sadrozinski, H. F.-W., Steinberg, D., Bashkirov, V., Hurley, F. and Schulte, R. W. [2012], 'Development of a range counter with SiPM readout for proton CT', *2012 IEEE Nuclear Science Symposium and Medical Imaging Conference Record (NSS/MIC)* pp. 1326–1329. 57

Zenklusen, S. M., Pedroni, E. and Meer, D. [2010], 'A study on repainting strategies for treating moderately moving targets with proton pencil beam scanning at the new Gantry 2 at PSI.', *Physics in medicine and biology* **55**(17), 5103–21. 8

Zhao, H. and Reader, A. [2002], 'Fast projection algorithm for voxel arrays with object dependent boundaries', *2002 IEEE Nuclear Science Symposium Conference Record (NSS/MIC)* **3**(4), 1490–1494. 77

Zhao, H. and Reader, A. [2003], 'Fast ray-tracing technique to calculate line integral paths in voxel arrays', *2003 IEEE Nuclear Science Symposium Conference Record (NSS/MIC)* pp. 2808–2812. 76

Zubal, G. [n.d.], 'Zubal phantom'.
URL: *noodle.med.yale.edu/zubal* 62

Zubal, I., Harrell, C., Smith, E. and Rattner, Z. [1994], 'Computerized three-dimensional segmented human anatomy', *Medical Physics* . 62

Zygmanski, P. and Gall, K. [2000], 'The measurement of proton stopping power using proton-cone-beam computed tomography', *Physics in medicine and biology* **45**, 511–528. 44

Cécile BOPP

LE PROTON : SONDE DOSIMÉTRIQUE ET DIAGNOSTIQUE

THE PROTON AS A DOSIMETRIC AND DIAGNOSTIC PROBE

Résumé

L'imagerie proton est étudiée comme alternative à la tomodensitométrie X pour la planification de traitement en hadronthérapie. En obtenant directement les pouvoirs d'arrêt relatifs des tissus, l'incertitude sur le parcours des particules pourrait être réduite. Un scanner à protons est constitué d'un calorimètre ou d'un détecteur de parcours afin d'obtenir l'information sur l'énergie déposée par chaque proton dans l'objet imagé et de deux ensembles de trajectographes enregistrant la position et direction de chaque particule en amont et en aval de l'objet.

Ce travail concerne l'étude des données d'un scanner à protons et l'utilisation possible de toutes les informations enregistrées. Une étude de reconstruction d'image a permis de montrer que les informations sur le taux de transmission et sur la déviation de chaque particule peuvent être utilisées pour produire des images aux propriétés visuelles intéressantes pour le diagnostic. La preuve de concept de la possibilité d'une imagerie quantitative utilisant ces informations est présentée. Ces résultats sont une première étape vers l'imagerie proton utilisant toutes les données enregistrées.

Mots clefs : Imagerie proton, Reconstruction, Hadronthérapie, Planification de traitement

Résumé en anglais / Summary in English

Proton computed tomography is being studied as an alternative to X-ray CT imaging for charged particle therapy treatment planning. By directly mapping the relative stopping power of the tissues, the uncertainty on the range of the particles could be reduced. A proton scanner consists in a calorimeter or range-meter to obtain the information on the energy lost by each proton in the object, as well as two sets of tracking planes to record the position and direction of each particle upstream and downstream from the object.

This work concerns the study of the outputs of a proton scanner and the possible use of all the recorded information. A reconstruction study made it possible to show that the information on the transmission rate and on the scattering of each particle can be used to produce images with visual properties that could be of interest for diagnostics. The proof of concept of the possibility of quantitative imaging using this information is also put forward. These results are the first step towards a clinical use of proton imaging with all the recorded data.

Keywords: Proton computed tomography, Image reconstruction, Charged particle therapy, Treatment planning